

Influence of Shear and Temperature on
the Crystallisation of Long Chain
Hydrocarbon Formulation Ingredients

By

Paul Lewis

Submitted in accordance with the requirements for the
degree of

DOCTOR OF PHILOSOPHY
(Chemical Engineering)

THE UNIVERSITY OF LEEDS
School of Chemical and Process Engineering
September 2019

The candidate confirms that the work submitted is his own, and that appropriate credit has been given where reference has been made to the work of others. This copy has been supplied on the understanding that it is copyright material and that no quotation from the thesis may be published without proper acknowledgement.

© 2019 The University of Leeds Paul Lewis

Acknowledgements

First, I would like to thank both my supervisor's Dr Xiaojun Lai and Professor Kevin Roberts for guiding me through my PhD. I am especially grateful to Dr Xiaojun Lai and Dr Guilherme Calligaris for helping make the synchrotron experiments in Brazil a success, through planning and getting hands-on during data collection.

I would also like to thank Dr Simon Connell for taking the time to personally help conduct AFM experiments in his laboratory in Physics and help me understand the meaning of the results. Also, I would like to thank Simon Greener and Dave Sturgis at P&G for their meaningful insights, supply of materials and use of analytical equipment. Another thanks extend to past and present members of the crystallisation group, including Pete, Ian, Tom, Hien, Xue, David, Mo, Ulrike, Pablo, Boyang and Jabbar who have made working in the lab and group meetings a pleasurable experience.

I am grateful to have a fun, friendly office and housemates who I have lived with. Often, I have read online of PhD students feeling isolated, and this certainly hasn't been my experience. Thanks to Andy, Scott, Evan, Ben, Guilherme, Frasier, Yefeng, Toby, Andy, Jess, Jamie, Josh, Alex, Matt, Julio, Alex, Joe, Mo, Abdul, Georgina, Charlotte, Alastair, Serish and James.

Finally, I would like to thank my family, Jude, Mark, Alfie, Maureen and my girlfriend Timi for giving me the support and encouragement I needed to finish these studies.

Contents

ACKNOWLEDGEMENTS	3
ABSTRACT	8
LIST OF SYMBOLS	9
LIST OF ABBREVIATIONS	12
LIST OF FIGURES	14
LIST OF TABLES	25
1 INDUSTRIAL RELEVANCE, RESEARCH AIMS AND OBJECTIVES	29
1.1 INTRODUCTION	29
1.2 INDUSTRIAL CONTEXT	29
1.2.1 <i>The mechanism behind the sweating of humans</i>	30
1.3 INDUSTRIAL RELEVANCE	32
1.3.1 <i>Typical Formulation of Wax Deodorant Sticks</i>	34
1.4 RESEARCH AIMS AND OBJECTIVES	35
1.5 JUSTIFICATION FOR MATERIAL SELECTION	38
1.6 PROJECT MANAGEMENT	38
1.7 REPORT STRUCTURE	38
2 UNDERLYING SCIENCE AND LITERATURE REVIEW	42
2.1 INTRODUCTION	42
2.2 UNDERLYING SCIENCE	42
2.2.1 <i>Crystallisation Theory</i>	42
2.2.2 <i>Mixtures and Phase Diagrams</i>	46
2.2.3 <i>Thermodynamics</i>	48
2.2.4 <i>Crystallisation and Crystallisation Kinetics</i>	49
2.3 POLYMORPHISM OF LONG-CHAIN ALCOHOLS, ALKANES AND TRIGLYCERIDES	52
2.3.1 <i>Hydrogenated Castor Oil and Triglycerides</i>	52
2.3.2 <i>1-Octadecanol and n-Alkanols</i>	58
2.3.3 <i>Petrolatum and n-alkanes</i>	63
2.3.4 <i>Relevant Binary Mixtures Studied in the Literature</i>	65
2.3.1 <i>Shearing of Hydrocarbons</i>	69
2.3.2 <i>Comparing and Contrasting Alkanes, Alcohols and Triglycerides</i>	71
2.4 CHARACTERISATION TECHNIQUES	71
2.4.1 <i>Lab Conducted Powder X-ray Diffraction</i>	71
2.4.1 <i>Rheology</i>	72
2.4.2 <i>DSC</i>	73
2.4.1 <i>Measuring Mechanical Properties and Morphology of Phases within Binary Mixtures</i>	74
2.4.2 <i>Hot Stage Microscopy</i>	78

2.4.3	<i>Gas Chromatography</i>	78
2.4.4	<i>SEM</i>	79
2.4.5	<i>Polythermal Turbidity Studies</i>	79
2.5	CONCLUSION	80
3	METHODS AND MATERIALS	82
3.1	INTRODUCTION	82
3.2	MATERIALS OF STUDY	82
3.2.1	<i>Solvents</i>	82
3.2.2	<i>Standard Binary Mixture Sample Preparation Method</i>	82
3.3	EXPERIMENTAL METHODS	83
3.3.2	<i>Polythermal Shear Synchrotron Radiation Experiments (LNLS)</i>	83
3.3.3	<i>Rheological Measurements</i>	88
3.3.4	<i>Differential Scanning Calorimetry (DSC)</i>	89
3.3.5	<i>Thermal Gravimetric Analysis (TGA)</i>	89
3.3.6	<i>Gas Chromatography (GC-MS)</i>	90
3.3.7	<i>Hot Stage Optical Microscopy</i>	90
3.3.8	<i>Growth Cell</i>	91
3.3.9	<i>Atomic Force Microscopy (AFM)</i>	91
3.3.10	<i>Scanning Electron Microscopy (SEM)</i>	93
3.3.11	<i>Poly-thermal Turbidity Studies</i>	94
3.4	CONCLUSION	99
4	CHARACTERISATION OF FORMULATION INGREDIENTS	101
4.1	INTRODUCTION	101
4.2	1-OCTADECANOL	101
4.3	HYDROGENATED CASTOR OIL	109
4.4	PETROLATUM	117
4.5	CONCLUSION	122
5	CRYSTALLISATION KINETICS AND MORPHOLOGY OF 1-OCTADECANOL AND HYDROGENATED CASTOR OIL IN POLAR AND NON- POLAR SOLVENTS	125
5.1	INTRODUCTION	125
5.2	SOLUBILITY AND METASTABLE ZONE WIDTH MEASUREMENTS	125
5.2.1	<i>Measurement of Metastable Zone Width</i>	126
5.2.2	<i>Relating Nature of Solute and Solvent to Solubility</i>	140
5.3	THERMODYNAMIC ANALYSIS USING THE VAN 'T HOFF EQUATION	142
5.4	INSIGHT INTO THE NUCLEATION MECHANISM USING THE KBHR APPROACH	147
5.5	CRYSTAL MORPHOLOGY OBSERVED OF 1-OCTADECANOL IN DODECANE AND D5 SOLVENTS	157
5.6	CONCLUSION	161

6	PHASES, CRYSTAL MORPHOLOGY AND MECHANICAL PROPERTIES OF 1-OCTADECANOL AND HYDROGENATED CASTOR OIL MIXTURES -----	164
6.1	INTRODUCTION -----	164
6.2	1-OCTADECANOL AND HYDROGENATED CASTOR OIL -----	165
6.2.1	<i>Thermal Analysis of 1-Octadecanol and Hydrogenated Castor Oil</i> -----	165
6.2.2	<i>X-ray Diffraction Patterns of Hydrogenated Castor Oil and 1-Octadecanol.</i> -----	171
6.2.3	<i>Binary Phase Diagram of 1-Octadecanol and Hydrogenated Castor Oil</i> -----	172
6.2.4	<i>Atomic Force Microscopy of Hydrogenated Castor Oil and 1-Octadecanol Binary Mixture</i> -----	174
6.3	1-OCTADECANOL AND ALKANES -----	186
6.3.1	<i>Thermal Analysis of 1-Octadecanol and Dodecane Binary Mixtures</i> -----	186
6.3.2	<i>Thermal Analysis of 1-Octadecanol and Petrolatum Binary Mixtures</i> -----	189
6.3.3	<i>XRD patterns of 1-Octadecanol and Petrolatum binary mixtures</i> -----	194
6.3.4	<i>Binary Phase Diagram of 1-Octadecanol and Petrolatum</i> -----	195
6.4	1-OCTADECANOL IN D5 SOLVENT -----	195
6.5	DISCUSSION -----	197
6.6	CONCLUSION -----	199
7	INFLUENCE OF SHEAR ON THE STRUCTURE OF 1-OCTADECANOL IN SOLUTION -----	201
7.1	INTRODUCTION -----	201
7.2	PREPARATION WORK FOR TEMPERATURE AND SHEAR SYNCHROTRON STUDY AT THE BRAZILIAN SYNCHROTRON LIGHT LABORATORY -----	202
7.2.1	<i>Influence of Shear on the Crystallisation and Melting Temperature of Long-chain Hydrocarbons</i> -----	202
7.2.2	<i>Shear Cell Design</i> -----	207
7.2.3	<i>Calibration of the Anton Parr Rheometer and the Brookfield Viscometer</i> -----	210
7.3	ONLINE SIMULTANEOUS SHEAR/TEMPERATURE STUDIES ON 1-OCTADECANOL WITH AND WITHOUT SOLVENT -----	213
7.3.1	<i>1-Octadecanol</i> -----	215
7.3.2	<i>1-Octadecanol with Decamethylcyclopentasiloxane (D5) Solvent</i> -----	224
7.3.3	<i>1-Octadecanol with Dodecane Solvent</i> -----	232
7.4	DISCUSSION -----	236
7.5	CONCLUSION -----	237
8	CONCLUSIONS -----	240
8.1	INTRODUCTION -----	240
8.2	CONCLUSIONS FOCUSED ON RELATIONSHIPS BETWEEN PROCESS PARAMETERS, CRYSTALLISATION, POLYMORPHISM AND PHYSICAL PROPERTIES OF WAX STICK STRUCTURING INGREDIENTS -----	241
8.2.1	<i>Characterisation of the Structuring Long Chain Hydrocarbon Ingredients</i> -----	241
8.2.2	<i>Combining of Formulation Ingredients in Mixtures</i> -----	243
8.2.3	<i>Influence of Shear and Solvent on Crystal Structure of Formulation Ingredients</i> -----	244
8.3	REVISITING THE ORIGINAL AIMS AND OBJECTIVES -----	246

8.4 IDEAS FOR FUTURE WORK-----246

9 BIBLIOGRAPHY ----- 249

Abstract

The thesis studies mixtures of alkanes, alkanols, and triglycerides that are used to provide structure to cosmetic products. These materials are blended together in such a way to create a product that is stable and rigid in the packaging, but deposits a thin film of material when rubbed on the skin. This research is driven by the industrial need to understand further the fundamental mechanisms occurring when the product is processed for the purpose of predicting scale-up behaviour. The aim of the project is to discover links between process conditions, crystallisation, polymorphism, physical properties and product performance.

The morphology, crystal structure, composition, thermal and physical properties of individual components, HCO, Petrolatum and 1-Octadecanol, was characterised using an array of analytical techniques including DSC, TGA, XRD, GC, SEM, AFM and Hot-Stage Microscopy. The properties of the three structuring materials were compared and contrasted to discover their role in the formulation.

Before studying the binary mixtures of 1-Octadecanol; HCO, solubility, thermodynamics and crystallisation kinetics of these materials were studied in a range of relevant non-polar and polar solvents including Dodecane, Undecane, Ethanol, Acetone and D5 using polythermal turbidity data. The data was analysed using van 't Hoff, and KBHR analysis and both materials were found to be most soluble in protic polar solvents and least soluble in non-polar solvents.

Binary mixtures have been studied through creating a series of phase diagrams using DSC and morphology, and mechanical property information has been superimposed with respect to composition using AFM. Binary mixtures of HCO and 1-Octadecanol have found to exhibit 4 distinct morphologies.

The final part of the project focused on the impact of shear and solvent on the crystal structure, polymorphism and rheology of the main structuring ingredient. Experiments using an online custom-made shear cell at a synchrotron allowed structural, rheological, and temperature data to be captured simultaneously, giving insight into mechanisms occurring during processing of the cosmetic products. The presence of shear and solvent has been found to induce phase separation of the rotator and gamma phases of 1-Octadecanol.

List of Symbols

Symbol	Definition	Units
Å	Angstrom	Å
A	Activity	
B	Dimensionless thermodynamic parameter	
°C	Degrees Celsius	°C
cP	Centipoise	Pa.s
D	Position	M
D	Lattice spacing	Å
E	Energy	J
E	Young's modulus	Pa
eV	Electron volt	J
F	Force	N
F	Degrees of freedom	
G	grams	G
H	Hexagonal	
Hz	Hertz	Hz
ΔH_{diss}	Enthalpy of dissolution	kJmol^{-1}
ΔH_{fus}	Enthalpy of fusion	kJmol^{-1}
i^*	Critical nucleus size	
J	Joules	J
K	Boltzmann's constant	JK^{-1}
k_n	Nucleus shape factor	

K	Kelvin	K
L	Litre	L
M	Meter	M
M	Mass	G
N	Number of independent components	
Nm	Newton meter	Nm
O_⊥	Perpendicular	
P	Number of phases	
Pa	Pascal	Pa
Q	Cooling rate	°Cmin ⁻¹
R	Radius	Nm
R	Ideal gas constant	Jmol ⁻¹ K ⁻¹
R	Carbon chain	
r*	Critical radius	Nm
S	second	S
ΔS_{diss}	Enthalpy of dissolution	kJmol ⁻¹
T	Temperature	K
T_c	Crystallisation temperature	K
T_{diss}	Dissolution temperature	K
T_e	Equilibrium temperature	K
T_m	Melting temperature	K
T_{//}	Parallel	
u_c	Critical undercooling	
V	Volt	V

v_0	Volume occupied	m^3
Wt	Weight	G
Z	Charge	C
Θ	Bragg angle	$^\circ$
Γ	Activity coefficient	
Λ	Wavelength	\AA
H	Apparent viscosity	cP
T	Shear stress	Pa
$\dot{\Gamma}$	Shear rate	s^{-1}
X	Mole fraction	
Λ_{eff}	Interfacial tension	mJm^{-2}

List of Abbreviations

Abbreviation	Definition
AFM	Atomic Force Microscope
APDO	Antiperspirant and/or deodorant
D5	Decamethylcyclopentasiloxane
DCM	Dichloromethane
DOD	Dodecane
DSC	Differential Scanning Calorimetry
FAME	Fatty acid methyl ester
FDA	Food and Drug Administration
FWHM	Full Width Half Maximum
GC	Gas Chromatography
HCO	Hydrogenated Castor Oil
HPLC	High Pressure Liquid Chromatography
KBHR	Kashchiev-Borissova-Hammond-Roberts approach
LNLS	Brazilian Synchrotron Light Laboratory
NMR	Nuclear Magnetic Resonance
MF	Mole Fraction
MSZW	Metastable Zone Width
OCT	1-Octadecanol
OH	Hydroxy
P&G	Procter and Gamble
PET	Petrolatum

PF-QNM Peak Force Quantitative Nanomechanical Mapping

ppm Parts per million

Rpm Revolutions per minute

SAXS Small Angle X-ray Scattering

SEM Scanning Electron Microscope

STD Standard Deviation

TAG Triacylglycerol

TGA Thermogravimetric Analysis

USAXS Ultra Small Angle Scattering

XRD X-ray Diffraction

List of Figures

Figure 1-1 Schematic diagram of the two types of human sweat gland. a) eccrine gland and b) apocrine gland.[1]	31
Figure 1-2 Diagram showing the production process of wax stick deodorant, based on communications with P&G.[10, 11]	33
Figure 1-3 Two examples of wax stick deodorant products currently available for sale on P&G's online store in North America.[13].....	34
Figure 1-4 The methodology used throughout this project displayed using flow diagram detailing the links between process conditions, formulation, crystallisation, physical properties and product performance.	37
Figure 1-5 Flow diagram schematic of the report structure.....	40
Figure 2-1 A general three-dimensional unit cell with lattice parameters $(a,b,c,\alpha,\beta,\gamma)$. [22]	43
Figure 2-2 The fourteen Bravais lattices grouped by the seven crystal systems.[24].....	44
Figure 2-3 Gibbs phase rule.[23]	47
Figure 2-4 Model example of a phase diagram where materials A and B are mixed in the solid and liquid phase.	48
Figure 2-5 Diagram displaying metastable zone width, super-solubility curve passing through CC'C'' and solubility curve passing through BB'B''.[31]	51
Figure 2-6 Kossel model of crystal surface displaying growth mechanism.[34].....	52
Figure 2-7 Hydrogenation reaction of the main component of Castor Oil to form Hydrogenated Castor Oil (tri-12-hydroxylstearin).....	53
Figure 2-8 Diagram displaying the components of Castor Oil. ^[38]	53
Figure 2-9 On the left shows the molecular structure of triacylglycerol (TAG) with R ₁ , R ₂ and R ₃ being individual fatty acid chains. Top right and bottom left are saturated and unsaturated fatty acid, respectively. The figure was taken from C. Himawan <i>et al.</i> review paper.[36].....	55

Figure 2-10 The “chair” configuration packing structures (left) and the subcell structure of the three most common TAG polymorphs viewed from above the crystal planes (right). The figure was taken from C. Himawan <i>et al.</i> review paper.[36]	56
Figure 2-11 Powder X-ray diffraction patterns of the α , β' and β polymorphs of Tristearin taken from E. Da Silva <i>et al.</i> [46]	57
Figure 2-12 Spherulites in the β' polymorphic form crystallised from 30%-w SSS of PPP/SSS binary mixture at (left) 52.5°C and (right) 49°C. The figure was taken from C. Himawan <i>et al.</i> review paper.[36, 50].....	58
Figure 2-13 The molecular structure of 1-Octadecanol (C ₁₈ H ₃₇ OH).....	59
Figure 2-14 Unit cell of 1-Octadecanol γ phase (Space Group: A 2/a (15), Cell: a 8.998(5)Å b 4.940(2)Å c 98.01(3)Å, α 90° β 122.59(1)° γ 90°) sourced from the Cambridge Crystallographic Data Centre.[54].....	60
Figure 2-15 a) X-ray topography of a single cell of 1-Octadecanol, which contains large inclusions of lattice defects. b) Phase-contrast optical microscope image of 1-Octadecanol. Sourced from Izumi <i>et al.</i> [56].....	60
Figure 2-16 a) DSC Crystallisation curves of commercial-grade C ₁₉ H ₃₉ OH and C ₂₀ H ₄₁ OH upon heating and cooling at 2K min ⁻¹ sourced from Ventola <i>et al.</i> [53] b) Hydrogen bonding present in the γ phase crystal structure of n-hexadecanol with gauss (G) and trans (T) configurations taken from Ishikawa <i>et al.</i> [55].....	61
Figure 2-17 X-ray diffraction pattern of quenched C ₂₀ H ₄₁ OH immediately after sample preparation. Sourced from Ventola <i>et al.</i> [53]	62
Figure 2-18 Image showing the Guiner-Simon photographs for C ₁₉ H ₃₉ OH and C ₂₀ H ₄₁ OH, sourced from Ventola <i>et al.</i> [53].....	62
Figure 2-19 DSC curve of C ₂₃ H ₄₈ at a range of heating and cooling rates (K min ⁻¹) a) cooling and b) heating.[81]	65
Figure 2-20 A) shows DSC crystallisation curves of C ₂₀ OH in peanut oil binary mixtures and B) shows the crystallisation curves of a range of pure fatty alcohols taken from the study by Fabio Valoppi <i>et al.</i> [57].....	66
Figure 2-21 XRD patterns of C ₂₀ OH (A) and C ₁₄ OH (B) binary mixtures in peanut oil taken from the study by Fabio Valoppi <i>et al.</i> [57].....	67

Figure 2-22 Polarized light microscope images of 5% C ₂₂ OH, C ₂₀ OH, C ₁₈ OH, C ₁₆ OH in Peanut Oil mixtures crystallised under slow and fast cooling after 1 day of storage. Scale bar 200µm. Sourced from Valoppi <i>et al.</i> ^[87]	68
Figure 2-23 Cryo-SEM of fatty alcohol oleogels formed upon slow cooling (left) and fast cooling (right) taken from Valoppi <i>et al.</i> ^[87]	69
Figure 2-24 The shear cell used (left) and the SAXS experimental data upon cooling cocoa butter to 20°C whilst shearing at 3s ⁻¹ (right). Sourced from MacMillan <i>et al.</i> ^[90]	70
Figure 2-25 Diagram showing X-ray Diffraction (XRD) experimental set up where T is the X-ray source, C is the crystal sample, O is the axis the beam and crystal are rotated about, and D is the detector that measures the intensity of diffracted X-rays. ^[92]	72
Figure 2-26 Plot displaying the four possible flow behaviours. a) displaying shear stress vs shear rate (deformation rate) and b) displaying apparent viscosity vs shear rate (deformation rate). ^[94]	73
Figure 2-27 Stress vs strain graph displaying plastic and elastic deformation regions. ..	75
Figure 2-28 Stress vs strain displaying brittle, strong non-ductile, ductile and plastic material profiles.....	76
Figure 2-29 Diagram of force vs separation for a single cycle of the tip movement during peak-force tapping AFM. The blue line is the tip approaching, and the red line is the tip withdrawing. The peak force is a constant value, and once peak-force is reached the tip withdraws. This image is adapted from Ref. ^[102] and taken from the paper by P. Trtik <i>et al.</i> ^[97]	77
Figure 2-30 Elastic modulus map of Hardened Cement, a) elastic modulus, b) segmentation to porosity (black), unhydrated residues (white), Calcium hydroxide (light grey) and other hydrates (dark grey), c) displays the average elastic modulus of each region. P. Trtik <i>et al.</i> ^[97]	78
Figure 2-31 Hot stage microscope experimental set up.....	78
Figure 3-1 Image showing the shear cell experimental set up at the Brazilian Synchrotron Light Laboratory.	87
Figure 3-2 Images captured during calibration of the AFM PF-QNM experiments using a blend of polystyrene and low-density polyethylene. a) displays height map of the sample	

surface, b) Young's modulus map of the surface, c) optical image of the area studied, and d) plot of Young's modulus distribution across the surface.....	93
Figure 3-3 Example of polythermal method experiment were temperature was cycled between 0-100-0°C over time, and the change in light transmission (turbidity) was measured.	95
Figure 3-4 Change in turbidity measurement as the temperature is cycled during the polythermal method.	95
Figure 4-1 Differential Scanning Calorimetry (DSC) graph showing the liquid-rotator-gamma phase transitions of 1-Octadecanol when heated and cooled at 1°C/min using Mettler Toledo DSC1 at Leeds	102
Figure 4-2 TGA graph showing the mass loss of 1-Octadecanol when heated at 5°C/min to 500°C.	103
Figure 4-3 Stacked XRD graph displayed the metastable rotator phase at 55°C and the stable gamma phase at room temperature of 1-Octadecanol.....	104
Figure 4-4 A series of optical images capturing, the transitions between liquid, rotator and gamma phases upon cooling 1-Octadecanol from the melt.	105
Figure 4-5 Atomic Force Microscope (AFM) and Optical Microscope (OM) images of 1-Octadecanol cooled from the melt to room temperature at 1°C/min. a) Height map of surface (AFM), b) Youngs Modulus map (AFM), c) High magnification optical image of the area studied (OM) and d) Low magnification optical image of the sample surface (OM).	106
Figure 4-6 Atomic Force Microscope (AFM) and Optical Microscope (OM) images of 1-Octadecanol cooled from the melt to room temperature at 5°C/min. a) Height map of surface (AFM), b) Youngs Modulus map (AFM), c) High magnification optical image of the area studied (OM) and d) Low magnification optical image of the sample surface (OM).	107
Figure 4-7 Atomic Force Microscope (AFM) and Optical Microscope (OM) images of 1-Octadecanol cooled from the melt to room temperature at 20°C/min. a) Height map of surface (AFM), b) Youngs Modulus map (AFM), c) High magnification optical image of the area studied (OM) and d) Low magnification optical image of the sample surface (OM).	108

Figure 4-8 Change in Viscosity (left) and Shear Stress (right) upon ramping Shear Rate for 1-Octadecanol at a series of different temperatures.....	109
Figure 4-9 Differential Scanning Calorimetry (DSC) graph showing the phase transitions of Hydrogenated Castor Oil when heated and cooled at 1°C/min.....	110
Figure 4-10 Thermal Gravimetric Analysis graph showing the mass loss of Hydrogenated Castor Oil when heated at 5°C/min to 600°C.....	111
Figure 4-11 Stacked X-ray Diffraction patterns of HCO captured upon cooling from the melt at 95°C to 33°C.....	112
Figure 4-12 Two stacked X-ray Diffraction patterns of Hydrogenated Castor Oil as received from P&G (Black) and twice recrystallised(Red).	112
Figure 4-13 A series of optical images taken upon cooling Hydrogenated Castor Oil from the melt.....	113
Figure 4-14 Atomic Force Microscope (AFM) and Optical Microscope (OM) images of Hydrogenated Castor Oil cooled from the melt to room temperature at 1°C/min. a) Height map of surface (AFM), b) Youngs Modulus map (AFM), c) High magnification optical image of the area studied (OM) and d) Low magnification optical image of the sample surface (OM).....	114
Figure 4-15 Atomic Force Microscope (AFM) and Optical Microscope (OM) images of Hydrogenated Castor Oil cooled from the melt to room temperature at 5°C/min. a) Height map of surface (AFM), b) Youngs Modulus map (AFM), c) High magnification optical image of the area studied (OM) and d) Low magnification optical image of the sample surface (OM).....	115
Figure 4-16 Atomic Force Microscope (AFM) and Optical Microscope (OM) images of Hydrogenated Castor Oil cooled from the melt to room temperature at 20°C/min. a) Height map of surface (AFM), b) Youngs Modulus map (AFM), c) High magnification optical image of the area studied (OM) and d) Low magnification optical image of the sample surface (OM).....	116
Figure 4-17 Change in Viscosity (right) and Shear Stress (left) upon ramping Shear Rate for Hydrogenated Castor Oil at a series of different temperatures.....	117
Figure 4-18 Differential Scanning Calorimetry (DSC) graph showing the phase transitions of Petrolatum when heated and cooled at 1°C/min.....	118

Figure 4-19 TGA graph showing the mass loss of Petrolatum when heated at 5°C/min to 600°C	119
Figure 4-20 A series of optical images of needle-shaped crystals taken upon cooling Petrolatum from the melt taken using a hot stage microscope.....	121
Figure 4-21 Change in Viscosity (left) and Shear Stress (right) upon ramping Shear Rate for Petrolatum at a series of different temperatures.....	122
Figure 5-1 Determining the Metastable Zone Width through extrapolation of the crystallisation and dissolution temperatures recorded at 0.25, 1, 2 and 3.2 °C/min, back to zero cooling rate.....	127
Figure 5-2 Metastable Zone Width of 1-Octadecanol in a range of solvents.....	139
Figure 5-3 Metastable Zone Width of Hydrogenated Castor Oil in a range of solvents.	139
Figure 5-4 Solubility Curves of 1-Octadecanol in Ethanol, Dodecane, Undecane, D5 and Acetone solvents.....	141
Figure 5-5 Solubility Curves of Hydrogenated Castor Oil in Ethanol and Acetone solvents.....	142
Figure 5-6 van 't Hoff plot displaying the ideal solubility of 1-Octadecanol and 1-Octadecanol in Dodecane and Undecane solvents.....	144
Figure 5-7 van 't Hoff plot displaying the ideal solubility of 1-Octadecanol and 1-Octadecanol in Ethanol, Acetone and D5 solvents.	144
Figure 5-8 van 't Hoff plot displaying the ideal solubility of 1-Octadecanol and 1-Octadecanol in Ethanol, Acetone, Dodecane, Undecane and D5 solvents.....	145
Figure 5-9 van 't Hoff plot displaying the ideal solubility of HCO and HCO in Ethanol and Acetone solvents.	145
Figure 5-10 Dielectric constants plotted against enthalpy and entropy values of 1-Octadecanol in Ethanol, Acetone, Dodecane, Undecane and D5 solvents.....	146
Figure 5-11 a) relative critical undercooling (u_c) plotted against ln cooling rate (q) for 1-Octadecanol in Ethanol at 143g/l, and the data were fitted to Equation 3-9. b-h) plot of q vs u_c in ln-ln coordinates for 1-Octadecanol and Hydrogenated Castor Oil dissolved in Ethanol, Acetone, Dodecane, Undecane and D5 solvents.	151

Figure 5-12 Images taken of 1-Octadecanol crystallising and dissolving in a 25g/l Dodecane solution using a 5x optical lens.159

Figure 5-13 A series of SEM images of 1-Octadecanol crystals formed from Acetone solution using secondary electron mode.160

Figure 5-14 A series SEM image of Hydrogenated Castor Oil crystals formed from Acetone solution using secondary electron mode.161

Figure 6-1 Peak Integral (Enthalpy) of Hydrogenated Castor Oil Crystallisation with respect to changing composition. Hydrogenated Castor Oil is represented by the blue line (peak 3), and Hydrogenated Castor Oil/1-Octadecanol is represented by the red line (peak 4) in the Differential Scanning Calorimetry (DSC) results upon cooling (Figure 6-2).166

Figure 6-2 Stacked normalised Differential Scanning Calorimetry (DSC) measurements of binary mixtures of 1-Octadecanol and Hydrogenated Castor Oil when cooled from the melt at 1°C/min. 1) 1-Octadecanol rotator phase crystallisation, 2) 1-Octadecanol rotator gamma phase transition, 3) Hydrogenated Castor Oil crystallisation, 4) 1-Octadecanol/Hydrogenated Castor Oil crystallisation and 5) Hydrogenated Castor Oil low temperature transition.....167

Figure 6-3 Stacked normalised Differential Scanning Calorimetry (DSC) measurements of binary mixtures of 1-Octadecanol and Hydrogenated Castor Oil when heated from 0°C at 1°C/min. 1) 1-Octadecanol rotator phase melting, 2) 1-Octadecanol rotator gamma phase transition, 3) 1-Octadecanol rotator/gamma phase melting and 4) Hydrogenated Castor Oil melting.168

Figure 6-4 Stacked X-ray Diffraction (XRD) patterns of binary mixtures of Hydrogenated Castor Oil and 1-Octadecanol.....172

Figure 6-5 Binary phase diagram of Hydrogenated Castor Oil and 1-Octadecanol mixtures produced by plotting the onset of phase transitions measured by Differential Scanning Calorimetry (DSC) upon cooling at 1°C/min (left). Diagram only includes the descriptions of the morphologies observed in each binary mixture with Atomic Force Microscopy (AFM) at room temperature with a legend displayed above the phase diagram. A graph to show measured Young’s modulus vs composition (right)173

Figure 6-6 Studying Hydrogenated Castor Oil/1-Octadecanol (0.2/0.8) cooled at 1°C/min using Atomic Force (AFM) and Optical (OM) Microscopy. A ridge of hard 1-

Octadecanol plate was observed a) is a 3D render of the surface measured (AFM), b) Young's modulus map of the surface (AFM), c) Peak force error displaying topographical information (AFM), d) Optical image of area measured (OM) and e) the edge of the bulk sample (OM).....177

Figure 6-7 Studying Hydrogenated Castor Oil/1-Octadecanol (0.4/0.6) cooled at 1°C/min using Atomic Force (AFM) and Optical (OM) Microscopy. 1st and 2nd region displays adjacent 1-Octadecanol and Hydrogenated Castor Oil plates: a, c) is a height map across the area measured (AFM), b, d) Young's modulus map of the surface (AFM), e) Optical image of area measured (OM) and f) the edge of the bulk sample (OM)....178

Figure 6-8 Studying Hydrogenated Castor Oil/1-Octadecanol (0.6/0.4) cooled at 1°C/min using Atomic Force (AFM) and Optical (OM) Microscopy. 1st region displays adjacent 1-Octadecanol and Hydrogenated Castor Oil plates; a) is a height map across the area measured (AFM), b) Young's modulus map of the surface (AFM), c) is a map of the peak force error (AFM) and d) the edge of the bulk sample (OM).....179

Figure 6-9 Studying Hydrogenated Castor Oil/1-Octadecanol (0.6/0.4) cooled at 1°C/min using Atomic Force (AFM) and Optical (OM) Microscopy. 2nd region displays a eutectic mixture between 1-Octadecanol and Hydrogenated Castor Oil; a) is a height map across the area measured (AFM) and b) is Young's modulus map of the surface (AFM), c, d, e and f) displays enlarged areas of the height and Young's modulus maps..180

Figure 6-10 Studying Hydrogenated Castor Oil/1-Octadecanol (0.8/0.2) cooled at 1°C/min using Atomic Force (AFM) and Optical (OM) Microscopy. The region observed is a eutectic mixture between Hydrogenated Castor Oil and 1-Octadecanol; a) is a height map across the area measured (AFM), b) Young's modulus map of the surface (AFM), c) Peak force error displaying topographical information (AFM) and d) Optical image of the area of the sample measured (OM).....182

Figure 6-11 Studying Hydrogenated Castor Oil/1-Octadecanol (0.8/0.2) at 1°C/min using Atomic Force (AFM) and Optical (OM) Microscopy. The region displays soft HCO flat plates; a) is a height map across the area measured (AFM), b) Young's modulus map of the surface (AFM), c) Peak force error displaying topographical information (AFM) and d) Optical image of the area of the sample measured (OM).183

Figure 6-12 Studying Hydrogenated Castor Oil/1-Octadecanol (0.8/0.2) at cooled 1°C/min using Atomic Force (AFM) and Optical (OM) Microscopy. The region displays hard 1-Octadecanol plates; a) is a height map across the area measured (AFM), b) Young's modulus map of the surface (AFM), c) Peak force error displaying topographical information (AFM), d) Optical image of the area of the sample measured (OM) and e) the bulk sample (OM).	184
Figure 6-13 Studying Hydrogenated Castor Oil/1-Octadecanol/Petrolatum (0.8/0.2/0.01) cooled at 20°C/min using Atomic Force (AFM) and Optical (OM) Microscopy; a) is a height map across the area measured (AFM), b) c) Optical image of the area of the sample measured (OM) and d) the bulk sample (OM).	185
Figure 6-14 Studying Hydrogenated Castor Oil/1-Octadecanol (0.8/0.2) cooled at 10°C/min under shear at 200s ⁻¹ using Atomic Force (AFM) and Optical (OM) Microscopy; a) is a height map across the area measured (AFM), b) Young's modulus map of the surface (AFM) c) Optical image of the area of the sample measured (OM) and d) the bulk sample (OM).	186
Figure 6-15 Stacked normalised Differential Scanning Calorimetry (DSC) measurements of binary mixtures of 1-Octadecanol and Dodecane when cooled from the melt at 1°C/min.	188
Figure 6-16 Binary phase diagram of Dodecane and 1-Octadecanol mixtures produced by plotting the onset of phase transitions measured by Differential Scanning Calorimetry (DSC) upon cooling at 1°C/min.	189
Figure 6-17 Stacked normalised Differential Scanning Calorimetry (DSC) measurements of binary mixtures of 1-Octadecanol and Petrolatum when cooled from the melt at 1°C/min. 1) 1-Octadecanol rotator phase crystallisation, 2) 1-Octadecanol rotator-gamma phase transition and 3) Petrolatum crystallisation.	190
Figure 6-18 Stacked normalised Differential Scanning Calorimetry (DSC) measurements of binary mixtures of 1-Octadecanol and Petrolatum when cooled from the melt at 1°C/min. 1) 1-Octadecanol rotator phase melting, 2) 1-Octadecanol rotator-gamma phase transition, 3) 1-Octadecanol Rotator/Gamma Phase Melting and 4) Petrolatum melting.	191
Figure 6-19 Stacked X-ray Diffraction (XRD) patterns of 1-Octadecanol and Petrolatum binary mixtures.	194

Figure 6-20 Binary phase diagram of Petrolatum and 1-Octadecanol mixtures produced by plotting the onset of phase transitions measured by Differential Scanning Calorimetry (DSC) upon cooling at 1°C/min.	195
Figure 6-21 Stacked normalised Differential Scanning Calorimetry (DSC) measurements of binary mixtures of 1-Octadecanol and D5 when cooled from the melt at 1°C/min. 1) 1-Octadecanol rotator phase crystallisation, 2) 1-Octadecanol rotator-gamma phase transition.	196
Figure 6-22 Binary phase diagram of D5 and 1-Octadecanol mixtures produced by plotting the onset of phase transitions measured by Differential Scanning Calorimetry (DSC) upon cooling at 1°C/min.	197
Figure 7-1 Graphs displaying the 1st derivative of torque measured against temperature for 1-Octadecanol (left), Hydrogenated Castor Oil (middle) and Petrolatum (right) whilst being cooled (bottom) and heated (top) at 10 °C/min and sheared at 100s ⁻¹	204
Figure 7-2 Image of Scott Macmillan’s shear cell taken from Scott Macmillan’s thesis.[134]	208
Figure 7-3 Image a) of shear cell in-situ at LNLS beamline, b) 2D cross section design of shear cell with dimensions[135] and c) a 3D image of the shear cell design where water inlet and outlet, along with the cup can be clearly seen.[136]	209
Figure 7-4 Viscosity of S600 standard fluid measured in a) using Brookfield viscometer and Anton Parr rheometer during a temperature sweep, b) Anton Parr viscosity plotted as a function of Brookfield viscosity during the temperature sweep and c) Linear region of the graph where Anton Parr viscosity has been plotted as a function of Brookfield viscosity.	212
Figure 7-5 Experimental temperature profiles for heating, cooling and crash cooling OCT/PET (0.2/0.8) mole fraction binary mixture of 1-Octadecanol in Dodecane, along with the line of best fits and the equation.	214
Figure 7-6 3D Waterfall Plot displaying crystallisation of 1-Octadecanol’s rotator phase and the transition of rotator to gamma phase upon slow cooling from the melt under static conditions.	217
Figure 7-7 Stacked plots display 1-Octadecanol cooled under static conditions from the melt probing a range of q from 0.5 – 2.5 nm ⁻¹ (a) and 2.5 – 5.2 nm ⁻¹ (b). 1-Octadecanol	

crash cooled under static conditions from the melt observing a range of q from 0.5 – 2.5 nm^{-1} (c) and 2.5 – 5.2 nm^{-1} (d).....	218
Figure 7-8 1 st Order Crystallisation Peaks of 1-Octadecanol with a) no shear, b) shear @ 20rpm and c) shear @ 100rpm.	221
Figure 7-9 Heating 1-Octadecanol which had been at 100rpm under static conditions, a) 0.5-2.5 nm^{-1} and b) 2.5-5.75 nm^{-1}	222
Figure 7-10 Variation in d spacing of a) rotator and b) gamma and Full-Width Half Maximum c) rotator and d) gamma phases of 1-Octadecanol upon cooling at different shear regimes	223
Figure 7-11 1 st Order Crystallisation Peaks of D5/OCT (0.2/0.8) with a) no shear, b) shear @ 20rpm and c) shear @ 100rpm	227
Figure 7-12 1 st Order Melting Peaks of D5/OCT (0.2/0.8) with a) no shear, b) shear @ 20rpm and c) shear @ 100rpm	228
Figure 7-13 Variation in d spacing of a) rotator and b) gamma and Full-Width Half Maximum c) rotator, d) gamma phases of D5/OCT (0.2/0.8) mole fraction upon cooling at shear regimes of 0rpm, 20rpm, and 100rpm.	230
Figure 7-14 Displaying relationship between viscosity measured using Brookfield viscometer and changing peak area of the 1 st order 1-Octadecanol gamma and rotator phases with and without solvent being formed during slow cooling. a) Pure 1-Octadecanol, b) D5/OCT (0.2/0.8), c) DOD/OCT (0.8/0.2) and d) DOD/OCT (0.2/0.8) mole fraction.....	231
Figure 7-15 Turbidity study to measure the solubility of 1-Octadecanol's rotator phase in Dodecane	233
Figure 7-16 1 st order rotator and gamma phases of 1-Octadecanol upon slow cooling when sheared. Dodecane/1-Octadecanol (0.8/0.2) at a) 0rpm and b) 100rpm shear. Dodecane/1-Octadecanol (0.2/0.8) at c) 0rpm and d) 100rpm shear.....	234
Figure 7-17 Variation in a) d spacing and b) FWHM with temperature and shear of 1 st order gamma phase of Dodecane/1-Octadecanol (0.2/0.8).....	235

List of Tables

Table 1-1 Typical formulation of wax deodorant stick based on P&G's formulation patent. ^[15]	35
Table 2-1 Description of types of bonds and interactions which create crystal structures.[25]	45
Table 2-2 Table showing physical properties of Hydrogenated Castor Oil.....	54
Table 3-1 The table below details all variable temperature and shear experiments completed at LNLS synchrotron, using the shear cell.	85
Table 4-1 Melting temperatures and enthalpies of 1-Octadecanol on Heating at normal pressure.	102
Table 4-2 Gas Chromatography Analysis of Petrolatum.....	119
Table 5-1 Crystallisation and Dissolution temperatures of Hydrogenated Castor Oil in Ethanol.....	128
Table 5-2 Crystallisation and Dissolution temperatures of Hydrogenated Castor Oil in Acetone solution.....	129
Table 5-3 Crystallisation and Dissolution temperatures of 1-Octadecanol in Ethanol solution.....	130
Table 5-4 Crystallisation and Dissolution temperatures of 1-Octadecanol in Acetone solution.....	131
Table 5-5 Crystallisation and Dissolution temperatures of 1-Octadecanol in Dodecane solution.....	132
Table 5-6 Crystallisation and Dissolution temperatures of 1-Octadecanol in Undecane solution.....	133
Table 5-7 Crystallisation and Dissolution temperatures of 1-Octadecanol in D5 solution.	134
Table 5-8 Crystallisation temperature at the kinetic limit (T_c), Equilibrium temperature (T_e) and Meta Stable Zone Width (ΔT) derived by extrapolation back to zero cooling using cooling rate vs crystallisation/dissolution temperature graph for Hydrogenated Castor Oil in Ethanol and Acetone solutions.....	135

Table 5-9 Crystallisation temperature at the kinetic limit (T_c), Equilibrium temperature (T_e) and Meta Stable Zone Width (ΔT) derived by extrapolation back to zero cooling using cooling rate vs crystallisation/dissolution temperature graph for 1-Octadecanol in Ethanol, Acetone and Dodecane solutions.	136
Table 5-10 Crystallisation temperature at the kinetic limit (T_c), Equilibrium temperature (T_e) and Meta Stable Zone Width (ΔT) derived by extrapolation back to zero cooling using cooling rate vs crystallisation/dissolution temperature graph for 1-Octadecanol in Undecane and D5 solutions.	137
Table 5-11 The gradient, y cut and error of the van 't Hoff plot are tabulated alongside, Activity (γ), Entropy (ΔS) and Enthalpy (ΔH). The thermodynamic data was derived from the van 't Hoff plot of Hydrogenated Castor Oil, and 1-Octadecanol dissolved in a range of solvents. ΔH_{soln} calculated using a ΔH_{sub} value of 44.8 kcal mol ⁻¹ for 1-Octadecanol.[130]	146
Table 5-12 The relative critical undercooling (u_c) as a function of cooling rate for Hydrogenated Castor Oil in Ethanol and Acetone.	148
Table 5-13 The relative critical undercooling (u_c) as a function of cooling rate for 1-Octadecanol in Ethanol, Acetone, Dodecane and Undecane.	149
Table 5-14 The relative critical undercooling (u_c) as a function of cooling rate for 1-Octadecanol in D5.	150
Table 5-15 Parameters derived from the KBHR method applied to Hydrogenated Castor Oil crystallising from Ethanol and Acetone solutions. Nucleation mechanism is determined using the gradient of the $\ln q$ vs $\ln u_c$ and the parameters (a_1 , a_2 and $\ln q_0$) are obtained by fitting the equation to $\ln q$ vs u_c	153
Table 5-16 Parameters derived from the KBHR method applied to 1-Octadecanol crystallising from Ethanol, Acetone and Dodecane solutions. Nucleation mechanism is determined using the gradient of the $\ln q$ vs $\ln u_c$ and the parameters (a_1 , a_2 and $\ln q_0$) are obtained by fitting the equation to $\ln q$ vs u_c	154
Table 5-17 Parameters derived from the KBHR method applied to 1-Octadecanol crystallising from Undecane and D5 solutions. Nucleation mechanism is determined using the gradient of the $\ln q$ vs $\ln u_c$ and the parameters (a_1 , a_2 and $\ln q_0$) are obtained by fitting the equation to $\ln q$ vs u_c	155

Table 5-18 Interfacial tension, critical radius and number of molecules in the cluster for Hydrogenated Castor Oil in Acetone and Ethanol solutions.	156
Table 5-19 Interfacial tension, critical radius and number of molecules in the cluster for 1-Octadecanol in Acetone, Ethanol, Dodecane, Undecane and D5 solutions.....	157
Table 6-1 Phase transitions of binary mixtures of Hydrogenated Castor Oil and 1-Octadecanol upon cooling at 1°C/min measured by Differential Scanning Calorimetry (DSC).....	169
Table 6-2 Phase transitions of binary mixtures of Hydrogenated Castor Oil and 1-Octadecanol upon heating at 1°C/min measured by Differential Scanning Calorimetry (DSC).....	170
Table 6-3 Phase transitions of binary mixtures of Petrolatum and 1-Octadecanol upon cooling at 1°C/min measured by Differential Scanning Calorimetry (DSC).....	192
Table 6-4 Phase transitions of binary mixtures of Petrolatum and 1-Octadecanol upon heating at 1°C/min measured by Differential Scanning Calorimetry (DSC).....	193
Table 7-1 Crystallisation and melting temperatures of 1-Octadecanol, Hydrogenated Castor Oil and Petrolatum measured using the Anton Parr rheometer at a cooling and heating rate of 10°C/min and a shear rate of 100s ⁻¹	205
Table 7-2 Table displaying attenuation length calculations of materials the X-ray beam will pass through at the LNLS synchrotron.....	210
Table 7-3 Comparison between dynamic viscosity stated on the bottle of the S600 calibration standard, and measured viscosity of the calibration standard using the Anton Parr rheometer fitted 50mm-1° cone and plate shearing at 100s ⁻¹ while heating at 1°C/min.....	211

Chapter 1: Industrial Relevance, Research Aims and Objectives

This chapter provides an introduction to this thesis by providing a summary of the industrial relevance before revealing the aims and objectives of this research.

1 Industrial Relevance, Research Aims and Objectives

1.1 Introduction

This chapter identifies the scientific needs of the research associated with industrial processing of mixtures of long-chain hydrocarbon. This chapter aims to introduce the reader to cosmetic science and provide a scientific context for this study. This has been achieved through providing the industrial background, product function, industrial process and typical formulation, before stating the aims and objectives of the research. This chapter also defines how this thesis was structured and how this research was conducted.

1.2 Industrial Context

Antiperspirant and/or deodorant (APDO) products are used to keep bodily occurs under control whilst reducing underarm moisture. On the market, there are many different formulations and application methods available to the consumer for applying antiperspirant and/or deodorant. This currently consists of roll-ons, wax deodorant sticks, creams, soft solids, gels, suspension roll-ons, squeeze sprays, pump sprays and pads. In this project, we are investigating the formulation and manufacturing process behind the wax deodorant stick, which currently dominates the market in the United States.[1]

In the United States, during the 1960s, the aerosol used to be the most popular APDO format; however, consumer confidence in the aerosol was knocked by a series of events. First, in 1977, the Food and Drug Administration (FDA) banned Aluminium zirconium complexes from being formulated into aerosols after Gillette reported lung problems in animals which had been subjected to long term inhalation testing. Shortly after this, the Environmental Protection Agency imposed measures to limit the ChlorofluoroCarbon propellants used in aerosols, since they were shown to be depleting the ozone layer in the 1974 Nature publication by MJ Molina and FS Rowlands.[2] By the 1980s, consumers in the United States had lost confidence in aerosol antiperspirants. In Europe, however, APDO sprays are still the most popular format, with wax stick APDO being less commonly used.[3]

Over this time period, the formulations have also evolved to meet consumer need and to meet the regulations of the FDA, such as to remove banned active ingredients, reduce damage to clothes, improve skin irritation or to prevent white residue being visible on skin and clothing after application of a high Silicon product.[1]

1.2.1 The mechanism behind the sweating of humans

Sweating is the process where a fluid is secreted on to a body's surface from sweat glands contained within the skin. Certain mammals have evolved the ability to sweat with the function of maintaining healthy, lubricating skin that has contact surfaces and thermoregulation of body temperature. Without the ability to sweat, humans would not be able to live in all the extreme temperatures the world has to offer or to run a marathon without overheating.[1]

The sweat gland was discovered by Purkinje in 1833, and an estimated 2-4 million sweat glands are present on the surface of the human body. Sweat glands are not evenly distributed across the surface of the skin, with highest densities found on the forehead, chest and back.[1] There is known to be two types of sweat gland. Eccrine glands mainly secrete water and salt to regulate body temperature and apocrine glands transport fats and proteins along with water and salt to the upper skin layers.[4]

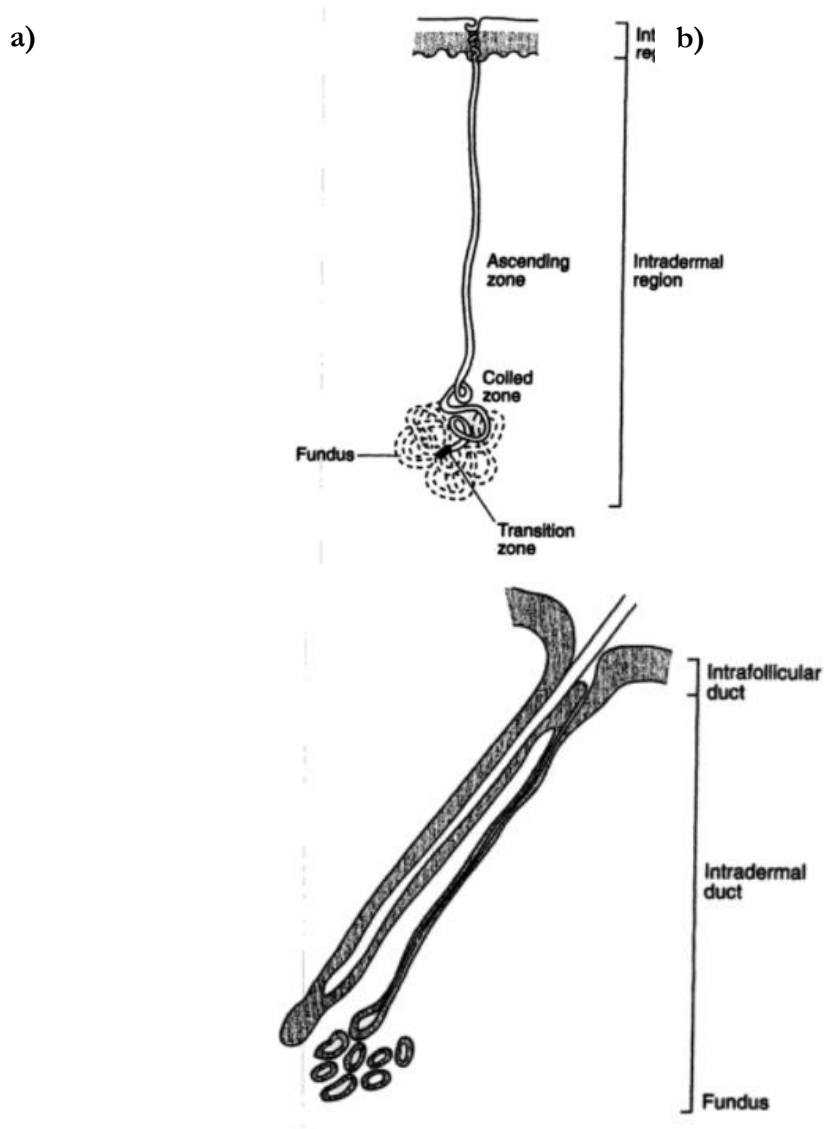


Figure 1-1 Schematic diagram of the two types of human sweat gland. a) eccrine gland and b) apocrine gland.[1]

The source of body odour mainly originates from underneath the arms where there is a high concentration of sweat glands. Initially, the sweat glands produce no odour; however, the natural oils, known as lipids within the apocrine glands, provide a medium for bacteria to grow on the skin. This bacteria breaks down some of the lipids on the skin into compounds that have the characteristic odour of sweat, such as Isovaleric acid.[5]

APDO sticks rely on two mechanisms to keep body odour under control. The first mechanism is for the deodorant to kill bacteria on the skin, reducing the production of compounds associated with body odour. Antiperspirants have a different mechanism, whereby they temporarily inhibit the activity of the sweat glands.[6] As a result, less moisture is produced underarm, reducing the unwanted wetness, whilst reducing body

odour, since there is less moisture in the skin for the bacteria to react upon. It is thought that this works by Aluminium salts, which are contained within the antiperspirant formulation, temporarily block the sweat glands, preventing moisture from being secreted.[7]

1.3 Industrial Relevance

In the factory for APDO stick production seen in Figure 1-2, there are two tanks both fitted with an agitator. The cold phase tank contains emollients, colourants, perfumes and emulsifiers and hot phase tank contains molten wax components dissolved in the Silicone solvent.[8] The hot phase tank is heated using steam, and during the blending process, temperature control and mixing are crucial to ensure the wax components aren't burnt whilst they are added to the tank and melted. Once all the wax components are added to the batch, the batch is mixed until uniform. The core wax components consist of a mixture of high melting point waxes (hydrogenated castor wax) and low melting point waxes (1-Octadecanol and Petrolatum), dissolved in Silicone to produce a sensory pleasing product.[9] The two mixtures are both fed by a pipe from the two tanks to a single static mixing block. Here the cold-active phase combines with the molten wax, crash cooling the wax components from 70-90°C to 55-60°C.[8] The wax stick deodorant formulation, containing the molten crystalline wax components is fed through the nozzle filling the empty APDO stick canisters at less than 2°C above the temperature, which the composition fully solidifies.[8] The empty canisters are filled whilst they are moving on a conveyor belt. The temperature, which the canisters are filled is crucial. If the molten wax is too hot, the solids in the formulation may settle at the bottom of the canister. If the molten wax is too cold, the molten wax will have too high a viscosity, and air bubbles will get trapped in the canister.

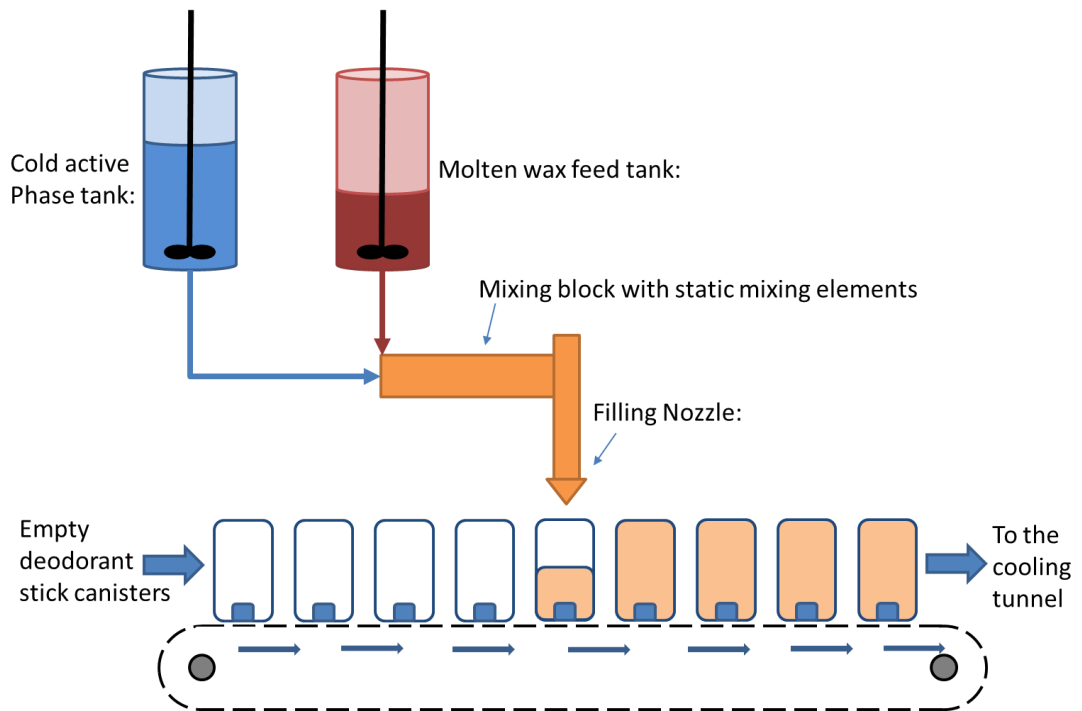


Figure 1-2 Diagram showing the production process of wax stick deodorant, based on communications with P&G.[10, 11]

After the canisters are filled, they are passed through various finishing operations at the end of the production process. Infrared light is used to heat the surface of the wax stick to ensure it is smooth and free of air. Then a probe is stuck into the centre of the stick, allowing air to escape and then the canister is reheated to fill the void created. Next, the canisters are passed through a refrigeration tunnel which cools the product rapidly, forcing the product to solidify. Finally, the canisters are cleaned and placed into cartons ready for shipping.[11]

Samples of the production run are taken and used for quality control testing. The final hardness of the wax is measured by using a needle of a particular weight and size which is allowed to travel through the wax over a pre-determined period of time.[12] The relative hardness of the wax is measured by the distance which the needle has travelled through the wax in the given time period.[12]



Figure 1-3 Two examples of wax stick deodorant products currently available for sale on P&G's online store in North America.[13]

1.3.1 Typical Formulation of Wax Deodorant Sticks

Formulation science is the process of creating a product through blending a range of components, each of which has a certain function in the final fully formulated product. The order and level of addition are key, for making a product which has functional, active ingredients and creates the correct structure for suspending components, whilst having the correct rheology and pH for the products intended function. Typical cosmetic formulations include a range of functional ingredients including pH adjusters, fragrance, rheology modifiers, dyes, preservatives, surfactants and appearance modifiers etc.[11, 14]

In the case of the wax deodorant stick, the formulation has to be hard and rigid to only deposit a small layer when rubbed on the skin and to maintain form inside the canister but needs to be soft enough to feel nice upon application to the skin.[11] The product needs to have a pleasant smell and inhibit sweating. The following table details the categories of functional materials present in wax deodorant sticks and how each material works to achieve the products brief.

Table 1-1 Typical formulation of wax deodorant stick based on P&G's formulation patent.^[15]

Name	wt% of composition	Typical examples	Function
Astringent metal	0.5-10%	Aluminium zirconium complex's	Antiperspirant active ingredient
Solidifying agent	5-40%	1-Octadecanol, Hydrogenated Castor Oil, Petrolatum	Solid structuring
Volatile emollients	20-70%	Decamethylcycl opentasiloxane (D5)	Silicone to provide lubrication upon application to the skin then evaporates leaving the skin feeling smooth and dry
Non-volatile emollients	10-50%	Talc, starches	To control stick consistency. Also gives a smooth, dry feel.
Solubilizing agent	0.05-10%	Fragrance	To dissolve solid powder material

1.4 Research Aims and Objectives

The nature of how materials are processed in industry can have a significant impact on the final physical properties and performance of the manufactured product. This project aims to explore this phenomenon by studying the crystallisation and phase behaviour of the long-chain structuring hydrocarbons used in the formulation of wax stick deodorants.

The underlying question of this PhD is:

How does composition and process parameters such as shear and temperature impact the solid form behaviour of a typical wax stick formulation?

This research can be delivered by completing the following objectives:

- Determine phase diagrams between the structuring ingredients.
- Establish the solubility and solution ideality in different solvents to probe behaviour and compare with industrial solvent.
- Study morphology of the structuring ingredients in model solvents.
- Study impact of temperature control and shear on the physical properties.

- Study the X-ray structure of the structuring ingredients upon shear and temperature.

Formulation

- Intermolecular forces between molecules
- Miscibility of ingredients
- Density
- Ingredient composition/purity

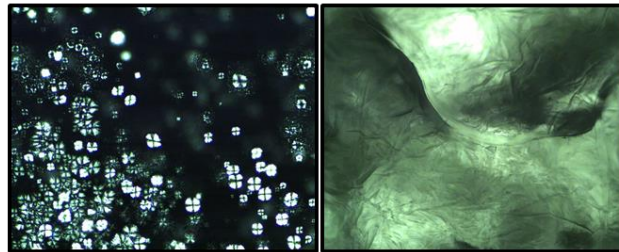
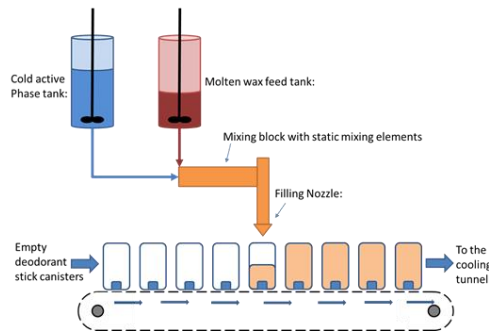


Crystallisation and Polymorphism within the complex mixture

- Crystal size and morphology
- Crystallisation temperature
- Polymorphic transitions
- Crystal structure

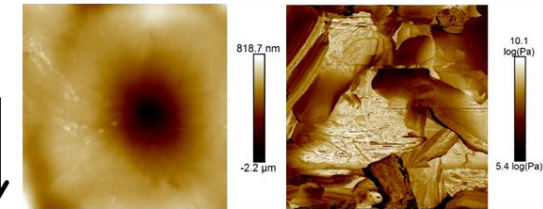
Process Conditions

- Mixing speed
- Cooling rate
- Reaction Vessel



Physical Properties

- Rheology
- Surface morphology
- Mechanical properties



Product Performance

- Sensory feel
- Product stability
- Ease of application
- Dosage upon application



Figure 1-4 The methodology used throughout this project displayed using flow diagram detailing the links between process conditions, formulation, crystallisation, physical properties and product performance.

1.5 Justification for Material Selection

After discussions with Procter and Gamble (P&G) and searching the patents it was apparent three groups of long-chain organic molecules are used to provide to structure wax stick deodorant formulations.[9, 16-20] These three groups are alkanes, alcohols and triglycerides. Combined mixtures of these molecule groups structure the mixture of volatile emollients, non-volatile emollients and astringent materials present in wax stick formulations upon cooling through forming a crystal structure network, throughout the complex material mixture. These materials are combined together to structure the product, so that the product is rigidly contained in the canister, but deposits a thin film upon rubbing the product on the skin. I choose to use commonly used industrial materials as the focus of this research and requested industrial samples of 1-Octadecanol, Petrolatum and HCO from P&G.

1.6 Project Management

This PhD project is sponsored and supported by Procter and Gamble. The work has predominately been completed at the School of Chemical Engineering, University of Leeds and as part of the Complex Particulate Products and Processes Centre for Doctoral Training (cP³ CDT), using EPSRC Grant EP/L015285/1. The cP³ CDT has an industrial focus with every PhD project having an industrial sponsor and a planned industrial placement. This work has been carried out under the supervision of Primary supervisor Dr Xiaojun Lai and Secondary supervisor Professor Kevin Roberts, both of whom are based at the University of Leeds. Input was also gained from progress meetings with industrial contacts, Simon Greener and Dave Sturgis, based at P&G's R&D facilities at Newcastle, UK and Cincinnati, USA. Majority of the experimental work was carried out at the University of Leeds, Chemical Engineering department. However, some of the experiments were conducted through collaborations, Atomic Force Microscopy was conducted with Dr Simon Connell at School of Physics and Astronomy, Synchrotron experiments were conducted at Brazilian Synchrotron Light Laboratory, and Unicamp with Dr Guilherme Calligaris and Thermal Analysis was carried out at P&G, Newcastle.

1.7 Report Structure

This thesis contains eight chapters with the references listed in the bibliography at the end of the document.

Chapter 1 introduces the thesis by describing the industrial context, before detailing the research question, aims and objectives and report structure.

Chapter 2 gives an overview of the underlying science, discusses relevant literature and describes the characterising techniques use.

Chapter 3 details the materials and experimental methods used throughout this research.

Chapter 4 details the results upon characterising 1-Octadecanol, Hydrogenated Castor Oil and Petrolatum using a range of techniques.

Chapter 5 covers solubility and nucleation kinetics of 1-Octadecanol and Hydrogenated Castor Oil gained through conducting a series of polythermal turbidity experiments in a range of non-polar and polar solvents.

Chapter 6 presents a series of binary phase diagrams that have been created using thermal analysis, complemented changing by measured mechanical and morphological properties of the surface.

Chapter 7 describes the development process of building a novel shear cell, before detailing the results obtained from simultaneous polythermal, shear and X-ray experiments.

Chapter 8 details the conclusions and future work of this research project.

A schematic of the thesis structure was provided in Figure 1-5.

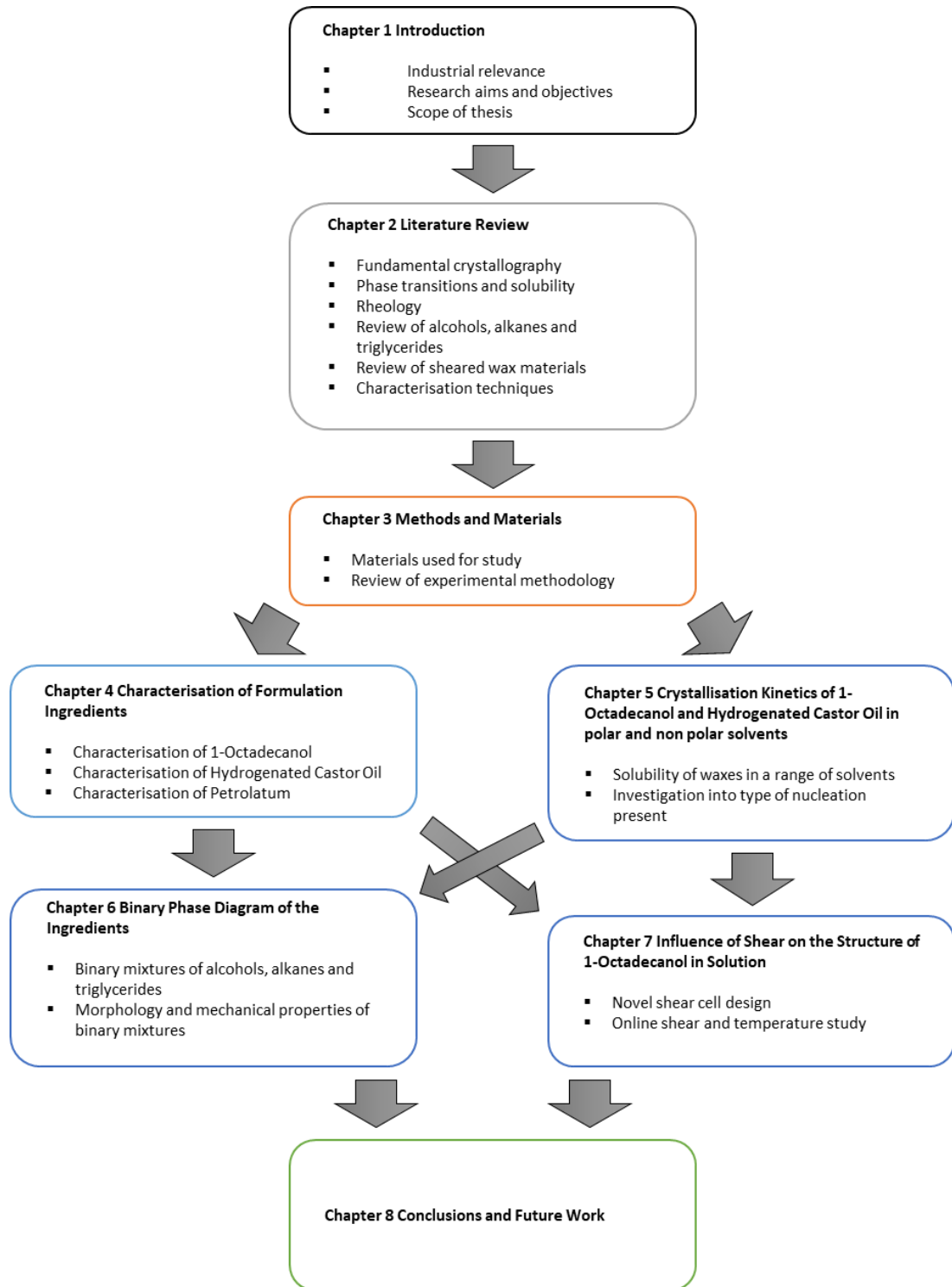


Figure 1-5 Flow diagram schematic of the report structure

Chapter 2: Underlying Science and Literature Review

This chapter covers the fundamental science underpinning this project, before providing a literature review of the work previously carried out in the scientific area.

2 Underlying Science and Literature Review

2.1 Introduction

This chapter introduces the scientific landscape underpinning this project. First; the fundamental knowledge is covered, including the theory of crystallisation science, formulation science, thermodynamics and rheology, before moving into the literature review. The literature review provides details of previous studies that have used relevant materials and techniques. The theory behind key characterisation techniques will be covered towards the end of this chapter.

2.2 Underlying Science

2.2.1 Crystallisation Theory

Within the three states, solid, liquid and gas, the atoms and molecules have very different atomic mobility. The motion of atoms/molecules contained within liquids and gases is free and random. Solids can be either crystalline or amorphous. Crystalline solids have fixed atoms/molecules/ions in a regular order called a lattice, and amorphous solids have atoms/molecules/ions fixed in a random long-range order.[21]

2.2.1.1 Crystallography

A crystalline solid has atoms/molecules/ions in a three-dimensional repeating pattern throughout the ordered structure. The position of the atoms is not static within a crystalline solid. Each atom vibrates around a mean point due to the thermal energy it possesses.[21]

A lattice is used to describe the positions of motifs (atoms, molecules or ions) throughout the three-dimensional crystal structure. The smallest building block of the crystal is called the unit cell, and if it is repeated in three-dimensional space, it forms the lattice. A three-dimensional unit cell is a parallelepiped (Figure 2.1), defined by its lattice parameters which consist of three distances (a, b and c) and three angles (α , β and γ). The distances are parallel to the axes of the lattice (x, y and z) and the angles are between each of the axes.[21, 22]

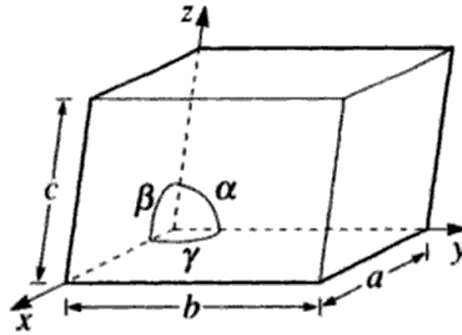


Figure 2-1 A general three-dimensional unit cell with lattice parameters (a,b,c, α , β , γ).[22]

In crystals, interactive forces between molecules are due to van der Waal's forces, electrostatic forces or hydrogen bonding. The strength of these interactions between molecules rapidly decreases with distance. As a result, the nearest-neighbour interactions determine the energetics of the structure and only certain symmetric crystal structures are allowed.[23]

Symmetry is another method of describing a crystal and its unit cell. In general, all crystals display some symmetry, and this allows crystals to be grouped. The four symmetrical elements a crystal possesses are an axis of rotation, an axis of rotation-inversion, a plane of symmetry and a centre of inversion.[21]

It has been found there are 32 sets of symmetrical operations that characterise possible all crystal structures. These symmetrical operations are known as point groups and help define the seven possible crystal systems (Cubic, Tetragonal, Orthorhombic, Monoclinic, Triclinic, Trigonal and Hexagonal).[21]

In 1848 through geometric mathematical reasoning, Bravais calculated that there are only 14 possible basic types of the lattice which are derived from the seven crystal systems.[21]

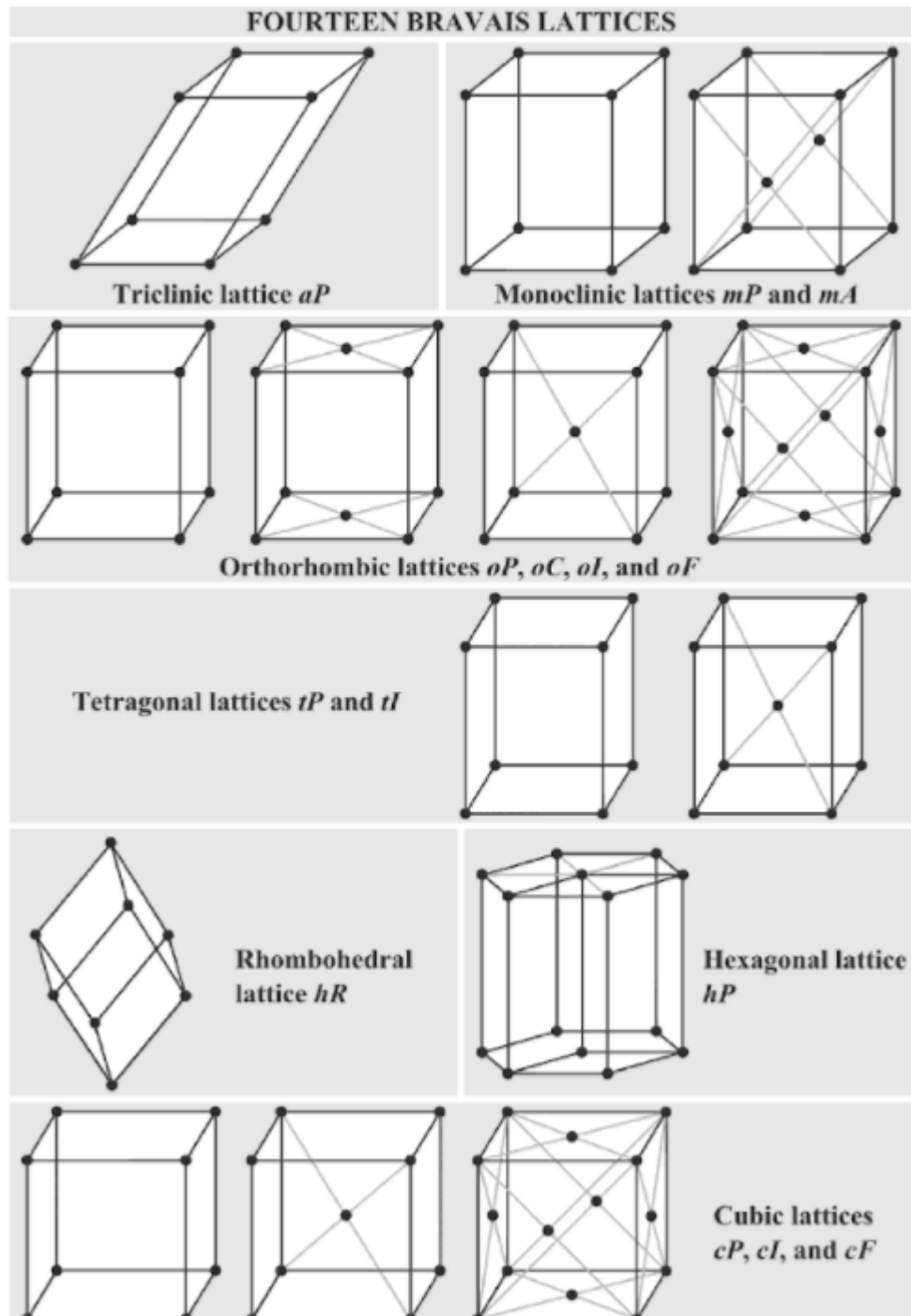
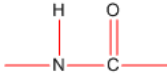
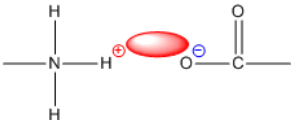
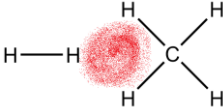
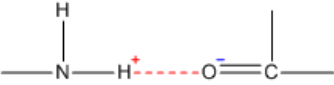


Figure 2-2 The fourteen Bravais lattices grouped by the seven crystal systems.[24]

2.2.1.2 Chemistry of Crystals and Polymorphism

The chemistry and nature of a crystal are very much dependent on the bonds and interaction forces within the crystalline structure. The many types of chemical bonds and interactions between atoms and molecules including covalent bonds, ionic bonds, metallic bonds, hydrogen bonding, van der Waal's forces and dipole-dipole interactions.

Table 2-1 Description of types of bonds and interactions which create crystal structures.[25]

Name	Description of interaction	Structure	Bond Energy (kJ/mol)
Covalent bond	Sharing of electron pairs between atoms to form a chemical bond.		63-920
Ionic bond	A chemical bond formed between two ions of opposite charge. An ionic bond is formed when one ion donates one or more electrons to another ion.		335-105
Van der Waal's force	Weak temporary dipole electrostatic interaction between atoms or molecules at close range		2-10
Dipole-dipole interaction	Electrostatic interaction between two dipolar molecules. Hydrogen bonding is an extreme example of dipole-dipole interaction.		4-21

Organic crystalline solids tend to consist of covalently bonded molecules held together by weak van der Waal's forces and occasionally hydrogen bonding and/or electrostatic forces.

When a substance has the potential to crystallise into different crystalline forms whilst being chemically identical, it's described as exhibiting polymorphism. Different polymorphs despite being chemically identical tend to exhibit very different physical properties. Each polymorph can have different crystallisation and melting point

temperatures of chemically similar substances. A substance can interconvert between polymorphic forms upon a change in the conditions the substance is exposed too. If a substance cannot interconvert between the different polymorphic forms, it is known as monotropic, and if a substance can convert reversibly between polymorphs, it's known as enantiotropic. A good example of a monotropic substance is graphite and diamond.[21] Ostwald's law of stages says that the most unstable polymorphic structure will nucleate first.[23] In some cases solid-solid transitions can occur over long time periods, eventually forming the stable polymorphic structure.

2.2.1.3 Morphology

The external shape of a single or group of crystals defines its habit and morphology. A crystal's shape is determined by the relative growth speed in axes direction.

2.2.2 Mixtures and Phase Diagrams

2.2.2.1 The solubility of Mixtures.

In general, solubility refers to the ability for a solid to be dissolved in a liquid and miscibility refers to the ability to mix two liquids. Solubility can be expressed in grams per litre.[26]

Dissolution occurs when the solute molecules separate from one another; the solvent molecules create a gap between them for the solute molecules to position and interactions occur between solute and solvent molecules to form a stable solution. For this to occur there will be certain energy barriers to overcome for solute separation, solvent separation, solution formation and the size of these energy barriers depend on the nature of interactions between the solute and solvent.

Scientists often use modelling to predict the solubility of a certain solute in a solvent.[27] There are two main types of solution to consider: a molecular solution where a solute and solvent are covalently bonded and an ionic solution where the solute is ionic and able to dissociate into its ions in solution.[26]

2.2.2.2 Binary Phase Diagram

A phase is a part of a system that is homogenous and uniform respect to physical composition and physical state.[23] Phase diagrams are used to describe how changing a condition such as a temperature or pressure impacts the phase present of a material.

A system is in equilibrium if no changes occur once it is isolated from its surroundings and a system is in phase equilibrium if no phase transformation occurs between one phase and another.[28] When a system is in a state of equilibrium at a given temperature and pressure, the Gibbs function is at a minimum. When a system is not at equilibrium, there is a driving force towards equilibrium. An example of this is a wet T-shirt will dry at a faster rate if its outside in a dry environment, rather than a humid environment.[28] The phase equilibrium will change if pressure or temperature is changed, as demonstrated when a phase diagram is produced using DSC. Also, in the case of DSC, the size of the driving force to reach equilibrium will depend on the heating or cooling rate.

In 1875, Gibbs defined the phase rule, which shows the relationship between the number of co-existing phases P , number of independent components N and the number of degrees of freedom F using the equation listed below. For all systems in thermodynamic equilibrium, the phase rule is valid and provides the theoretical foundations behind all phase diagrams.[23]

$$P + F = N + 2$$

Figure 2-3 Gibbs phase rule.[23]

The number of independent components N is defined as the number of chemical species, required to completely describe the phases in the system completely.[23]

The number of degrees of freedom F , is defined by the number of independent variables at the systems given state of equilibrium. Variables such as mole fraction x , temperature T and pressure p can be individually verified without, altering the number of phases in the system.[23]

To provide an introduction phase diagrams, I will describe a model example of a binary phase diagram in Graph 4-1.

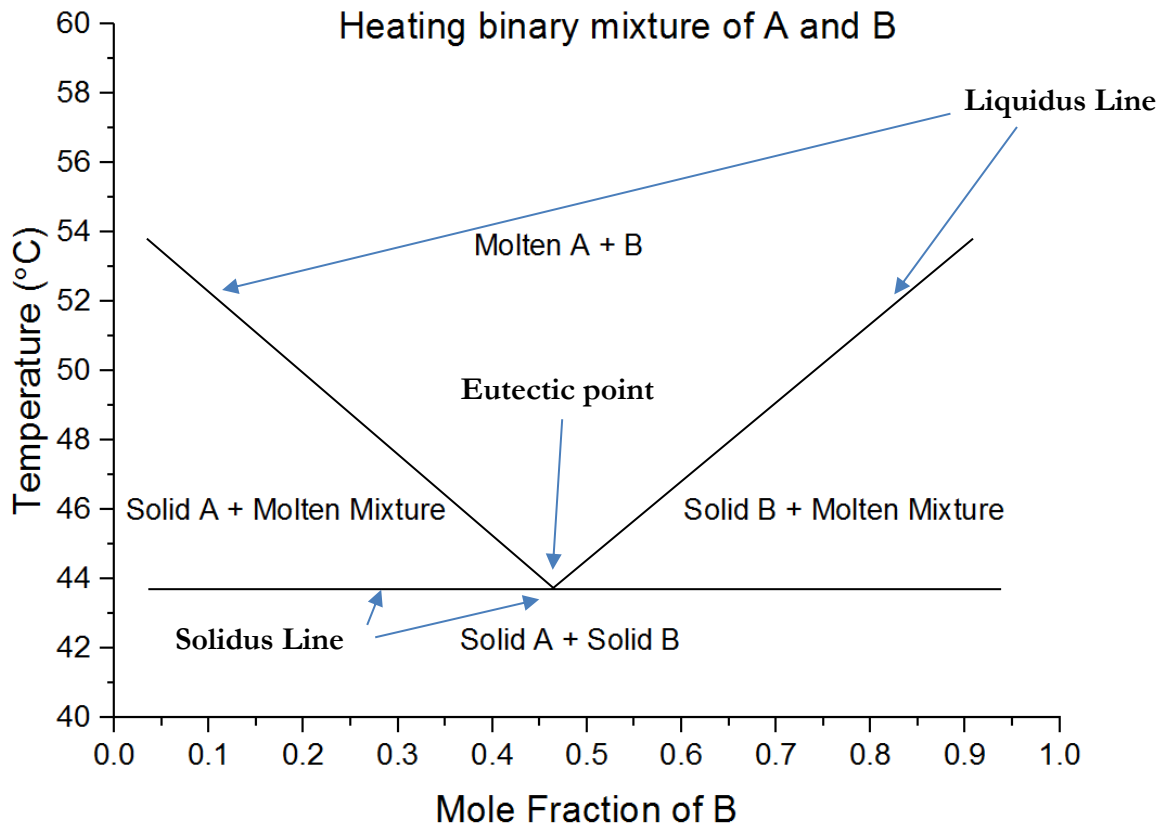


Figure 2-4 Model example of a phase diagram where materials A and B are mixed in the solid and liquid phase.

The above phase diagram shows the impact of temperature and composition on the phases present. The temperature was plotted on the y-axis, and relative composition was plotted on the x-axis. At 0.0 mole fraction of B, we have 100% composition of A, and at 1.0 mole fraction of B, we have 100% composition of B. At a mole fraction of 0.2 of B, as the temperature is cooled from 60 °C molten phases of A and B are initially present. At around 50 °C, solid A starts to crystallise, and by around 44 °C, solid B starts to crystallise. The solidus line is the line at which the system becomes completely solid and the liquidus line, is the line at which the system becomes completely liquid. The eutectic point is the point at which liquid A and liquid B both solidify at the same time.

At solid-liquid interfaces with a given temperature, some of the solid phase dissolves into the liquid phase. The degree to which this happens depends on the solubility of the solid within the liquid.[28]

2.2.3 Thermodynamics

Thermodynamics is the science describing the relationships between heat, work, temperature and energy. In general, thermodynamics concerns the conversion of energy

between different forms and the transfer of energy to and from different places. Thermodynamics is described by four laws which are listed below.[29]

2.2.3.1 Zeroth Law of Thermodynamics

When two thermodynamic systems are both in equilibrium with a third thermodynamic system, then the two systems must be in thermodynamic equilibrium with each other.

2.2.3.2 First Law of Thermodynamics

Energy can only be converted between different forms and cannot be created or destroyed. As a result, throughout any process, the total energy in the universe remains constant.

2.2.3.3 Second Law of Thermodynamics

For an isolated system which isn't at equilibrium, the entropy of the system will increase to a maximum value, until the system is in equilibrium.

2.2.3.4 Third Law of Thermodynamics

The entropy of a system will reach a constant minimum when the temperature of the system nears absolute zero.

The second and third law of thermodynamics both concern entropy. The term entropy relates to how disordered and random a system is. Temperature is defined as the heat intensity present within a material and measured on the Kelvin scale, which starts at absolute zero. Thermodynamic equilibrium as a concept is defined as a system with no likelihood of changing state spontaneously.

To understand the laws of thermodynamics, basic thermodynamic concepts such as temperature, thermodynamic equilibrium, thermodynamic states, heat and work and total energy of a system must be understood.

2.2.4 Crystallisation and Crystallisation Kinetics

2.2.4.1 Supersaturation

The concept of solubility has been discussed in the previous section and refers to the solubility at equilibrium with a saturated solution. Through cooling or evaporating a saturated solution, it is possible for a solution to contain more dissolved solute than its equilibrium concentration at a given temperature. When a solution contains more solute

than its equilibrium concentration, the solution is known to be supersaturated and is essential for crystallisation to occur.

Supersaturation is the driving force behind both nucleation and growth of crystals.

2.2.4.2 Nucleation

Nucleation is the first step in the process to forming a crystal and is the process where multiple molecules/ions come together in a supersaturated solution to form a stable cluster or nuclei, after overcoming energy barriers for cluster stability. Once the initial cluster has formed, it becomes the basis for crystal growth.[21]

There are two types of nucleation in solution: primary and secondary. Primary nucleation occurs without the presence of any other particulate matter in solution, and secondary nucleation occurs in the presence of particulate matter, for example, in a seeded solution. Primary nucleation is homogenous and spontaneous, meanwhile, secondary nucleation is heterogeneous and induced by the presence of particulate matter.[21]

2.2.4.3 Meta-Stable Zone Width

The meta-stable zone width is the temperature difference between the solubility curve and the super-solubility curve as displayed in Figure 2-5. Figure 2-5 describes the concept of super-solubility, and there are three clear regions, labile, metastable and stable which first defined by Ostwald in 1897.[30]

The lower solid line represents the equilibrium solubility curve, and the upper dashed line represents the super-solubility curve beyond which the labile region exists. The region between these two lines exists the meta-stable zone. A supersaturated solution can be created in three possible ways. Cooling is represented by the line passing through ABCD, evaporation is represented by line AB'C', or a combination of both represented is represented by AB''C''. The temperature difference between the labile and stable region is the metastable zone width. In the stable region, it is impossible for nucleation to occur, in metastable region nucleation is improbable, but can be induced by seeding and in the labile region nucleation is probable.[31, 32] The size of the metastable zone width depends on many factors including cooling rate, solvent evaporation, impurities and seeding.

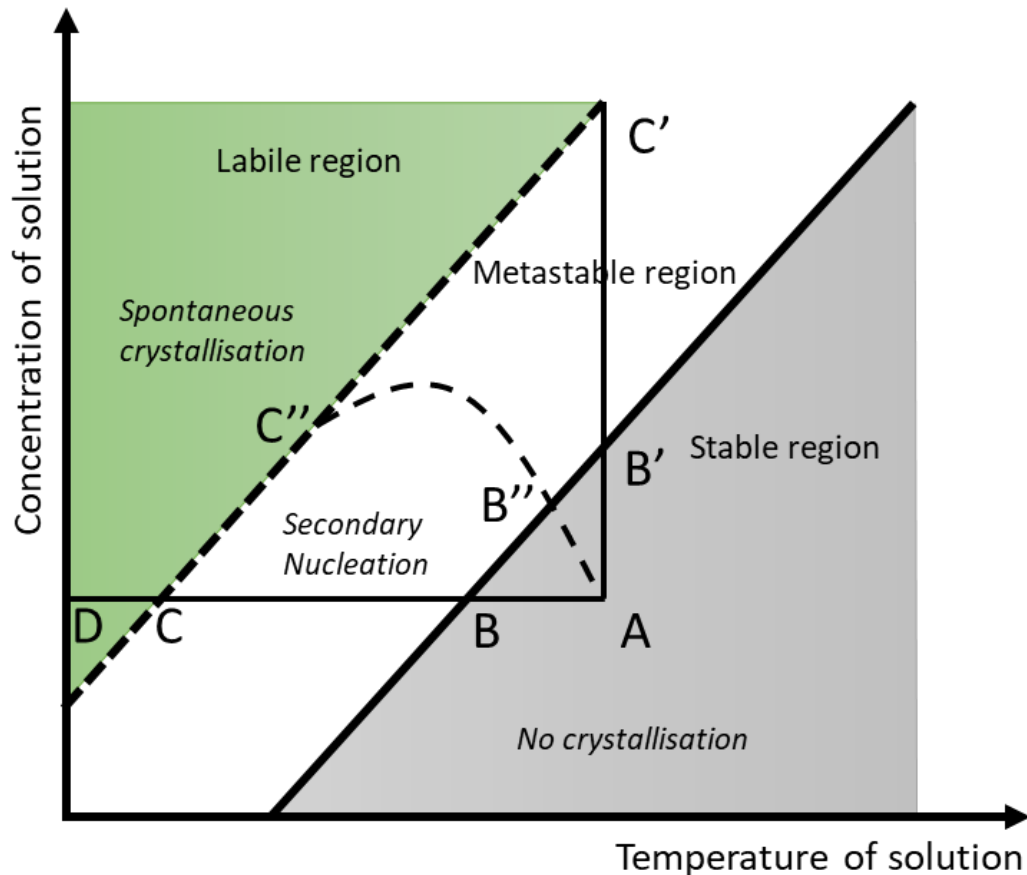


Figure 2-5 Diagram displaying metastable zone width, super-solubility curve passing through CC'C'' and solubility curve passing through BB'B''. [31]

2.2.4.4 Crystal Growth

After a stable cluster has formed in solution, a crystal can form through the growth of the cluster. Nucleation and crystal growth processes both compete for the available solute in solution, and the relative rate of each process impacts the crystal size distribution. Crystal growth depends on various solution factors such as temperature, type of solvent, solvent purity and supersaturation, as well as internal factors such as crystal defects and interactions between solution and crystal surface. [33]

Processes occurring during crystal growth:

- Transportation of solute molecules to the crystal surface-solution interface.
- Diffusion of solute across the concentration gradient towards the growing crystal.
- Adsorption of the solute on the crystal surface.
- Diffusion of the solute molecules across the crystal surface to the most energetically favourable position, before de-solvation at the desired binding site.

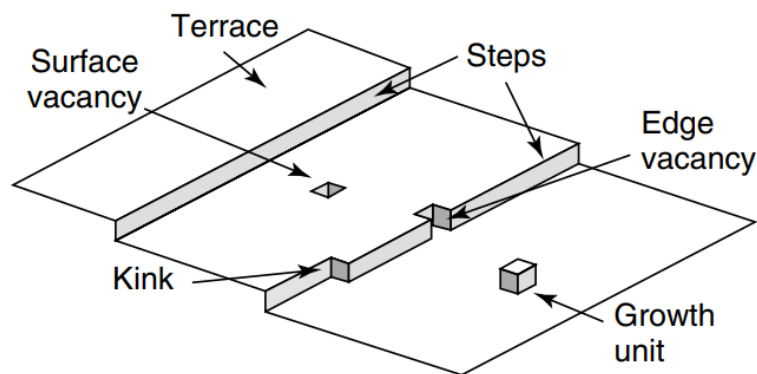


Figure 2-6 Kossel model of crystal surface displaying growth mechanism.[34]

2.3 Polymorphism of Long-Chain Alcohols, Alkanes and Triglycerides

2.3.1 Hydrogenated Castor Oil and Triglycerides

Fats found in nature typically consist of complex multi-component mixtures of triacylglycerols (TAGs). TAGs are essential to the growth and development of plants, through many processes including sugar building blocks being synthesised from TAGs, ATP production from β -oxidation of fatty acids and sequester harmful free fatty acids from the plant.[35] Fats are widely used in food and other consumer goods industries such as cosmetics. The significance of fats to industry has driven research into fat crystallisation over many years, where the intricate of triglyceride interactions and polymorphism has been identified.[36]

Hydrogenated castor oil (HCO), also known as castor wax is a synthetic compound produced through the hydrogenation of castor oil in the presence of a nickel catalyst, and the reaction is shown in Figure 2-7.[37] Castor oil is extracted by pressing the seeds of the castor oil plant. The chemical structure of natural castor oil is that of a triglyceride with three Carbon chains, and the nature of these Carbon chains is described in Figure 2-8.

HCO is a triacylglycerol (TAG), and its main component is known to be tri-12-hydroxylstearin.^[38] HCO is composed of the glyceride of 12-hydroxystearic acid mixed with minor quantities of other glycerides of 12-hydroxystearic, dihydroxystearic and stearic acid. HCO is hard, brittle wax-like powder, that is insoluble in water, odourless and practically tasteless. It is typically supplied as uniform, free-flowing wax flakes and when molten transforms into a colourless clear liquid.

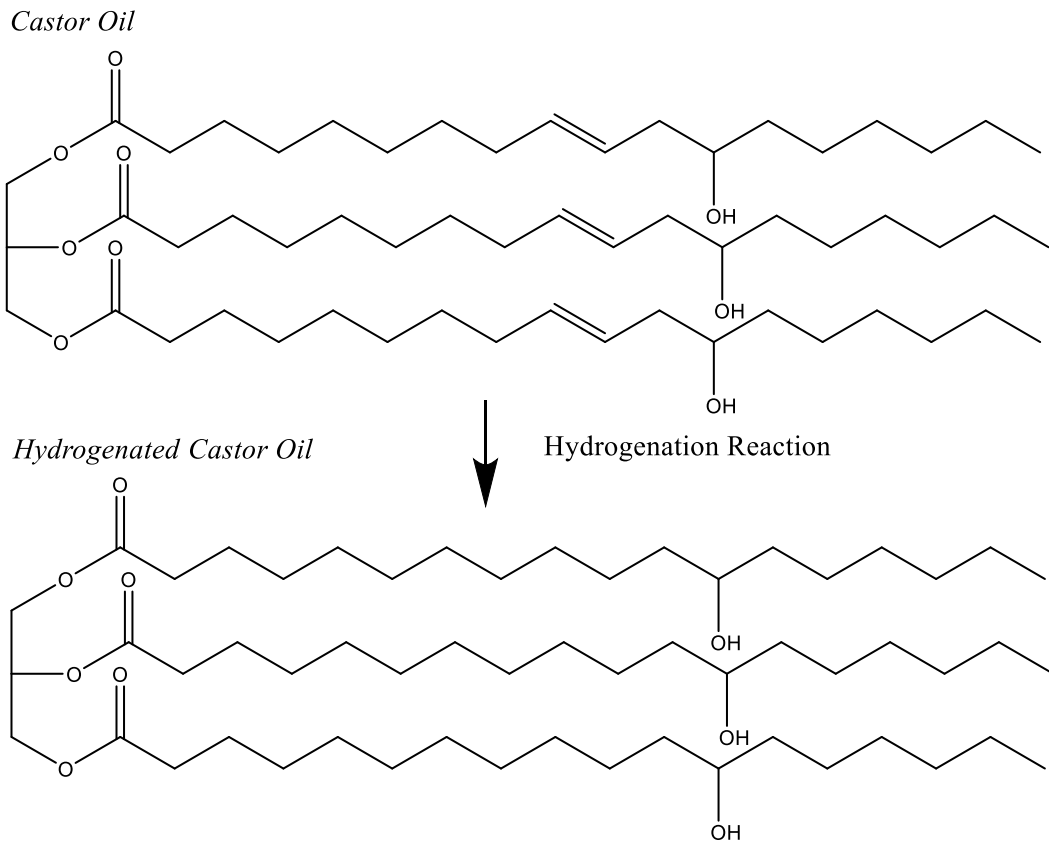
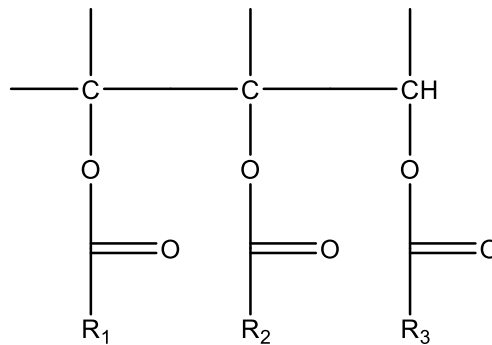


Figure 2-7 Hydrogenation reaction of the main component of Castor Oil to form Hydrogenated Castor Oil (tri-12-hydroxylstearin)

2.3.1.1 Components of Castor Oil



- 2% of R_i = C₁₅ and 98% = C₁₇
- 88% of R_i has an OH group at position 12 and a double bond between 9, 10 Carbons.
- 10% of R_i has no OH group, but may or may not have a double bond between 9, 10 Carbons.
- R_i = R₁ and/or R₂ and/or R₃

Figure 2-8 Diagram displaying the components of Castor Oil.^[38]

Table 2-2 Table showing physical properties of Hydrogenated Castor Oil

Material	Viscosity (centistokes)	Boiling range/point (°C)	Melting Point (°C)	Flash Point (°C)	Density at 25 °C (kg/m³)
Castor Oil[39]	889.3	313	-2 to -5	145	959
Hydrogenated Castor Oil[40]	Solid	>300	82-87	>310	990

The hydrogenation process of Castor Oil radically changes the physical properties of castor oil at room temperature. Castor Oil is a liquid and HCO solid at room temperature, due to saturation of the double bond present between the 9th and 10th Carbon atom. Fully saturated molecules have a straight Carbon chain, and unsaturated fats in nature tend to have a double bond in the cis position and create a kink in the Carbon chain, as seen in Figure 2-9. The kink in the Carbon chain radically affects the ability for the molecules to stack in the solid form, creating the differential in melting point between Castor Oil and HCO.

Very little previous work in the literature has been carried out, and the crystal structure of HCO and unit cell has not yet been determined. The crystallisation of triacylglycerols (TAG) in general, however, has been studied extensively.[41, 42] This is potentially due to the difficulty of growing a single crystal of HCO.

2.3.1.2 Composition and Molecular Structure of Naturally Occurring Fats

Edible naturally occurring fats and oils typically contain multicomponent mixtures of TAGs along with trace amounts of other minor components. Each naturally occurring edible fat and oil often contains over a hundred different types of TAG. The chemical structure of a TAG is a triester of glycerol with three fatty acid molecules attached and is shown in Figure 2-9. A fatty acid is a hydrocarbon chain with the carboxylic acid functional group on the last Carbon. The length of the hydrocarbon chains most commonly found in TAGs is between 12 and 24 Carbon atoms and usually has an even chain length with a linear chain. If the hydrocarbon chain contains a double bond, the chain can become kinked in shape. The Carbon atoms present in 'linear' hydrocarbon chains are arranged in a zig-zag pattern.[36]

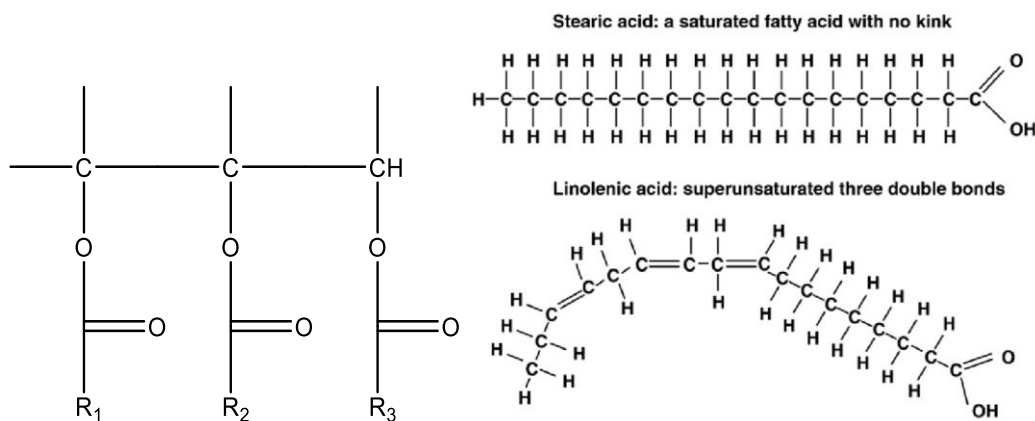


Figure 2-9 On the left shows the molecular structure of triacylglycerol (TAG) with R_1 , R_2 and R_3 being individual fatty acid chains. Top right and bottom left are saturated and unsaturated fatty acid, respectively. The figure was taken from C. Himawan *et al.* review paper.[36]

In the literature, TAGs are named using a three-letter coding system. The second letter of the code denotes the fatty acid attached to the 2-position of the glycerol. If all the fatty acids attached to the glycerol have the same structure, the TAG is known as a monoacid, and if the fatty acids are different, the TAG is known as a mixed-acid. If any of the fatty acids in the TAG contain a C=C the TAG is known as being unsaturated, alternately the TAG is known as being saturated.[36]

2.3.1.3 Simple Triacylglycerol Polymorphism

The structure of TAG molecules allows packing in multiple crystalline arrangements called polymorphs. Different polymorphs tend to exhibit a significant difference in melting point from each other. In the literature, TAGs are described as having 3 main polymorphic forms α , β' and the β . This polymorphic naming system was first developed by Kåre Larsson in 1966; however, some fats exhibit more polymorphic forms than described by this system.[36, 43]

TAG molecules consist of glycerol with three long-chain fatty acid molecules attached creating “three-legged” structure that can arrange into two configurations, none of which have all three “legs” alongside each other. One of these configurations is called the “tuning fork”, where 2 position fatty acid is alone and the 1 and 3 position fatty acids pack next to each other. The other configuration is known as the “chair” configuration, where the 2 position fatty acid packs alongside either the 1 or 3 position fatty acid. These “chairs” can either be stacked in double or triple chain length structure, as seen in Figure 2-10 alongside a top-down view of the three main TAG polymorphs. These polymorphs can be identified experimentally using powder X-ray diffraction by the diffraction pattern.[36, 44] The long spacing in the XRD pattern gives information about the repeat

distances between the crystal planes, and short spacing gives information about the distances within the sub-cell. The distance between the crystal planes can be impacted by the zigzag nature of the aliphatic chains. The TAG molecules can be closer packed if the adjacent aliphatic chains are in step (parallel), rather than out of step (perpendicular).[36]

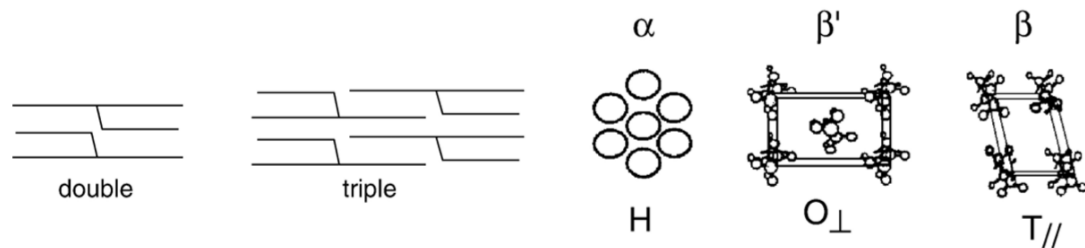


Figure 2-10 The “chair” configuration packing structures (left) and the subcell structure of the three most common TAG polymorphs viewed from above the crystal planes (right). The figure was taken from C. Himawan *et al.* review paper.[36]

The α form has the chains arranged in a hexagonal structure (H), without any tilt and a large enough distance between planes for there to be no influence of the zigzag chains on the packing distance. The α form can be identified by an XRD pattern with one strong short spacing peak at around 0.42 nm.[36] The α form, in general, is known to be unstable.[45]

The β' form has an orthorhombic and perpendicular chain packing (O_{\perp}) and the adjacent chains are out of step with each other (perpendicular), preventing close packing. The chains exhibit an angle of tilt between 50° and 70° . The β' form can be identified by an XRD pattern with two strong spacing peaks at 0.37-0.40 nm and at 0.42-0.43 nm.[36] The β' form, in general, is metastable.[45]

The β form has a triclinic chain packing with the adjacent chains being in step with each other (parallel) ($T_{//}$), resulting in β being the densest and close-packed polymorphic form. The chains also exhibit an angle of tilt between 50° and 70° . The β form can be identified by an XRD pattern with one strong spacing peaks at close to 0.46 nm and a number of strong peaks between 0.36-0.39 nm.[36] The β form, in general, is known to be the stable form.[45]

Both β and β' polymorphs can be found in double and triple chain structures. Double chain structures tend to occur when the TAG has the same (monoacid) or a very similar fatty acids chains attached the glycerol. Triple chain structures occur when the TAG contains different fatty acids in its structure (mixed-acid). The α form only tends to be found exhibiting the double-chain structure.[36]

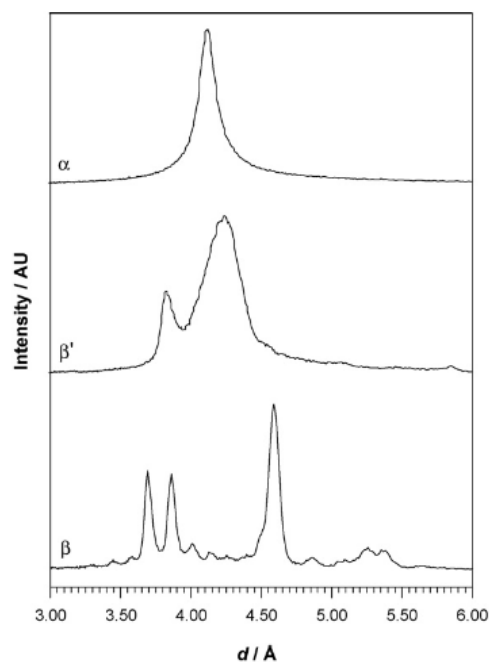


Figure 2-11 Powder X-ray diffraction patterns of the α , β' and β polymorphs of Tristearin taken from E. Da Silva *et al.*[46]

All three polymorphs of Tristearin have been characterised using DSC, XRD and Raman spectroscopy.[46] Through DSC the polymorphs of Tristearin can be distinguished by melting point with α , β' and β at 54.9, 65.3 and 72.4°C and enthalpy of fusion with α , β' and β at 128, 154.2 and 219.6J/g.[47] The polymorphs were prepared using by heating Tristearin to 90°C until molten and holding for 5 minutes to remove crystalline memory, before cooling at 50°C/min to 25°C to form the α polymorph and holding isothermally for 10 minutes to crystallise. The β' polymorph was formed by cooling from the melt at 50°C/min to 57°C and holding for 100mins, and the β polymorph was formed by cooling from the melt at 50°C/min to 61°C and holding for 60 minutes.

2.3.1.4 Triacylglycerol Morphology

Morphology of a crystal is dictated by relative growth rates at each crystal face. The slower the growth rate at crystal face, the higher the probability that the crystal face will have a large surface area in the final crystal habit. In the case of TAG crystals, they are anisotropic and have a large difference in growth rate at each crystal face.

Each TAG crystal polymorph has been found to exhibit very different morphology. In general, when examining TAG crystals under a microscope, the α form exists as an amorphous mass of very small crystals, the β' form appears as spherulitic or bulky shapes, and the β form is observed to have needle-shaped crystals.[48]

Fats, in general, are mostly seen to crystallise into spherulites, and an optical microscope study on Tripalmitin demonstrates how varying crystallisation conditions leads to multiple morphologies for a single material. The crystal polymorphs identified of each morphological structure were determined by measuring the melting point.[49]

Spherulite structures are formed from an aggregation of crystalline ribbons growing out in a radial fashion from a single nucleus. Quite often, the ribbons which build up the spherulite are needle-shaped. More irregular structures can be created under certain conditions. The difference in spherulite morphology has been explained by the magnitude of the driving force, which influences whether secondary nucleation occurs as the crystal layers are being formed. At low driving forces, the secondary nucleation mechanism is too slow and ensuring a crystalline layer is completely formed before the next layer is created. At high driving forces, secondary nucleation occurs before the completion of each layer creating irregular structures.

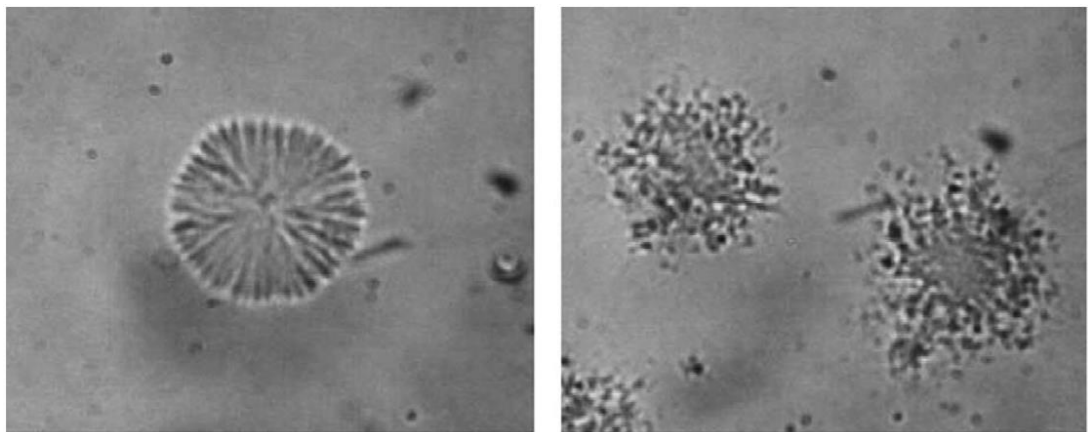


Figure 2-12 Spherulites in the β' polymorphic form crystallised from 30%-w SSS of PPP/SSS binary mixture at (left) 52.5°C and (right) 49°C. The figure was taken from C. Himawan *et al.* review paper.[36, 50]

2.3.2 1-Octadecanol and n-Alkanols

1-Octadecanol, also known as Stearyl Alcohol, is one of the chosen materials of study in this project. 1-Octadecanol is typically synthesised through hydrogenation of stearic acid. Stearic acid is a naturally occurring fatty acid found in cocoa and shea butter.[51] The cosmetic industry usually extracts stearic acid from coconut or a palm source.[51] However, in recent years there has been pressure on the industry to move from a palm source since palm oil plantations have been linked to rainforest destruction and further endangering species such as the orangutan.[52] The molecular structure of the n-alkanol, 1-Octadecanol is displayed in Figure 2-13 and has the hydroxy functional group in position 1 on the 18-chain length, straight, saturated Carbon chain.

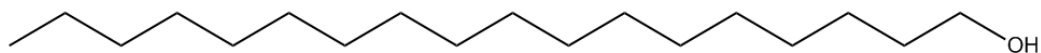


Figure 2-13 The molecular structure of 1-Octadecanol ($C_{18}H_{37}OH$).

The research paper by Ventola *et al.* reports the polymorphism behaviour of 1-Heptadecanol ($C_{17}H_{35}OH$), 1-Octadecanol ($C_{18}H_{37}OH$), 1-Nonadecanol ($C_{19}H_{39}OH$) and 1-Eicosanol ($C_{20}H_{41}OH$) purified using recrystallisation in Acetone or ether using a range of complementary techniques including X-ray powder diffraction, DSC, Raman scattering and infrared spectroscopy.[53] Polymorphism is reported to be very similar to n-alkanes, and as a result, n-alkanol polymorphs are given similar nomenclature. Odd and even chain length N-alkanols of between 12-20 Carbon atoms exhibit different polymorphism at room temperature, γ is stable for an even Carbon chain length, and β is stable for an odd Carbon chain length. A few degrees below the melting point, both odd and even chain length N-alkanols have a solid-solid transition to the rotator form R'_{IV} . A metastable β form of 1-Octadecanol and 1-Eicosanol was observed after quenching in a bath of liquid Nitrogen.

N-alkanol chains pack in an ordered, regular and parallel fashion to create a crystallographic structure, which can be defined by a repeating unit called the sub-cell. Each polymorph can be distinguished by its crystallographic structure and its sub-cell.

A subcell has three axes which are referred to as: c_s , a_s and b_s . a_s and b_s are both lateral translations and c_s is a translation among equivalent points within the Carbon chain. The γ polymorph is present when the long axis of the molecule tilts over the shortest axis of the rectangular subcell.[54] The β polymorph is present when the long axis of the molecule tilts over the longest axis of the subcell. At just below the melting point, the solid phase transforms into a rotator phase upon heating. In the rotator phase, the long molecules are free to rotate along their long axis, and conformational defects are reported to occur.[53, 55]

At room temperature, 1-Octadecanol $C_{18}H_{37}OH$ is present in the stable monoclinic γ form which has a space group $A2/a$ and 8 molecules present in the unit cell. The chains are parallel to the $[1\ 0\ \bar{6}]$ direction and packed in layers positioned by the OH-OH hydrogen bonds, as shown in Figure 2-16 b). Just below the melting point, 1-Octadecanol is in the rotator phase, R'_{IV} with a space group of $C2/m$ with 4 molecules in the unit cell

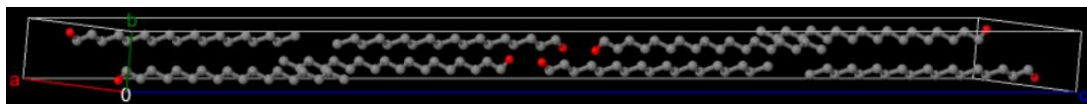


Figure 2-14 Unit cell of 1-Octadecanol γ phase (Space Group: $A 2/a (15)$, Cell: $a 8.998(5)\text{\AA}$ $b 4.940(2)\text{\AA}$ $c 98.01(3)\text{\AA}$, $\alpha 90^\circ$ $\beta 122.59(1)^\circ$ $\gamma 90^\circ$) sourced from the Cambridge Crystallographic Data Centre.[54]

Single crystals of 1-Octadecanol have been previously grown from solution through evaporation of *p*-xylene at room temperature. K Izumi used a combination of X-ray topography and optical microscopy to study lattice defects contained within the single crystal.[56]

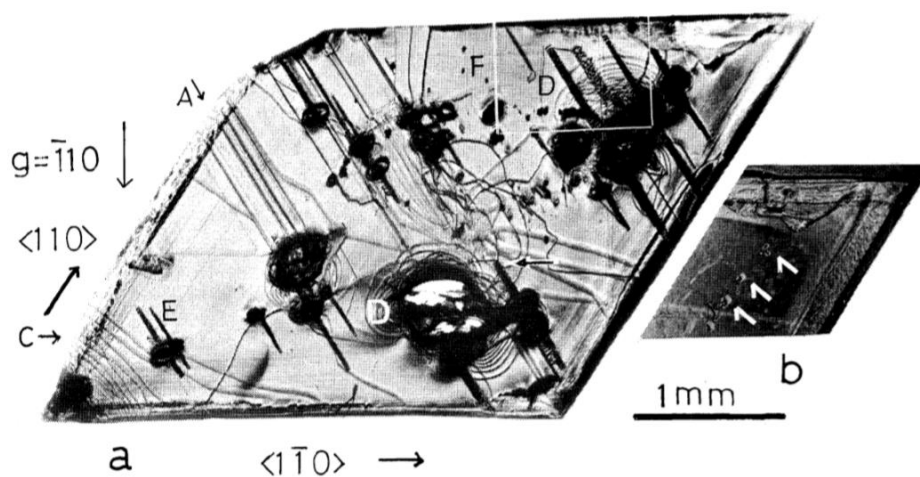


Figure 2-15 a) X-ray topography of a single cell of 1-Octadecanol, which contains large inclusions of lattice defects. b) Phase-contrast optical microscope image of 1-Octadecanol. Sourced from Izumi *et al.*[56]

DSC analysis of commercial-grade $C_{19}H_{39}OH$ and $C_{20}H_{39}OH$ upon 2K/min per minute heating and cooling is displayed in Figure 2-16. The enthalpy of all the phase transitions upon heating and cooling have been recorded for all the *n*-alkanols studied and compared to previous work in the literature.

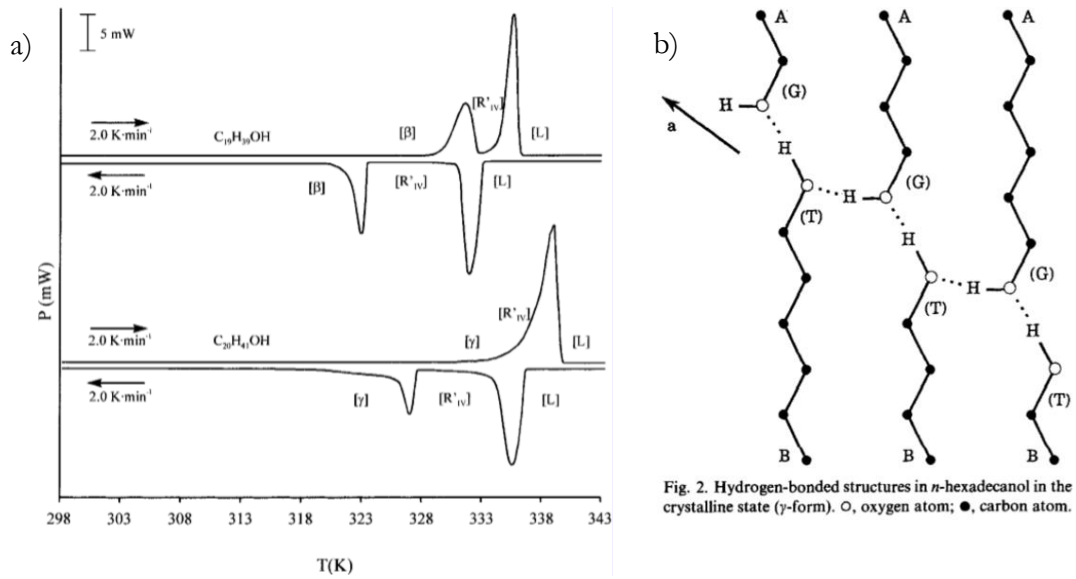


Figure 2-16 a) DSC Crystallisation curves of commercial-grade $C_{19}H_{39}OH$ and $C_{20}H_{41}OH$ upon heating and cooling at $2K\ min^{-1}$ sourced from Ventola *et al.*[53] b) Hydrogen bonding present in the γ phase crystal structure of *n*-hexadecanol with gauss (G) and trans (T) configurations taken from Ishikawa *et al.*[55]

Quenched samples of $C_{17}H_{35}OH$ and $C_{19}H_{35}OH$ were found to be in the same β phase, as observed at room temperature; however, X-ray powder diffraction patterns of $C_{18}H_{37}OH$ and $C_{20}H_{41}OH$ show the material to be in a mixture of majority γ with a minority in β form. The powder X-ray diffraction heating study of quenched $C_{20}H_{40}OH$ is displayed in Figure 2-17, where transitions between β , γ and R'_{IV} are observed upon increasing temperature. The metastable β form produced after quenching was found to be stable after three months, and DSC thermal analysis of the β form showed that it transitioned to the R'_{IV} form at a lower temperature than the γ form, further proving that the β form is metastable.

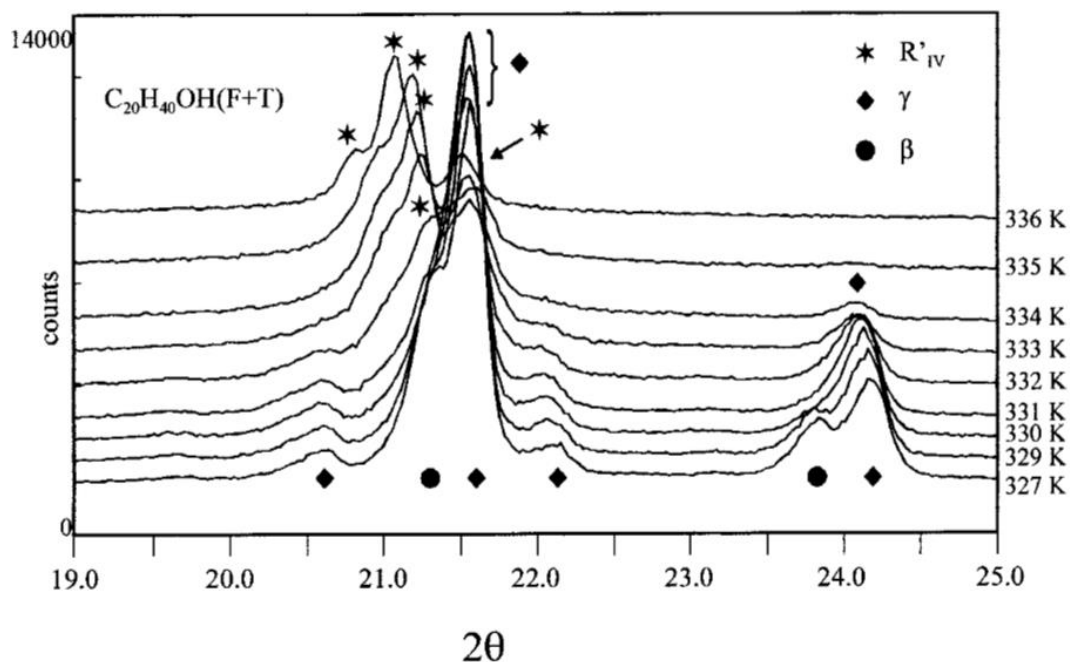


Figure 2-17 X-ray diffraction pattern of quenched $C_{20}H_{41}OH$ immediately after sample preparation. Sourced from Ventola *et al.*[53]

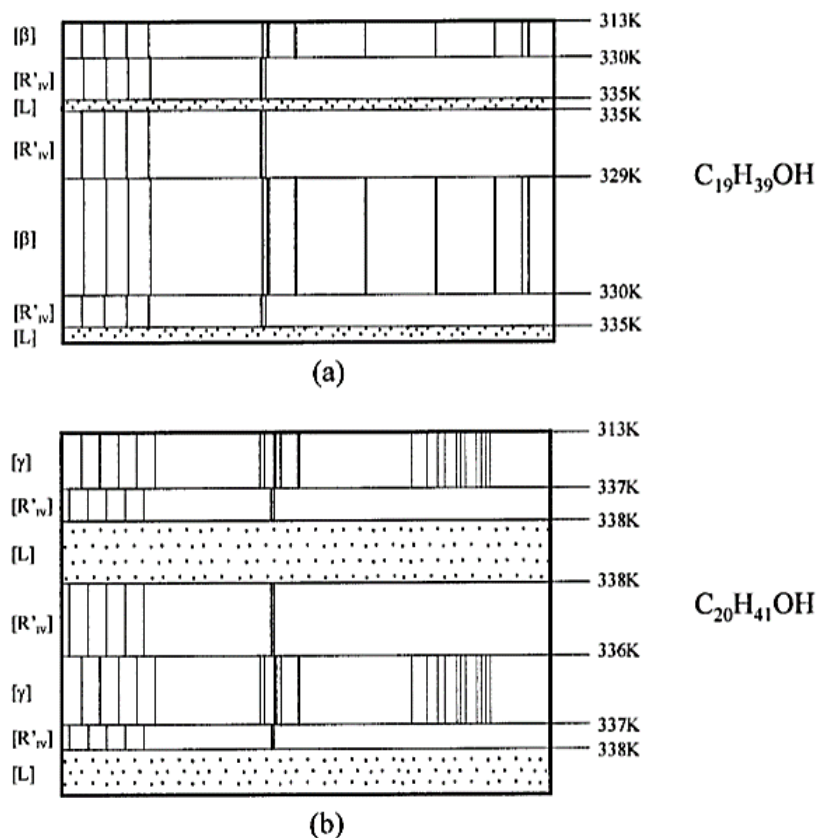


Figure 2-18 Image showing the Guiner-Simon photographs for $C_{19}H_{39}OH$ and $C_{20}H_{41}OH$, sourced from Ventola *et al.*[53]

The Guiner-Simon photographs display the change in X-ray reflection patterns of $C_{19}H_{39}OH$ and $C_{20}H_{41}OH$ with respect to temperature and polymorph. Other studies

have since documented the powder X-ray patterns of n-alkanols rotator phase at low and high angles.[57]

Raman Scattering and Infrared Spectroscopy also have been used to study the β , γ and R'_{IV} structures present in the n-alkanols investigated. Peak assignments were made with respect to previous n-alkane studies, and the findings were compared to previous structural studies of 1-Octadecanol using ^{13}C NMR spectroscopy.[55]

In addition to studying pure component n-alkanols, Ventola *et al.* have studied the melting behaviour[58] and stability[59] of different chain length n-alkanol binary mixtures. They studied the melting behaviour of mixtures with a chain length difference of 1, 2 and 4 Carbon atoms. The n-alkanol's studied have a rotator phase in either of the R'_{II} and R'_{IV} forms. Phase diagrams were produced to demonstrate the phases present upon mixing n-alkanol chain lengths with enthalpy and entropy values upon melting reported.[58] The stability study compared the polymorphic structural stability of binary mixtures prepared using melting and quenching using liquid Nitrogen with mixtures prepared using dissolution and evaporating in diethyl ether.[59]

2.3.3 Petrolatum and n-alkanes

Petrolatum is produced from the long-chain components of crude oil through fractional distillation. The crude Petrolatum fraction is purified through reaction with Sulphuric acid and subsequent filtration steps to produce the colourless and odourless final product.[60] Highly refined petroleum wax has been found to contain a high percentage of n-paraffin and exhibits similar crystal morphology and sizes to pure n-paraffin.[61-64] This observation points to the fact n-paraffin are compatible with each other, and if there is a small amount of different chain length n-paraffin present, the crystal structure is not changed drastically. According to Sasol Chemical Industries Limited's patent, Petrolatum comprises of a mixture hydrocarbons with an average chain length of between C_{25} and C_{70} .[65] The hydrocarbons present are 5 and 50 wt% branched in which the branches are methyl and ethyl groups.[65] Of the linear alkanes present between 10 and 60 wt% have a Carbon chain length of between C_{10} and C_{20} . Petrolatum does not contain any aromatic components, Sulphur or other irritants, so can be used in skin cosmetics.[65]

A review of petroleum waxes was published in Nature and summarises all the work carried out on petroleum wax crystals up until 1966.[66] X-ray studies on pure hydrocarbons have found that n-paraffin's crystallize in monoclinic, triclinic,

orthorhombic and hexagonal structures. The nature of the crystal structure has been found to depend on the molecular structure of the hydrocarbon and temperature.[67-70] Kitaigorodskii discusses in his book the impact of odd-even chain length and packing has on the symmetry of crystal structure on hydrocarbons.[68] Many hydrocarbons display a solid-solid transition in their crystal structure, but this is not always the case.[61, 68, 71-73] All n-paraffin have been found crystallise with the Carbon chain axis parallel to each other and the crystallographic axis. Hexagonal and orthorhombic lattices have the ends of all the Carbon chains in each layer in a plane. As a result, the bonds joining each layer are different to the bonds within each layer. This results in tabular or plate crystals for n-paraffin. The most common form of plates is hexagonal or rhombic.[72] Pure branched paraffin have been found to crystallise as plates with an orthorhombic structure. Through X-ray experiments on pure aromatic hydrocarbons, it has been found they mostly crystallise in the monoclinic forms with some orthorhombic crystals being formed.[74] Mainly these crystals were observed as plates.[72]

Less refined petroleum waxes which have a lower n-paraffin content and impurities, almost never crystallise as plates but instead crystallise as needles[61, 62, 71, 75, 76] and mal crystals[62, 77].

The crystal behaviour of paraffin wax was studied by S. W. Ferris and H. C. Cowles in 1945.[62] The paper describes the use of a hot stage microscope to study the crystals formed from cooling the distilled paraffin wax. They identified three types of wax crystal formation, plates, needles, and what they describe as ‘mal’ crystals and include images of each taken from there experiment.

The thermal behaviour and polymorphic transitions of n-alkanes have been reported in the literature. The stable low-temperature polymorphic phase for short-chain n-alkanes is predominately triclinic or orthorhombic; however, in certain circumstances, monoclinic.[78, 79] Between the solid crystalline phase and the liquid phase over a narrow temperature range exists one or more rotator meta-stable phases.[80-82] For example, the thermal transitions of $C_{23}H_{48}$ have been captured using DSC and displayed in Figure 2-19.[81] Upon cooling the α rotator phase initially crystallises and just below the crystallisation temperature, a solid-solid transition occurs when the β stable phase forms.

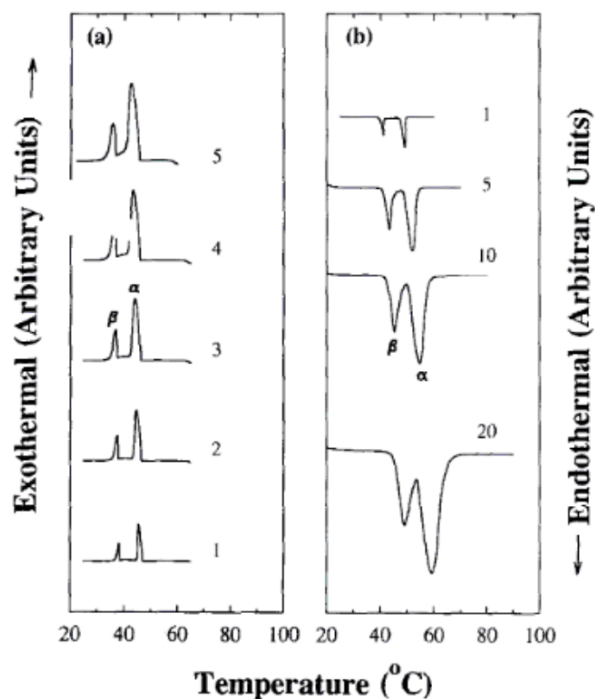


Figure 2-19 DSC curve of $C_{23}H_{48}$ at a range of heating and cooling rates ($K\ min^{-1}$) a) cooling and b) heating.[81]

In the literature, alkanes have been studied using data collected from a synchrotron. Binary mixtures of n-eicosane and n-docosane have been studied along with their pure individual components which have been crystallised from the melt and solution.[83] They carried out a structural analysis using XRD and gained kinetic information by measuring the turbidity of the system. This paper presents a new approach to measure kinetic and structural information simultaneously. The design of a novel crystallisation cell, with a set of preliminary results, are detailed in the paper. The design takes advantage of the high intensity and high energy of X-rays available at a synchrotron, where X-ray structure data can be collected over a short time period with high resolution. Energy dispersive X-ray diffraction was used, which allows data from all angles to be measured simultaneously. The kinetics can be calculated by measuring turbidity and temperature simultaneously. Their preliminary results show an addition of 10% of n-docosane to a solution containing only n-eicosane radically changes the kinetics of crystallisation.

2.3.4 Relevant Binary Mixtures Studied in the Literature

In this research, we focus on studying the individual waxes before studying the binary mixtures. In this section, we will examine previous relevant binary mixture studies that have already been published.

2.3.4.1 Binary Mixtures of Fatty Alcohols and Edible Oils

The behaviour of fatty alcohols of various chain lengths in edible oils has been the focus of study in many previous studies.[57, 84-87] Schaink *et al.*[86], Gandolfo *et al.*[85] and Blach *et al.*[84] studied fatty acid, fatty alcohol, and edible oil tertiary systems, however in this review, I am going to focus on the fatty alcohols in peanut oil binary system researched by Fabio Valoppi *et al.*[57, 87] In the first study they document the polymorphic behaviour and crystal structure of the fatty alcohols when in the binary mixture and in the second study they characterised the structure and properties the oleogel formed.

Peanut oil is an edible oil and contains a mixture of oleic acid, linoleic acid, and other unsaturated fatty acids. Thermal behaviour of Eicosanol Peanut Oil binary mixtures was studied using DSC and displayed in Figure 2-20. Two peaks exothermic upon cooling are seen to converge as the concentration of peanut oil is increased until one exothermic peak is seen. They also found that at concentrations of 5% weight fatty Eicosanol in Peanut oil the orthorhombic β' -form was detected and the monoclinic was detected at concentrations of 30% weight and above as seen Figure 2-21. They found upon storage of the 5% mixture the less stable polymorphic form converted to the stable form. They also studied the particle size of the binary mixtures using USAXS.

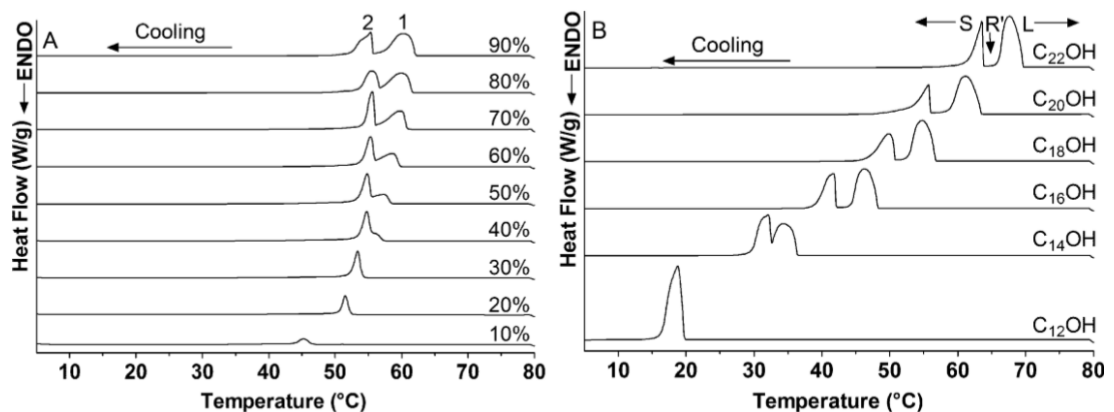


Figure 2-20 A) shows DSC crystallisation curves of $C_{20}OH$ in peanut oil binary mixtures and B) shows the crystallisation curves of a range of pure fatty alcohols taken from the study by Fabio Valoppi *et al.*[57]

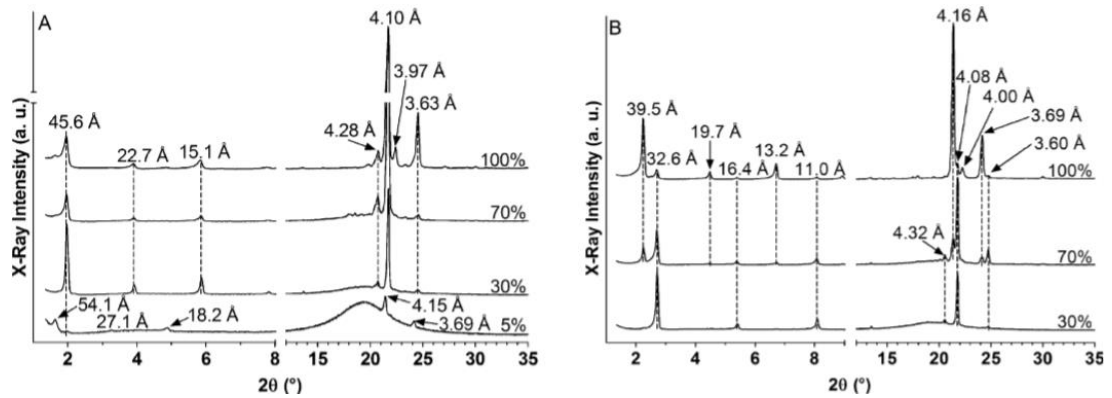


Figure 2-21 XRD patterns of $C_{20}OH$ (A) and $C_{14}OH$ (B) binary mixtures in peanut oil taken from the study by Fabio Valoppi *et al.*[57]

Valoppi *et al.* have extensively studied n-alkanol oleogels.[57, 87] The minimum gelling concentration and the solid fat content were calculated for fatty alcohols in peanut oil, before back extrusion measurements, DSC, optical microscopy and Cryo-SEM where images were taken. The extrusion measurements were performed to measure the mechanical properties of oleogels prepared under fast and cooling rates, stored at either 1 or 24 days. They reported a reduction in firmness and ability to entrap oils upon faster cooling rates with smaller crystals being observed.

Polarised light optical images have been taken of 5% n-alkanol/peanut oil mixtures. These mixtures form oleogels upon fast and slow cooling and are displayed in Figure 2-22. They observed large platelet crystals and needle structures for $C_{18}OH$ similar to previous reports[84-86] and small crystals positioned alongside larger rosette aggregates. They found the longer the fatty alcohol chains and faster cooling resulted in smaller the crystal size.

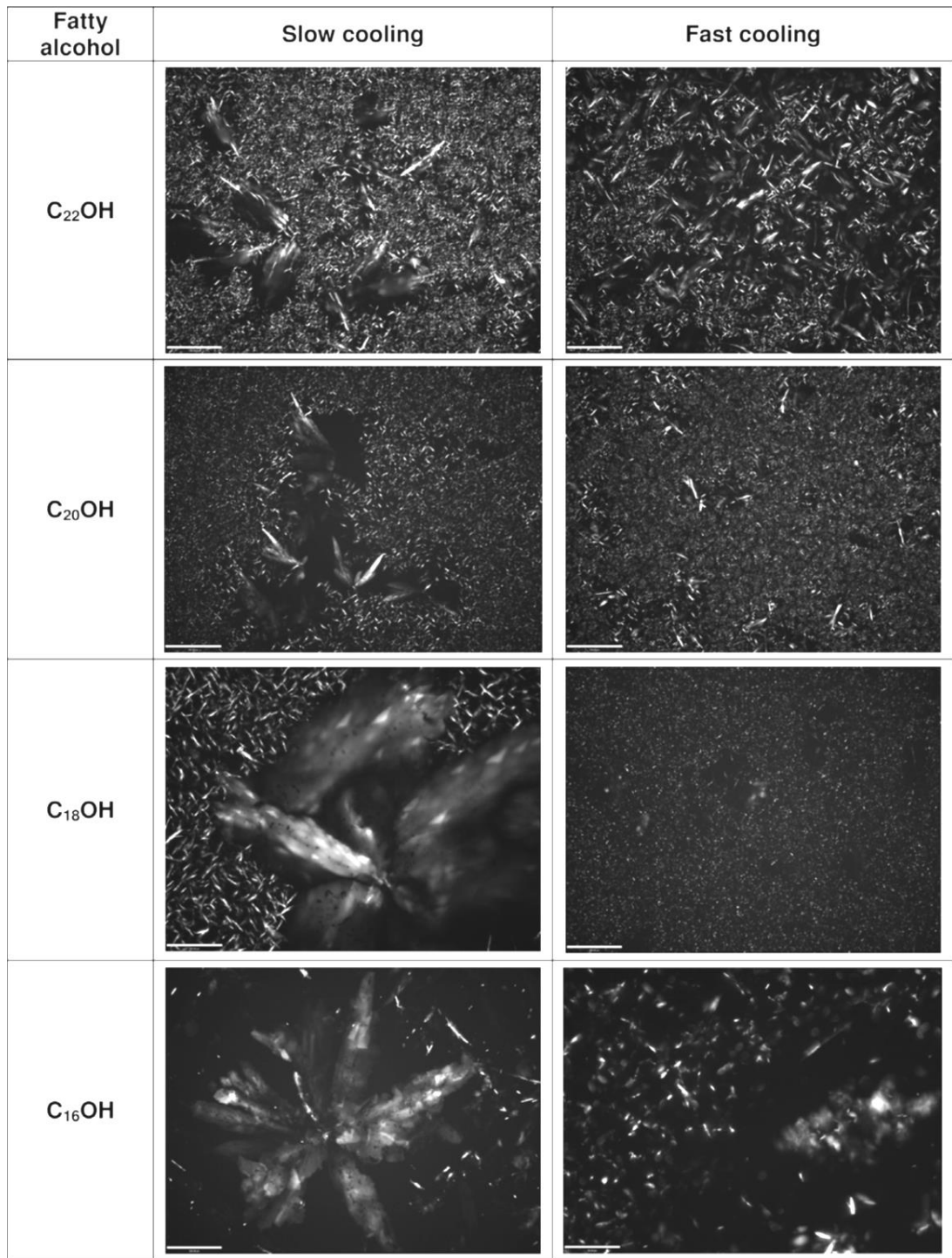


Figure 2-22 Polarized light microscope images of 5% C₂₂OH, C₂₀OH, C₁₈OH, C₁₆OH in Peanut Oil mixtures crystallised under slow and fast cooling after 1 day of storage. Scale bar 200µm. Sourced from Valoppi *et al.*^[87]

Cryo-SEM images display the structure of the fatty alcohol network present within the oleogel formed under fast and slow cooling and are displayed in Figure 2-23. They observed platelet crystals for fatty alcohol samples and found that the crystal structures were approximately 10x smaller upon fast cooling compared to slow cooling. Microchannels and pores on the surface of each crystal increased relative to increasing

fatty alcohol chain length and are thought to be related to increased lamellar phase separation.

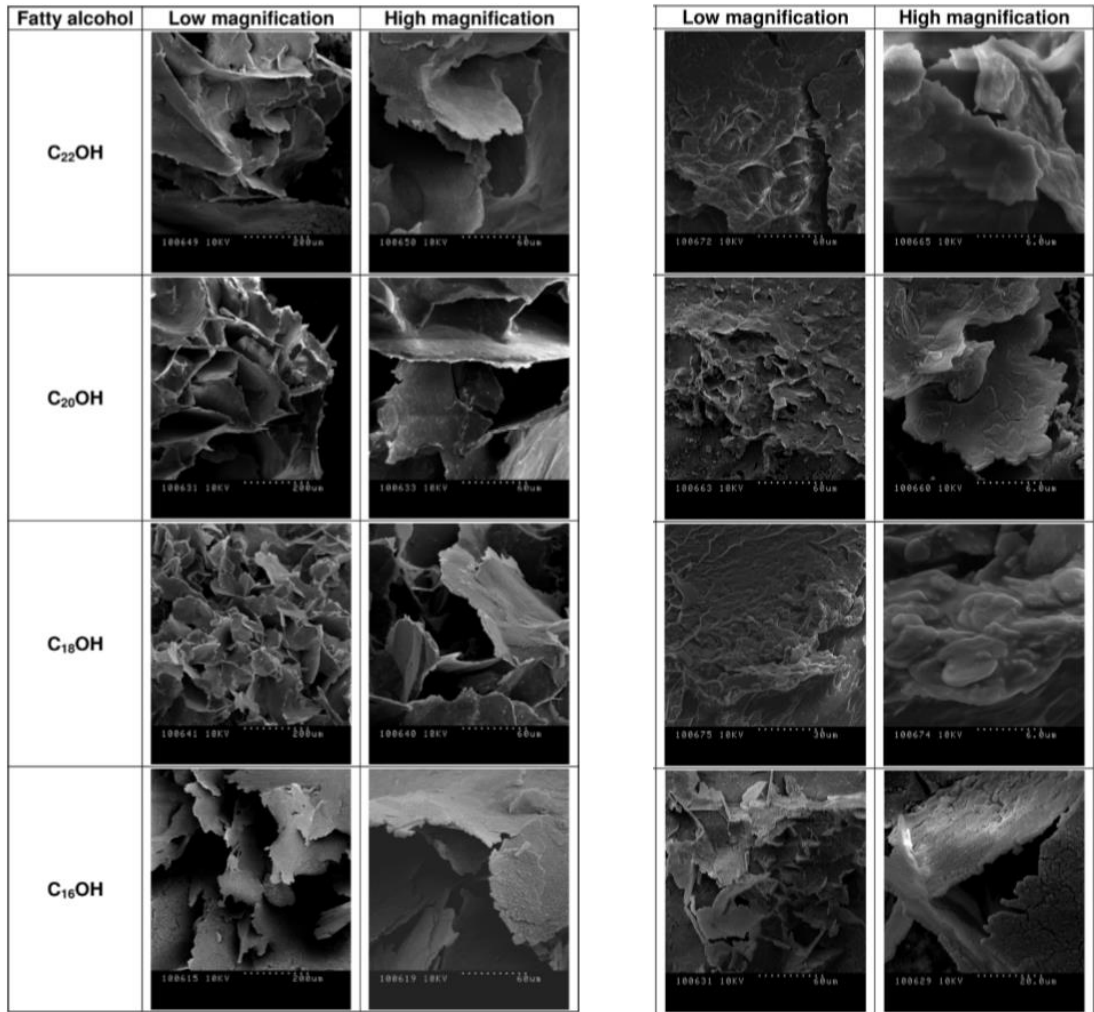


Figure 2-23 Cryo-SEM of fatty alcohol oleogels formed upon slow cooling (left) and fast cooling (right) taken from Valoppi *et al.*[87]

2.3.1 Shearing of Hydrocarbons

For many years X-ray diffraction has been used as a tool for measuring residual stress within crystallisation materials. Residual stress within a crystalline material can be caused by either mechanical, thermal or chemical action.[88] Experimentally residual stress can be measured through a comparison between the X-ray patterns of the stressed lattice with the unstressed lattice. Residual stress causes a shift in the d-spacing of the lattice; lower d-space is as a result of compression, and higher d space is as a result of lattice tension.

The polymorphism of a material can be impacted by the presence of shear. Cocoa butter is an excellent example of this phenomenon and has been extensively studied in the literature.

In the paper by S. Sonwai *et al.* they initially describe the 6 polymorphic forms of cocoa butter and including form V which is desired in the confectionery industry, because of its melting point range and physical properties.[89] In industry the chocolate is tempered by shearing the chocolate under a well-monitored temperature program to ensure it is in form V. Experimentally they investigate how shear influences the polymorphic structure of cocoa butter using a Rheo-X-ray facility which combines a capillary rheometer with an XRD facility. The sample was characterised using small-angle X-ray scattering (SAXS) and wide-angle X-ray (WAXS) modes.

Using these techniques, they observed transitions between different polymorphic forms at 20°C under different shear conditions. They correlated the X-ray results to images taken with a microscope equipped with a shear cell and imaged the crystals over a 1 hour time period. The results from all three techniques complemented each other and helped form an overall picture. They produced a schematic diagram displaying static and shear conditions to demonstrate what they observed.

Another study using a shear cell and small-angle scattering of X-rays on cocoa butter has been carried out by S. Macmillan and K. Roberts.[90] They observed III and IV polymorphs of cocoa butter under static and III and V polymorphs under shear conditions. They found that increasing shear rate increases the temperature that polymorphs are observed. An image of the shear cell used and the experimental results are displayed in Figure 2-24.

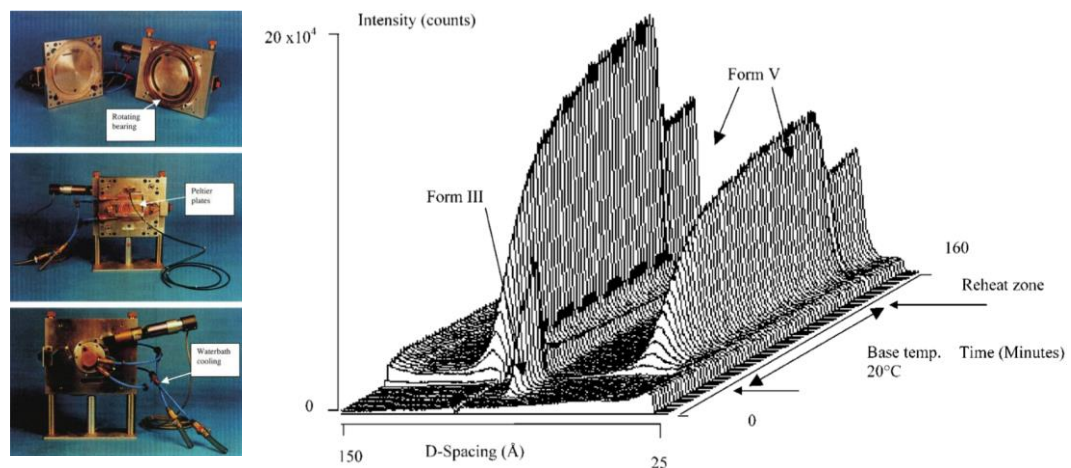


Figure 2-24 The shear cell used (left) and the SAXS experimental data upon cooling cocoa butter to 20°C whilst shearing at 3s⁻¹ (right). Sourced from MacMillan *et al.*[90]

2.3.2 Comparing and Contrasting Alkanes, Alcohols and Triglycerides

Alkanes, Alcohols and Triglycerides are all made from the same constituent parts, Carbon, Oxygen and Hydrogen atoms; however, they arranged in different ways to form different functional groups and structural shapes. The thermal behaviour and physical properties are strongly dependant on the intermolecular forces. The Alkanes and Alcohols studied in this research both have straight-chain structures, exhibiting very similar thermal behaviour, polymorphism and morphology however have different intermolecular interaction and melting temperatures. Alkanes consist of a straight Carbon chain without a functional group and alcohols have a Carbon chain with a hydroxy-functional group attached. Alkane molecules exhibit only weak van der Waal's forces, and alcohol molecules exhibit both strong hydrogen bonding and van der Waal's forces. This results in higher melting points for alcohols compared to alkanes for the same chain length. Alcohols and alkanes both exhibit similar morphologies, crystallising as needles or plates in solvent. Triglycerides exhibit a very different thermal behaviour, polymorphism, morphology, and molecular structure. A Triglyceride is an ester derived from three fatty acid molecules and glycerol. Triglycerides tend to be non-polar and only experience van der Waal's intermolecular forces. Triglycerides tend to form spherulites when crystallised from the melt and solution.

2.4 Characterisation Techniques

2.4.1 Lab Conducted Powder X-ray Diffraction

X-ray diffraction (XRD) is a technique, which enables the structure of crystalline materials to be characterised. X-rays are a part of the electromagnetic spectrum that is invisible to the eye, and they have a wavelength between 0.1\AA and 100\AA . This wavelength of X-rays is of a similar magnitude to the intermolecular distances in crystals and hence allowing crystal structures to be observed. A crystalline material consists of a large number of identical molecules arranged in a regular pattern in all directions creating symmetry.[91] When X-rays travel through a crystalline material, constructive and destructive interference occurs, creating a diffraction pattern. X-rays are particularly useful due to the fact they travel in a straight line, penetrating through metal and opaque materials such as the human body. Experimentally the d spacing of different planes in the crystal can be determined by using X-rays of known wavelength and measuring the

angle θ . The d spacing can be calculated by applying Bragg's law of diffraction. The X-ray beam is incident on the surface of the object at angle θ to the sample surface, and the diffracted beam is detected at angle θ to the sample surface, as shown in Figure 2-25. An XRD pattern is created by repeating this experiment for a range of angles of θ . [92] XRD can be conducted on a powdered sample or a single crystal.

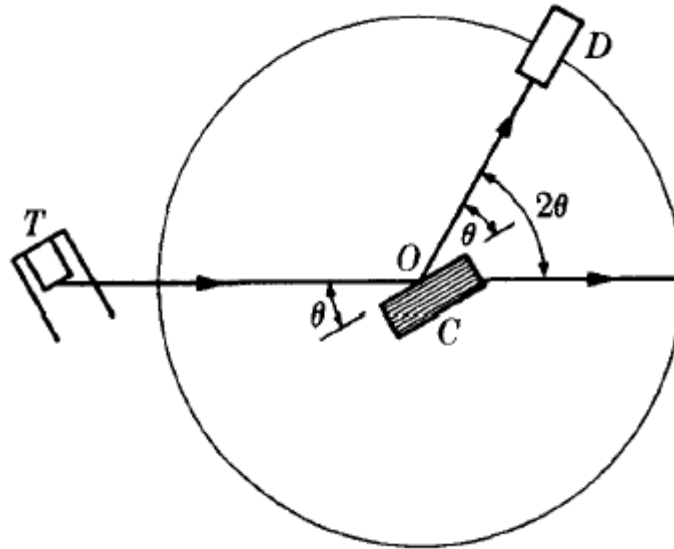


Figure 2-25 Diagram showing X-ray Diffraction (XRD) experimental set up where T is the X-ray source, C is the crystal sample, O is the axis the beam and crystal are rotated about, and D is the detector that measures the intensity of diffracted X-rays. [92]

2.4.1 Rheology

Rheology studies the flow of matter and mainly concerns liquids and soft solids. Materials can be defined by how they respond to an applied force. The flow of material often is measured using shear stress (τ) and shear rate ($\dot{\gamma}$) parameters with the apparent viscosity (η) defined as shear stress applied/shear rate. These parameters are calculated from the measured torque and flow rate. [93, 94]

Shear rate is defined as the rate which a fluid is sheared. Shear rate essentially rate at which the fluid layers move past each other as the fluid is sheared.

Shear stress is defined as a 'force tending to cause deformation of a material by slippage along a plane or planes parallel to the imposed stress'. [95]

The types of possible flow behaviour are displayed in Figure 2-26, and the gradient of each line indicates the viscosity. The simplest behaviour is called the Newtonian, where stress and strain rate have a linear relationship, and zero stress is measured at zero shear rate. Other behaviours include Bingham plastic, where flow only occurs above a yield

stress threshold and once the yield has been achieved, there is a linear relationship between stress and shear rate. Pseudoplastic behaviour, also known as shear thinning, resulting in the viscosity decreasing upon increasing shear rate. Dilatant, shear thickening behaviour exhibits an increasing viscosity with increasing shear rate.[93, 94]

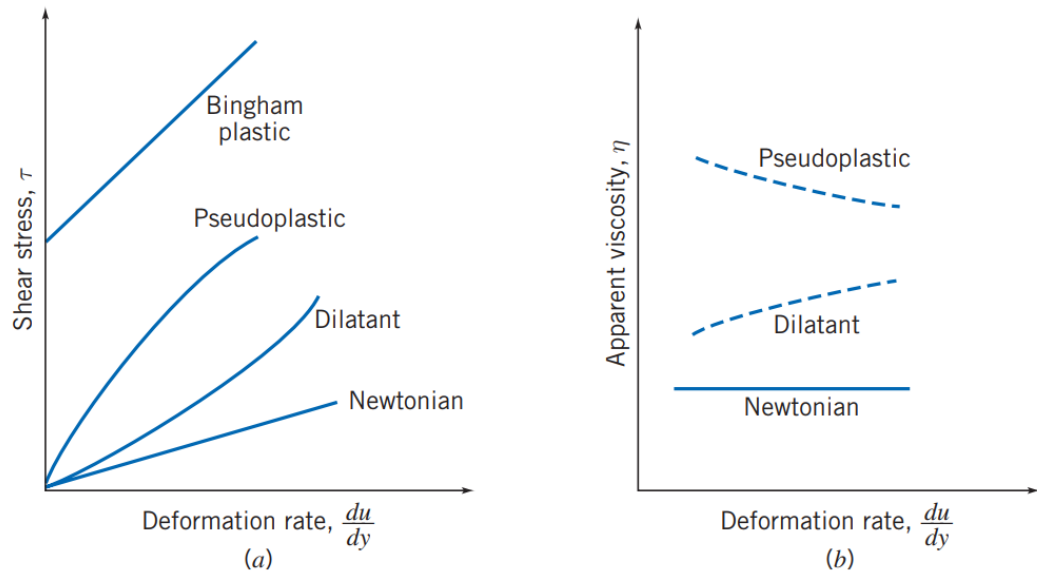


Figure 2-26 Plot displaying the four possible flow behaviours. a) displaying shear stress vs shear rate (deformation rate) and b) displaying apparent viscosity vs shear rate (deformation rate).[94]

2.4.2 DSC

Differential Scanning Calorimetry (DSC) was invented by Emmett Watson and Michael O'Neill in 1962. DSC is a thermal analytical technique, which measures the change in heat flow rate to the sample and a reference sample, whilst they are both subjected to the same programmed temperature ramp[96]. The sample and the reference sample are kept at nearly the same temperature throughout the experiment, and the heat capacity of the reference sample is well known over the temperature range.

The technique can be utilised to detect phase transitions of the sample measured. When the sample undergoes a physical phase transformation, more or less heat is required for the reference sample and studied sample to maintain a similar temperature. If the transition is endothermic, it requires more heat, and if it's exothermic, it requires less heat. The DSC technique is very sensitive and can detect transitions between polymorphic forms, as well as between solids and liquids.

2.4.1 Measuring Mechanical Properties and Morphology of Phases within Binary Mixtures.

The mechanical properties of a material can be measured by applying a force and measuring its reaction to the force. The most simple method of measuring the mechanical properties of a material, such as an elastic band, is to apply a force and measure the extension. Hooke's law (Equation 2-1) states that force is proportional to extension, where F is the force applied, k is a force constant and e is the extension of the material.

$$F = ke$$

Equation 2-1 Hooke's Law

The amount the elastic band will extend depends upon the length, the material composition, and its cross sectional area. Young's modulus (E) defines how easy a material can stretch and deform and is defined as the ratio of stress to strain and defined by the equations in Equation 2-2.

$$\text{Stress} = \sigma = \frac{\text{Tension}}{\text{Cross sectional area}} = \frac{F}{A}$$

$$\text{Strain} = \varepsilon = \frac{\text{Extension}}{\text{Original Length}} = \frac{\Delta L}{L}$$

$$\text{Young's modulus} = E = \frac{\text{Stress}}{\text{Strain}} = \frac{\sigma}{\varepsilon}$$

Equation 2-2 Stress, Strain and Young's modulus.

Figure 2-27 displays stress vs strain for a typical material that exhibits elastic properties below the yield stress and plastic behaviour above the yield stress. Hooke's law applies in the linear region until the limit of proportionality and in the elastic region, the material does not deform and returns to its original shape once the applied stress is removed. Young's modulus is also known as the elastic modulus if the deformation is measured in the elastic region with no permanent deformation.

If the yield stress is exceeded, the material will be deformed once the applied stress is removed, as shown by the dashed line from A to B in Figure 2-27. At the fracture point to material fails and breaks apart.

Figure 2-28 displays typical stress vs strain profiles for brittle, strong non-ductile, ductile and plastic materials. Hard brittle materials have a large Young's modulus and suddenly

fracture with no plastic deformation. In contrast, soft plastic materials have a low Young's modulus and have a very small elastic region. Ductile materials exhibit both plastic and elastic behaviour.

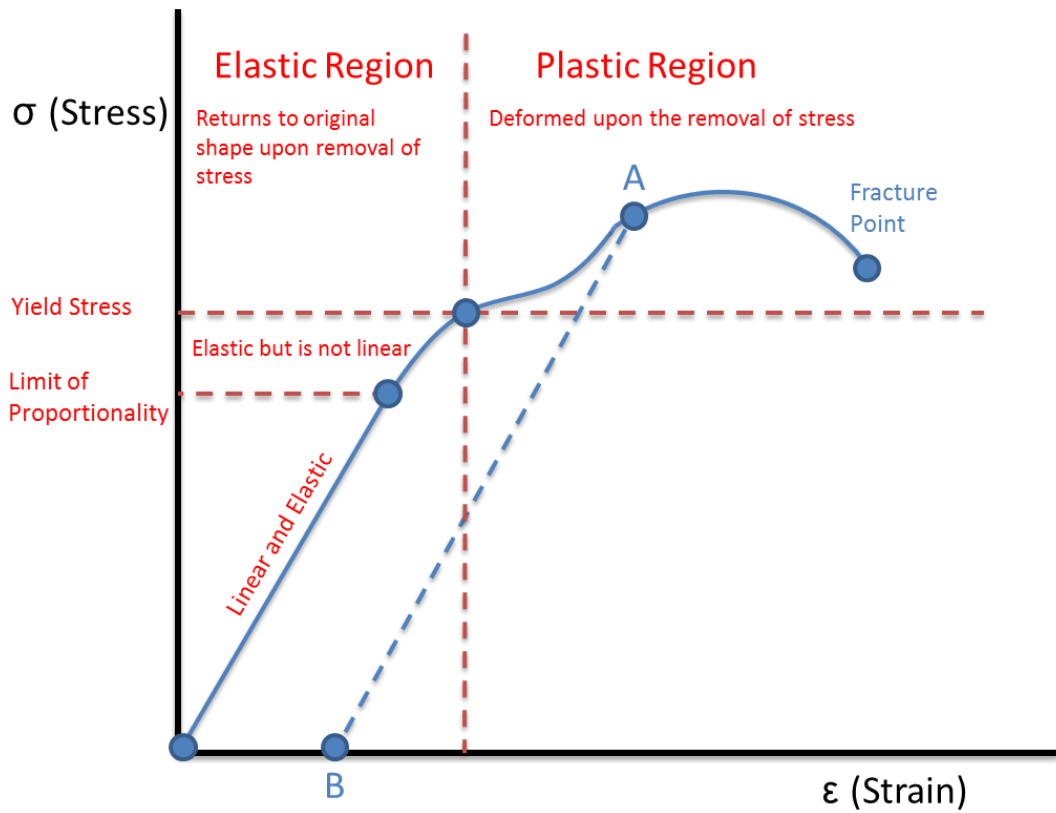


Figure 2-27 Stress vs strain graph displaying plastic and elastic deformation regions.

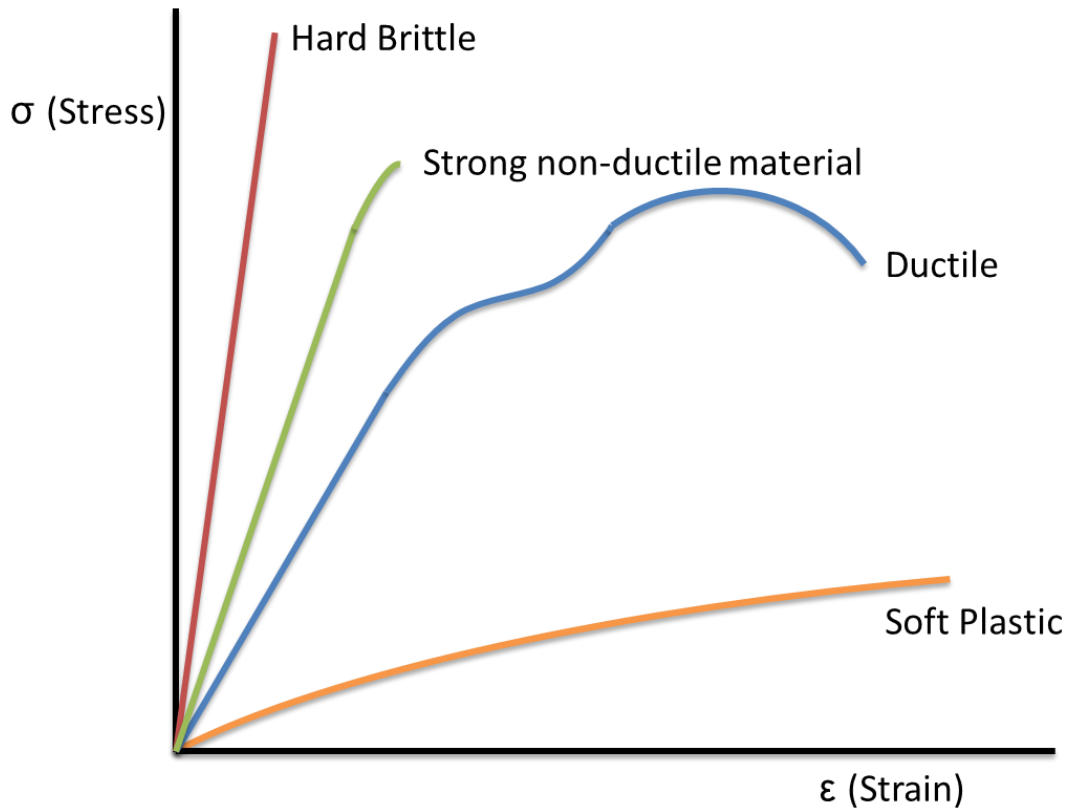


Figure 2-28 Stress vs strain displaying brittle, strong non-ductile, ductile and plastic material profiles

Recent advances in AFM have allowed the mechanical properties of the surface to be mapped out, allowing regions of the surface with different compositions and mechanical properties to be distinguished. Peak force tapping AFM with quantitative nanomechanical mapping (QNM) has been used previously in the literature to map out the surface of hardened cement[97], phase-separated polyurethanes,[98] a range of polymers[99] and a tertiary phase diagram of lipids.[100] The technique relies on the Derjaguin-Muller-Toporov (DMT) model to estimate the elastic modulus of the surface.[101] Equation 2-3 describes the forces occurring upon the tip coming into contact with the surface according to this model, where $F_{interaction}$ is the interaction force between tip and sample, E^* is the tip and sample reduced elastic modulus, R is the radius of the tip, d_0 is the resting position of the tip, $(d-d_0)$ is the deformation of the sample and F_{adh} is the adhesion force when the tip is in contact with the surface.

$$F_{interaction} = \frac{4}{3}E^*\sqrt{R(d-d_0)^3} + F_{adh}$$

Equation 2-3 Derjaguin-Muller-Toporov Force Equation.[97, 101]

Figure 2-29 displays the force vs separation graph for one cycle of the AFM tip, where the tip initially approaches the surface, makes contact, deforms the surface until peak-

force is reached, then withdraws from the surface and experiences an adhesion force until the tip loses contact with the surface.

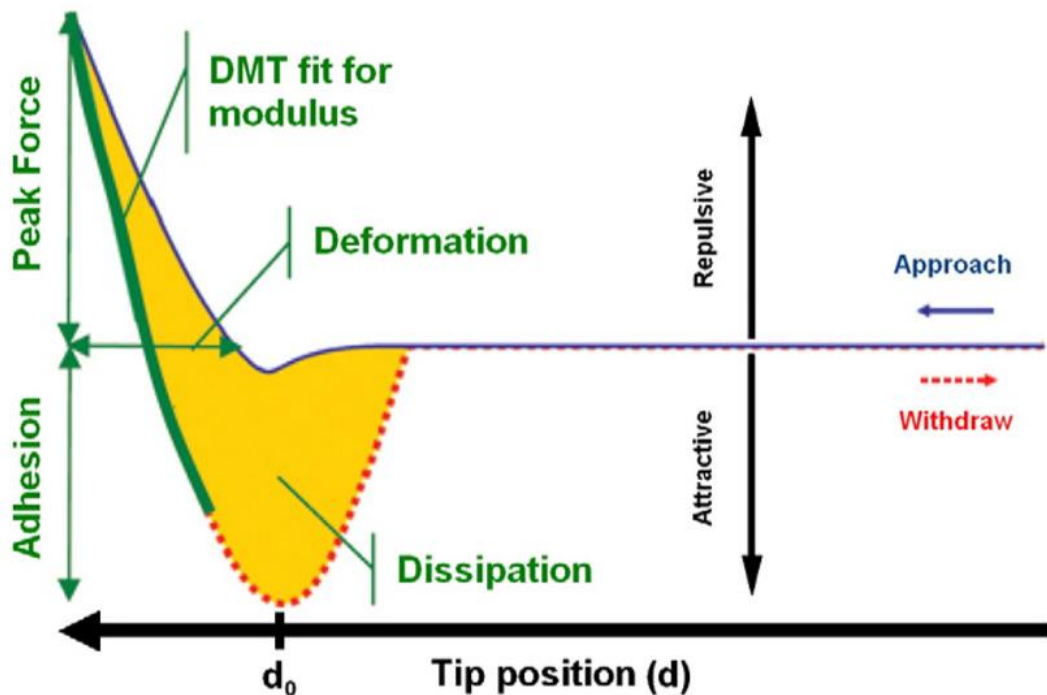


Figure 2-29 Diagram of force vs separation for a single cycle of the tip movement during peak-force tapping AFM. The blue line is the tip approaching, and the red line is the tip withdrawing. The peak force is a constant value, and once peak-force is reached the tip withdraws. This image is adapted from Ref.[102] and taken from the paper by P. Trtik *et al.*[97]

In P. Trtik *et al.* they use peak-force mapping with QNM to measure the local elastic modulus across the hardened cement surface, as shown in Figure 2-30.[97] The sample surface was also studied using back-scattered scanning electron microscopy (SEM) and energy-dispersive X-ray spectroscopy (EDX). High atomic number elements more strongly back-scatter electrons than lighter element, creating an image with material where heavy elements appear lighter, and light elements appear darker. EDX was used to create elemental maps displaying the location Carbon, Oxygen, Calcium, Aluminium, Sulphur and Silicon atoms on the surface. They found the AFM result correlated with the SEM and EDX results, and the technique was shown to work on a sample with a hardness of between 0.7 to 133 GPa. In the paper, they found that rough surfaces lowered the apparent elastic modulus and increased adhesion, demonstrating that smooth surfaces are key for obtaining a reliable result. A similar study was completed on phase-separated polyurethanes by P. Schon *et al.*, where peak-force tapping was compared with another AFM mode called HarmoniX and found the two modes to be in agreement.[98]

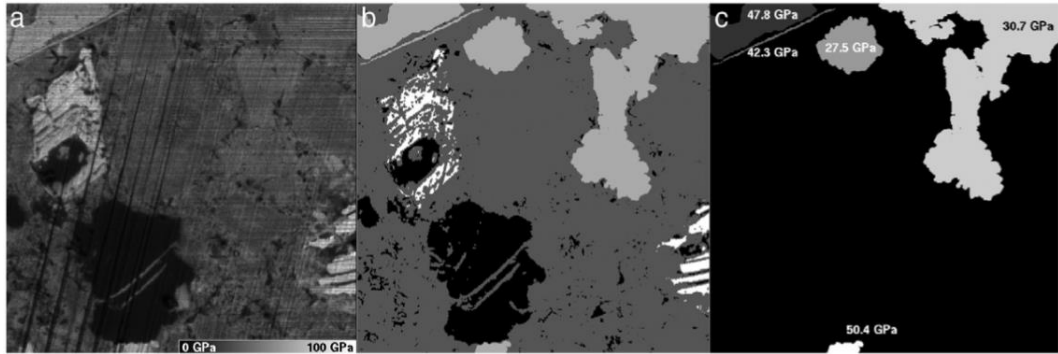


Figure 2-30 Elastic modulus map of Hardened Cement, a) elastic modulus, b) segmentation to porosity (black), unhydrated residues (white), Calcium hydroxide (light grey) and other hydrates (dark grey), c) displays the average elastic modulus of each region. P. Trtik *et al.*[97]

2.4.2 Hot Stage Microscopy

Hot stage microscopy is essentially an optical microscope, which is focused on a sample that is attached to a heating and cooling stage. This technique is a useful tool to enable continuous visual monitoring of the morphology changes at a phase transition, whilst the sample is being heated or cooled. The software allows temperature profiles to be preprogrammed, with images being taken at specific intervals between predetermined temperatures. This technique is particularly useful to gain a visual understanding of the different polymorphic forms, that have been found in the wax systems.[103]

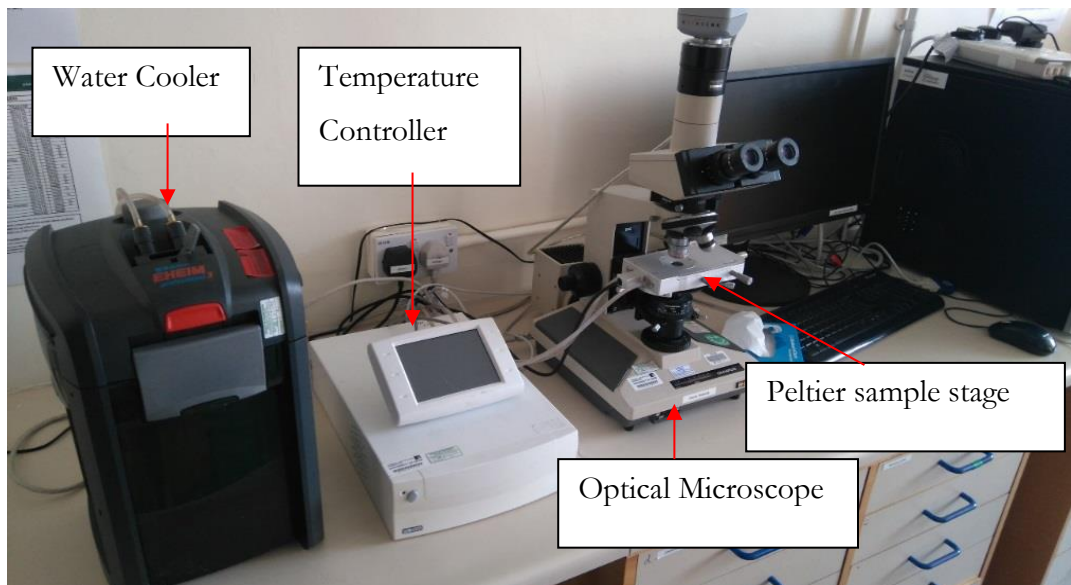


Figure 2-31 Hot stage microscope experimental set up.

2.4.3 Gas Chromatography

A Gas Chromatography Mass Spectrometer (GC-MS) is an extremely powerful tool and comprises of a Gas Chromatograph and a Mass Spectrometer. The sample is dissolved in a carrier solvent, vaporised and then injected into the column. The gas chromatograph

separates the components of the mixture, whilst mass spectrometer provides information about each component, which can help lead to deduce the structure of each component. The mass spectrometer works through capturing each separated component after it has passed through the column of the gas chromatograph. Each component is ionised into fragments. The fragments are accelerated, then deflected, and finally detected.[104]

2.4.4 SEM

Scanning electron microscopy (SEM) is a commonly used technique for investigating topography, microstructure, and composition of material surfaces.[105] SEM images are formed by detecting secondary electrons, backscattered electrons or both combined, after a small area of the surface has been struck with the electron beam. The electron beam scans across the sample surface in a fashion similar to a CRT television, forming a live image of the whole sample. Detecting secondary electrons tends to give an image with a higher spatial resolution and clearly shows the topography of the surface imaged. This is due to the secondary electrons being emitted from the smallest interaction volume.[106] The backscattered electrons form an image with a large amount of composite and topographical information. Backscattered electrons interact strongly with the nucleus and detected yield increases with increasing atomic number.[107] This enables areas of the sample containing atoms of a different average atomic number to be distinguished. Hydrogenated castor wax, Petrolatum, and stearyl alcohol are mainly Carbon-based, so each wax component will be difficult to distinguish, through atomic contrast using backscattered electrons or energy-dispersive X-ray techniques.

2.4.5 Polythermal Turbidity Studies

The Technobis Crystal16 is a parallel crystalliser that accelerates crystallisation research by allowing 16 separate crystallisation experiments to be carried out simultaneously. The Crystal16 unit consists of four independent Aluminium heating blocks, with each block containing four 1ml volume reactors. Each block exhibits electronically controlled heating and cooling through the combination of Peltier elements and a cryostat. Standard 11.5 mm diameter, flat bottomed HPLC vials fit into each reactor with each reaction mixture being agitated by a magnetic stirrer. Each reaction vessel contains a turbidity probe to monitor crystallisation and dissolution. The Crystal16 mainly has applications in the pharmaceutical industry; however, it has been used to study the materials in this project.

2.5 Conclusion

In this project, we aim to investigate how the process parameters such as shear and temperature impact the crystallisation structure and phase behaviour of typical wax stick formulation. The industrial sponsor P&G have an interest in this project due to experiencing scale-up issues with their wax stick formulation. I selected to study three groups of structuring ingredients which are n-alkanes, n-alkanol and triglyceride using Petrolatum, 1-Octadecanol, and HCO specifically. The thermal behaviour, polymorphism, morphology and physical properties of each material group that has been reported in the literature has been summarised, along with previous studies using relevant binary mixtures. Mixtures of the specific industrial relevant materials chosen have not been previously reported in the literature; however, similar systems have been studied, such as 1-Octadecanol in peanut oil. Another novel aspect of the research proposed will be studying the impact of shear on the individual materials and binary mixtures. No previous study has investigated to relationships between process conditions, crystallisation, polymorphism and physical properties for mixtures of n-alkanes, n-alkanols, and triglycerides.

Chapter 3 Methods and Materials

This chapter details the exact specification of the materials used, along with a detailed explanation of the method used for each experimental technique, including sample preparation, methodology and data analysis. This should allow the reader to repeat any of the experiments carried out if they should choose.

3 Methods and Materials

3.1 Introduction

A whole range of techniques has been utilised throughout this project in order to gain an understanding of the crystal structure, crystallisation kinetics, thermal behaviour, chemical composition and morphology of 1-Octadecanol, HCO and Petrolatum structured formulations. In this chapter, the sample preparation, methodology, data processing and analysis used for each technique will be covered along with an explanation of the theory. This will give the reader the possibility of repeating the experiments conducted in this study.

3.2 Materials of Study

All Materials used in this PhD were supplied from North America by our contacts at P&G. 1-Octadecanol had a purity of 98.4%, as stated by the certificate of analysis of the batch received. The exact material composition of HCO due is unknown due to its lack of solubility in Gas Chromatography compatible solvents, and the Petrolatum had an average chain length of 36.43 after analysing it with Gas Chromatography.

3.2.1 Solvents

Dodecane (purity of $\geq 99\%$), Acetone (purity of $\geq 99.9\%$) and Ethanol (purity of $\geq 99.9\%$) were supplied by Sigma Aldrich. D5 (purity $\geq 99\%$) was supplied by P&G.

3.2.2 Standard Binary Mixture Sample Preparation Method

Binary mixtures were measured out by weighing HCO, 1-Octadecanol, and Petrolatum using an analytical balance in glass vials at mole fractions of 0.1, 0.2, 0.3, 0.4, 0.5, 0.6, 0.7, 0.8 and 0.9MF. The mixtures made up, contained specific molar proportions of each material, for example, 1-Octadecanol/Petrolatum has relative moles of 0.25/1, so the mole fraction (MF) of 1-Octadecanol $x = 0.2MF$. The binary mixtures were heated on an 80-100°C hot plate whilst stirring with a magnetic stirrer until molten and homogenous, before being cooled on the lab bench with stirring until the mixture has solidified and room temperature has been reached.

3.3 Experimental Methods

3.3.1.1 XRD Sample Preparation

HCO, 1-Octadecanol, Petrolatum and the binary mixtures have been studied using XRD. The binary mixtures were prepared using the standard preparation method described in 3.2.2. Each sample was compressed into a powder specimen holder for measurement. Different sample holders were selected, depending on the volume of sample and instrument being used. A flat piece of plastic was used to ensure a flat surface, and the surface of the sample was in level with the top of the sample holder.

3.3.1.2 XRD Methodology

All samples were measured at the University of Leeds, Chemical Engineering Department, in the powder form and measured between angles of 4° and 40° , at 0.05° steps over a 5 minute scan time. Experiments have been carried out using either the Bruker D8 or the Phillips X-pert XRD. The Phillips X-pert can be fitted with a temperature stage, allowing samples to be measured between 25-100°C.

3.3.2 Polythermal Shear Synchrotron Radiation Experiments (LNLS)

One of the main aims of this project is to discover links between processing conditions, crystalline structure and the resulting physical properties of 1-Octadecanol structured formulations. A custom shear cell was designed and fabricated to examine the impact of processing on the structuring hydrocarbons. For the shear cell experiments to work, a high energy photon beam is needed for a large attenuation length through the sample and for experiments with a high time resolution.

Diffraction patterns from the shear and temperature study were collected using beamline SAXS1 at the Brazilian Synchrotron Light Laboratory.

SAXS1 has the capability for small and wide-angle X-ray diffraction in two different setups at a fixed beam energy of 8.3 keV with a $\Delta E/E$ of 0.1 keV. The camera length is variable, allowing structures to be resolved between 1-1000Å in two setups. The flight path of the X-ray beam was fully vacuumed at 10^{-2} mbar up until the shear cell and the detector. The detector used to capture the scattered X-ray beam was a Dectris, Pilatus 300K with 487 x 689 pixels of 172 μm in size with a frame rate 200Hz.

The X-ray beam passed through a 2 mm wide slit cut through the outer edge of the cylindrical shear cell. The slit exposed the Kapton film and the sheared sample to the X-ray beam. For more details of the shear cell design, see Chapter 8.

A Brookfield HBDV-II+P viscometer was utilised as a part of the shear cell set up, at the Brazil Synchrotron Light Laboratory. The viscometer was used to provide a shearing force on the sample whilst measuring the torque, allowing a viscosity to be calculated. The viscometer was used with a DIN-87 spindle and calibrated using Viscosity Standard Oil S600.

The Brookfield DV-II+ viscometer works by driving the spindle through a calibrated spring. The viscous drag from the rotating spindle causes a deflection in the spring that is measured by a rotary transducer. The torque of the calibrated spring contained within the Brookfield viscometer is 5.7496 mNm. The viscosity measurement in centipoise is determined by accounting for rotational speed, dimensions of the spindle, and the dimensions of the container and the torque of the calibrated spring.[108]

3.3.2.1 Sample Preparation

1-Octadecanol was recrystallised in Acetone, increasing the purity beyond 98.4%. From the Crystal16 experiments, 1-Octadecanol was known to have a solubility of 75 mg/ml at 33°C. 101.01 grams of 1-Octadecanol was dissolved in 4.25 litres of Acetone at 33°C and left to cool in an air-conditioned lab. 51.26 grams of purified 1-Octadecanol was obtained, with a percentage yield of 50.73%. Purified 1-Octadecanol was used to make binary mixtures of 1-Octadecanol/D5 and 1-Octadecanol/Dodecane at concentrations of 0.1, 0.2, 0.3, 0.4, 0.5, 0.6, 0.7, 0.8 and 0.9 mole fractions. The mixtures were melted together and crystallised whilst stirring to ensure a homogenous. A DSC scan of each sample was made to capture the thermal profile and to make a representative phase diagram for use at the synchrotron.

3.3.2.2 Methodology

Due to time constraints, only five different compositions of 1-Octadecanol with and without solvent were studied with respect to shear and temperature. The mixtures made up contained different molar proportions of (1-Octadecanol/D5) and (1-Octadecanol/Dodecane) in 0.25/1 (mole fraction (MF) of 1-Octadecanol $x = 0.2$), 4/1 (1-Octadecanol $x = 0.8$ MF) and 1/0 (1-Octadecanol $x = 1$ MF). A full breakdown of the

slow cooling, heating, and crash cooling experiments completed under different shear regimes using the shear cell are listed in Table 3-1.

Table 3-1 The table below details all variable temperature and shear experiments completed at LNLS synchrotron, using the shear cell.

Composition	Cooling / Heating			Crash cool	
	0 RPM	20 RPM	100 RPM	0 RPM	100 RPM
1-Octadecanol	✓	✓	✓	✓	✓
1-Octadecanol/Dodecane (0.2/0.8MF)	✓		✓	✓	✓
1-Octadecanol/Dodecane (0.8/0.2MF)	✓		✓	✓	✓
1-Octadecanol/D5 (0.2/0.8MF) (No signal observed)	✓				
1-Octadecanol/D5 (0.8/0.2MF)	✓	✓	✓		

Experiments were conducted under constant shear of 0rpm, 20rpm, and 100rpm, whilst the temperature cycled from 80°C – 40°C – 80°C and changes to the sample's crystal structure were observed upon crystallisation and melting.

Shear was provided, and torque was measured by a Brookfield Viscometer attached to a DIN-87 spindle. Temperature control came from a water bath which pumped water through the jacket engineering into the shear cell, and the temperature was measured using a temperature probe positioned inside the water inlet of the shear cell.

The crash cool experiments used two water baths. The first water bath held water at 80°C and the second water bath held water at 25°C. Initially, the 80°C water bath pumped water through the shear cell, melting the sample held in the shear cell, then the 80°C water bath was switched off, the piping disconnected and reconnected to 25°C water bath. The hutch was then closed, the beam switched on and then the 25°C water was turned on remotely using an extension lead with the plug located outside the hutch.

A background measurement was taken using the shear cell filled with water, as a model for the solvents used. This was because no D5 and Dodecane samples were taken to the

synchrotron in Brazil. Background measurements were taken using exposure times of 29 and 4 seconds.

At the synchrotron, temperature, rheology and X-ray diffraction experimental data were collected simultaneously. X-ray data were collected using a desktop PC running CS-Studio and 2D-SAXS, positioned outside the hutch. The GUI program running within CS-Studio was used for X-ray data acquisition after the following parameters had been entered, experimental name (filename), exposure time, deadtime (waiting time), number of images and polder path. The 2D-SAXS program displayed the acquired data in real-time during the experiment. Rheology and temperature data was recorded using a laptop running Rheocalc32 was connected to the Brookfield Viscometer via a serial cable inside the hutch.[109] This laptop was controlled remotely through Anydesk remote desktop software installed on a laptop located outside the hutch, enabling the viscometer to be controlled remotely.[110] Parallel's software was used to record the screen displaying the Rheocalc32 software with the temperature and rheology data.[111]

An exposure time of 29, 29 and 4 seconds was used for recording each image of the heating, cooling and crash-cooling runs respectively with a waiting time of 1 second. The number of images chosen was dictated by the heating/cooling rate and the desired finishing temperature.

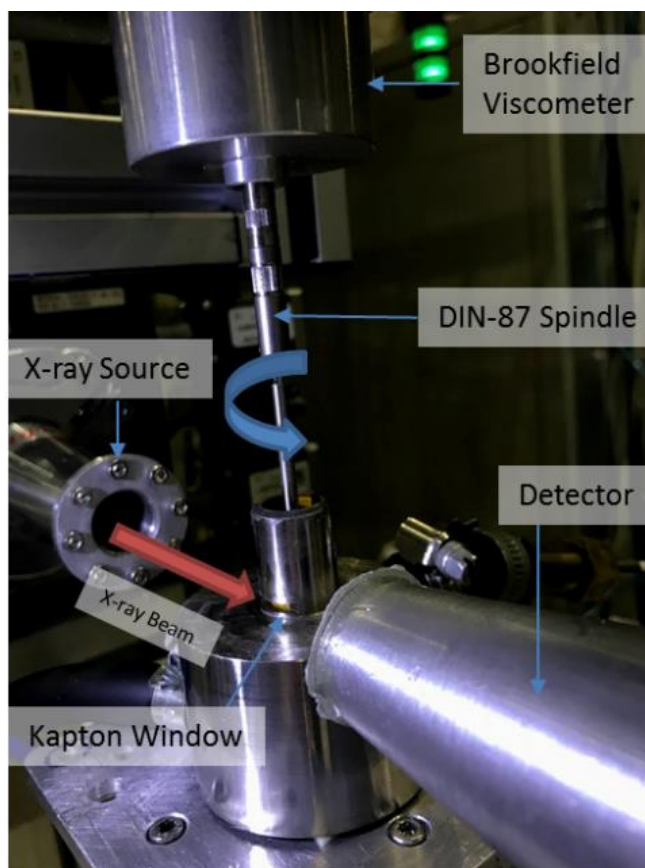


Figure 3-1 Image showing the shear cell experimental set up at the Brazilian Synchrotron Light Laboratory.

3.3.2.3 Data Processing and Analysis

At the synchrotron, initial data treatment steps were performed using 2D-SAXS, before the data was transferred on to an external hard drive. The data was normalised by the transmission, and the normalised images were integrated using a cake plot command.

At the synchrotron, the calibration of the beam was carried out using a calibration sample that wasn't contained in the shear cell. For data correction, a calibration curve was created between the measured gamma phase peaks when cooling of 1-Octadecanol and the VESTA predicted peak positions based on the published gamma phase unit cell. This calibration curve was used to correct all the measured data using this experimental setup.

The data was background corrected, and the low q data which displays flaring around the beam stop has been removed. Stacked graphs and 3D waterfall graphs have been drawn in Origin to display the changes in crystal structure with temperature and shear.

The Rheocalc software failed to save the rheology and temperature data, so the data was manually collected and tabulated in excel with reference to the screen recording of the Rheocalc software.

Origin was used to fit the peaks with Gaussian curves to accurately measure the peak position and the full-width half maximum (FWHM).

3.3.3 Rheological Measurements

Rheology measurements were conducted using the Anton Paar Physica MCR301 fitted with a 50mm/1° cone and plate geometry and a Peltier stage for temperature control. Temperature control was used to measure the rheological properties of the molten materials, as well as measuring the changes in rheological properties as the wax materials crystallise from the melt.

3.3.3.1 Sample Preparation

Samples measured included HCO, 1-Octadecanol, Petrolatum and Viscosity Oil Standard S600.

3.3.3.2 Methodology

Solid samples were loaded on to the Peltier plate at room temperature with the geometry in the raised position. Every sample was melted through raising the temperature of the Peltier before lowering the geometry. The excess sample was wiped away using a paper towel before performing measurements.

Two experimental methods were performed: temperature variation at a fixed shear rate and shear rate sweep at a fixed temperature. Variable temperature experiments were performed at fixed shear rates of 5, 25, 100, 200, 500 and 1000 s⁻¹ upon cooling from the liquid phase at 10°C/min. Shear sweep experiments were performed over a 1-1000s⁻¹ range at various isothermal temperatures. Shear rate was plotted against shear stress to determine the rheological behaviour of the material tested. The data was plotted using origin pro.

The viscosity of the calibration fluid was measured at 20, 25, 40 and 50°C whilst shearing was measured at a shear rate of 100s⁻¹. The measured values were compared against the values of the viscosity standard which were stated on the bottle.

3.3.4 Differential Scanning Calorimetry (DSC)

3.3.4.1 Sample Preparation

Binary mixtures of HCO/1-Octadecanol and Petrolatum/1-Octadecanol were prepared using the standard method at 0.0, 0.1, 0.2, 0.3, 0.4, 0.5, 0.6, 0.7, 0.8, 0.9 and 1.0 mole fractions.

3.3.4.2 Methodology

DSC was used to measure the thermal profile and phase transitions of the core components and their binary mixtures. These experiments were conducted at P&G Newcastle, on the TA Instruments, Discovery DSC, attached with a supply of Nitrogen. Each measurement used between 2 and 10 mg of material, contained in a 70 μ l Alumina crucible. Before the measurement of core components, the sample was cycled at least once, to ensure any material memory had been lost. Binary mixtures were cycled, from 30-100-30°C at a ramp rate of 10°C per minute, before being measured at 1°C per minute under Nitrogen atmosphere (50cm³ per minute supply of Nitrogen). The individual wax components were cycled at a range of temperature ramps.

The data for DSC was acquired and analysed using TA Advantage software before the data were plotted using Origin Pro.

The DSC instrument was maintained by P&G with routine calibrations performed.

3.3.5 Thermal Gravimetric Analysis (TGA)

HCO, Petrolatum, and 1-Octadecanol were measured, using the TA Discovery TGA at P&G, Newcastle, UK.

3.3.5.1 Sample Preparation

Between 10-20mg of wax material was weighted into a TGA pan for measurement.

3.3.5.2 Methodology

All samples were heated at 5°C per minute in the air. Petrolatum and HCO were heated until 700°C, and 1-Octadecanol was heated until 500°C. Before and after the temperature ramp, a two-minute isothermal step was performed.

The data for TGA was acquired and analysed using TA Advantage software before the data were plotted using Origin Pro.

3.3.6 Gas Chromatography (GC-MS)

The mass spectrometer outputs the mass to charge ratio of each fragment along with its relative quantity. This technique allows the exact components to be identified. At Leeds, Petrolatum was analysed using a PerkinElmer Clarus 560S in combination with a Clarus 580 GC, to observe the chain length distribution of the sample.

GC-MS was not used to assess the purity of HCO since the triacylglycerides are too large to be effectively vaporised, and they would likely decompose in the process. The triacylglycerides could be transformed into fatty acid methyl esters (FAME) through derivatisation; however, the distribution of fatty acid information in the original triacylglycerides would be lost.

3.3.6.1 Sample Preparation

The Petrolatum sample was run against an external sample of decane for comparison. Both samples were prepared by dissolving ~0.1g in 1.5ml of DCM to achieve approximately 2000ppm.

3.3.6.2 Methodology

For the Petrolatum study, 1 μ l of the sample was injected at a split ratio of 20:1 at 300 °C. The column used was a PerkinElmer Elite 5 MS, which was 30 meters long, with a 0.25 mm diameter and 0.25 microfilm thickness. The Mass Spectrometer used a transfer line temperature of 250 °C, a source temperature of 180 °C, electron impact mode and the mass to charge ratio was scanned between 50 to 500 m/z.

3.3.7 Hot Stage Optical Microscopy

3.3.7.1 Sample Preparation

Approximately 10mg of pre-prepared pure material or binary mixture was placed on a clear glass slide. The glass slide was inserted into the Peltier sample stage, and before measurement, the sample was heated until in the molten phase.

3.3.7.2 Methodology

The materials were analysed using an Olympus microscope with a 10x optical lens and x1.25 eyepiece attached to a Linkam LTS120 Peltier stage for heating, water recirculation pump for cooling and a temperature control system connected to a computer. This set up allows materials to be imaged at temperatures between 20 - 120°C.

Software called Linksys32 by Linkam was used to program the heating and cooling ramps of the Peltier plate at 1, 5, 20°C/minute, whilst also allowing the image capture frequency to be set for the camera attached to the microscope. The images captured have been viewed and processed using windows photo viewer. Scale bar was added to the images using image J, after imaging a 1mm long scale bar using the same microscope and lens set up.

3.3.8 Growth Cell

3.3.8.1 Sample Preparation

50.9mg of 1-Octadecanol was weighted into 2 ml of Dodecane, before being heated gently to dissolve the solute fully. The 25g/l solution was injected into the 2ml capacity glass cuvette before being stopped and sealed using parafilm.

3.3.8.2 Methodology

The glass cuvette was positioned inside the growth cell before the growth cell was reassembled with the screws fastened tightly to ensure no leaks. The growth cell was fitted to a Huber water bath, which pumped water through the growth cell, allowing temperature control. The solution contained within the cuvette was imaged using an optical microscope attached with x5 optical lens.

3.3.9 Atomic Force Microscopy (AFM)

Atomic Force Microscopy (AFM) is a technique that enables very high-resolution topographical images of surfaces to be generated. AFM works through a probe scanning across a surface, whilst collecting positional information as it encounters the surface. The probe is positioned at the end of a mirror cantilever, which moves in tiny movements across the surface and controlled by piezoelectrics. The position of the probe is monitored by a laser reflecting off the mirror cantilever and hitting a photosensor. The cantilever has a known spring constant allowing the force of the probe hitting the surface to be measured. Using this force information, AFM is able to measure the mechanical properties of the surface, such as Young's modulus (stiffness).

3.3.9.1 Sample Preparation

Pure material or pre-prepared binary mixtures with a range of compositions were placed on to hot stage microscope glass slides. The Linkam hot stage was used to melt the

samples at 80-90°C, before control cooling each binary mixture at 1°C/minute to room temperature. AFM sheared samples were prepared in a similar way on a glass slide, but using an Anton Parr viscometer for controlled heating/cooling at 10°C/min, whilst shearing using a 50mm 1° cone and plate arrangement.

3.3.9.2 Methodology

Experiments performed on the wax samples used the Bruker Icon, fitted with TAP 150 cantilevers and attached to a computer running Nanoscope V controller software. Experiments were conducted using PeakForce Quantitative Nanoscale Mechanical Characterisation (PF-QNM) at a frequency of 2kHz to capture surface topography and Young's modulus along with the optical image of each sample. Measuring mechanical properties enabled material contrast to be obtained and the composition of the microstructure to identified. Optical images of the sample area studied were taken to compare to the AFM result. Before performing force measurements, the instrument was calibrated using a blend of polystyrene and low-density polyethylene with known values of Young's modulus, as shown in Figure 3-2.

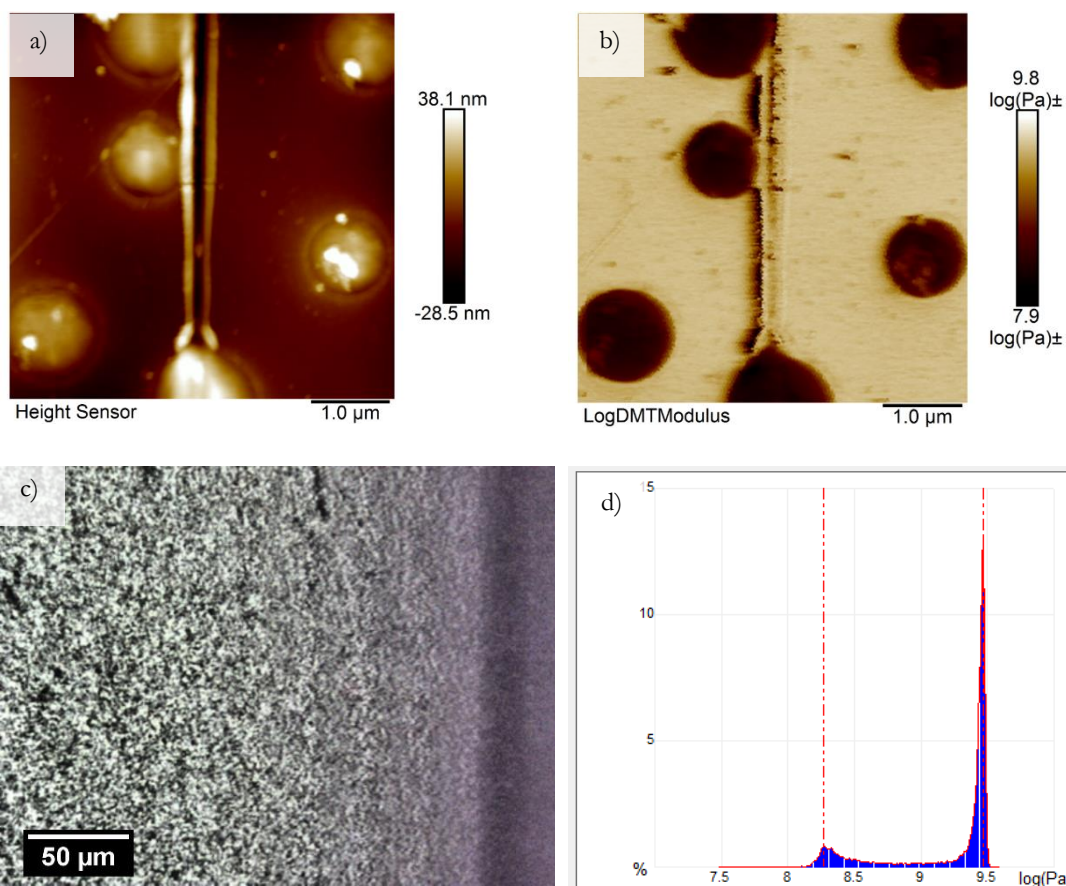


Figure 3-2 Images captured during calibration of the AFM PF-QNM experiments using a blend of polystyrene and low-density polyethylene. a) displays height map of the sample surface, b) Young's modulus map of the surface, c) optical image of the area studied, and d) plot of Young's modulus distribution across the surface.

3.3.10 Scanning Electron Microscopy (SEM)

3.3.10.1 Sample Preparation

The industry-grade 1-Octadecanol and HCO were recrystallised in Acetone, before being filtered. The Crystals were left to dry overnight before being placed on top of an Aluminium SEM stub with the surface covered in Carbon tape.

3.3.10.2 Methodology

The wax materials were analysed using the Hitachi tabletop microscope TM3030 at an acceleration voltage of 5kV in secondary electron mode, to observe the topography of the crystalline structure formed on the Aluminium surface. Various regions of the sample were studied at a range of magnifications.

3.3.11 Poly-thermal Turbidity Studies

3.3.11.1 Sample Preparation

Solutions of 1-Octadecanol in Ethanol were prepared at 45.1, 92.7, 143.4 and 193.5 mg/ml, in Acetone 3.5, 7.1, 14.8, 36.2, 75.5, 151.4 and 318.8 mg/ml, in Dodecane 6.0, 12.0, 24.3, 96.4, 169.1, 210.0 and 297.9 mg/ml, in Undecane 6.5, 12.9, 27.0, 51.7, 103.6, 182.7, 225.8 and 319.9 mg/ml and in D5 at 7.1, 14.4, 21.7, 29.0, 36.7, 44.6, 52.6 and 60.8 mg/ml. Solutions of HCO were prepared in Ethanol at 0.8, 1.2, 1.6, 2.4, 3.9, 7.9, 20.0, 24.0 and 28.0 mg/ml and in Acetone at 0.8, 1.0, 1.3, 1.5, 1.8 and 2.0 mg/ml. Crystal 16 experiments were conducted at concentrations at which the crystalline material can be dissolved in a solvent, without approaching the boiling point of the solvent. The crystalline material was weighted out using an analytical balance and before the solvent was added by weight. Stock solutions were stirred and heated on a hotplate until crystalline material was completely dissolved and then transferred into four 1.5ml Crystal16 vials using pre-heated pipettes to avoid crystallisation inside the pipette.

3.3.11.2 Methodology

The solutions were heated and cooled using Crystal16 in a pre-programmed cycle at heating and cooling rates of 0.25, 1, 2 and 3.2°C/minute typically between 50°C and 0°C whilst continuously being stirred at 700rpm using a micromagnetic stirrer bar. The temperature range used was adjusted to suit the solutions being measured, allowing crystallisation and dissolution to be studied. Each solution was cycled being held at high temperature for over 20 minutes between cycles to ensure complete dissolution.

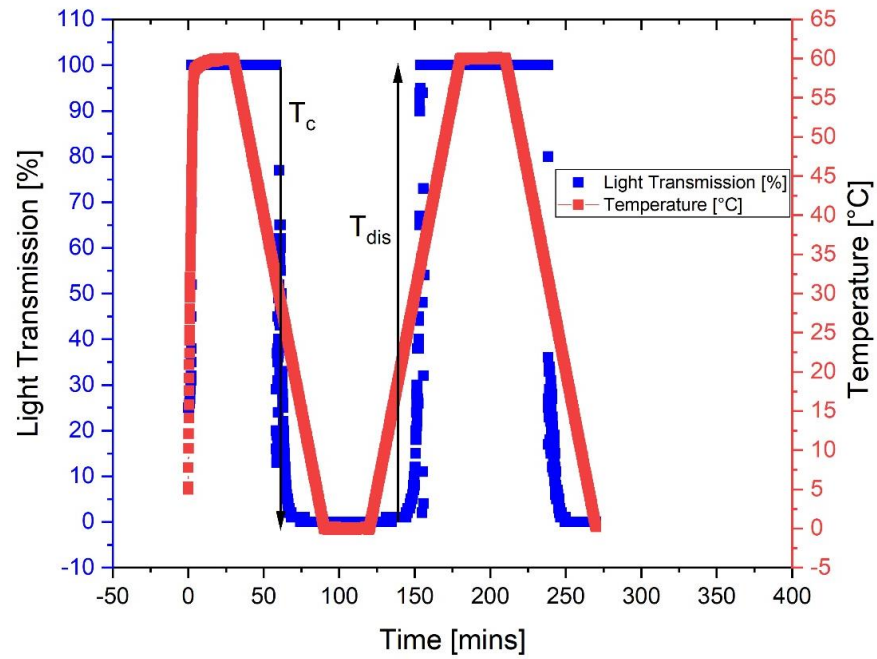


Figure 3-3 Example of polythermal method experiment where temperature was cycled between 0-100-0°C over time, and the change in light transmission (turbidity) was measured.

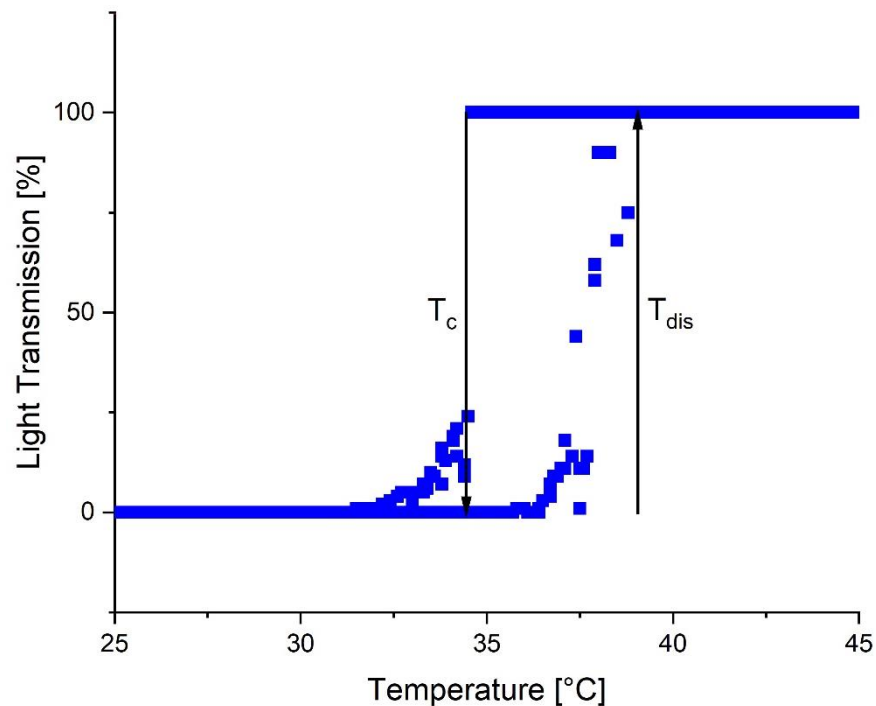


Figure 3-4 Change in turbidity measurement as the temperature is cycled during the polythermal method.

3.3.11.3 Data Processing and Analysis

Values of dissolution and crystallisation temperatures were recorded, and the average value with its error was tabulated measurements for all compositions, at each cooling and heating rate studied. For each composition, dissolution and crystallisation temperature were plotted with respect to cooling/heating rate. Two lines of best fit were placed

through the dissolution and crystallisation temperatures and extrapolated to zero cooling rate to generate values of the clear and cloud points respectively, as seen in Figure 5-1. The clear point is also known as the equilibrium temperature (T_c) and the cloud point is known the crystallisation temperature at the kinetic limit (T_c). The difference between dissolution and crystallisation temperatures at zero cooling is the metastable zone width.

The van 't Hoff plot has been used as a tool to derive the enthalpy and entropy of dissolution and enthalpy of solvation through plotting $1/\text{clear point (Kelvin)}$ vs $\ln X$ (mole fraction). The van 't Hoff plot relies on fitting the data to a linear form of the van 't Hoff equation, where R is the ideal gas constant.[112]

$$\ln X = -\frac{\Delta H_{diss}}{RT} + \frac{\Delta S_{diss}}{R}$$

$$\Delta H_{diss} = -R \times \text{slope}$$

$$\Delta S_{diss} = R \times \text{intercept}$$

Equation 3-1 van 't Hoff equation

The experimentally measured data was plotted against the ideal solubility line of a crystalline material in a solvent. The ideal solubility was determined using Equation 3-2 where ΔH_{fus} is the molar enthalpy of fusion of the solution calculated from the area under the DSC melting peak, T_m is the melting point in Kelvin and T is the solution temperature also in Kelvin.[112]

$$\ln X = \frac{\Delta H_{fus}}{R} \left(\frac{1}{T_m} - \frac{1}{T} \right)$$

Equation 3-2 Ideal Solubility Equation

Activity coefficient γ can be used to relate, the experimentally measured molar solubility of solute at equilibrium, x with the solubility of the ideal state, x_{ideal} using Equation 3-3. This equation was derived by equating the activity values of the ideal and non-ideal states from the normal activity definition.[113]

$$\gamma = \frac{x_{ideal}}{x}$$

Equation 3-3 Activity Coefficient Equation[113]

$$a_i^{sat} = x_i^{sat} \gamma_i^{sat}$$

Equation 3-4 Definition of activity

According to Raoult's law activity is defined by Equation 3-4, where a_i^{sat} is the activity, γ_i^{sat} is the activity coefficient and x_i^{sat} is the mole fraction of the solute i in a saturated solution. In an ideal solution $a_i^{sat} = x_i^{sat}$. [112]

Values of x_{ideal} were calculated using the ideal solubility at a particular temperature, Equation 3-2 and values of x were calculated from the polythermal experimental data using the van 't Hoff equation, Equation 3-1. Values of activity coefficient are often presented over temperature range for polythermal experiments.

Enthalpy of solvation can be calculated from the enthalpy of dissolution and enthalpy of sublimation. A more favourable dissolution process often has a lower enthalpy of solvation. [21, 114, 115]

$$\Delta H_{solv} = \Delta H_{diss} - \Delta H_{sub}$$

Equation 3-5 Enthalpy of Solvation

The collected turbidity data can also be analysed to provide insight into the nucleation mechanism of the system using the KBHR method. [113, 116, 117] The KBHR method distinguishes between two types of nucleation, progressive or instantaneous. Progressive nucleation is when new nuclei form in the presence of existing growing crystals, and Instantaneous nucleation is when all the nuclei form at the start of crystallisation then grow to develop into crystals.

The first stage of KBHR method involves constructing a plot of $\ln q$ vs $\ln u_c$ where q is cooling rate (K/s), u_c is critical undercooling, T_e is equilibrium temperature, and T_c is crystallisation temperature at each cooling rate. When a straight line was fitted to the plot the 'rule of three' was applied, and if the gradient of the line is above 3, the nucleation mechanism is progressive and below 3 is instantaneous.

$$\Delta T_c = T_e - T_c$$

$$u_c = \frac{\Delta T_c}{T_e}$$

Equation 3-6 Critical undercooling (u_c)

Before further analysing the dependence of u_c on q , the following inequalities must be met.

$$u_c < 0.1, \quad au_c < 1$$

Equation 3-7 Criteria for inequalities of u_c

Where values of a are calculated using Equation 3-8, k is the Boltzmann constant and λ is the latent heat of crystallisation.

$$a = \frac{\lambda}{kT_e}$$

Equation 3-8 Calculation of a

HCO and 1-Octadecanol predominately exhibited progressive nucleation mechanisms, so the data of each concentration was plotted $\ln q$ vs u_c graph. A derived expression of the dependence of u_c on cooling rate was fitted to the data and values of three free equation parameters could be calculated.[116, 117]

$$\ln q = \ln q_0 + a_1 \ln u_c - \frac{a_2}{(1 - u_c)u_c^2}$$

The three free equation parameters are given by:

$$a_1 = 3$$

$$a_2 = b$$

$$q_0 = \frac{VK_J T_e}{N_{det} 2b}$$

Equation 3-9 Derived expression for the dependence u_c on q

The nucleus effective interfacial tension λ_{eff} can be calculated using the dimensionless thermodynamic parameter of 3D nucleation, b . [117] Where k_n is the nucleus shape factor ($16\pi/3$ for spherical nuclei), v_0 is the volume occupied by a solute molecule calculated from the unit cell of Tristerin [118] and 1-Octadecanol [119] respectively (HCO = $1.696 \times 10^{-27} \text{m}^3$ and 1-Octadecanol = $5.446 \times 10^{-28} \text{m}^3$), k is Boltzmann's constant and T_e is the equilibrium temperature. Molecular volume of Tristerin was used as an approximation, since the crystal structure of Hydrogenated Castor is unknown, and Tristearin has the same molecular structure as Trihydroxystearin, apart from a missing Oxygen atom from position twelve on each Carbon chain.

$$b = \frac{k_n v_0^2 \gamma_{eff}^3}{k T_e \lambda^2}$$

Equation 3-10 Expression for the dimensionless thermodynamic parameter of 3D nucleation, b

From previously calculated and known parameters, values of the critical radius of the nucleus (r^*) and the number of molecules in the critical nucleus (i^*) can be calculated, using the maximum and minimum values of u_c to give a range of r^* and i^* [117]

$$r^* = \frac{2\gamma_{eff}v_0}{\lambda u}$$

$$i^* = \frac{2bkT_e}{\lambda u^3}$$

Equation 3-11 Expressions for the critical radius of the nucleus (r^*) and the number of molecules in the critical nucleus (i^*)

3.4 Conclusion

This chapter has provided an overview of the experimental methodologies of the employed in this study, as well as a description of the materials used. This will give the reader the opportunity for the reader to repeat any of the experiments conducted in this study. This includes an overview of the polythermal shear synchrotron study at LNLS, detailing the methods of collection and data analysis. Also, an overview of lab techniques used including powder XRD, DSC, TGA, GC-MS, Growth Cell and SEM has been provided, detailing the sample preparation, methodology and data analysis. For the AFM study, sample preparation and methodology has been provided, including Figure 3-2 which displays data collected during the calibration. This chapter closes with a detailed explanation of the polythermal studies conducted, data collection methodology, and analysis including the KBHR method and van 't Hoff analysis.

Chapter 4 Characterisation of Formulation Ingredients

In the first results chapter, 1-Octadecanol, HCO and Petrolatum have been characterised using a range of techniques, providing a reference to compare more complex systems too.

4 Characterisation of Formulation Ingredients

4.1 Introduction

This project focuses on three types of wax materials used in cosmetic formulations, n-alkanols, triglycerides, and n-alkanes. Industrial grade material 1-Octadecanol, HCO and Petrolatum were supplied by P&G and used throughout this study. In this chapter, these supplied materials have been characterised using microscopic, rheological, chromatography, thermal and X-ray techniques to reveal their morphology, composition, polymorphism and physical properties upon comparison to the literature. Through understanding the individual components, will provide a basis to understand the binary mixtures, solution chemistry, shear behaviour in the following chapters.

4.2 1-Octadecanol

The thermal behaviour has been studied upon heating and cooling the industrial sample of 1-Octadecanol at 1°C per minute using Differential Scanning Calorimetry (DSC) under Nitrogen. The 1-Octadecanol was supplied at a purity of 98.4% from P&G and thermal behaviour compared against previous studies in the literature. The DSC curve of heat flow plotted against temperature is displayed in Figure 4-1. Upon cooling, two exothermic peaks are observed due to the crystallisation of the rotator phase from the melt and solid-solid transition from the rotator phase to the stable gamma phase at just below the crystallisation temperature. Upon heating, there are two endothermic peaks representing the solid-solid from the gamma phase to the rotator phase at just below the melting point and the melting of the rotator phase. The melting temperature and enthalpies for 1-Octadecanol have been compared to previous studies in the literature in Table 4-1. The polymorphism and thermal behaviour in the n-alkanols are very similar to the n-alkanes, hence share the naming for different phases. From the research into n-alkanols by Ventola *et al.*, we know the stable phase of 1-Octadecanol is the gamma phase γ , and the rotator phase is in the R_{IV} form.[53] Ventola *et al.* found it's possible the form the metastable β upon quenching 1-Octadecanol with liquid Nitrogen.[53]

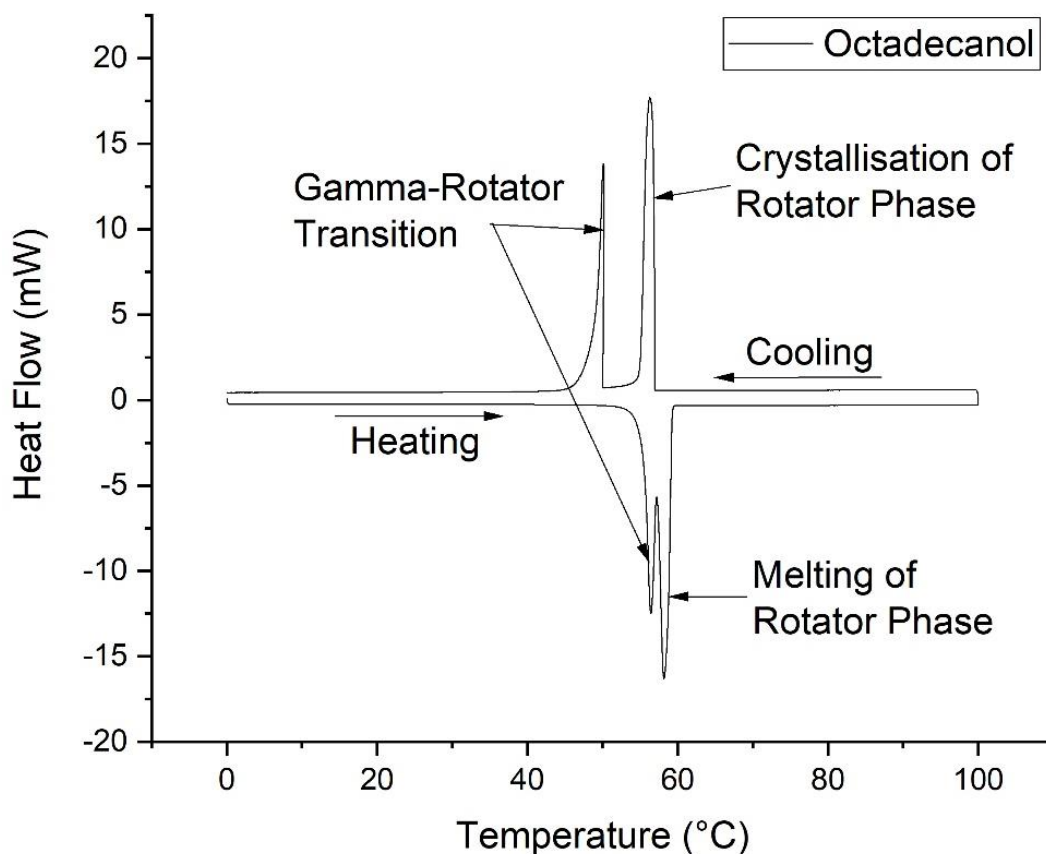


Figure 4-1 Differential Scanning Calorimetry (DSC) graph showing the liquid-rotator-gamma phase transitions of 1-Octadecanol when heated and cooled at 1°C/min using Mettler Toledo DSC1 at Leeds

Table 4-1 Melting temperatures and enthalpies of 1-Octadecanol on Heating at normal pressure.

Solid-solid transition		Solid-liquid transition		ΔH_{total} (kJ mol ⁻¹)	Reference
$T_{\gamma \rightarrow R'IV}$ (K)	$\Delta H_{\gamma \rightarrow R'IV}$ (kJ mol ⁻¹)	$T_{R'IV \rightarrow L}$ (K)	$\Delta H_{R'IV \rightarrow L}$ (kJ mol ⁻¹)		
329.63	25.22	331.42	38.19	63.41	This work using TA DSC at P&G, Newcastle.
329.5	26.5	330.3	40.1	66.6	Ventola <i>et al.</i> [53]
330	26	331	43	69	Reuter <i>et al.</i> [120]
330.6	25.6	331.2	41.1	66.7	Van Miltenburg <i>et al.</i> [121]

Thermal gravimetric analysis (TGA) was also performed on 1-Octadecanol upon heating at a ramp rate of 5°C min per minute in the air. Figure 4-2 displays the % weight loss as

a function of temperature. A tiny mass loss of 0.0053% was recorded by 100°C and possibly is due to the desorption of water. The 1-Octadecanol is known to have a boiling point of approximately 210°C, and 97% of the mass loss occurs between 150°C and 250°C. This suggested that the mass loss is due to 1-Octadecanol boiling rather than any thermal degradation. The smooth sharp curve confirms that the 1-Octadecanol studied has high purity.

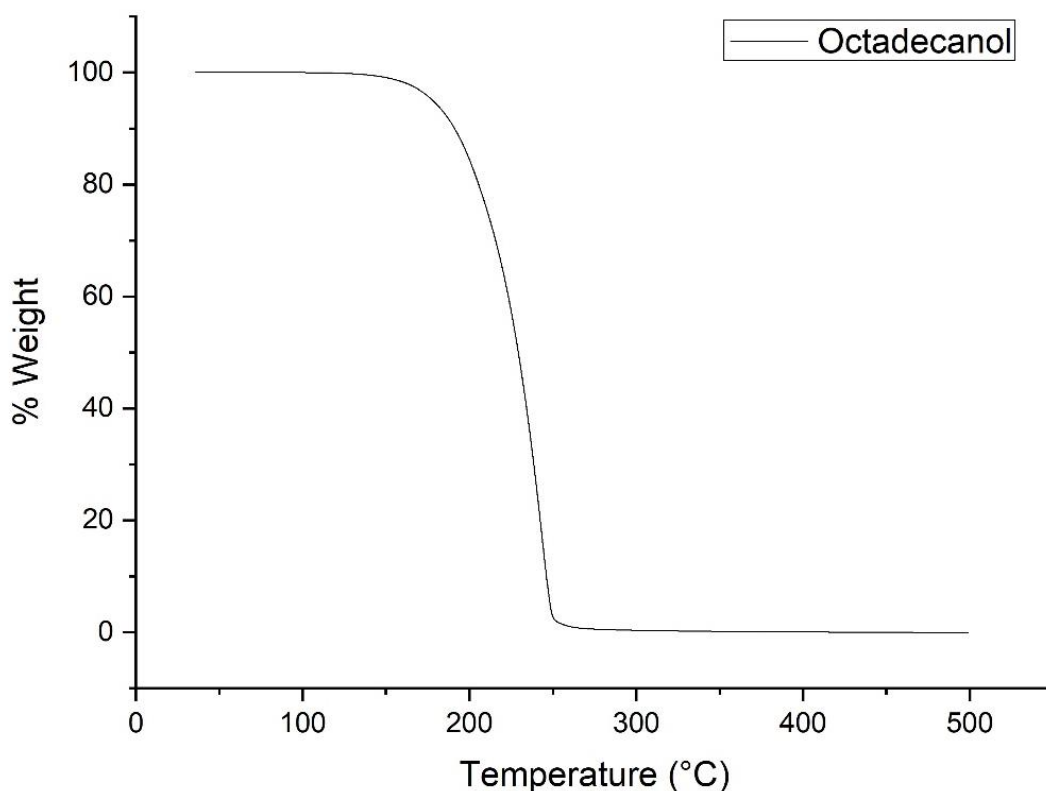


Figure 4-2 TGA graph showing the mass loss of 1-Octadecanol when heated at 5°C/min to 500°C.

The X-ray diffraction (XRD) pattern of 1-Octadecanol was measured at room temperature and at 55°C to observe the gamma and rotator forms, respectively. Both XRD patterns are displayed in Figure 4-3. X-ray patterns of n-alkanols have been previously studied on numerous occasions by many groups and the solved ambient temperature 1-Octadecanol X-ray structure has been solved and uploaded to the Cambridge Crystallographic Data Centre (CCDC).[119]

The Guiner-Simon photographs of the rotator and gamma phases of 1-Eicosanol are shown in Figure 2-18. Here the X-ray diffraction patterns of the two polymorphs are displayed. The peaks of the ambient temperature XRD pattern have been identified with reference to the .cif file using XRD pattern prediction software VESTA, and the d-spacing of each peak has been labelled. The X-ray pattern measured at 55°C matches

previously measured rotator phase patterns between 5-23°C; however, other aspects fail to match such as an amorphous bump is observed 15-25°C and peaks present between 25-40°C. The amorphous bump likely due to the sample being partially in the molten phase and the three extra peaks are likely to be due to HCO impurity from not cleaning the sample holder properly.

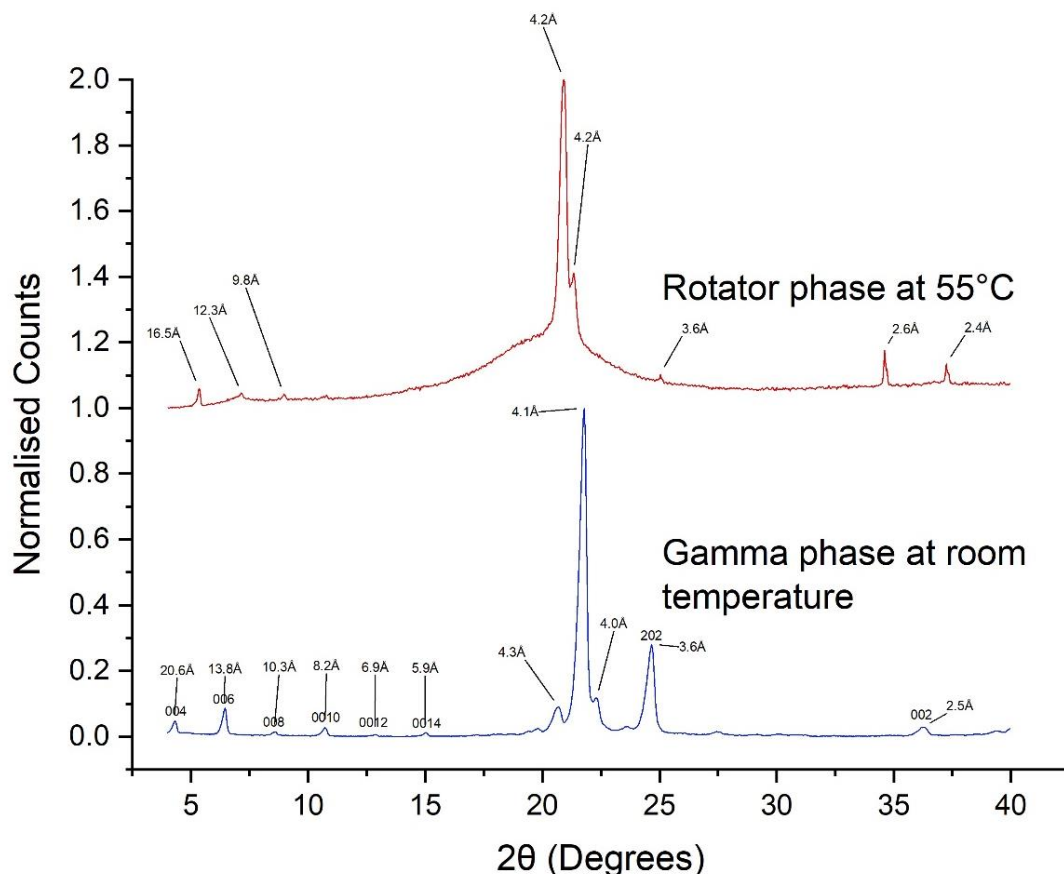
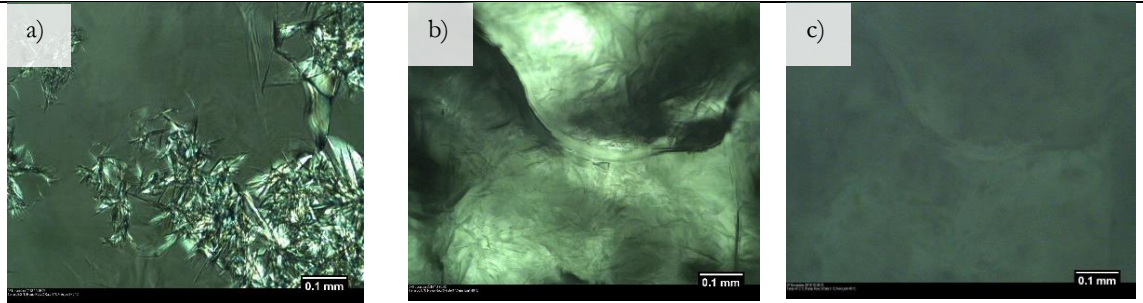


Figure 4-3 Stacked XRD graph displayed the metastable rotator phase at 55°C and the stable gamma phase at room temperature of 1-Octadecanol.

The crystallisation of 1-Octadecanol has been captured using a hot-stage microscope upon cooling. The rotator phase initially crystallises at 59°C, and needle-shaped crystals rapidly grow through the melt creating a crystal structure as seen in Figure 4-4 a) and d). A dense transparent crystal structure forms as all the liquid melt transforms into the solid rotator phase. At 50°C small regions of the bulk crystal structure suddenly, from clear to opaque one by one, until the whole bulk crystal becomes opaque as witnessed between images b) and c). Each region that suddenly transforms is most likely to be a single crystallite, and each crystallite has no uniform shape. The clear to opaque visual transformation is due to the solid-solid rotator to the gamma phase transition. At higher cooling rates, a decrease in microstructure size of the rotator phase is observed when

comparing images a), e) and g) at 1°C, 5°C and 20°C per minute respectively. The bulk of the gamma phase is difficult to image because the material is opaque.

1-Octadecanol cooling from the melt at 1°C/min

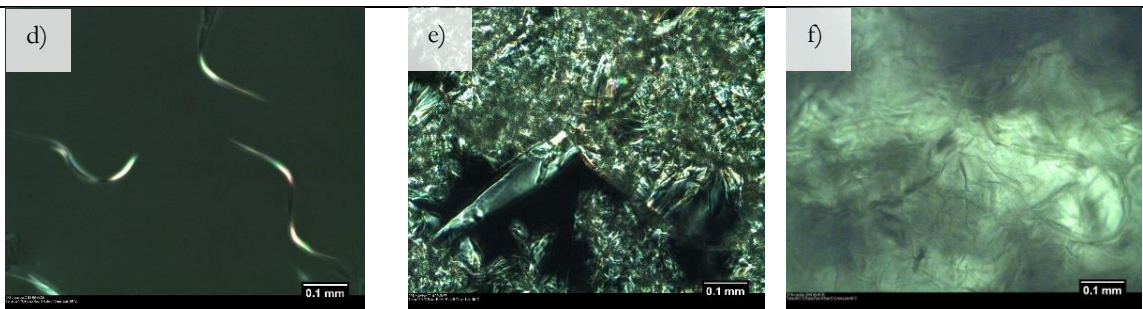


The crystallisation of the rotator phase at 59.2°C

The transition between rotator and gamma phase at 50.0°C

Stable Gamma phase at 47.2°C

1-Octadecanol cooling from the melt at 5°C/min

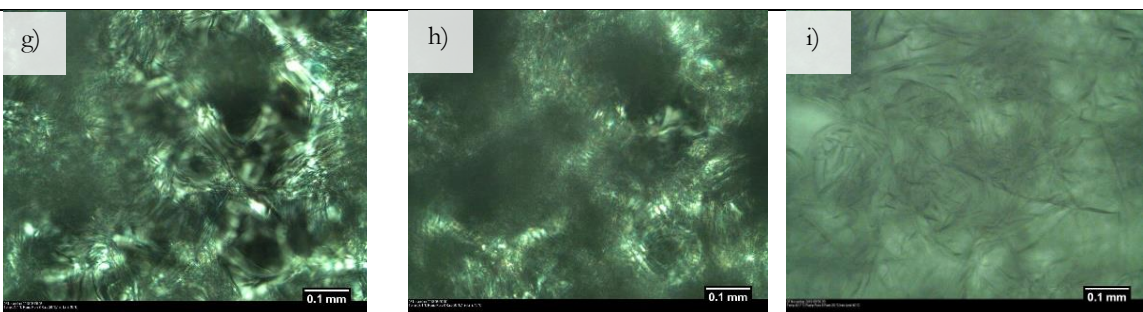


Early Stages of Crystallisation at 59.1°C

The developing rotator phase at 57.4°C

The transition between rotator and gamma phase at 49.1°C

1-Octadecanol cooling from the melt at 20°C/min



Early Stages of Crystallisation at 54.7°C

The developing rotator phase at 53.4°C

The transition between rotator and gamma phase at 42.7°C

Figure 4-4 A series of optical images capturing, the transitions between liquid, rotator and gamma phases upon cooling 1-Octadecanol from the melt.

The surface of the gamma phase has been studied at room temperature using an Atomic Force Microscope to identify the mechanical properties and morphology. The samples

were prepared by cooling from the melt at 1°C (Figure 4-5), 5°C (Figure 4-6) and 20°C per minute (Figure 4-7), before being captured at room temperature using an optical microscope and measured studied using AFM. The surface of 1-Octadecanol was observed to be smooth with a series of steps, and the Young's modulus force map shows that the stiffness was uniform across the surface. As the surface is flat and AFM studies a very small area there is no noticeable difference when cooling at 1°C, 5°C and 20°C per minute, however, a clear difference can be observed when comparing the macroscopic optical images with smaller crystals observed at faster cooling rates.

Cooling 1-Octadecanol at 1°C/min

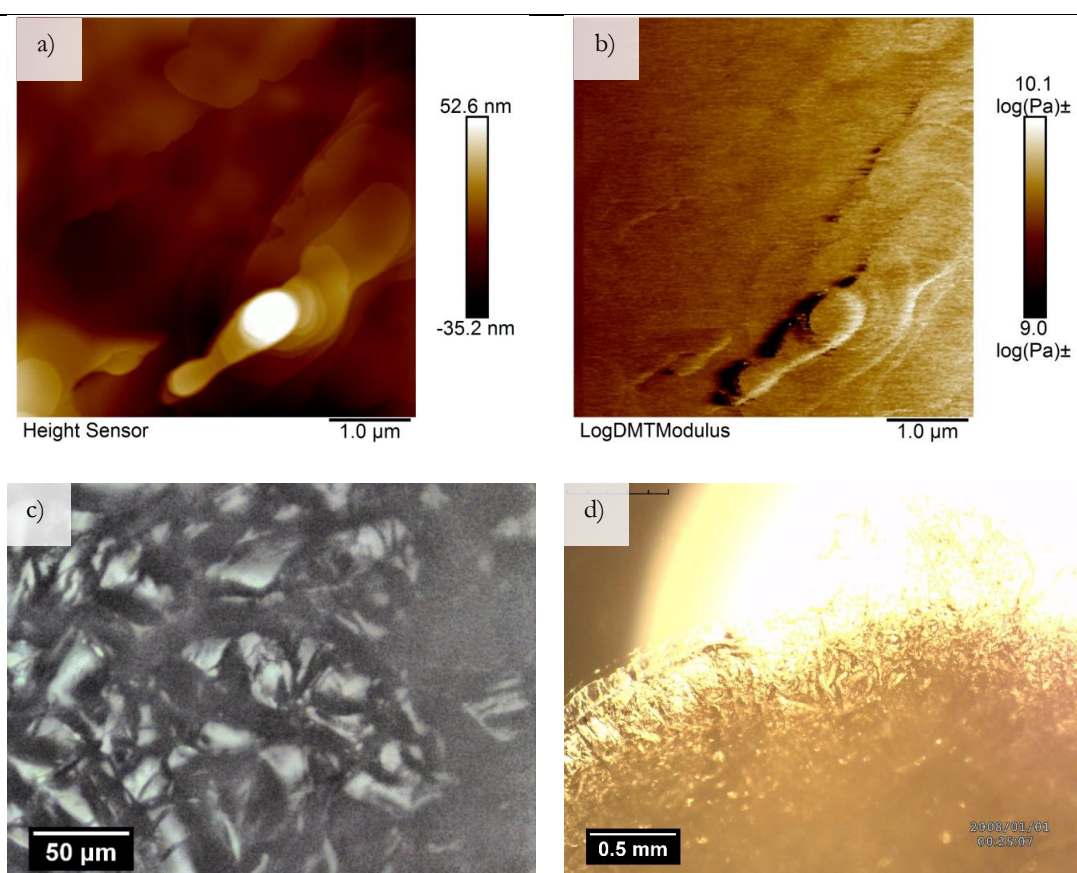


Figure 4-5 Atomic Force Microscope (AFM) and Optical Microscope (OM) images of 1-Octadecanol cooled from the melt to room temperature at 1°C/min. a) Height map of surface (AFM), b) Young's Modulus map (AFM), c) High magnification optical image of the area studied (OM) and d) Low magnification optical image of the sample surface (OM).

Cooling 1-Octadecanol at 5°C/min

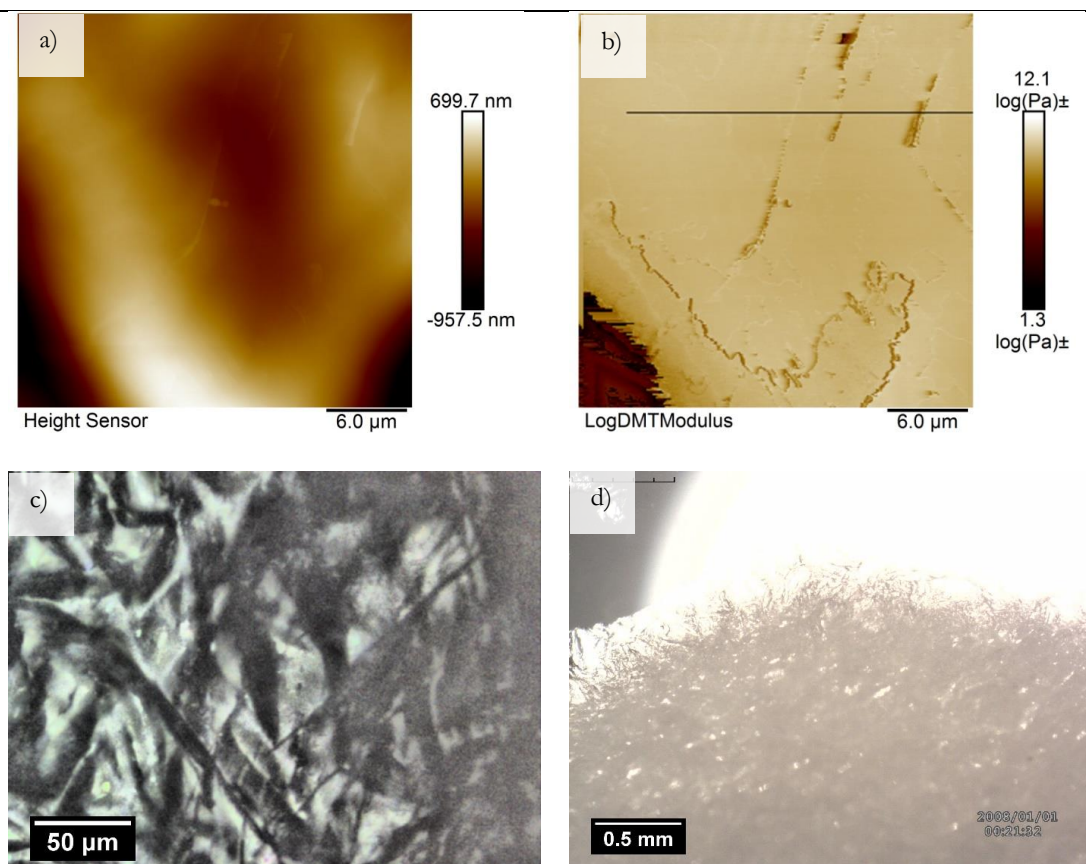


Figure 4-6 Atomic Force Microscope (AFM) and Optical Microscope (OM) images of 1-Octadecanol cooled from the melt to room temperature at 5°C/min. a) Height map of surface (AFM), b) Youngs Modulus map (AFM), c) High magnification optical image of the area studied (OM) and d) Low magnification optical image of the sample surface (OM).

Cooling 1-Octadecanol at 20°C/min

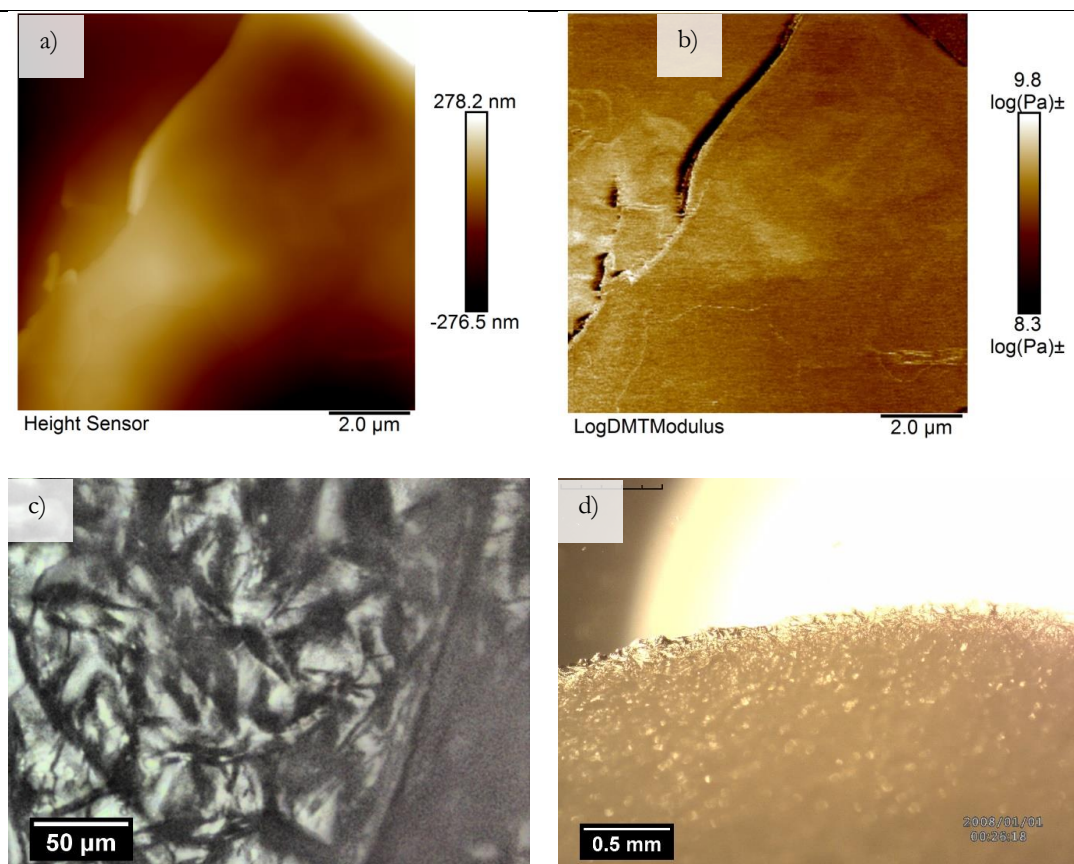


Figure 4-7 Atomic Force Microscope (AFM) and Optical Microscope (OM) images of 1-Octadecanol cooled from the melt to room temperature at 20°C/min. a) Height map of surface (AFM), b) Youngs Modulus map (AFM), c) High magnification optical image of the area studied (OM) and d) Low magnification optical image of the sample surface (OM).

The rheological behaviour of 1-Octadecanol has been measured at a range of shear rates from 1 to 1000s⁻¹ at temperatures between 58°C and 95°C using a 75mm diameter cone and plate arrangement. Molten 1-Octadecanol is a free-flowing liquid with a viscosity of 0.00373 Pa.s and shear stress of 0.0373 Pa at 95°C with a shear rate of 10s⁻¹. On cooling, 1-Octadecanol starts to crystallise at around 58°C and solidifies upon further cooling. When solid 1-Octadecanol is brittle, its rheological properties can be not measured using a rheometer. Upon performing a shear sweep, molten 1-Octadecanol is shown to be shear thickening (dilatant fluid), where the shear stress increases with shear rate. This is common for suspensions containing high levels of dispersed solid and explains the increased shear thickening behaviour at the crystallisation temperature.

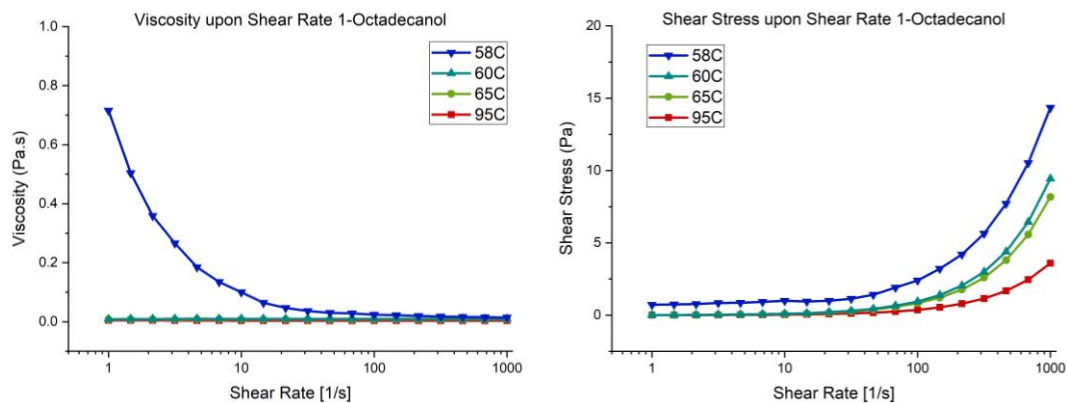


Figure 4-8 Change in Viscosity (left) and Shear Stress (right) upon ramping Shear Rate for 1-Octadecanol at a series of different temperatures

4.3 Hydrogenated Castor Oil

Industrial grade Hydrogenated Castor Oil (HCO) was supplied by P&G with an unknown composition. Unlike the relatively pure 1-Octadecanol, HCO contains a blend of many mono, di and triglycerides with the tri-hydroxystearin as the main constituent. Little work has been previously published on HCO despite its wide industrial use.

The thermal behaviour of HCO was studied using DSC whilst heating and cooling at 1°C per minute between 0°C and 90°C. Upon cooling, HCO exhibits an exothermic crystallisation peak at 68.2°C, along with three low enthalpy very broad peaks between 55°C and 30°C. On heating, an endothermic melting peak is observed at 71.1°C and a series of low energy peaks are observed between 30°C and 70°C. The identity of the low enthalpy peaks is unknown.

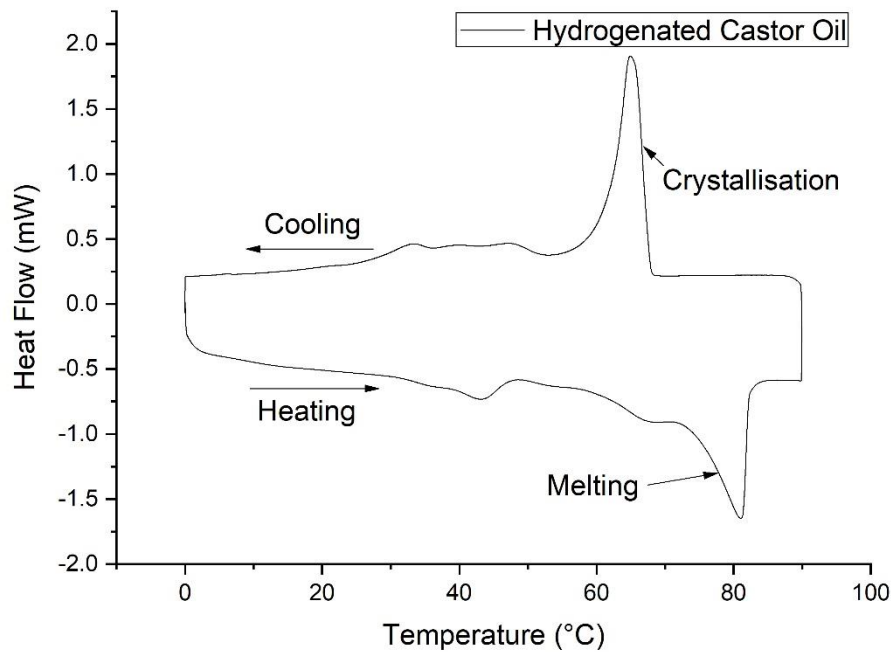


Figure 4-9 Differential Scanning Calorimetry (DSC) graph showing the phase transitions of Hydrogenated Castor Oil when heated and cooled at 1°C/min

Thermal gravimetric analysis has been conducted on HCO upon heating at 5°C per minute from 0°C to 600°C in air, as displayed in Figure 4-10. Only a mass loss of 0.7% was observed between 25-250°C. Heating beyond 250°C, 74% mass loss occurred between 250-415°C with the rate of mass loss decreasing at 380°C. At 415°C, a sharp increase in the rate of mass loss occurred before decreasing again at 450°C and total mass loss was achieved by 550°C. The initial mass loss at 250°C is likely due to boiling points of HCO's main components being reached; however, it is not clear whether the further mass loss events are due to decomposition or other molecules boiling off.

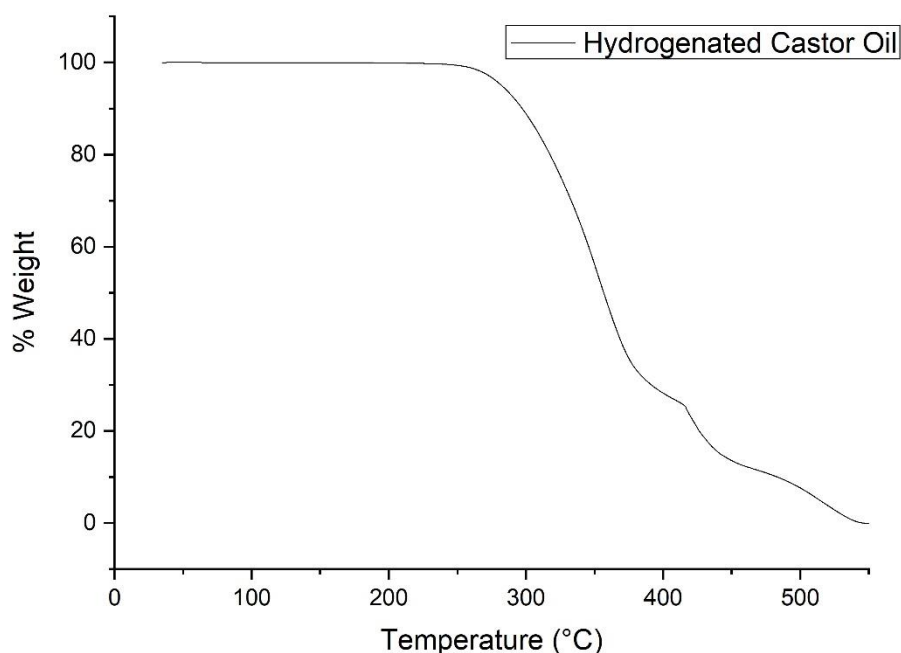


Figure 4-10 Thermal Gravimetric Analysis graph showing the mass loss of Hydrogenated Castor Oil when heated at 5°C/min to 600°C.

The X-ray pattern of industrial-grade HCO has been measured at a series of temperatures whilst cooling from the melt, as shown in Figure 4-11. In Figure 4-12, the X-ray pattern of HCO twice recrystallised in Acetone was compared against the industrial-grade HCO. At 95°C HCO is molten and displays an amorphous bump at 20° along with a series of peaks at 12.6, 3.5, 3.0, 2.9, 2.7, 2.6 and 2.4Å. HCO crystallised after cooling to 53°C and the amorphous bump transformed into two large peaks at 4.5 and 4.0Å which indicates the presence of the β' triglyceride polymorph. In addition to the two main peaks, extra small peaks form at 16.7 and 6.3Å upon crystallisation. Upon further cooling to 33°C, no change to the X-ray pattern was observed showing that no polymorphic transitions had occurred and HCO is semi-amorphous at room temperature. Upon recrystallisation of HCO, the two large peaks remain, however, peaks at 3.0, 2.9 and 2.7Å disappear and the peaks at 3.6, 2.6 and 2.4Å become sharper and larger in intensity. The peak disappearance could be due to certain molecules being removed during the recrystallisation. The low angle peaks are all broad, and high angle peaks are all very sharp with a very different appearance.

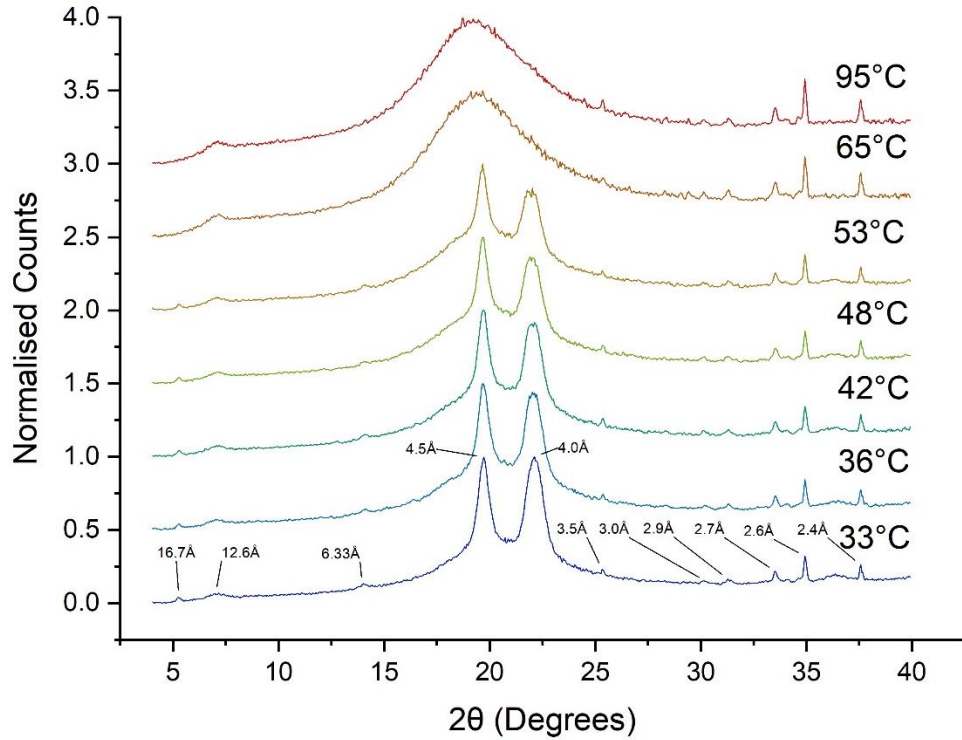


Figure 4-11 Stacked X-ray Diffraction patterns of HCO captured upon cooling from the melt at 95°C to 33°C.

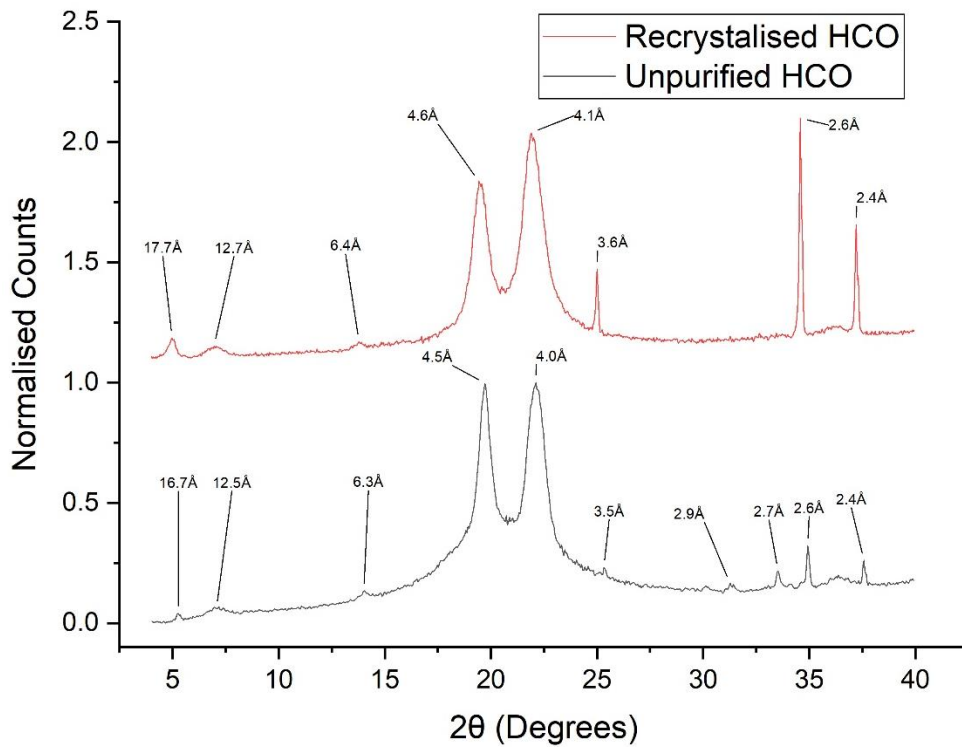
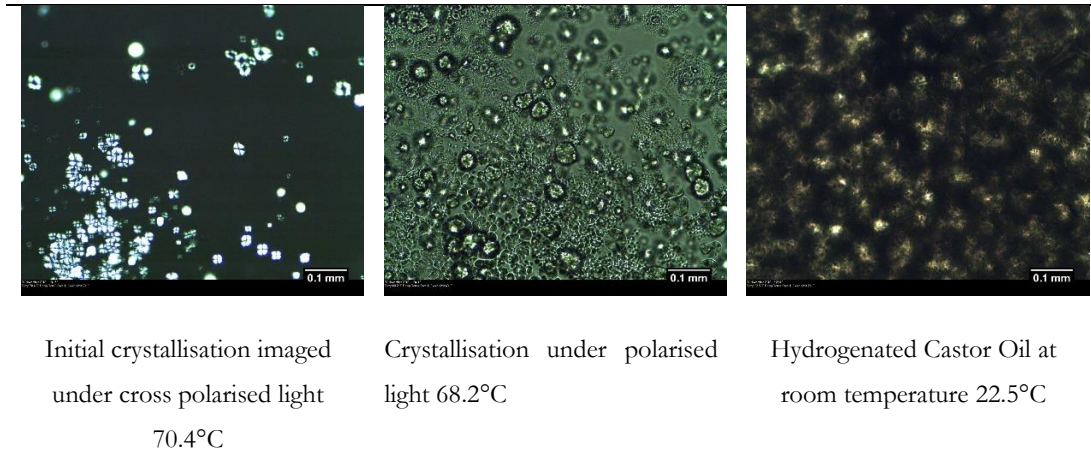


Figure 4-12 Two stacked X-ray Diffraction patterns of Hydrogenated Castor Oil as received from P&G (Black) and twice recrystallised (Red).

HCO has also been imaged upon cooling from the melt using a hot-stage microscope at 1 and 5°C per min. Initial crystallisation was observed in the form of spherulitic crystals and using cross polarised light, multiple Maltese cross patterns can be observed. Maltese

cross patterns are synonymous with a liquid crystalline phase and spherulites.[122, 123] Without cross polarisation, this symmetry cannot be observed. Upon further cooling, more and more spherulitic crystals formed from the melt until at room temperature all the melt had converted to spherulites that area arranged throughout the bulk and surface.

Hydrogenated Castor Oil cooling from the melt at 1°C/min



Hydrogenated Castor Oil cooling from the melt at 5°C/min

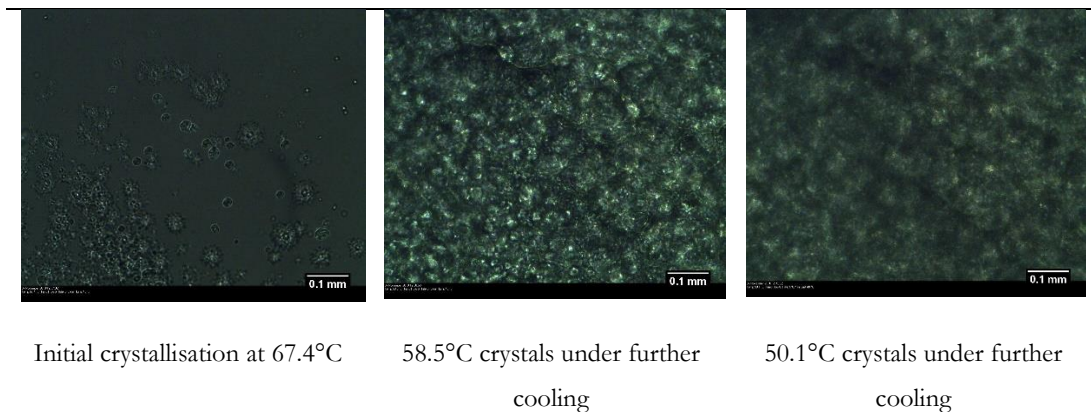


Figure 4-13 A series of optical images taken upon cooling Hydrogenated Castor Oil from the melt.

The spherulitic structures formed when cooling from the melt at 1°C, 5°C and 20°C per minute have been studied at room temperature using Atomic Force Microscopy (AFM). At 1°C per minute, spherulites formed are relatively very large with a diameter of approximately 35µm as displayed in Figure 4-14 a). In the literature, spherulites are described as forming through the radial growth of crystalline ribbons from a single nucleus. Image a) displays the radial nature of the ribbon growth forming doughnut-shaped spherulite. The centre of doughnut-shaped spherulite was measured to be 0.8µm lower than the highest part of the outer ring. The Young's modulus of the surface was measured to be 390 MPa uniformly across the spherulite apart from a small area at the centre where it was measured to be softer, as seen in image b). Image c) displays the

region of the surface that the AFM measurement was carried out and image d) displays the same surface at low magnification. Upon increasing the cooling rate, the number of nucleation sites increases and the size of each spherulite decreases from $35\mu\text{m}$ at 1°C per minute to $7\mu\text{m}$ at 5°C per minute to around $1\mu\text{m}$ at 20°C per minute. This trend can also be observed when looking at the microstructure on the surface using a low magnification microscope.

Cooling Hydrogenated Castor Oil at $1^\circ\text{C}/\text{min}$

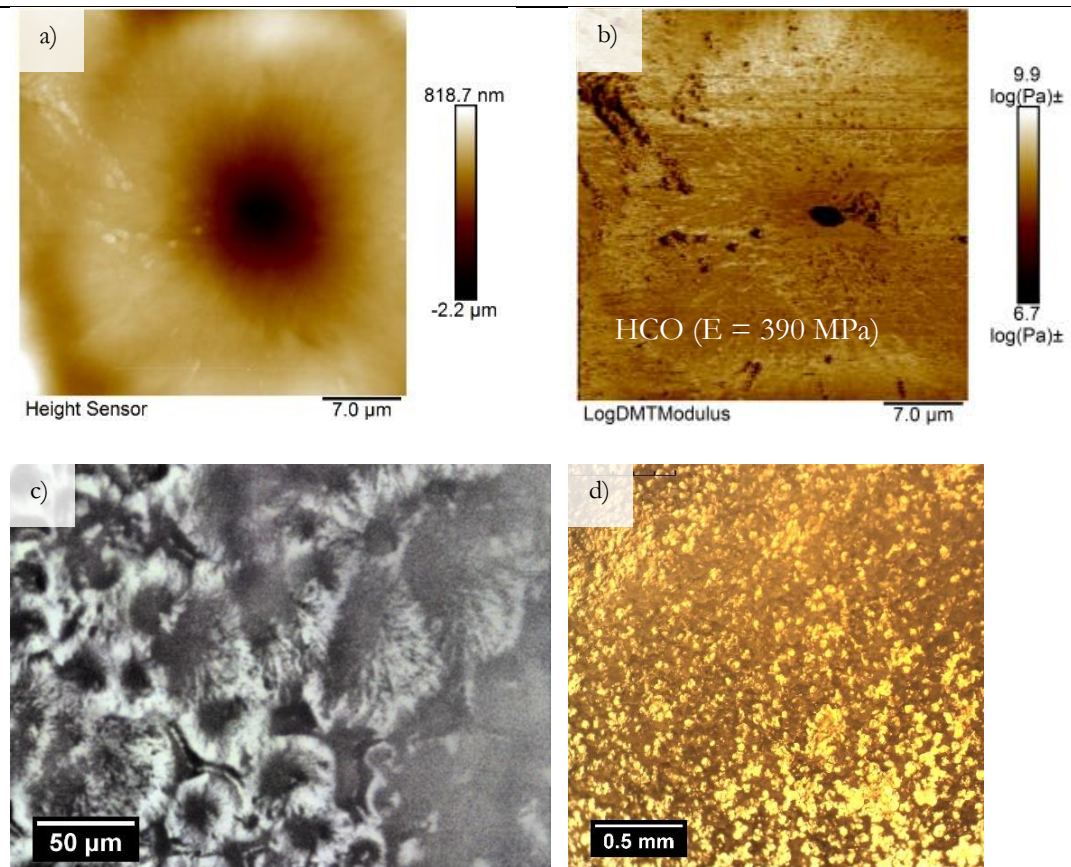


Figure 4-14 Atomic Force Microscope (AFM) and Optical Microscope (OM) images of Hydrogenated Castor Oil cooled from the melt to room temperature at $1^\circ\text{C}/\text{min}$. a) Height map of surface (AFM), b) Youngs Modulus map (AFM), c) High magnification optical image of the area studied (OM) and d) Low magnification optical image of the sample surface (OM).

Cooling Hydrogenated Castor Oil at 5°C/min

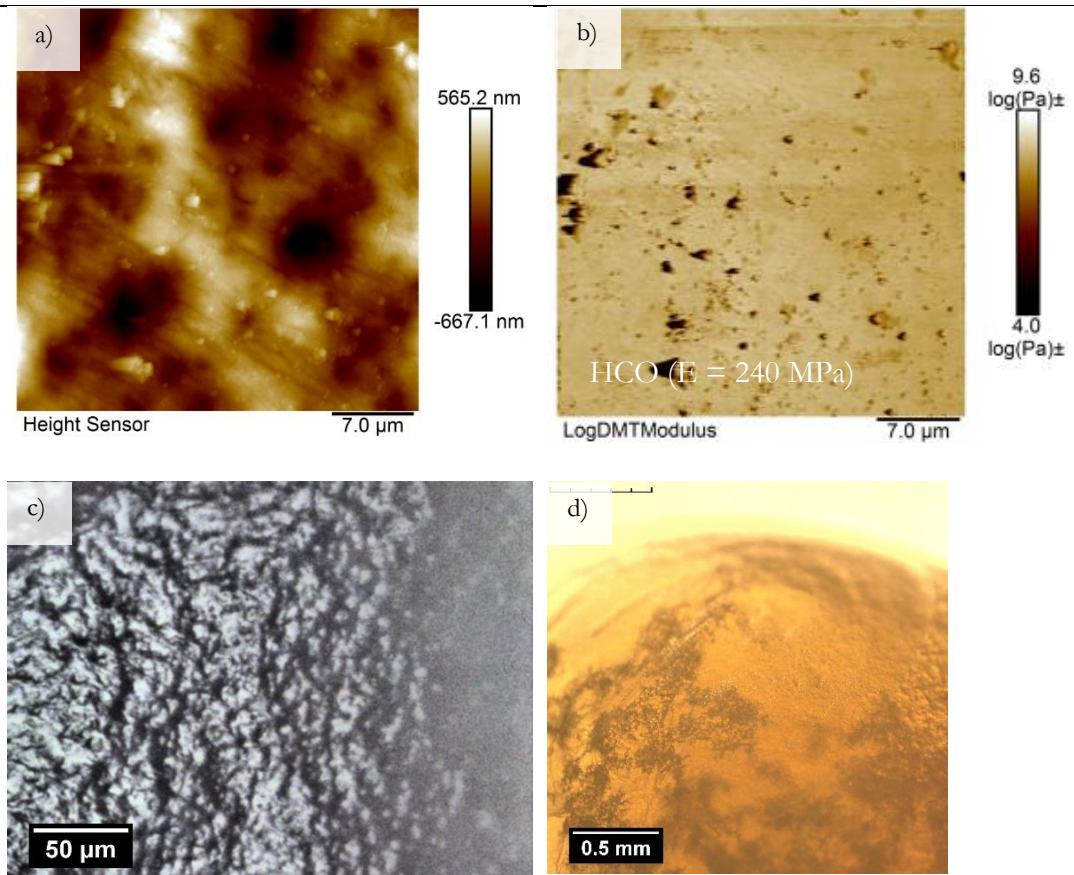


Figure 4-15 Atomic Force Microscope (AFM) and Optical Microscope (OM) images of Hydrogenated Castor Oil cooled from the melt to room temperature at 5°C/min. a) Height map of surface (AFM), b) Youngs Modulus map (AFM), c) High magnification optical image of the area studied (OM) and d) Low magnification optical image of the sample surface (OM).

Cooling Hydrogenated Castor Oil at 20°C/min

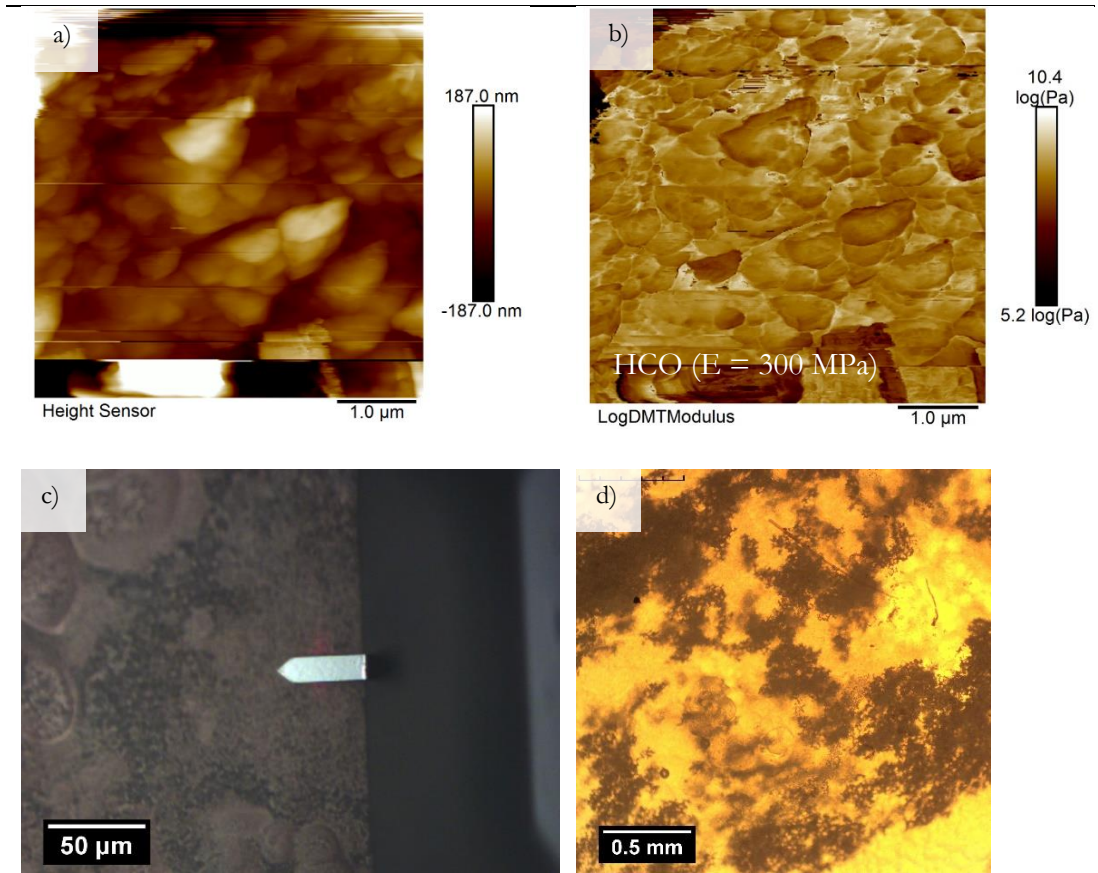


Figure 4-16 Atomic Force Microscope (AFM) and Optical Microscope (OM) images of Hydrogenated Castor Oil cooled from the melt to room temperature at 20°C/min. a) Height map of surface (AFM), b) Youngs Modulus map (AFM), c) High magnification optical image of the area studied (OM) and d) Low magnification optical image of the sample surface (OM).

The rheological properties of molten HCO have been measured at a series of temperatures at and above the point of crystallisation. At 95°C is viscosity is 0.0268 Pa.s when sheared at 10s^{-1} using a 75mm diameter cone and plate. HCO is shear thickening as demonstrated upon a shear rate ramp where the shear stress increased with shear rate. As the temperature is decreased the shear thickening behaviour increases. Below the crystallisation temperature, HCO solidifies, and the rheological behaviour cannot be measured using a rheometer.

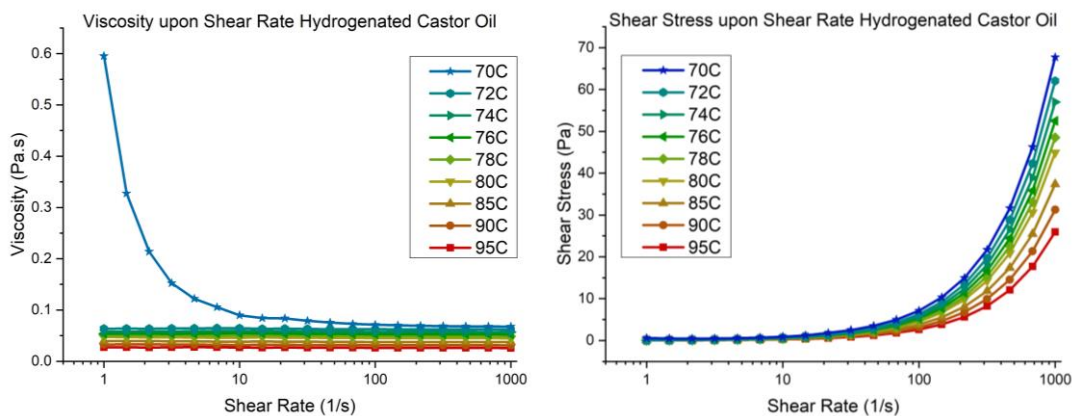


Figure 4-17 Change in Viscosity (right) and Shear Stress (left) upon ramping Shear Rate for Hydrogenated Castor Oil at a series of different temperatures

4.4 Petrolatum

Industrial grade Petrolatum was supplied by P&G for this project. Petrolatum is known to contain a mixture of unbranched n-alkanes with a large range of different chain lengths. The thermal properties of Petrolatum have been measured using DSC upon heating and cooling at 1°C per minute. The onset of crystallisation upon cooling was found to be 59°C, where the largest chain length molecules would crystallise out of the melt first. After the initial onset, a very broad exothermic crystallisation peak is observed between 59°C and 0°C. The broad nature of the peak is due to the wide range of chain lengths which exhibit a large range of crystallisation temperatures. Upon heating, a very broad endothermic melting peak is observed between 0°C and 71°C, with the peak centre at around 33°C. For reference, the melting points of Tetradecane ($C_{14}H_{30}$) is 4°C, Octadecane ($C_{18}H_{38}$) is 30°C and Tetraconane ($C_{40}H_{82}$) is 82°C to give an insight into the molecular chain lengths present.

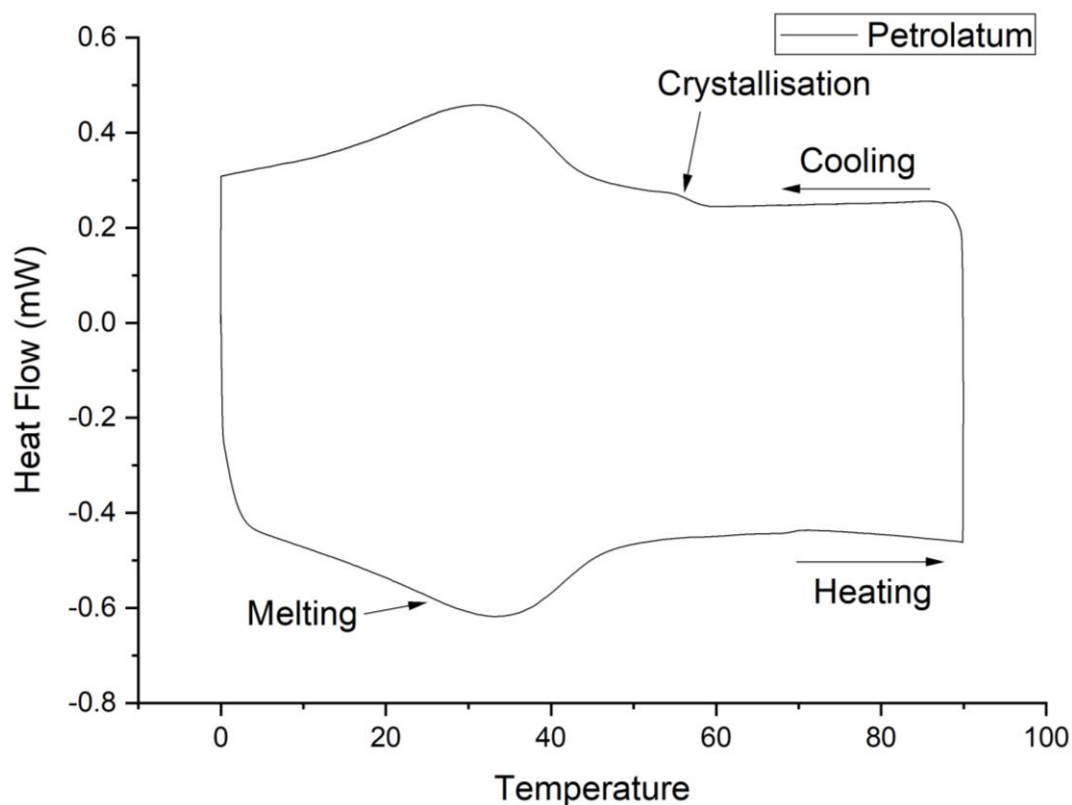


Figure 4-18 Differential Scanning Calorimetry (DSC) graph showing the phase transitions of Petrolatum when heated and cooled at 1°C/min.

Thermal Gravimetric Analysis was also performed on Petrolatum by heating the sample at 5°C per minute from room temperature to 600°C in air. 0.1% mass loss was observed between 25°C and 150°C, 78% between 150°C and 380°C and the last 22% was lost between 380°C and 550°C. The mass loss could be due to either the boiling of each molecular component, combustion or decomposition. To understand the result, a comparison should be drawn between the TGA result with the Gas Chromatography Analysis of Petrolatum and the known boiling point of each component. Octadecane ($C_{18}H_{38}$) is the smallest and molecules with a chain length longer than $C_{47}H_{96}$ being the largest detected using GC. The average chain length is calculated to be 36.43 and is used to calculate the mole fraction of Petrolatum binary mixtures. These components have a boiling point of between 317°C and above 569°C. The initial mass loss was at 150°C, due to vaporisation below the boiling point of the low molecular weight components; however, I am not sure vaporisation completely explains the mass loss of 24% of the components by weight with a chain length of 47 and above. The GC result cannot reveal the maximum chain length present because the column did not separate the longest chain length components. The experiments were conducted in the air making combustion possible, and the thermal cracking of the n-alkanes is known to occur in certain conditions above 800°C, so it might occur to a small degree below 600°C.

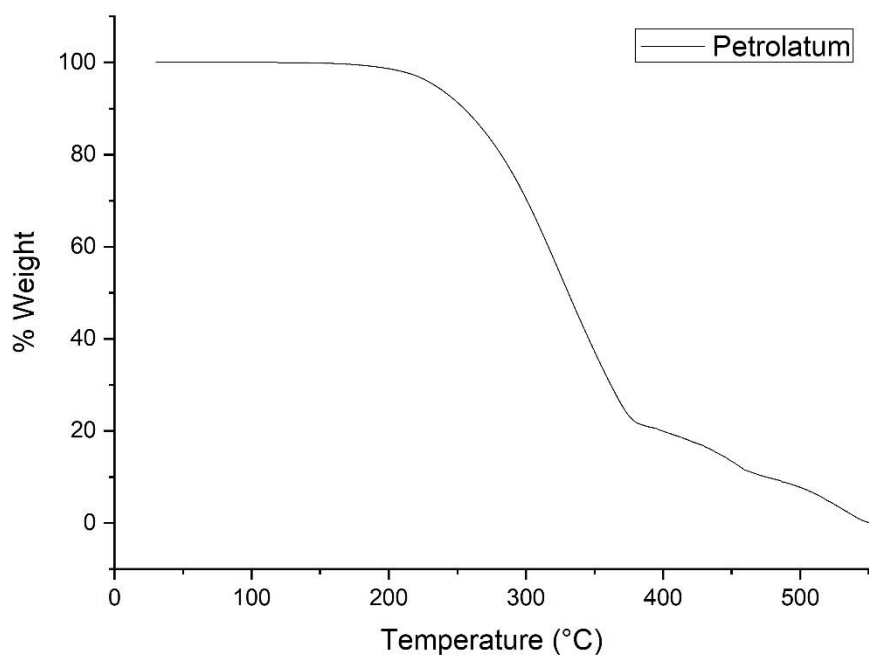


Figure 4-19 TGA graph showing the mass loss of Petrolatum when heated at 5°C/min to 600°C

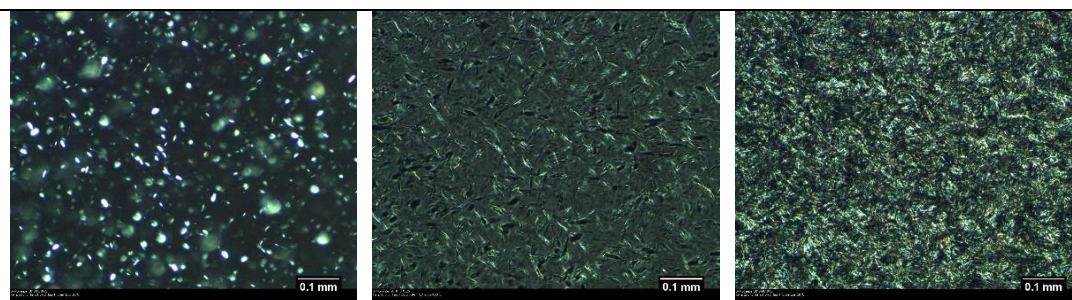
Table 4-2 Gas Chromatography Analysis of Petrolatum

Carbon Number	% Area
18	0.23
19	0.42
20	0.75
21	1.31
22	2.1
23	2.68
24	2.93
25	3.39
26	3.51
27	3.55
28	3.41
29	3.34
30	3.24

31	3.23
32	3.14
33	2.73
34	3.47
35	2.9
36	2.46
37	2.66
38	2.46
39	3.52
40	3.26
41	3.01
42	2.86
43	2.53
44	2.45
45	2.52
46	1.86
47 & Above	24.07
Average Chain Length = 36.43	

The crystal morphology of Petrolatum has been captured upon cooling at 1°C, 5°C and 20°C per minute. The first crystals seen upon cooling at 1°C per minute appear at 58.3°C, are needle-shaped and randomly orientated throughout the melt. Upon further cooling to room temperature, the needle crystals grow up to 0.1mm and are randomly orientated respect to each other, creating a dense gel network. Upon faster cooling, the needle crystals become smaller and harder to distinguish.

Petrolatum cooling from the melt at 1°C/min

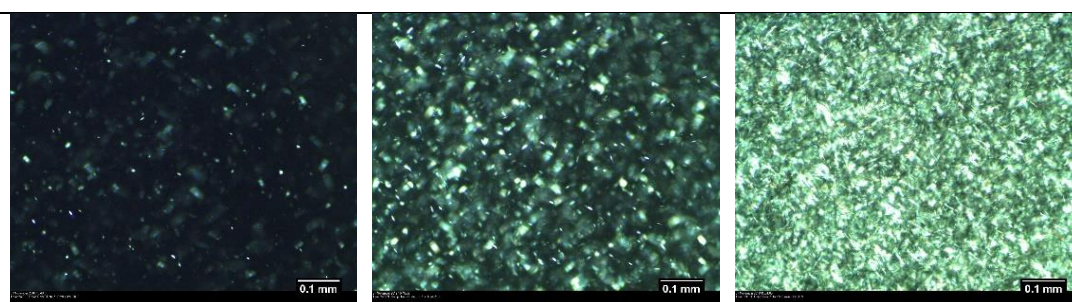


Initial crystallisation at 58.3°C

Crystals at 47.3°C

Crystals at 26.8°C

Petrolatum cooling from the melt at 5°C/min



Initial crystallisation at 54.8°C

Crystals at 52.1°C

Crystals at 39.6°C

Petrolatum cooling from the melt at 20°C/min



Initial crystallisation at 49.8°C

Crystals at 46.9°C

Crystals at 39.8°C

Figure 4-20 A series of optical images of needle-shaped crystals taken upon cooling Petrolatum from the melt taken using a hot stage microscope.

The rheological behaviour of Petrolatum has been studied at a range of temperatures from 20°C to 95°C over a range of shear rates. When completely molten at 95°C Petrolatum has a viscosity of 0.01191 Pa.s at a shear rate of 10s⁻¹. Unlike HCO and 1-Octadecanol, Petrolatum does not solidify when it starts to crystallise, and its rheological properties can be measured at room temperature. Petrolatum is also shear thickening, and the shear stress increases with shear rate. The shear thickening behaviour increases upon decreasing temperature.

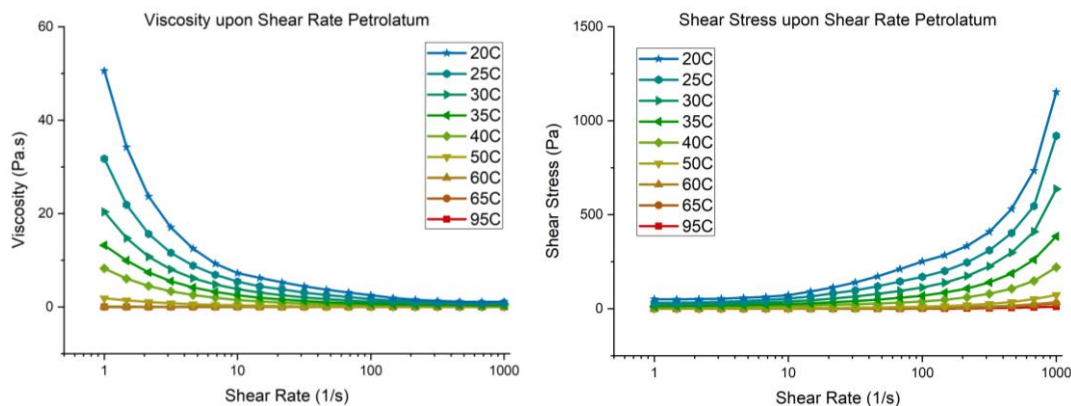


Figure 4-21 Change in Viscosity (left) and Shear Stress (right) upon ramping Shear Rate for Petrolatum at a series of different temperatures

4.5 Conclusion

1-Octadecanol, Petrolatum and HCO all have very different thermal profiles, but all melt and crystallise in the same temperature window between 58°C and 85°C. On paper, alcohol and alkanes have very similar polymorphism, but since petrolatum is such a complex mixture of different molecules and polymorphs that thermal techniques can only detect the net result of all the complex transitions. 1-Octadecanol, on the other hand, has a high purity and its polymorphic transitions between liquid, rotator and gamma phases can be clearly detected. The polymorphism of HCO hasn't been reported in the literature; however, when comparing the XRD pattern to other known triglycerides such tristearin, it's likely that HCO is in the β' phase. TGA showed that no mass was lost below 100°C for Petrolatum, 1-Octadecanol and Hydrogenated Castor confirming the reliability of the DSC results.

The crystal morphology of Petrolatum, HCO and 1-Octadecanol has been studied using a combination of AFM and optical microscopy. Both 1-Octadecanol and Petrolatum initially grow as needles; however, the length and rate of growth were far larger for 1-Octadecanol compared to Petrolatum. This was due to the high purity of 1-Octadecanol and the resulting narrow temperature range that the liquid to solid transition occurs. HCO crystallises as spherulites, similar to other triglycerides in the literature and faster cooling rates decreased crystal size for all materials studied. AFM also measured Young's modulus of 1-Octadecanol and HCO at values of 1.43 and 0.32 GPa. Petrolatum was not measured using AFM, but at room temperature, it is a viscous liquid, due to it containing a mixture of molecules which are solid and liquid. 1-Octadecanol is harder than HCO because it's a pure substance with molecules that stack uniformly throughout the structure held together by a combination of van der Waal's and hydrogen bonding.

HCO, however, is semi-amorphous and contains a mixture of components which don't stack together in a perfectly crystalline rigid structure. In the molten phase HCO, 1-Octadecanol and Petrolatum all behave as shear thickening liquids and has similar rheological behaviour.

*Chapter 5 Crystallisation Kinetics and Morphology of
1-Octadecanol and Hydrogenated Castor Oil in Polar
and Non-Polar Solvents*

This chapter explores the solution chemistry of 1-Octadecanol and Hydrogenated Castor Oil in a range of solvent types. Learnings from this enable further understanding of interactions between binary mixtures of the structuring ingredients and how these materials behave in other complex systems.

5 Crystallisation Kinetics and Morphology of 1-Octadecanol and Hydrogenated Castor Oil in Polar and Non-Polar Solvents

5.1 Introduction

In this chapter, turbidity experiments using the polythermal method has examined the influence of solvent selection on the crystallisation of 1-Octadecanol and Hydrogenated Castor Oil (HCO). Solution chemistry can influence nucleation, crystal growth, molecular assembly, morphology and size distribution of the crystals formed.[124-126] 1-Octadecanol has been studied in Ethanol, Acetone, Dodecane, Undecane and Decamethylcyclopentasiloxane (D5). HCO has been studied in Acetone and Ethanol after being found to be insoluble in Dodecane and D5. Non-polar Dodecane and Undecane solvents were selected to probe chain length parity of Alkanes and used as a simplified model of Petrolatum. Crystallisation in both polar protic and dipolar aprotic solvents has been studied using Ethanol and Acetone, respectively. The final solvent, D5, was used as it's the main solvent used in wax deodorant stick formulations.

The results obtained using the polythermal method have been analysed using the van 't Hoff equation to obtain thermodynamic information about each system and the KBHR approach to gain insight into the nucleation mechanism.[116, 127]

Morphology of HCO and 1-Octadecanol crystals has been examined using a custom growth cell and SEM. 1-Octadecanol was found to form rectangular plates and HCO forms spherulitic clusters.

Learnings from the crystallisation of HCO and 1-Octadecanol in various types of solvents can be applied to understanding binary systems in chapter 6.

5.2 Solubility and Metastable Zone Width Measurements

Measurements were carried out using the Technobis Crystal16,[128] to cycle known concentration mixtures at heating and cooling rates of 0.25, 1, 2 and 3.2°C/min. Each mixture was cycled 4 times, the average crystallisation and dissolution temperature with the respective standard deviation values for each composition has been tabulated in Table 5-1 and Table 5-2 for HCO and Table 5-3-Table 5-7 for 1-Octadecanol solutions.

5.2.1 Measurement of Metastable Zone Width

The plots used to calculate metastable zone width are displayed in Figure 5-1 and show the dependence of crystallisation and dissolution temperature on the heating/cooling rate of the solution. All 1-Octadecanol and HCO solutions, Figure 5-1 a)-g) display a very small variation in crystallisation and dissolution temperature with respect to heating/cooling rate. This suggests that the crystallisation process of these systems is likely to be limited by supersaturation generation rather than nucleation. Also, the gradient of the slope provides information about whether the crystallisation of solution is kinetically or thermodynamically controlled. Small gradients infer little change to the temperature cycle upon varying heating/cooling rate, as a result, show kinetic control, whereas large gradients show thermodynamic control.

The crystallisation and dissolution temperature for all solutes and solvents displayed a low dependence on the heating and cooling rate, as shown by the gradients of the graphs in Figure 5-1. Increasing the concentration of solutions of 1-Octadecanol in Undecane, Ethanol and Acetone was found to slightly increase the dependence of the dissolution temperature measured on cooling and heating rate. Concentration was found not to impact the dependence of crystallisation temperature on all systems studied on cooling and heating rate. The error bars on the graphs were predominately small, however, the turbidity measurement technique was more suitable for 1-Octadecanol than Hydrogenated Castor Oil. When 1-Octadecanol crystallises, it forms a crystalline network throughout the solution ideal for turbidity measurements, in contrast, Hydrogenated Castor Oil would crystallise as small spherulites floating in solution, less ideal for turbidity measurement. When Hydrogenated Castor Oil initially crystallised, the floating spherulite would only be briefly detected as it floats throughout the solution, and on occasions, it wouldn't be detected at all at low concentrations, as shown by the 0.77 and 1.16 g/l Hydrogenated Castor Oil in Ethanol and the 0.76 and 1.01 g/l Hydrogenated Castor Oil in Acetone measurements at a heating and cooling rate of 0.25°C/min. This was either because the spherulite stuck to the side of the container, or it was too small in size to be detected by the turbidity probe. The detection issues of Hydrogenated Castor Oil using the turbidity increased the measurement error on the results relative to 1-Octadecanol.

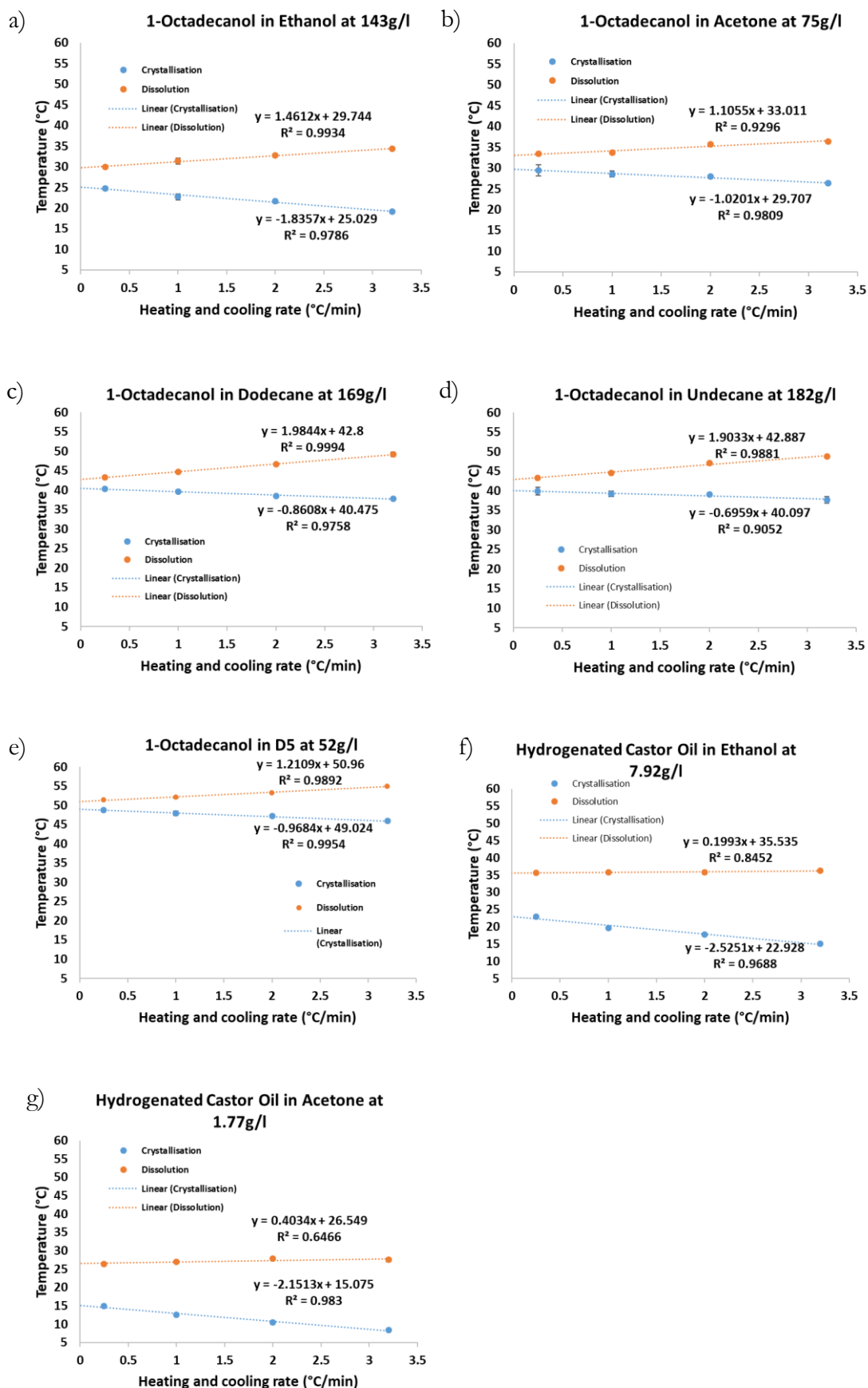


Figure 5-1 Determining the Metastable Zone Width through extrapolation of the crystallisation and dissolution temperatures recorded at 0.25, 1, 2 and 3.2 °C/min, back to zero cooling rate.

Table 5-1 Crystallisation and Dissolution temperatures of Hydrogenated Castor Oil in Ethanol.

q (°C/min)	T _c (°C)	STD (°C)	T _{diss} (°C)	STD (°C)	T _c (°C)	STD (°C)	T _{diss} (°C)	STD (°C)	T _c (°C)	STD (°C)	T _{diss} (°C)	STD (°C)	T _c (°C)	STD (°C)	T _{diss} (°C)	STD (°C)	T _c (°C)	STD (°C)	T _{diss} (°C)	STD (°C)
	Hydrogenated Castor Oil in Ethanol																			
	0.77 g/l				1.16 g/l				1.56 g/l				2.38 g/l				3.93 g/l			
0.25	2.350	0.642	-	-	5.500	0.851	-	-	7.575	0.415	18.150	1.050	11.525	0.238	24.400	0.510	14.750	0.350	28.500	0.000
1	-1.150	0.415	14.850	0.409	0.900	0.212	18.300	0.245	3.575	0.217	20.900	0.797	6.900	0.187	23.550	0.287	11.425	0.650	27.525	0.415
2	-3.900	0.100	16.025	0.715	-1.575	0.130	18.325	0.763	2.250	0.502	21.450	0.206	4.675	0.334	24.000	0.187	8.525	0.303	27.700	0.250
3.2	-5.900	0.784	15.425	1.137	-3.925	0.580	18.350	0.517	-1.900	0.274	21.300	0.510	1.500	0.367	23.950	0.482	7.025	0.580	27.825	0.476
	7.92 g/l				19.99 g/l				23.95 g/l				27.96 g/l							
0.25	22.900	0.100	35.600	0.000	25.275	0.377	37.950	0.757	25.925	0.191	38.725	0.844	28.525	0.719	40.433	0.974				
1	19.650	0.180	35.800	0.943	22.900	0.758	38.325	0.377	24.375	0.148	39.750	0.166	24.975	0.782	41.050	0.206				
2	17.775	0.327	35.775	0.130	23.100	0.255	40.975	0.148	23.525	0.076	42.775	0.826	24.250	0.403	43.575	0.130				
3.2	15.100	0.100	36.250	0.269	19.050	0.269	41.075	0.238	20.775	0.054	41.700	0.224	21.150	0.403	43.375	0.148				

Table 5-2 Crystallisation and Dissolution temperatures of Hydrogenated Castor Oil in Acetone solution.

q (°C/min)	T _c	STD	T _{diss}	STD	T _c	STD	T _{diss}	STD	T _c	STD	T _{diss}	STD	T _c	STD	T _{diss}	STD	T _c	STD	T _{diss}	STD
	(°C)	(°C)	(°C)	(°C)	(°C)	(°C)	(°C)	(°C)	(°C)	(°C)	(°C)	(°C)	(°C)	(°C)	(°C)	(°C)	(°C)	(°C)	(°C)	(°C)
	Hydrogenated Castor Oil in Acetone																			
	0.76 g/l				1.01 g/l				1.27 g/l				1.52 g/l				1.77 g/l			
0.25	-	-	-	-	-	-	-	-	12.167	0.047	24.400	2.491	13.467	0.125	25.967	1.452	14.900	0.535	26.450	1.450
1	5.825	0.864	22.125	0.148	7.975	0.363	24.400	0.308	8.925	0.517	25.925	0.363	11.850	0.364	26.825	0.327	12.600	0.245	26.925	0.558
2	5.325	0.610	22.150	1.172	6.175	0.228	25.050	0.409	8.125	0.746	26.767	0.377	9.550	0.559	27.650	0.206	10.475	0.497	27.900	0.822
3.2	5.500	0.324	22.050	0.180	6.200	0.406	24.350	1.036	5.825	0.746	25.600	0.245	7.150	0.492	27.575	0.148	8.450	0.492	27.525	0.295
	1.97 g/l																			
0.25	16.200	0.216	25.350	0.150																
1	18.600	0.218	28.600	0.187																
2	14.800	0.828	29.167	0.236																
3.2	13.500	0.476	29.133	0.125																

Table 5-3 Crystallisation and Dissolution temperatures of 1-Octadecanol in Ethanol solution.

q (°C/min)	T _c	STD	T _{diss}	STD	T _c	STD	T _{diss}	STD	T _c	STD	T _{diss}	STD	T _c	STD	T _{diss}	STD	T _c	STD	T _{diss}	STD
	(°C)	(°C)	(°C)	(°C)	(°C)	(°C)	(°C)	(°C)	(°C)	(°C)	(°C)	(°C)	(°C)	(°C)	(°C)	(°C)	(°C)	(°C)	(°C)	(°C)
	1-Octadecanol in Ethanol																			
	23.72 g/l				45.09 g/l				92.68 g/l				143.42 g/l				193.47 g/l			
0.25	7.100	1.084	14.400	0.122	16.750	1.069	21.575	0.043	21.350	0.461	27.025	0.148	24.800	0.394	29.950	0.050	27.200	0.418	31.925	0.083
1	7.750	1.087	15.775	0.148	12.675	0.043	22.200	0.490	20.050	0.450	27.850	0.559	22.725	0.746	31.400	0.755	25.400	0.354	33.575	0.832
2	6.025	0.613	18.400	0.100	13.150	0.976	23.100	0.122	18.425	0.148	29.075	0.083	21.650	0.472	32.700	0.000	23.650	0.589	35.175	0.286
3.2	4.300	3.673	18.375	0.622	10.750	0.269	24.525	0.109	17.175	0.618	30.350	0.112	19.100	0.100	34.350	0.112	21.875	0.554	36.475	0.083
	402.37 g/l																			
0.25	30.800	0.374	35.400	0.000																
1	30.275	0.228	39.600	0.100																
2	29.375	1.040	41.075	0.148																
3.2	24.900	1.002	40.825	0.083																

Table 5-4 Crystallisation and Dissolution temperatures of 1-Octadecanol in Acetone solution.

q (°C/min)	T _c	STD	T _{diss}	STD	T _c	STD	T _{diss}	STD	T _c	STD	T _{diss}	STD	T _c	STD	T _{diss}	STD	T _c	STD	T _{diss}	STD
	(°C)	(°C)	(°C)	(°C)	(°C)	(°C)	(°C)	(°C)	(°C)	(°C)	(°C)	(°C)	(°C)	(°C)	(°C)	(°C)	(°C)	(°C)	(°C)	(°C)
	1-Octadecanol in Acetone																			
	3.48 g/l				7.14 g/l				14.76 g/l				36.24 g/l				75.49 g/l			
0.25	3.150	0.415	8.050	1.368	10.100	0.718	14.900	0.122	16.975	0.580	20.650	0.218	25.000	0.495	28.375	0.130	29.450	1.301	33.375	0.148
1	1.575	0.729	9.175	0.192	8.000	0.245	15.125	0.259	16.925	0.249	21.425	0.083	23.350	0.206	29.075	0.482	28.550	0.789	33.725	0.217
2	0.950	1.472	10.125	0.668	7.775	0.904	16.000	0.141	13.900	0.308	22.500	0.212	22.650	0.364	30.500	0.354	27.925	0.179	35.725	0.043
3.2	0.350	0.150	11.200	1.447	6.750	1.408	16.067	0.094	12.350	0.087	22.900	0.071	22.150	0.350	31.100	0.245	26.325	0.327	36.350	0.087
	151.39 g/l				318.84 g/l															
0.25	34.625	0.130	37.075	0.083	37.450	0.296	41.625	0.083												
1	32.550	0.229	38.400	0.071	36.325	0.449	43.500	0.071												
2	32.350	0.250	40.300	0.141	37.225	0.396	46.800	0.187												
3.2	30.675	0.286	43.150	0.087	35.500	0.464	49.600	0.255												

Table 5-5 Crystallisation and Dissolution temperatures of 1-Octadecanol in Dodecane solution.

q (°C/min)	T _c (°C)	STD (°C)	T _{diss} (°C)	STD (°C)	T _c (°C)	STD (°C)	T _{diss} (°C)	STD (°C)	T _c (°C)	STD (°C)	T _{diss} (°C)	STD (°C)	T _c (°C)	STD (°C)	T _{diss} (°C)	STD (°C)	T _c (°C)	STD (°C)	T _{diss} (°C)	STD (°C)
	1-Octadecanol in Dodecane																			
	5.98 g/l				7.97 g/l				11.85 g/l				24.28 g/l				49.92 g/l			
0.25	22.050	0.150	23.550	0.150	23.350	0.743	27.225	0.334	27.775	0.955	29.900	0.909	30.350	0.450	33.700	0.100	35.825	0.680	39.400	0.696
1	20.950	0.650	26.600	0.900	22.575	0.626	28.125	0.687	25.900	0.200	30.850	0.180	30.450	0.550	34.950	0.350	35.075	0.531	39.925	0.760
2	19.800	0.200	27.600	0.400	22.025	0.286	29.175	0.249	24.800	0.430	31.850	0.497	31.500	0.100	38.650	0.150	33.125	0.482	42.325	1.377
3.2	20.450	0.150	26.950	0.650	20.075	0.576	30.300	1.089	24.225	0.801	32.375	0.377	28.950	0.350	39.150	0.050	33.350	0.112	42.025	0.507
	96.36 g/l				169.20 g/l				210.15 g/l				297.57 g/l							
0.25	38.050	0.250	41.700	0.000	40.300	0.300	43.350	0.050	40.350	0.350	44.150	0.050	42.550	0.150	45.900	0.000				
1	38.150	0.350	42.900	0.200	39.700	0.000	44.750	0.150	40.100	0.400	45.250	0.050	41.250	0.250	48.450	0.250				
2	36.600	0.200	43.850	0.350	38.500	0.100	46.700	0.000	39.850	0.750	47.450	0.050	41.150	0.250	50.700	0.600				
3.2	35.300	0.000	45.750	0.150	37.850	0.150	49.200	0.500	38.400	0.400	48.350	0.150	39.300	0.000	53.150	0.350				

Table 5-6 Crystallisation and Dissolution temperatures of 1-Octadecanol in Undecane solution.

q (°C/min)	T _c (°C)	STD (°C)	T _{diss} (°C)	STD (°C)	T _c (°C)	STD (°C)	T _{diss} (°C)	STD (°C)	T _c (°C)	STD (°C)	T _{diss} (°C)	STD (°C)	T _c (°C)	STD (°C)	T _{diss} (°C)	STD (°C)	T _c (°C)	STD (°C)	T _{diss} (°C)	STD (°C)
	1-Octadecanol in Undecane																			
	6.45 g/l				12.92 g/l				26.13 g/l				39.73 g/l				51.36 g/l			
0.25	22.967	0.094	24.500	0.163	28.300	0.200	30.100	0.100	32.500	0.400	35.050	0.250	33.550	0.497	37.925	0.567	35.133	0.519	38.000	0.497
1	21.500	0.158	24.600	0.173	26.975	0.179	30.600	0.324	31.425	0.576	37.075	0.554	32.325	0.521	37.600	0.587	34.400	0.235	38.750	0.456
2	20.675	0.390	27.050	0.391	26.275	0.083	31.900	0.163	30.925	0.295	37.950	1.650	32.200	0.570	38.975	0.370	33.775	0.268	40.775	1.134
3.2	19.400	0.274	27.150	0.150	24.925	0.179	32.700	0.100	30.175	0.205	38.725	1.635	30.825	0.238	40.525	0.593	32.675	0.249	41.150	0.087
	103.61 g/l				182.82 g/l				225.86 g/l				319.85g/l							
0.25	38.375	0.676	42.025	0.083	39.950	1.016	43.350	0.218	40.950	0.642	44.100	0.071	42.500	0.354	45.875	0.179				
1	36.675	0.327	42.175	0.164	39.150	0.709	44.600	0.122	40.725	0.109	45.975	0.164	42.150	0.250	47.725	0.286				
2	37.075	0.618	43.750	0.502	39.100	0.245	47.075	0.130	39.800	0.224	47.725	0.148	41.625	0.363	51.150	0.206				
3.2	35.175	0.867	46.100	0.464	37.700	0.834	48.800	0.300	39.150	0.087	48.925	0.249	40.000	0.579	53.475	0.205				

Table 5-7 Crystallisation and Dissolution temperatures of 1-Octadecanol in D5 solution.

q (°C/min)	T _c (°C)	STD (°C)	T _{diss} (°C)	STD (°C)	T _c (°C)	STD (°C)	T _{diss} (°C)	STD (°C)	T _c (°C)	STD (°C)	T _{diss} (°C)	STD (°C)	T _c (°C)	STD (°C)	T _{diss} (°C)	STD (°C)	T _c (°C)	STD (°C)	T _{diss} (°C)	STD (°C)	
	1-Octadecanol in D5																				
	7.10 g/l				14.38 g/l				21.66 g/l				28.98 g/l				36.72 g/l				
0.25	33.275	0.295	36.000	0.122	39.825	0.255	42.475	0.311	42.475	0.311	45.300	0.612	45.500	0.100	47.600	0.548	47.825	0.179	50.975	0.217	
1	33.325	0.109	39.100	0.374	40.700	0.000	43.475	0.130	43.475	0.130	48.425	1.006	45.900	0.255	50.675	0.249	46.725	0.277	51.200	0.158	
2	32.600	0.141	41.050	0.477	40.200	0.212	43.325	0.083	43.325	0.083	50.050	0.602	45.725	0.192	52.300	0.412	46.200	0.122	52.225	0.179	
3.2	30.900	0.187	40.575	0.847	38.700	0.255	41.150	0.180	41.150	0.180	50.625	0.760	44.325	0.179	53.575	0.356	44.425	0.205	54.075	0.521	
	44.59 g/l				52.62 g/l				60.80 g/l												
0.25	47.900	0.187	50.900	0.100	48.825	0.192	51.425	0.043	49.400	0.059	52.350	0.250									
1	46.850	0.384	51.600	0.316	47.950	0.568	52.025	0.043	48.875	0.037	53.800	0.406									
2	46.225	0.249	53.025	0.130	47.175	0.192	53.250	0.087	47.475	0.115	55.000	0.141									
3.2	44.700	0.430	54.200	0.122	45.900	0.406	54.950	0.087	47.025	0.054	55.600	0.212									

Table 5-8 Crystallisation temperature at the kinetic limit (T_c), Equilibrium temperature (T_e) and Meta Stable Zone Width (ΔT) derived by extrapolation back to zero cooling using cooling rate vs crystallisation/dissolution temperature graph for Hydrogenated Castor Oil in Ethanol and Acetone solutions.

Conc. g/l	T_c (°C)	STD (°C)	T_e (°C)	STD (°C)	ΔT (°C)	STD (°C)	Conc (g/l)	T_c (°C)	STD (°C)	T_e (°C)	STD (°C)	ΔT (°C)	STD (°C)
Hydrogenated Castor Oil in Ethanol							Hydrogenated Castor Oil in Acetone						
0.769	2.250	0.837	14.945	0.947	12.695	1.784	0.760	5.835	1.040	22.182	0.159	16.347	1.199
1.163	5.122	0.832	18.278	0.333	13.156	1.166	1.013	8.394	0.619	24.685	0.877	16.291	1.496
1.555	7.696	0.400	18.938	1.206	11.243	1.607	1.266	10.572	0.378	25.052	1.924	14.480	2.302
2.380	11.327	0.310	24.090	0.594	12.763	0.904	1.519	13.976	0.317	26.123	1.177	12.146	1.494
3.926	14.589	0.658	28.146	0.286	13.557	0.945	1.768	15.075	0.558	26.549	1.244	11.474	1.802
7.921	22.928	0.138	35.535	0.483	12.607	0.622	1.965	17.847	0.277	26.255	0.194	8.408	0.472
19.990	25.631	0.647	37.639	0.745	12.009	1.393							
23.952	26.333	0.206	38.874	0.624	12.541	0.829							
27.963	28.406	0.915	40.296	0.798	11.890	1.713							

Table 5-9 Crystallisation temperature at the kinetic limit (T_c), Equilibrium temperature (T_e) and Meta Stable Zone Width (ΔT) derived by extrapolation back to zero cooling using cooling rate vs crystallisation/dissolution temperature graph for 1-Octadecanol in Ethanol, Acetone and Dodecane solutions.

Conc. g/l	T_c (°C)	STD (°C)	T_e (°C)	STD (°C)	ΔT (°C)	STD (°C)	Conc (g/l)	T_c (°C)	STD (°C)	T_e (°C)	STD (°C)	ΔT (°C)	STD (°C)	Conc (g/l)	T_c (°C)	STD (°C)	T_e (°C)	STD (°C)	ΔT (°C)	STD (°C)
1-Octadecanol in Ethanol							1-Octadecanol in Acetone							1-Octadecanol in Dodecane						
23.717	8.024	2.173	14.429	0.309	6.405	2.482	3.482	2.932	0.480	7.955	1.354	5.023	1.834	5.981	21.713	0.415	24.498	0.639	2.785	1.054
45.090	16.102	0.720	21.241	0.266	5.139	0.986	7.143	9.779	0.884	14.819	0.211	5.040	1.095	7.965	23.729	0.923	27.033	0.810	3.304	1.733
92.681	21.541	0.675	26.744	0.376	5.202	1.051	14.764	17.835	0.503	20.614	0.183	2.779	0.686	11.850	27.530	0.922	29.894	0.758	2.364	1.680
143.417	25.029	0.581	29.744	0.406	4.715	0.987	36.237	24.743	0.489	28.210	0.331	3.467	0.821	11.459	27.035	0.488	29.312	0.037	2.276	0.525
193.471	27.402	0.530	31.830	0.421	4.428	0.951	75.493	29.707	1.332	33.011	0.219	3.304	1.551	24.283	30.917	0.646	33.387	0.223	2.470	0.869
402.366	31.994	0.510	36.515	0.050	4.520	0.559	151.389	34.485	0.241	36.415	0.096	1.930	0.337	49.920	35.829	0.686	39.281	0.798	3.452	1.484
							318.838	37.445	0.487	40.935	0.136	3.489	0.623	96.429	38.666	0.308	41.403	0.088	2.737	0.396
														169.197	40.475	0.238	42.800	0.239	2.325	0.477
														210.153	40.707	0.442	43.908	0.092	3.201	0.534

Table 5-10 Crystallisation temperature at the kinetic limit (T_c), Equilibrium temperature (T_e) and Meta Stable Zone Width (ΔT) derived by extrapolation back to zero cooling using cooling rate vs crystallisation/dissolution temperature graph for 1-Octadecanol in Undecane and D5 solutions.

Conc. g/l	T_c (°C)	STD (°C)	T_e (°C)	STD (°C)	ΔT (°C)	STD (°C)	Conc (g/l)	T_c (°C)	STD (°C)	T_e (°C)	STD (°C)	ΔT (°C)	STD (°C)
1-Octadecanol in Undecane							1-Octadecanol in D5						
6.450	22.995	0.164	24.136	0.185	1.142	0.349	7.101	33.861	0.289	36.773	0.185	-2.912	0.474
12.919	28.372	0.259	29.839	0.223	1.466	0.482	14.376	40.572	0.221	44.407	0.223	-3.835	0.445
26.125	32.455	0.559	35.319	0.667	2.865	1.226	21.660	43.391	0.315	45.843	0.667	-2.452	0.982
39.729	33.573	0.578	37.199	0.777	3.626	1.355	28.984	46.028	0.210	47.938	0.437	-1.910	0.647
53.361	35.305	0.503	37.821	0.437	2.516	0.940	36.719	48.055	0.291	50.386	0.197	-2.331	0.487
103.607	38.319	0.780	41.195	0.197	2.876	0.976	44.593	48.092	0.391	50.578	0.273	-2.486	0.664
182.822	40.097	1.226	42.887	0.273	2.790	1.500	52.615	49.024	0.478	50.960	0.173	-1.936	0.650
225.860	41.197	0.494	44.077	0.173	2.880	0.667	60.801	49.574	0.058	52.445	0.284	-2.871	0.343
319.855	42.915	0.473	44.794	0.703	1.878	1.176							

Crystallisation temperature at the kinetic limit (T_c) and Equilibrium temperature (T_e) values have been derived by extrapolation back to zero cooling using cooling rate vs crystallisation/dissolution temperature graph displayed in Figure 5-1. This crystallisation at the kinetic limit and equilibrium temperature, along with metastable zone width were tabulated for HCO solutions in Table 5-8 and 1-Octadecanol solutions in Table 5-9 and Table 5-10.

The metastable zone width at zero cooling rate, measured upon cycling 1-Octadecanol and HCO in a range of different solvents at different levels of concentration are displayed in Figure 5-2 and Figure 5-3. The largest MSZW values were measured for 1-Octadecanol in D5 solvent (4.78-10.73°C), and 1-Octadecanol in Ethanol (4.43-6.40°C) had the second-largest MSZW. Acetone (1.93-5.04°C), Undecane (1.14-3.63) and Dodecane (2.32-3.45°C) all displayed similar smaller magnitude MSZW's of between 1-5°C. HCO displayed larger MSZW's than 1-Octadecanol with Ethanol (11.24-13.16°C) and Acetone (8.41-16.35°C). Both the nature of the solute and solvent impacts the MSZW recorded.

For each system, the MSZW has a dependence with respect to concentration, heating and cooling rates. For all the systems studied, higher concentrations crystallise and dissolve at increased temperatures. In certain systems, increasing solvent concentration decreases the metastable zone width measured at zero cooling, such as D5 in 1-Octadecanol, Ethanol in 1-Octadecanol and HCO in Acetone as shown by Figure 5-2. A similar dependence has been seen previously in the literature when studying the behaviour of PABA in Ethanol, where the change in values of crystallisation temperature and dissolution temperature upon varying cooling rate decreased with lowering concentration.[113] This resulted in the gradients of the cooling rate vs crystallisation and dissolution temperature plots decreasing, as the concentration decreased, causing the extrapolated values MSZW at zero cooling to increase with concentration. In other systems, however, there is not such a clear trend, and MSZW maintains roughly constant with respect to increasing concentration.

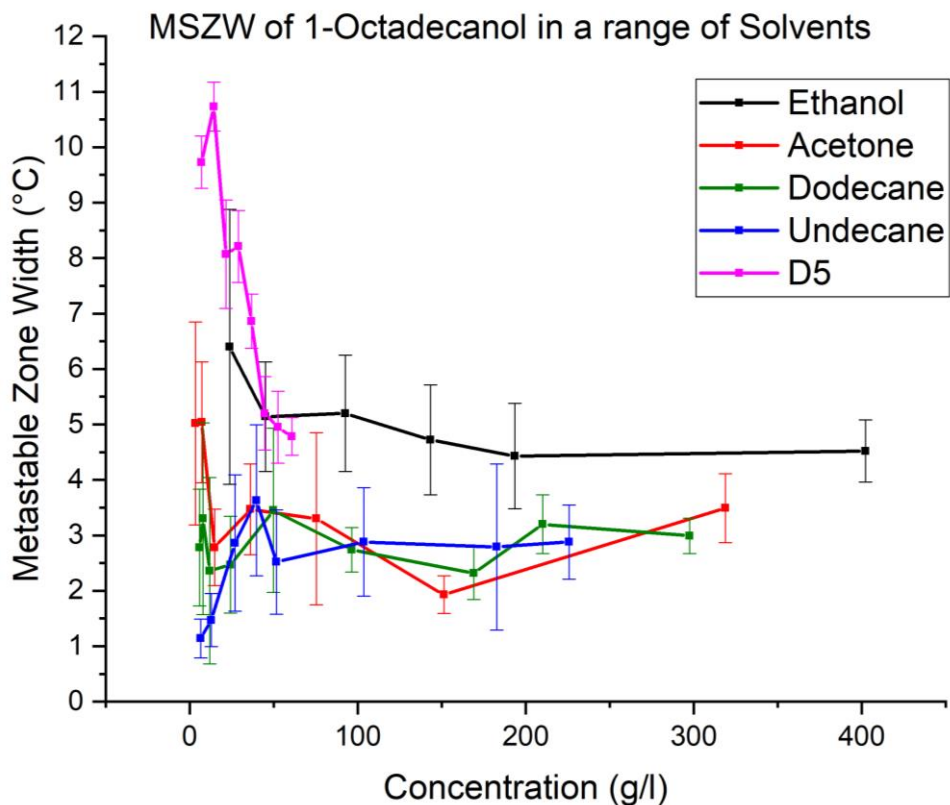


Figure 5-2 Metastable Zone Width of 1-Octadecanol in a range of solvents.

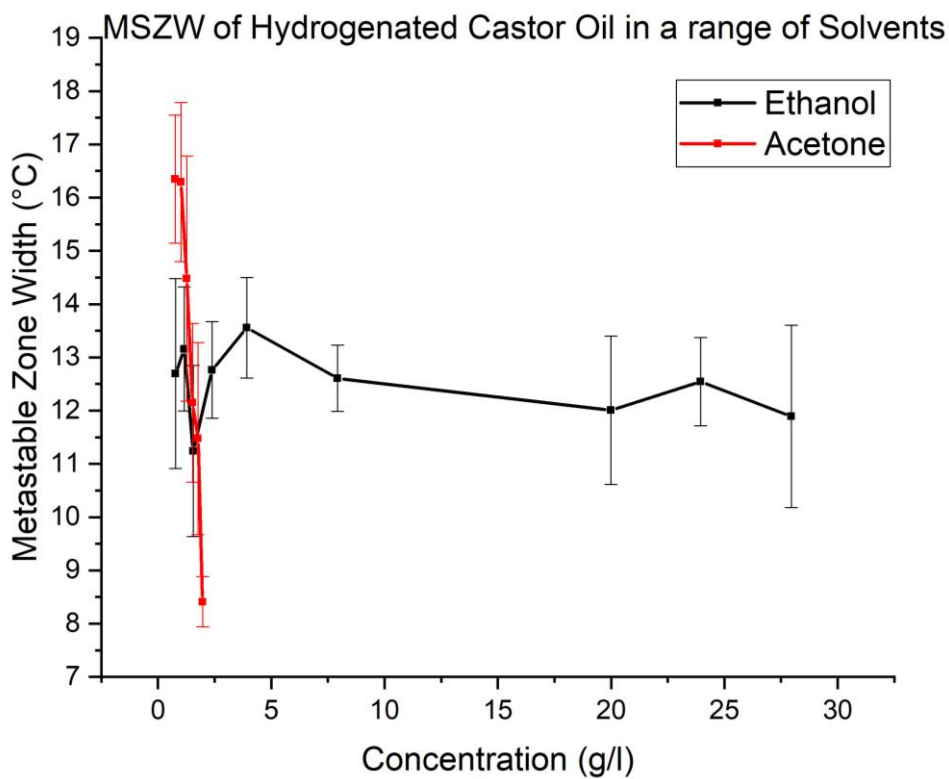


Figure 5-3 Metastable Zone Width of Hydrogenated Castor Oil in a range of solvents.

5.2.2 Relating Nature of Solute and Solvent to Solubility

The mainly non-polar 1-Octadecanol molecule features a single polar OH functional group situated at the end of the non-polar 18 Carbon alkyl chain. 1-Octadecanol is held together by hydrogen bonding, strong dipole-dipole and van der Waal's interactions in the solid phase and an energy barrier will need to be overcome to separate the molecules, resulting in a positive enthalpy change ($\Delta H_1 > 0$). For 1-Octadecanol to dissolve in the solvent, it needs to dissociate and position between solvent molecules. This requires the separation between the solvent molecules which are held together by either hydrogen bonding, dipole-dipole interactions or van der Waal's to increase, requiring a positive enthalpy change ($\Delta H_2 > 0$). Since the polar headgroup and non-polar Carbon chain of 1-Octadecanol can interact favourably with both polar and non-polar solvent molecules, forming a solution results in a negative enthalpy change ($\Delta H_3 < 0$). The overall enthalpy of dissolution depends on the relative magnitude between the separation of solute/solvent molecules and enthalpy of solution formation ($\Delta H_1 + \Delta H_2 + \Delta H_3$). The overall enthalpy and entropy magnitude dictate whether the Gibbs free energy is positive or negative ($\Delta G = \Delta H - T\Delta S$). A negative Gibbs free energy infers spontaneous dissolution.

Despite 1-Octadecanol being a mainly non-polar molecule, 1-Octadecanol was most soluble in Ethanol and Acetone due to hydrogen bonding being a very strong interaction. Non-polar solvents such as Dodecane, Undecane and D5 are non-polar and less soluble due to only weak van der Waal's forces being present between solute and solvent molecules. Chain length parity between Dodecane and Undecane solvents clearly makes little difference to the solubility of 1-Octadecanol. The solubility curves of 1-Octadecanol in Ethanol, Acetone, Dodecane, Undecane and D5 is displayed in Figure 5-4.

HCO consists of a complex mixture of mono, di and triglycerides with the main component being Trihydroxystearin.^[38] Trihydroxystearin is a fully saturated triglyceride with each leg having a Carbon chain length of 18 and hydroxy group situated on the 12th Carbon. HCO molecules in the solute will be held together by a predominately van der Waal's with small amounts of hydrogen bonding and dipole-dipole interactions and will have a lower enthalpy of separation than 1-Octadecanol. Trihydroxystearin consists of three non-polar Carbon chains attached to the polar glycerol group. The hydroxy group on the 12th Carbon can perform limited hydrogen bonding due to steric hindrance,

explaining the solubility in Ethanol and Acetone. The complex mixture of polar and non-polar features of HCO make it insoluble in non-polar solvents and poorly soluble in polar solvents.

Solubility data in Figure 5-5, show that HCO was only slightly soluble in polar solvents, Ethanol and Acetone, but completely insoluble in the non-polar solvents tested, Dodecane and D5.

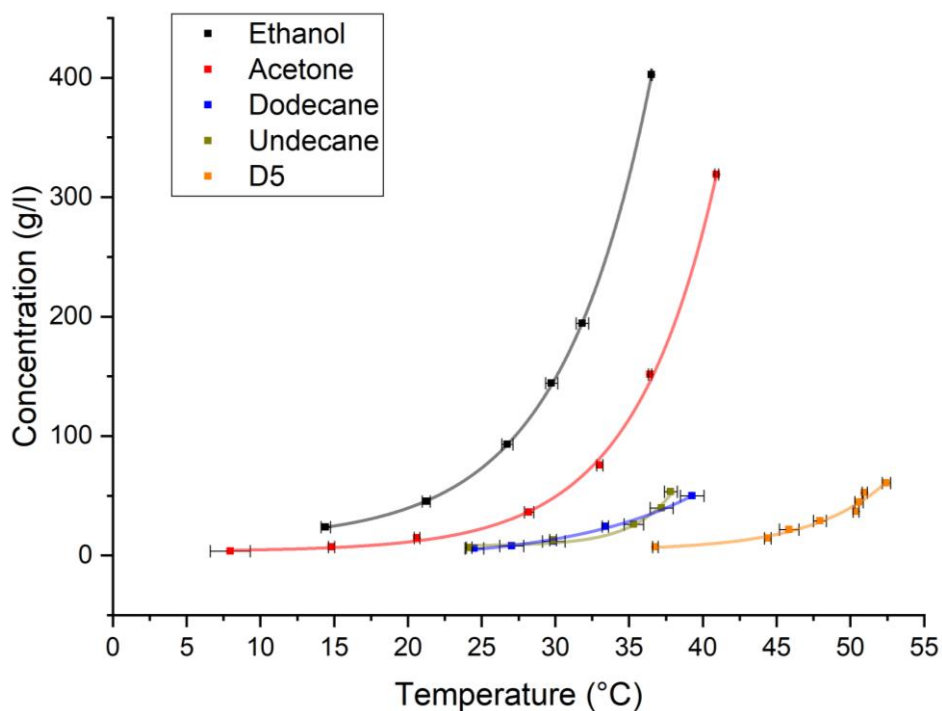


Figure 5-4 Solubility Curves of 1-Octadecanol in Ethanol, Dodecane, Undecane, D5 and Acetone solvents

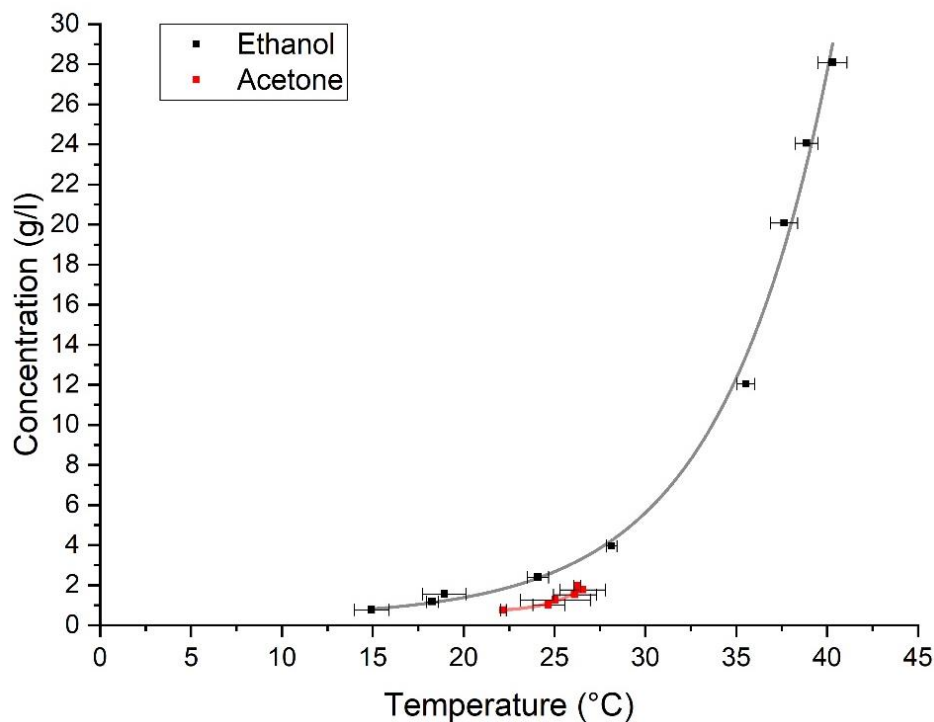


Figure 5-5 Solubility Curves of Hydrogenated Castor Oil in Ethanol and Acetone solvents

5.3 Thermodynamic Analysis using the van 't Hoff Equation

van 't Hoff analysis was performed on the polythermal data of HCO and 1-Octadecanol in polar and non-polar solvents.

The van 't Hoff plots of 1-Octadecanol in Dodecane and Undecane are shown in Figure 5-6, 1-Octadecanol in Ethanol, Acetone, and D5 are shown in Figure 5-7, 1-Octadecanol in all solvents studied in Figure 5-8. The van 't Hoff plot for HCO in Acetone and Ethanol was displayed in Figure 5-9.

The van 't Hoff analysis was used as a tool to assess the ideality of each solvent, compared to the ideal, no solvent condition, and reveals information about the interactions between solute and solvent. In an ideal system, all the interactions are uniform, in a more than ideal system, solute-solvent interactions are strongest and in a less than ideal system solute-solute interactions are the strongest.[129] Less than ideal behaviour was observed for all the solvents and solutes tested. For 1-Octadecanol, Ethanol was the closest to ideality, then Acetone, Undecane, Dodecane and D5 was the least ideal solvent. The order of solvent ideality matches the order of solubility where the closest to ideality having the highest solubility. HCO solvent mixtures were far less ideal the 1-Octadecanol solutions. Ethanol was shown to be closer to ideality than Acetone for HCO solutions.

Less than ideal behaviour shows that solute-solvent interactions are strongest for both HCO and 1-Octadecanol in solvent systems.

In van 't Hoff plots the ideal solubility line and the experimentally measured lines should not cross and should be parallel, however, this was not the case of the experimental data presented in Figure 5-6 - Figure 5-9. All the experimental data moved closer to ideality with increasing temperature and the most extreme example of this was observed in the data of Hydrogenated Castor Oil in Acetone. Turbidity measurements of Hydrogenated Castor Oil in Acetone were only obtained over a small temperature range, due to a combination of very poor solubility of Hydrogenated Castor Oil in Acetone and the low boiling point of Acetone. The small temperature range that the data was recorded increased the error on the gradient of the line when the line of best fit was extrapolated over a larger temperature range. This trend was also observed for 1-Octadecanol in both polar and non-polar solvents, with this behaviour being more extreme for 1-Octadecanol in the non-polar Dodecane, Undecane and the D5 solvents relative to when in polar Ethanol and Acetone solvents.

The values of entropy (ΔS_{diss}) and enthalpy of dissolution (ΔH_{diss}) were calculated from the gradient and intercept of the y-axis of the van 't Hoff plots. Enthalpy of solvation (ΔH_{solv}) was calculated using the enthalpy of sublimation of 1-Octadecanol. These values, along with the activity coefficient of each solution and the dielectric constant of each solvent, are tabulated in Table 5-11.

Concentrations of up to 300 g/l were measured for 1-Octadecanol in Dodecane and Undecane, however, above 50 g/l the solubility curve and van 't Hoff plots appeared to have a kink. This was most likely to be due to measurement errors when transferring saturated solution from the stock solution to the crystal16 vials and as a result data points above 50 g/l have been omitted from the van 't Hoff plot and solubility curve. Equally, the kink could also be due to a phase change within the system at higher concentrations resulting in a change of the thermodynamic parameters measured.

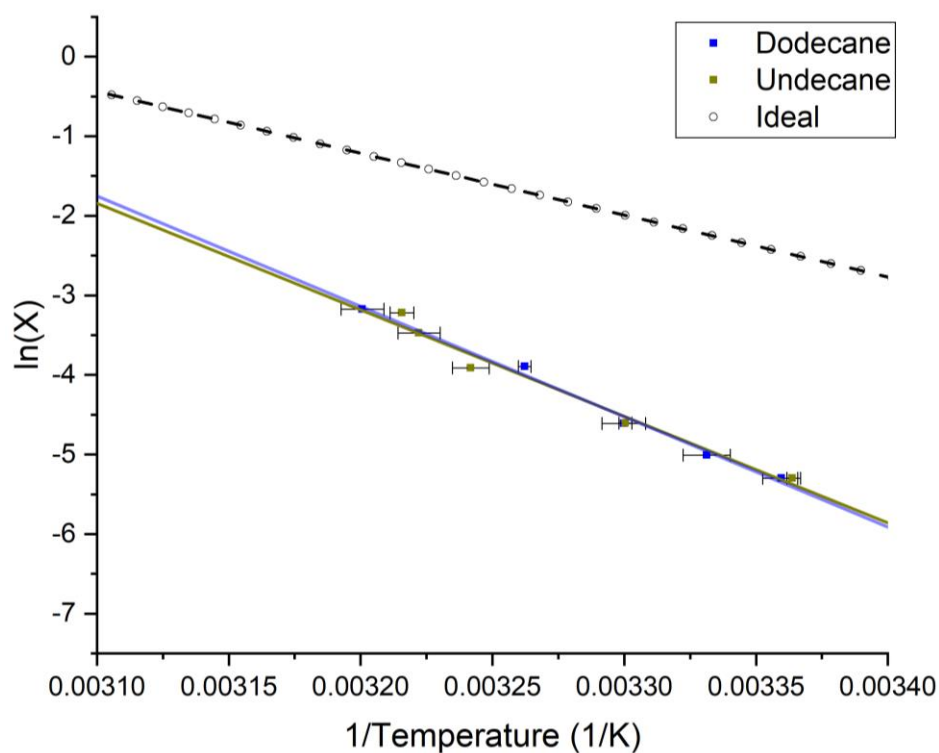


Figure 5-6 van 't Hoff plot displaying the ideal solubility of 1-Octadecanol and 1-Octadecanol in Dodecane and Undecane solvents.

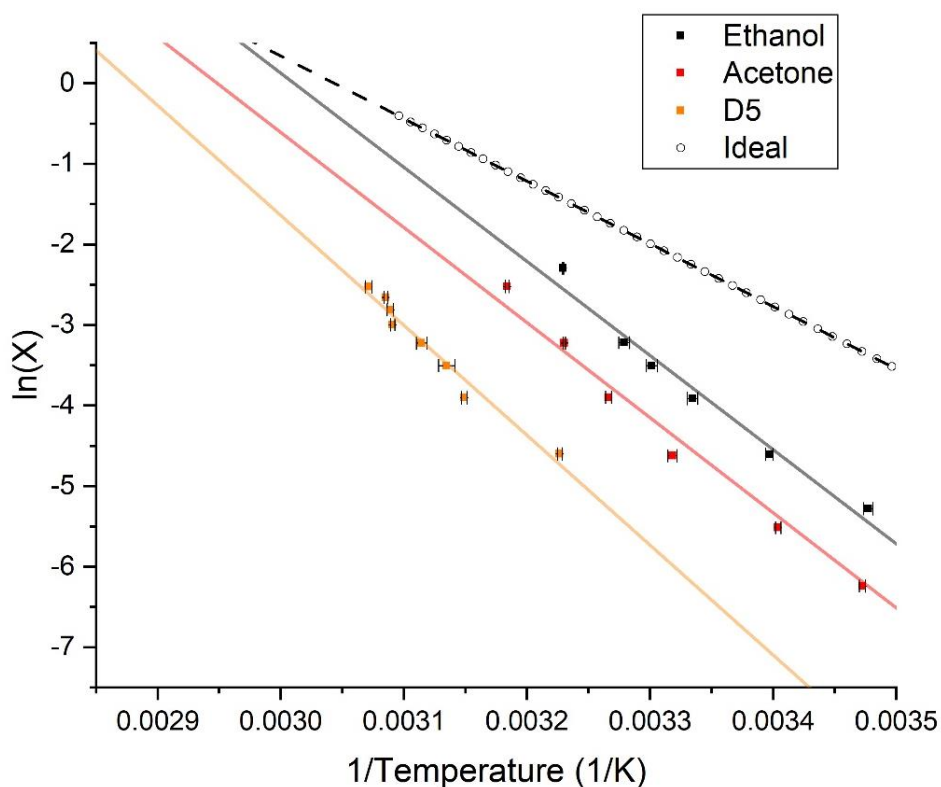


Figure 5-7 van 't Hoff plot displaying the ideal solubility of 1-Octadecanol and 1-Octadecanol in Ethanol, Acetone and D5 solvents.

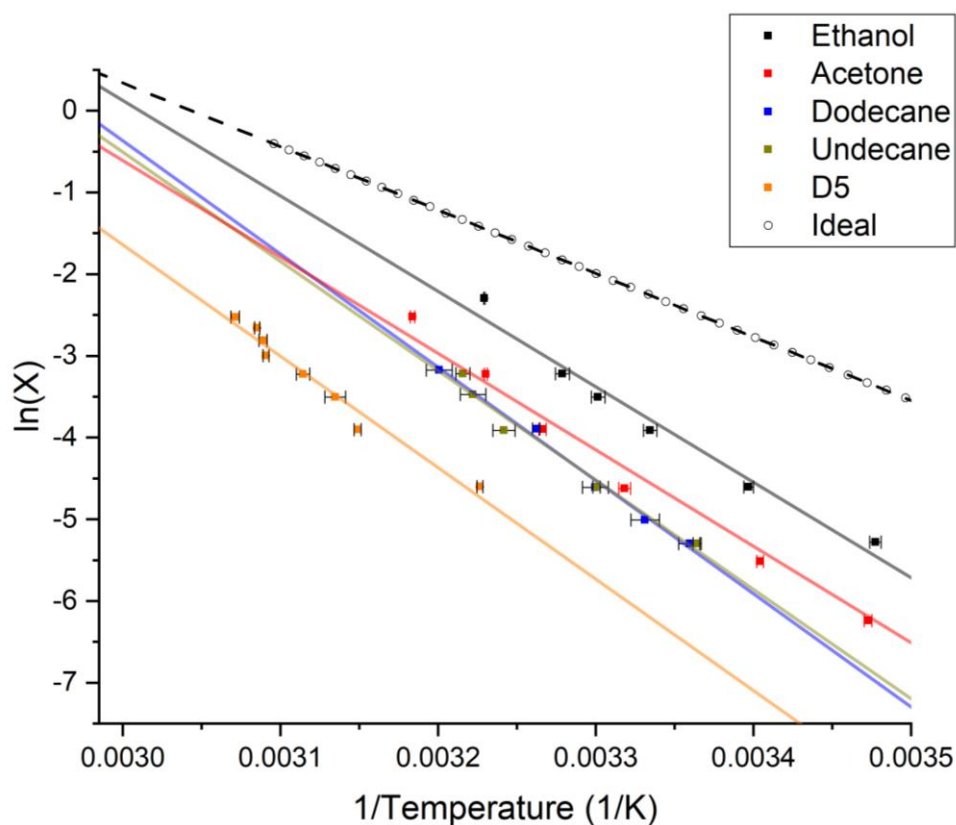


Figure 5-8 van't Hoff plot displaying the ideal solubility of 1-Octadecanol and 1-Octadecanol in Ethanol, Acetone, Dodecane, Undecane and D5 solvents.

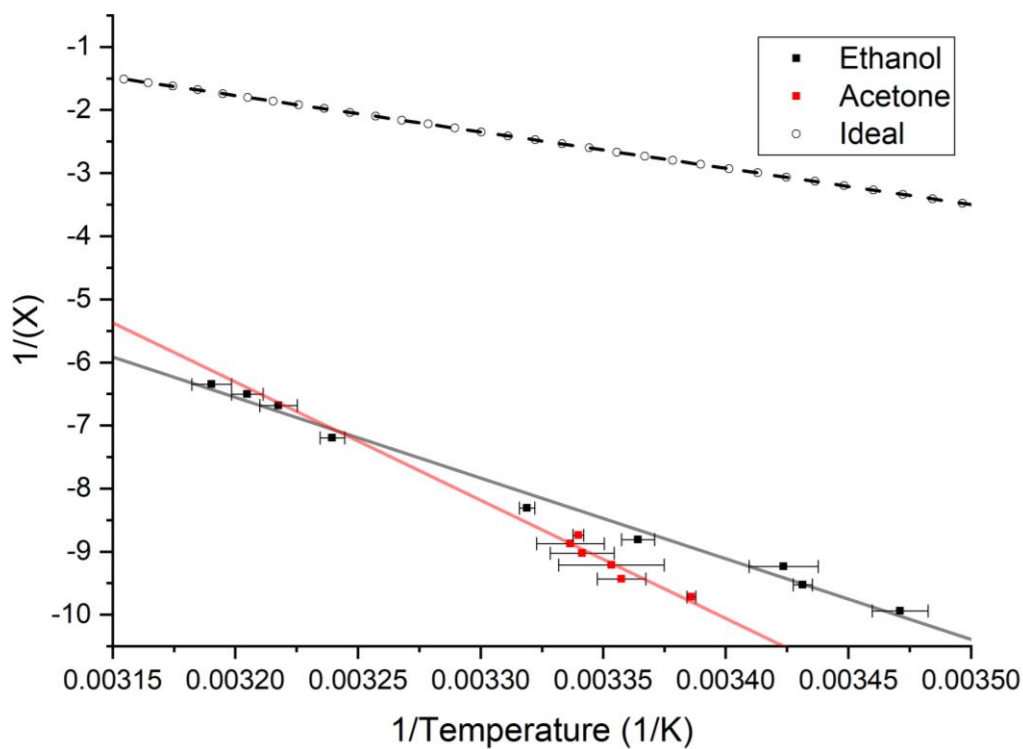


Figure 5-9 van't Hoff plot displaying the ideal solubility of HCO and HCO in Ethanol and Acetone solvents.

Table 5-11 The gradient, y cut and error of the van 't Hoff plot are tabulated alongside, Activity (γ), Entropy (ΔS) and Enthalpy (ΔH). The thermodynamic data was derived from the van 't Hoff plot of Hydrogenated Castor Oil, and 1-Octadecanol dissolved in a range of solvents. ΔH_{soln} calculated using a ΔH_{sub} value of 44.8 kcal mol⁻¹ for 1-Octadecanol. [130]

Solvent Condition	Slope	y ⁰	R ²	ΔH_{diss} (kJ mol ⁻¹)	ΔS_{diss} (kJ K ⁻¹ mol ⁻¹)	ΔH_{soln} (kJ mol ⁻¹)	γ (15°C – 35°)	Dielectric Constant of Solvent
Hydrogenated Castor Oil								
Ideal	-5756.07	16.65	1.00	47.86	0.14	-	-	-
Ethanol	-12790.95	34.37	0.99	106.34	0.29	-	824.11 - 168.44	25.02 [131]
Acetone	-18743.74	53.67	0.93	155.84	0.45	-	3285.76 – 175.23	21.30 [131]
1-Octadecanol								
Ideal	-7766.90	23.64	1.00	64.57	0.20	-122.87	-	-
Ethanol	-11685.29	35.18	0.97	97.15	0.29	-90.29	7.92 - 3.27	25.02 [131]
Acetone	-11805.46	34.81	0.98	98.15	0.29	-89.29	17.49 - 7.03	21.30 [131]
Dodecane	-13864.17	41.23	0.99	115.27	0.34	-72.18	36.40 – 9.19	1.994 [132]
Undecane	-13385.33	39.65	0.97	111.29	0.33	-76.16	33.31 – 9.37	2.002 [132]
D5	-13643.60	39.29	0.97	113.43	0.33	-74.01	117.15 - 31.10	2.5 [133]

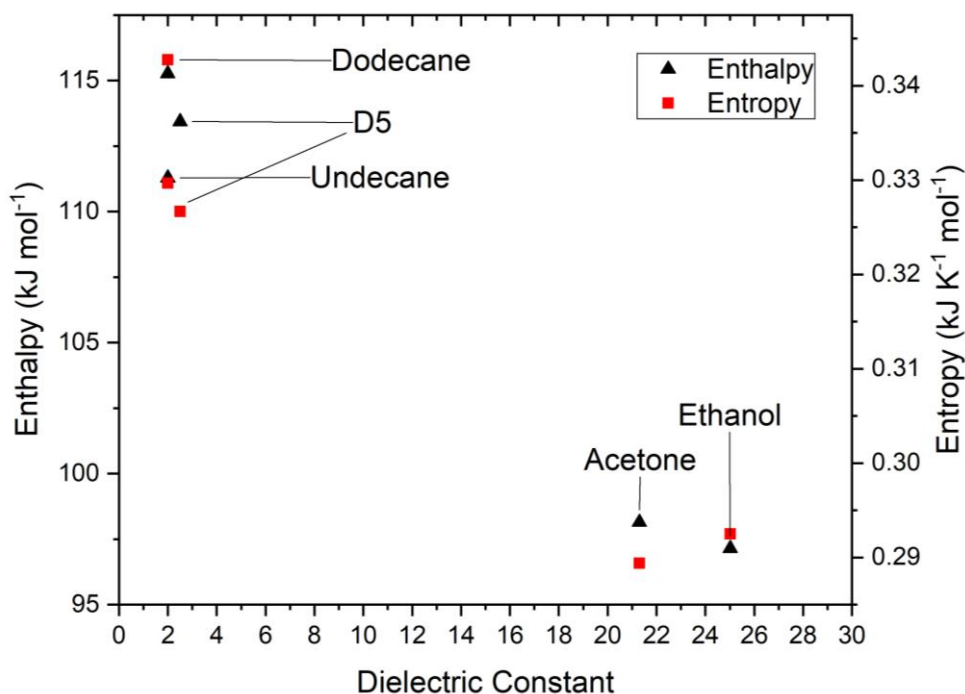


Figure 5-10 Dielectric constants plotted against enthalpy and entropy values of 1-Octadecanol in Ethanol, Acetone, Dodecane, Undecane and D5 solvents.

The Entropy and Enthalpy of dissolution of the solute vary depending on the solvent present. In the case of 1-Octadecanol, enthalpy and entropy of dissolution values are

higher in non-polar solvents compared to polar solvents. The dielectric constant is a measure of polarity with a high dielectric constant value indicating a polar molecule. The enthalpy and entropy of dissolution were plotted with respect to the polarity of the solvent present for 1-Octadecanol solutions (Figure 5-10). Higher values of entropy and enthalpy of dissolution are observed for non-polar solvents relative to polar solvents. The enthalpy of solvation can be defined as the energy required to desolvate a molecule of 1-Octadecanol saturated in solvent molecules. The data in Table 5-11 shows that it's most energetically favourable to desolvate 1-Octadecanol in Dodecane solution and least favourable in Ethanol solution.

Only dissolution experiments in polar solvents were completed using HCO, so a comparison between polar and non-polar solvents cannot be made. Despite HCO being measured in similarly polar solvents, the values of enthalpy and entropy measured are very different. HCO is very poorly soluble in Acetone but moderately soluble in Ethanol. Perhaps the protic or aprotic nature of the polar solvent influences solubility of Hydrogenated Castor Oil and 1-Octadecanol, for example, both waxes are more soluble in Ethanol (protic) than Acetone (aprotic). Further experiments would be needed to support this hypothesis.

5.4 Insight into the Nucleation Mechanism using the KBHR Approach

The nucleation mechanism of HCO in Ethanol and Acetone, and 1-Octadecanol in Ethanol, Acetone, Dodecane, Undecane and D5 solvents was investigated using the KBHR approach. The KBHR approach enables the determination of the nucleation mechanism and indicates whether the mechanism is instantaneous or progressive.

The first stage of implementing the KBHR approach involved calculating the relative critical undercooling (u_c), using Equation 3-6 and parameters (T_c) and (T_e) values tabulated in Table 5-1-Table 5-9. The relative critical undercooling values of HCO and 1-Octadecanol are listed in Table 5-12, Table 5-13 and

Table 5-14 as a function of cooling rate and solvent concentration. All the calculated values of u_c are less 0.1 and meet the inequalities of KBHR defined in Equation 3-7.

Table 5-12 The relative critical undercooling (u_c) as a function of cooling rate for Hydrogenated Castor Oil in Ethanol and Acetone.

Hydrogenated Castor Oil									
q (K/s)	Ethanol Concentration (g/l)								
	0.77	1.16	1.56	2.38	3.93	7.92	19.99	23.95	27.96
0.004	0.044	0.044	0.045	0.042	0.044	0.041	0.040	0.042	0.038
0.017	0.056	0.060	0.059	0.058	0.055	0.051	0.047	0.046	0.049
0.033	0.066	0.068	0.063	0.065	0.064	0.057	0.047	0.049	0.051
0.053	0.072	0.076	0.077	0.076	0.069	0.066	0.060	0.058	0.061
q (K/s)	Acetone Concentration (g/l)								
	0.76	1.01	1.27	1.52	1.77	1.97			
0.004	-	-	0.043	0.043	0.039	0.035			
0.017	0.055	0.056	0.054	0.048	0.047	0.027			
0.033	0.057	0.062	0.057	0.056	0.054	0.040			
0.053	0.056	0.062	0.065	0.064	0.061	0.044			

Table 5-13 The relative critical undercooling (u_c) as a function of cooling rate for 1-Octadecanol in Ethanol, Acetone, Dodecane and Undecane.

1-Octadecanol									
q (K/s)	Ethanol Concentration (g/l)								
	23.72	45.09	92.68	143.42	193.47	402.37			
0.004	0.025	0.015	0.018	0.016	0.015	0.018			
0.017	0.023	0.029	0.022	0.023	0.021	0.020			
0.033	0.029	0.027	0.028	0.027	0.027	0.023			
0.053	0.035	0.036	0.032	0.035	0.033	0.038			
q (K/s)	Acetone Concentration (g/l)								
	3.48	7.14	14.76	36.24	75.49	151.39	318.84		
0.004	0.017	0.016	0.012	0.011	0.012	0.006	0.011		
0.017	0.023	0.024	0.013	0.016	0.015	0.012	0.015		
0.033	0.025	0.024	0.023	0.018	0.017	0.013	0.012		
0.053	0.027	0.028	0.028	0.020	0.022	0.019	0.017		
q (K/s)	Dodecane Concentration (g/l)								
	5.98	7.97	11.85	24.28	49.92	96.36	169.20	210.15	297.15
0.004	0.008	0.012	0.007	0.010	0.011	0.011	0.008	0.011	0.010
0.017	0.012	0.015	0.013	0.010	0.013	0.010	0.010	0.012	0.014
0.033	0.016	0.017	0.017	0.006	0.020	0.015	0.014	0.013	0.014
0.053	0.014	0.023	0.019	0.014	0.019	0.019	0.016	0.017	0.020
q (K/s)	Undecane Concentration (g/l)								
	6.45	12.92	26.13	39.73	53.36	103.61	182.82	225.86	319.85
0.004	0.012	0.005	0.010	0.012	0.009	0.009	0.009	0.010	0.009
0.017	0.016	0.009	0.014	0.016	0.011	0.014	0.012	0.011	0.010
0.033	0.016	0.012	0.015	0.016	0.013	0.013	0.012	0.013	0.012
0.053	0.021	0.016	0.018	0.021	0.017	0.019	0.016	0.016	0.017

Table 5-14 The relative critical undercooling (u_c) as a function of cooling rate for 1-Octadecanol in D5.

1-Octadecanol								
q (K/s)	D5 Concentration (g/l)							
	7.10	14.38	21.66	28.98	36.72	44.59	52.62	60.80
0.004	0.011	0.008	0.011	0.008	0.008	0.008	0.007	0.009
0.017	0.011	0.005	0.007	0.006	0.011	0.012	0.009	0.011
0.033	0.013	0.007	0.008	0.007	0.013	0.013	0.012	0.015
0.053	0.019	0.011	0.015	0.011	0.018	0.018	0.016	0.017

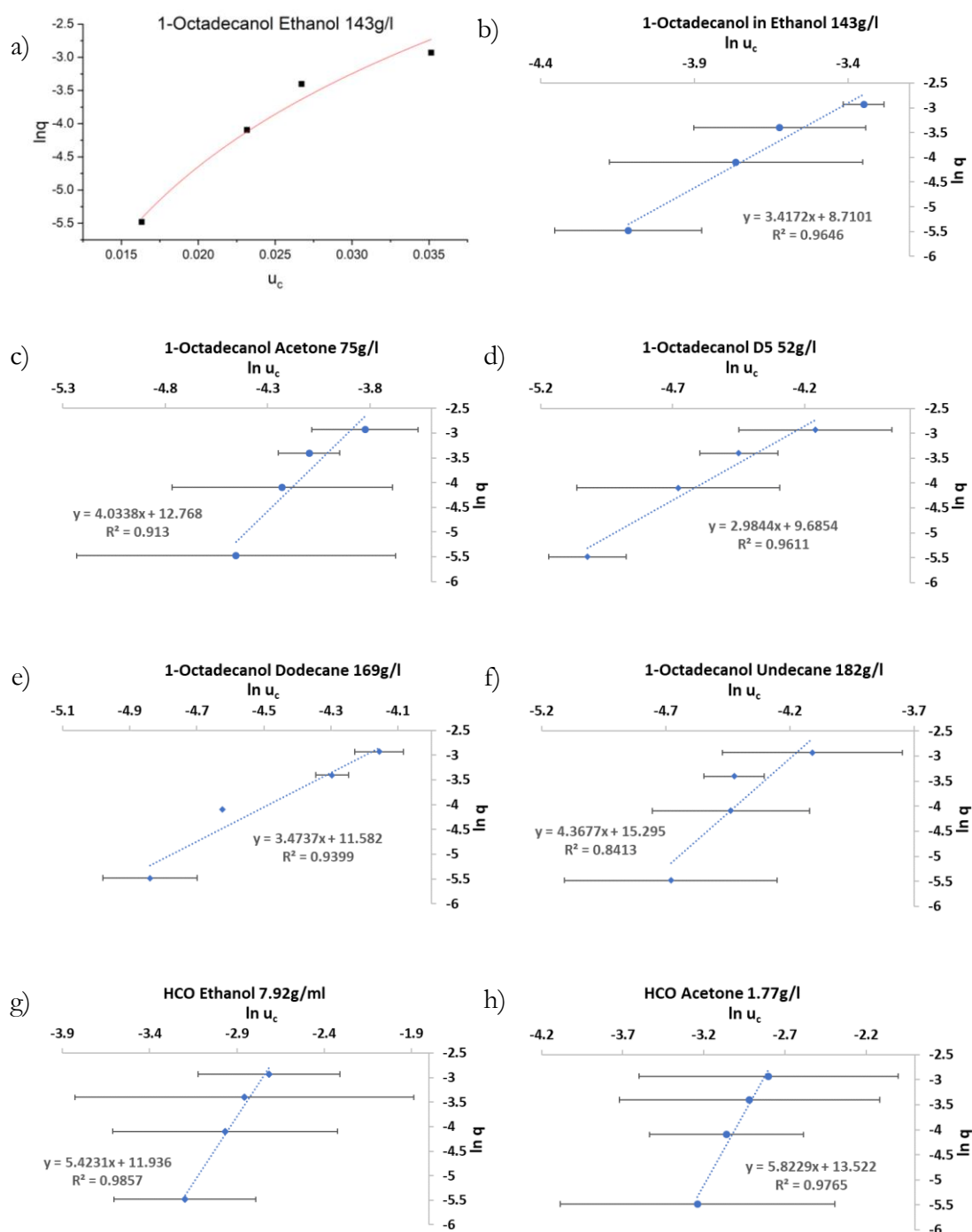


Figure 5-11 a) relative critical undercooling (u_c) plotted against \ln cooling rate (q) for 1-Octadecanol in Ethanol at 143g/l, and the data were fitted to Equation 3-9. b-h) plot of q vs u_c in \ln - \ln coordinates for 1-Octadecanol and Hydrogenated Castor Oil dissolved in Ethanol, Acetone, Dodecane, Undecane and D5 solvents.

Figure 5-11 b-h) displays $\ln q$ plotted against $\ln u_c$ for each solute and solvent, and the error bars demonstrate the stochastic nature of crystallisation.[113] The ‘rule of three’ was applied to the gradient of the line of best fit to indicate the nucleation mechanism present. A gradient of smaller than three indicates an instantaneous nucleation

mechanism (IN) and gradient of larger than three suggests a progressive nucleation mechanism (PN). The gradient, nucleation mechanism and R^2 of the straight-line fitting were tabulated in Table 5-15 for HCO and Table 5-16 for 1-Octadecanol. Further analysis was completed on compositions which exhibited progressive nucleation mechanisms. This analysis involved plotting $\ln q$ vs u_c for each composition and fitting Equation 3-9 to the polythermal data as displayed in Figure 5-11 a) for 1-Octadecanol in Ethanol at 143g/l. The line of best fit enabled three free parameters to be derived (a_1 , a_2 and $\ln q_0$) and the data along with the R^2 fitting value was tabulated in Table 5-15, Table 5-16 and Table 5-17. Further analysis using the molecular volume equilibrium temperature values (T_c), Equation 3-10 and Equation 3-11 enabled nucleation parameters to be calculated such as interfacial tension (γ_{eff}), critical nuclei radius size (r^*) and the number of molecules in a critical cluster (i^*). The calculated parameters have been tabulated in Table 5-18 for HCO and Table 5-19 for 1-Octadecanol.

The nucleation mechanism of HCO and 1-Octadecanol was found to be predominately progressive in all the solvents used and independent of concentration. This means that new nuclei can form in the presence of existing crystals for HCO and 1-Octadecanol systems. HCO, in general, was found to be more progressive in Ethanol and Acetone solvents than 1-Octadecanol. No previous studies have calculated values of interfacial tension, nuclei radius and number for 1-Octadecanol and HCO in Ethanol, Acetone, Dodecane, Undecane and D5 in the literature.

Table 5-15 Parameters derived from the KBHR method applied to Hydrogenated Castor Oil crystallising from Ethanol and Acetone solutions. Nucleation mechanism is determined using the gradient of the $\ln q$ vs $\ln u_c$ and the parameters (a_1 , a_2 and $\ln q_0$) are obtained by fitting the equation to $\ln q$ vs u_c .

Hydrogenated Castor Oil								
Conc (g/l)	Slope	Nucleation Mechanism	R ²	a ₁	a ₂ = b	ln q ₀	q ₀	R ²
Ethanol								
0.77	5.062	PN	0.996	3	3.030E-03	5.556	258.672	0.999
1.16	4.649	PN	0.994	3	2.440E-03	5.198	180.823	0.994
1.56	4.886	PN	0.959	3	3.140E-03	5.453	233.523	0.961
2.38	3.916	PN	0.987	3	2.070E-03	5.208	182.664	0.992
3.93	5.413	PN	0.994	3	3.420E-03	5.789	326.791	0.996
7.92	5.423	PN	0.986	3	3.080E-03	6.049	423.681	0.993
19.99	5.909	PN	0.797	3	3.640E-03	6.867	960.064	0.756
23.95	7.450	PN	0.875	3	5.480E-03	7.627	2052.738	0.872
27.96	5.420	PN	0.959	3	2.610E-03	6.279	533.170	0.953
Acetone								
1.27	6.596	PN	0.975	3	4.700E-03	6.521	679.149	0.967
1.52	6.083	PN	0.924	3	4.160E-03	6.613	744.989	0.926
1.77	5.823	PN	0.977	3	3.240E-03	6.503	667.454	0.987
1.97	2.588	IN	0.238	3				

Table 5-16 Parameters derived from the KBHR method applied to 1-Octadecanol crystallising from Ethanol, Acetone and Dodecane solutions. Nucleation mechanism is determined using the gradient of the $\ln q$ vs $\ln u_c$ and the parameters (a_1 , a_2 and $\ln q^0$) are obtained by fitting the equation to $\ln q$ vs u_c .

1-Octadecanol								
Ethanol Concentration								
Conc (g/l)	Slope	Nucleation Mechanism	R ²	a ₁	a ₂ = b	ln = q ⁰	q ⁰	R ²
23.72	4.355	PN	0.504	3				
45.09	2.884	IN	0.897	3				
92.68	4.348	PN	0.968	3	3.851E-04	7.888	2665.242	0.973
143.42	3.417	PN	0.965	3	1.323E-04	7.426	1678.809	0.961
193.47	3.338	PN	0.983	3	9.137E-05	7.547	1895.144	0.983
402.37	2.862	IN	0.665	3				
Acetone Concentration (g/l)								
3.48	5.536	PN	0.993	3	5.314E-04	8.523	5030.577	0.975
7.14	4.729	PN	0.958	3	3.453E-04	8.133	3403.808	0.925
14.76	2.302	IN	0.752	3				
36.24	3.744	PN	0.474	3	8.118E-05	8.822	6781.747	0.968
75.49	3.916	PN	0.987	3	1.471E-04	9.142	9335.130	0.913
318.84	2.206	IN	0.954	3				
Dodecane Concentration (g/l)								
5.98	3.672	PN	0.851	3	4.557E-05	9.641	15379.489	0.793
7.97	0.975	IN	0.376	3	1.515E-04	9.014	8213.710	0.826
11.85	2.538	IN	0.987	3				
49.92	3.767	PN	0.890	3	-1.222E-04	9.009	8172.335	0.857
96.36	3.059	PN	0.692	3	9.481E-05	8.983	7967.611	0.538
169.20	3.474	PN	0.940	3	3.393E-05	9.768	17459.165	0.925
297.57	3.600	PN	0.895	3	1.967E-04	9.233	10224.376	0.869

Table 5-17 Parameters derived from the KBHR method applied to 1-Octadecanol crystallising from Undecane and D5 solutions. Nucleation mechanism is determined using the gradient of the $\ln q$ vs $\ln u_c$ and the parameters (a_1 , a_2 and $\ln q_0$) are obtained by fitting the equation to $\ln q$ vs u_c .

Undecane Concentration (g/l)								
Conc (g/l)	Slope	Nucleation Mechanism	R ²	a ₁	a ₂ = b	ln = q ⁰	q ⁰	R ²
6.45	1.830	IN	0.995	3				
12.92	2.212	IN	0.990	3				
26.13	4.673	PN	0.993	3	1.359E-04	9.662	15703.674	0.991
39.73	4.670	PN	0.922	3	1.992E-04	9.367	11691.882	0.911
53.36	3.962	PN	0.943	3	7.498E-05	9.867	19275.883	0.947
103.61	3.251	PN	0.840	3	7.498E-05	9.867	19275.883	0.947
182.82	4.368	PN	0.841	3	1.179E-04	10.137	25258.298	0.817
225.86	4.8202	PN	0.844	3	1.43E-04	10.297	29656.601	0.79288
319.85	3.4973	PN	0.768	3	5.704E-05	9.962	21202.195	0.694
D5 Concentration (g/l)								
7.10	3.503	PN	0.611	3	6.535E-05	9.366	11687.907	0.429
36.72	3.073	PN	0.934	3	1.627E-05	9.404	12139.380	0.910
44.59	3.308	PN	0.950	3	3.048E-05	9.442	12609.553	0.941
52.62	2.984	IN	0.961	3	5.782E-06	9.824	18472.714	0.944
60.80	3.897	PN	0.912	3	7.484E-05	9.644	15434.029	0.889

Table 5-18 Interfacial tension, critical radius and number of molecules in the cluster for Hydrogenated Castor Oil in Acetone and Ethanol solutions.

Hydrogenated Castor Oil							
Conc. (mg/ml)	γ_{eff} (mJ/m ²)	r* (nm)	i*	Conc. (mg/ml)	γ_{eff} (mJ/m ²)	r* (nm)	i*
Ethanol				Acetone			
0.77	1.996	0.52 - 0.87	0 - 2	1.27	2.926	0.61 - 0.92	1 - 2
1.16	1.864	0.47 - 0.81	0 - 1	1.52	2.812	0.60 - 0.90	1 - 2
1.56	2.034	0.50 - 0.86	0 - 2	1.77	2.589	0.58 - 0.90	0 - 2
2.38	1.776	0.44 - 0.80	0 - 1				
3.93	2.109	0.58 - 0.92	0 - 2				
7.92	2.054	0.59 - 0.96	0 - 2				
19.99	2.176	0.69 - 1.04	1 - 3				
23.95	2.498	0.82 - 1.14	1 - 4				
27.96	1.953	0.61 - 0.99	1 - 2				

Table 5-19 Interfacial tension, critical radius and number of molecules in the cluster for 1-Octadecanol in Acetone, Ethanol, Dodecane, Undecane and D5 solutions.

1-Octadecanol							
Conc. (mg/ml)	γ_{eff} (mJ/m ²)	r^* (nm)	i^*	Conc. (mg/ml)	γ_{eff} (mJ/m ²)	r^* (nm)	i^*
Ethanol				Acetone			
92.68	2.032	0.29 - 0.76	1 - 3	3.48	2.210	0.55 - 0.87	1 - 5
143.42	1.428	0.27 - 0.59	0 - 2	7.14	1.930	0.47 - 0.80	1 - 4
193.47	1.265	0.26 - 0.56	0 - 1	36.24	1.209	0.41 - 0.77	1 - 3
				75.49	1.482	0.46 - 0.86	1 - 5
Dodecane				Undecane			
5.98	1.266	0.44 - 0.72	1 - 3	26.13	1.850	0.49 - 0.86	1 - 5
7.97	1.895	0.38 - 0.72	0 - 3	39.73	2.105	0.48 - 0.84	1 - 5
49.92	1.643	0.48 - 0.84	0 - 3	53.36	1.521	0.43 - 0.82	1 - 4
169.20	1.171	0.35 - 0.69	0 - 3	103.61	1.526	0.37 - 0.80	0 - 4
297.57	1.483	0.35 - 0.71	0 - 3	182.82	1.778	0.51 - 0.89	1 - 5
				225.86	1.898	0.57 - 0.90	1 - 6
				319.85	1.399	0.39 - 0.75	0 - 3
D5							
36.72	0.788	0.25 - 0.59	0 - 2				
44.59	0.972	0.32 - 0.70	0 - 3				
52.62	0.559	0.21 - 0.50	0 - 1				
60.80	1.314	0.47 - 0.84	0 - 5				

5.5 Crystal Morphology Observed of 1-Octadecanol in Dodecane and D5 solvents

A custom-made crystal growth cell was employed to observe single crystals of 1-Octadecanol in Dodecane at a concentration of 25g/l, and a selection of the images captured are displayed in Figure 5-12. The meta-stable zone width was known to exist

between 31-34°C for a 25g/l, 1-Octadecanol in Dodecane solution. The temperature of the water bath was held isothermally, and single crystals were captured using an optical microscope fitted with a 5x lens. Image a) displays two overlaying single crystals that nucleated in a supersaturated solution at the centre of the cell in the presence of existing crystals at the edge at 30.5°C. A clearer image of the two single crystals was obtained by raising the temperature to 31°C, which is above the equilibrium temperature, and the dissolving crystals were captured in image b). The shape of the single crystal appears to be rectangular with two rapidly growing faces and two slow growth faces. The edge of the rapidly growing face appears to be curved and difficult to observe. The rectangular shape is in contrast to the parallelogram-shaped single crystal of 1-Octadecanol (Figure 2-15) published in the literature which was formed in p-xylene solution.[56] The change in solvent must radically change the morphology of the 1-Octadecanol single-crystal. Image c) displays a large piece of 1-Octadecanol being dissolved to form multiple crystalline fragments. These fragments were cooled and held isothermally at 33.5°C and image d) displays secondary nucleation with new crystal plates extending from the fast-growing face after 2 minutes. Image e) displays the growth of these new plates after 4 minutes at 33.5°C. Image f) displays the dissolution of a large 1-Octadecanol crystal and steps can be observed on the surface as each crystalline plane is being dissolved.

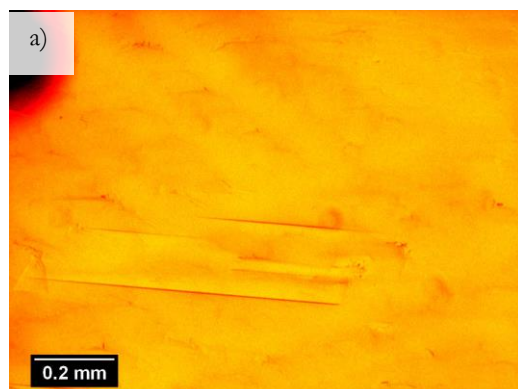
Experiments were conducted to attempt to form the single crystal of HCO; however, each experiment failed and resulted in spherulite clusters being formed.

The morphology of high purity samples of HCO and 1-Octadecanol have been imaged using SEM and shown in Figure 5-13. Acetone was found to be a suitable solvent for purification of HCO and 1-Octadecanol. Crystals formed during recrystallisation were filtered and dried before being imaged.

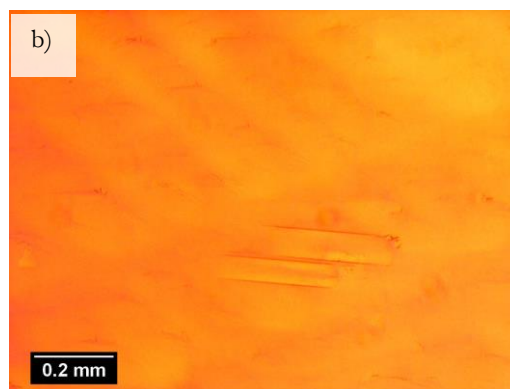
Plate crystals of 1-Octadecanol are observed at various magnifications from 60 to 2000 times magnification. The crystal plates appear to be between 20µm - 1mm in size with a flat surface, irregular shape and the plates stacked on top of each other to form layers. At 2000 times magnification, small steps in the flat surface can be observed and might be similar to the microchannels previously observed in the literature.[87]

The HCO crystals formed are spherulitic and distinctly different to 1-Octadecanol plates. The HCO crystals have been imaged at a range of magnifications and displayed in Figure 5-14. Each spherulite appears to be bound to its neighbour, to create clusters. The size of spherulite ranges from 0.5mm to 100µm, and the surface has a distinctive texture that

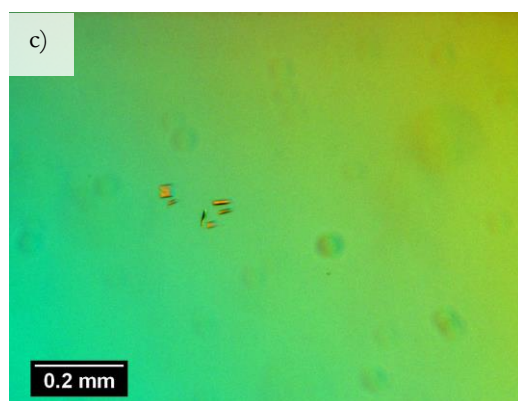
can be clearly observed with the x600 magnified image. The HCO crystals have been observed to have irregular morphology, as shown in images a) and d).



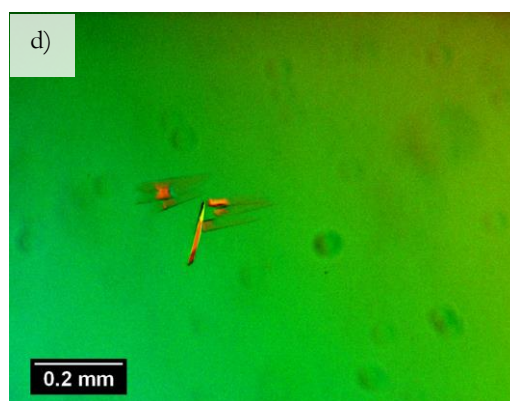
Two overlaying rectangular 1-Octadecanol single crystals at 30.5°C



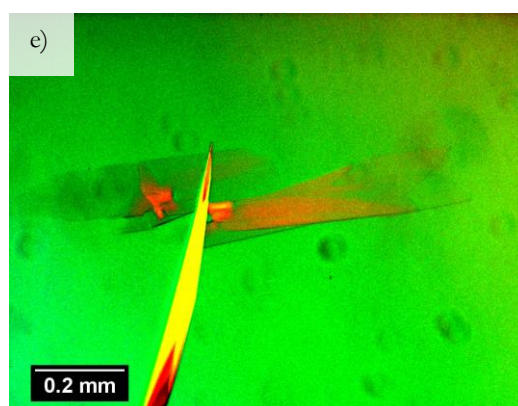
Two adjacent rectangular 1-Octadecanol single crystals at 31°C



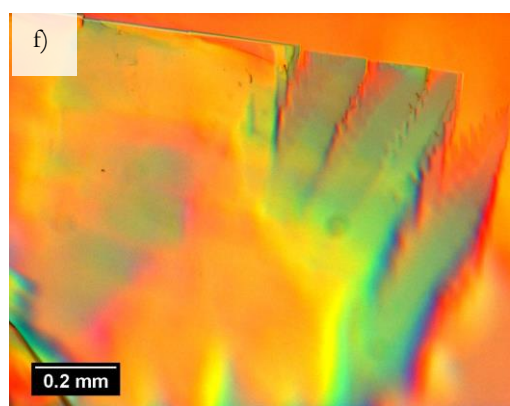
Heated large crystalline area of 1-Octadecanol until only small fragments remained.



Crystal growth of the fragments at 33.5°C after 2 minutes (Top of metastable zone width)

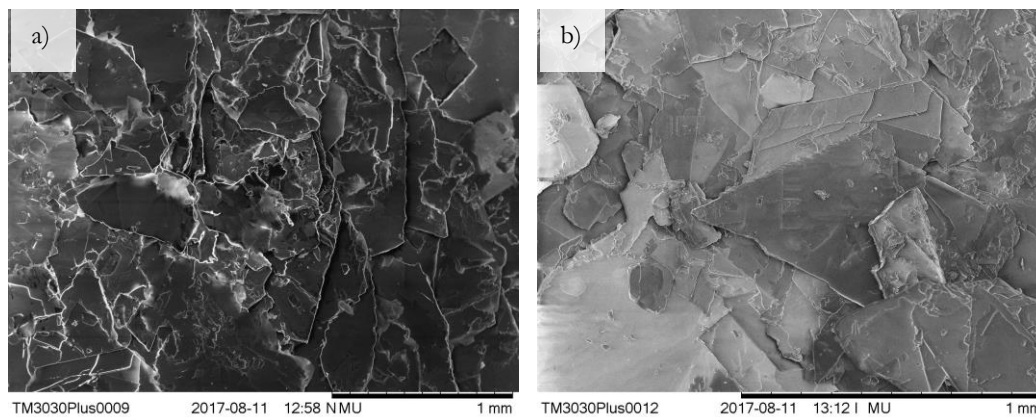


Crystal growth of the fragments at 33.5°C after 4 minutes (Top of metastable zone width)



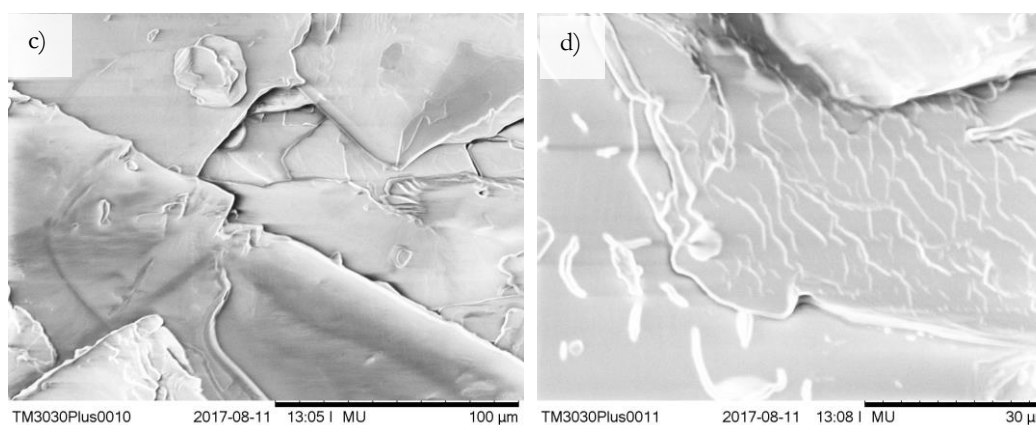
Dissolution of a large 1-Octadecanol plate.

Figure 5-12 Images taken of 1-Octadecanol crystallising and dissolving in a 25g/l Dodecane solution using a 5x optical lens.



1-Octadecanol imaged at x60 magnification using a 15kV accelerating voltage

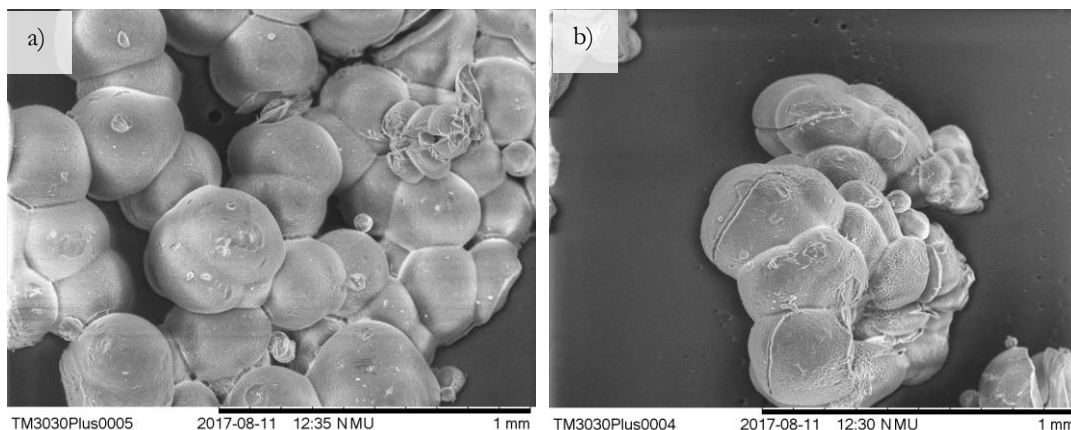
1-Octadecanol imaged at x100 magnification using a 5kV accelerating voltage.



1-Octadecanol imaged at x800 magnification using a 5kV accelerating voltage.

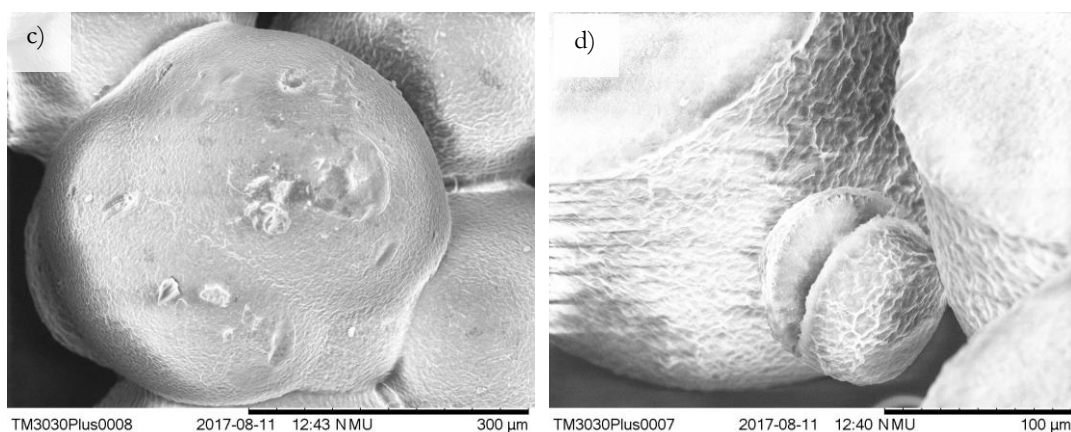
1-Octadecanol imaged at x2000 magnification using a 5kV accelerating voltage.

Figure 5-13 A series of SEM images of 1-Octadecanol crystals formed from Acetone solution using secondary electron mode.



Hydrogenated Castor Oil imaged at x100 magnification using a 15kV accelerating voltage.

Hydrogenated Castor Oil imaged at x100 magnification using a 15kV accelerating voltage.



Hydrogenated Castor Oil imaged at x300 magnification using a 15kV accelerating voltage.

Hydrogenated Castor Oil imaged at x600 magnification using a 15kV accelerating voltage.

Figure 5-14 A series SEM image of Hydrogenated Castor Oil crystals formed from Acetone solution using secondary electron mode.

5.6 Conclusion

A variety of different techniques and methods have been employed to study the crystallisation behaviour of 1-Octadecanol and HCO in a range of polar and non-polar solvents. Turbidity measurements conducted on HCO and 1-Octadecanol in Ethanol, Acetone, Dodecane, Undecane and D5 solvents gave insights into the solubility and meta-stable width of each system. Both 1-Octadecanol and HCO were found to be more soluble in polar solvents relative to non-polar solvents, and both wax hydrocarbons were found to be more soluble in the protic polar solvent than aprotic polar solvent. This was rationalised by the hydrogen bonding present between the waxes and the polar solvent, being a stronger interaction than the van der Waal's interactions between the non-polar solvent and the waxes. 1-Octadecanol was found to be far more soluble than HCO in

both non-polar solvents and polar solvents. In fact, in this study, HCO was found to be completely insoluble in the non-polar solvents tested. The higher solubility of 1-Octadecanol likely is due to its simple molecular structure with non-polar and polar features, compared to HCO, which has a three-legged structure with a complex blend of non-polar and polar features.

van 't Hoff analysis was employed on the turbidity data and found that systems with high solubility were closer to ideality, where solubility is a function of solute and solvent used. Values of entropy and enthalpy were lower for higher solubility systems, and in the case of 1-Octadecanol, these were non-polar solvent solutions. The resulted in an enthalpy of solvation, that favoured desolvation of Dodecane compared to Ethanol.

The KBHR approach was conducted, and the nucleation mechanism was found to be progressive for both HCO and 1-Octadecanol and mechanism was found to be independent of concentration. The nucleation mechanism of HCO was found to be to more progressive than 1-Octadecanol for the polar solvents tested. Nucleation parameters such as Interfacial tension, critical radius size and the number of molecules in a critical cluster has been successfully calculated for HCO and 1-Octadecanol.

The morphology of 1-Octadecanol and HCO upon solvent crystallisation has been studied using a growth cell and SEM. Two single crystals of 1-Octadecanol have been imaged and are rectangular plates with two opposite fast-growing faces and two opposite slow-growing faces. SEM images reveal that these plates stacked on top of each other to form layers and upon x2000 magnification microchannels on the surface of the plates can be observed, similar to what was previously reported in the literature.[87] HCO was found to crystallise as spherulite clusters. Majority of the spherulites are spherical in shape; however, examples of irregular spherulites have been imaged.

Chapter 6 Phases, Crystal Morphology and Mechanical Properties of 1-Octadecanol and Hydrogenated Castor Oil Mixtures

In this chapter, the structuring hydrocarbons are studied in their mixtures, through mapping the phases present in the mixtures and studying the impact on the mechanical properties and morphology.

6 Phases, Crystal Morphology and Mechanical Properties of 1-Octadecanol and Hydrogenated Castor Oil Mixtures

6.1 Introduction

Changing the formulation composition of a cosmetic product can drastically alter its performance, appearance, sensory feel and stability. Though creating binary phase diagrams of the main structuring ingredients using Differential Scanning Calorimetry (DSC), the different phases present at a range of compositions and temperatures can be mapped out. XRD has been used to capture the different crystal structures formed with respect to binary mixture composition. Physical and mechanical properties of Hydrogenated Castor Oil (HCO) and 1-Octadecanol phases created by controlled cooling a range of binary mixture compositions at 1°C/min have been studied simultaneously using Atomic Force Microscopy (AFM) and DSC. Using a combination of AFM and DSC, a phase diagram detailing morphology, structure and mechanical property information has been created.

HCO and 1-Octadecanol have been studied individually at a range of cooling rates using AFM. Results can be found in Chapter 4. HCO displayed spherulitic structures of ~35µm and ~1µm in diameter when cooled at 1°C/min and 20°C/min respectively, with a uniform Young's modulus across the surface of between 240-407 MPa. 1-Octadecanol's surface is rough and contains a series of flat planes, sharp ridges and steps, created through 1-Octadecanol crystallising as plates and stacking on top of each other. Optically the plates appear larger at slower cooling rates, and a uniform Young's modulus of 1.2-1.7 GPa was measured across the surface.

In this chapter, in addition to the detailed study on 1-Octadecanol and HCO, binary phase diagrams of 1-Octadecanol/Petrolatum, 1-Octadecanol/Dodecane and 1-Octadecanol/D5 have been created through tracking the change in onset temperature of each phase transition with respect to the binary mixture composition upon cooling at 1°C/min. HCO is immiscible in Petrolatum, and as a result, no phase diagram has been produced. The synchrotron study in Chapter 7 focuses on the impact of shear on 1-Octadecanol in Dodecane and D5 solvents, and in this chapter binary phases have been created to understand this result further.

6.2 1-Octadecanol and Hydrogenated Castor Oil

6.2.1 Thermal Analysis of 1-Octadecanol and Hydrogenated Castor Oil

The thermal phase transitions of HCO and 1-Octadecanol binary mixtures have been measured using DSC upon heating and cooling at 1°C/min. The normalised cooling DSC data has been presented in a stacked line graph in Figure 6-2 and the normalised heating data in Figure 6-3. The peak onset, peak centre and peak integral data have been displayed in Table 6-1 and Table 6-2 for cooling and heating respectively. In the table, empty cells infer that no peak is present at that given composition and a dash means that the software failed to measure information about the peak, such as the integral.

Upon cooling 1-Octadecanol displays an exothermic crystallisation peak to form the rotator phase at 56.7°C (peak 1) and the metastable rotator phase converts to form the stable gamma phase at 49.1°C (peak 2). The rotator-gamma phase transition is so exothermic it raises the sample temperature measured, so the peak centre is at a higher temperature than of the peak onset. Both phase transitions exhibit sharp peaks indicating a high level of sample purity. Figure 4-1 in chapter 4 displays the full heating and cooling cycle of 1-Octadecanol. Upon adding a small proportion of HCO to 1-Octadecanol (HCO/OCT = 0.1/0.9), the crystallisation onset temperature of 1-Octadecanol decreases from 57.1°C to 56.4°C and the onset of rotator-gamma transition increases from 49.1 to 50.8°C. When further increasing the proportion of HCO, the crystallisation and rotator-gamma phase incrementally decreases to 38.7°C and 37.1°C respectively at (HCO/OCT = 0.9/0.1). At compositions between (HCO/OCT = 0.1/0.9) and (HCO/OCT = 0.5/0.5), the HCO crystallisation peak resides between the 1-Octadecanol crystallisation peak and the rotator-gamma phase transition peak. In this region the enthalpy of the HCO crystallisation peak is higher than expected given the low proportion of HCO present in the binary mixture as shown in Figure 6-1, suggesting that this enthalpy of this peak is partially due to the crystallisation of HCO and partially due to the crystallisation of 1-Octadecanol (peak 4). The integral of the HCO peak (peak 3) changes linearly with respect to the mole fraction; however, the integral of peak 4 has a non-linear relationship. This suggests the contribution of 1-Octadecanol to peak 4 increases as it nears HCO/OCT = 0.5/0.5, where the crystallisation temperatures of HCO and 1-Octadecanol are the same.

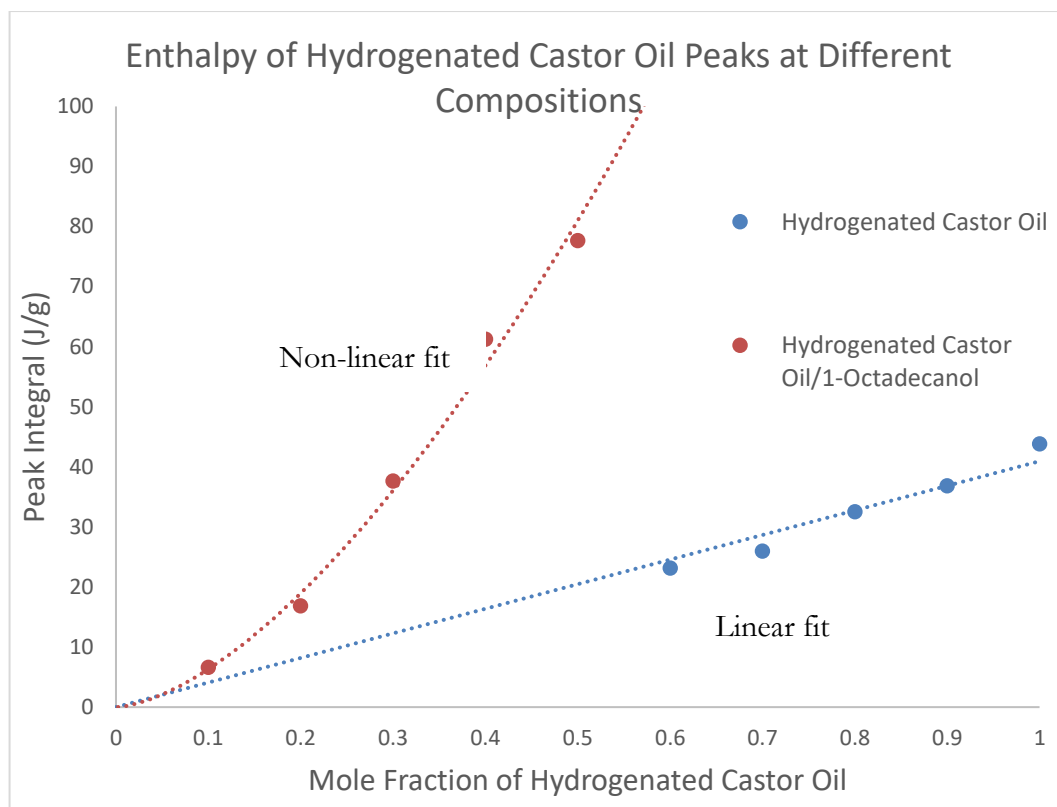


Figure 6-1 Peak Integral (Enthalpy) of Hydrogenated Castor Oil Crystallisation with respect to changing composition. Hydrogenated Castor Oil is represented by the blue line (peak 3), and Hydrogenated Castor Oil/1-Octadecanol is represented by the red line (peak 4) in the Differential Scanning Calorimetry (DSC) results upon cooling (Figure 6-2).

HCO displays a broad exothermic crystallisation peak at 67.7°C (peak 3), three very broad low enthalpy events with peak centres at 47.2°C, 39.7°C and 33.0°C and a sharp low temperature, very low enthalpy event at 6.8°C (peak 5). Figure 4-9 in chapter 4 displays the full heating and cooling cycle of HCO. Upon increasing concentration of 1-Octadecanol the crystallisation temperature of HCO decreases from 67.7°C to 51.6°C by (HCO/OCT = 0.9/0.1), however the low temperature sharp peak increases from 6.8°C to 14.52°C. The enthalpy of this low temperature transition increases upon increasing levels of 1-Octadecanol from 0.0645J/g (HCO/OCT = 1.0/0.0) to 0.908J/g (HCO/OCT = 0.8/0.2), suggesting a possible combined HCO/1-Octadecanol phase. Upon recrystallisation of HCO, the low temperature transition is still present, making it unlikely to be an impurity. At increasing levels of 1-Octadecanol beyond (HCO/OCT = 0.8/0.2), this phase transition disappears. For the simplification, only the crystallisation of HCO and unknown low temperature transition have been mapped out in the phase diagram.

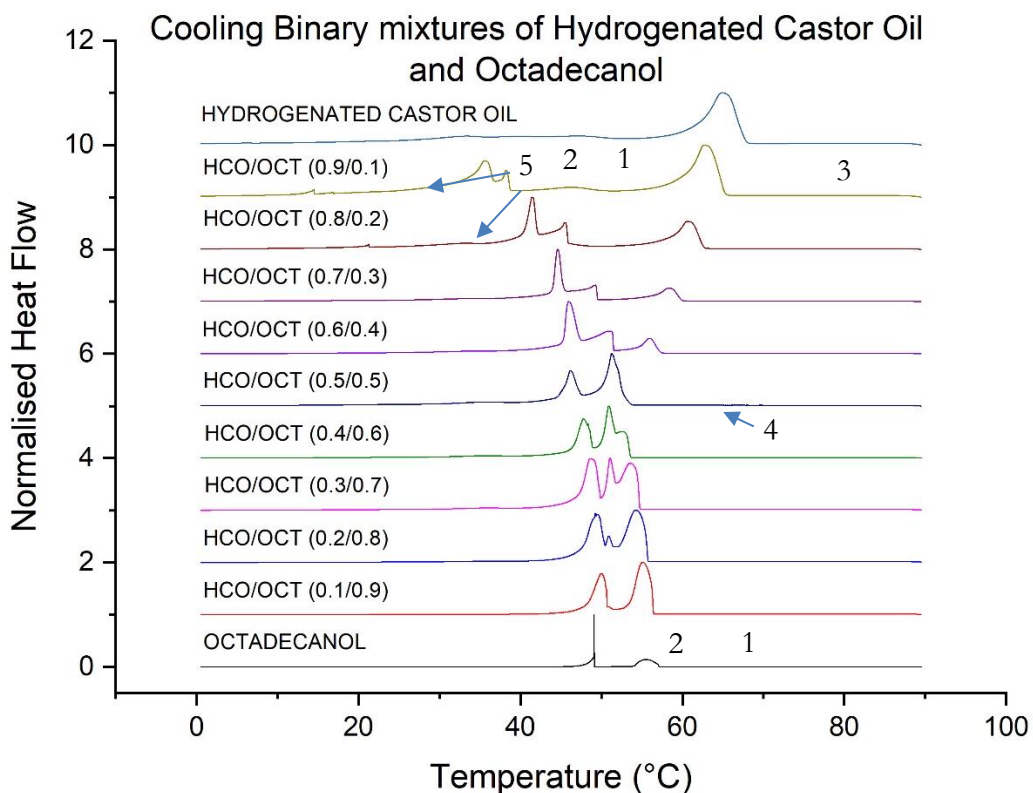


Figure 6-2 Stacked normalised Differential Scanning Calorimetry (DSC) measurements of binary mixtures of 1-Octadecanol and Hydrogenated Castor Oil when cooled from the melt at 1°C/min. 1) 1-Octadecanol rotator phase crystallisation, 2) 1-Octadecanol rotator gamma phase transition, 3) Hydrogenated Castor Oil crystallisation, 4) 1-Octadecanol/Hydrogenated Castor Oil crystallisation and 5) Hydrogenated Castor Oil low temperature transition.

Upon heating the gamma-rotator phase, transition (peak 2) can only be distinguished from the melting of the rotator phase when only 1-Octadecanol (peak 1) is present. Upon increasing addition of HCO, the gamma-rotator-gamma transition/melting peak (peak 3) moves to increasingly lower temperatures from 55.23°C (HCO/OCT = 0.1/0.9) to 46.12°C (HCO/OCT = 0.8/0.2). At very high levels of HCO (HCO/OCT = 0.9/0.1), it becomes difficult to distinguish the 1-Octadecanol phase transitions.

Upon increasing addition of 1-Octadecanol, the melting peak of HCO (peak 4) decreases in temperature from 72.59°C (HCO/OCT = 1.0/0.0) to 63.87°C (HCO/OCT = 0.4/0.6). At compositions of HCO, lower than (HCO/OCT = 0.4/0.6) the HCO melting peak cannot be distinguished.

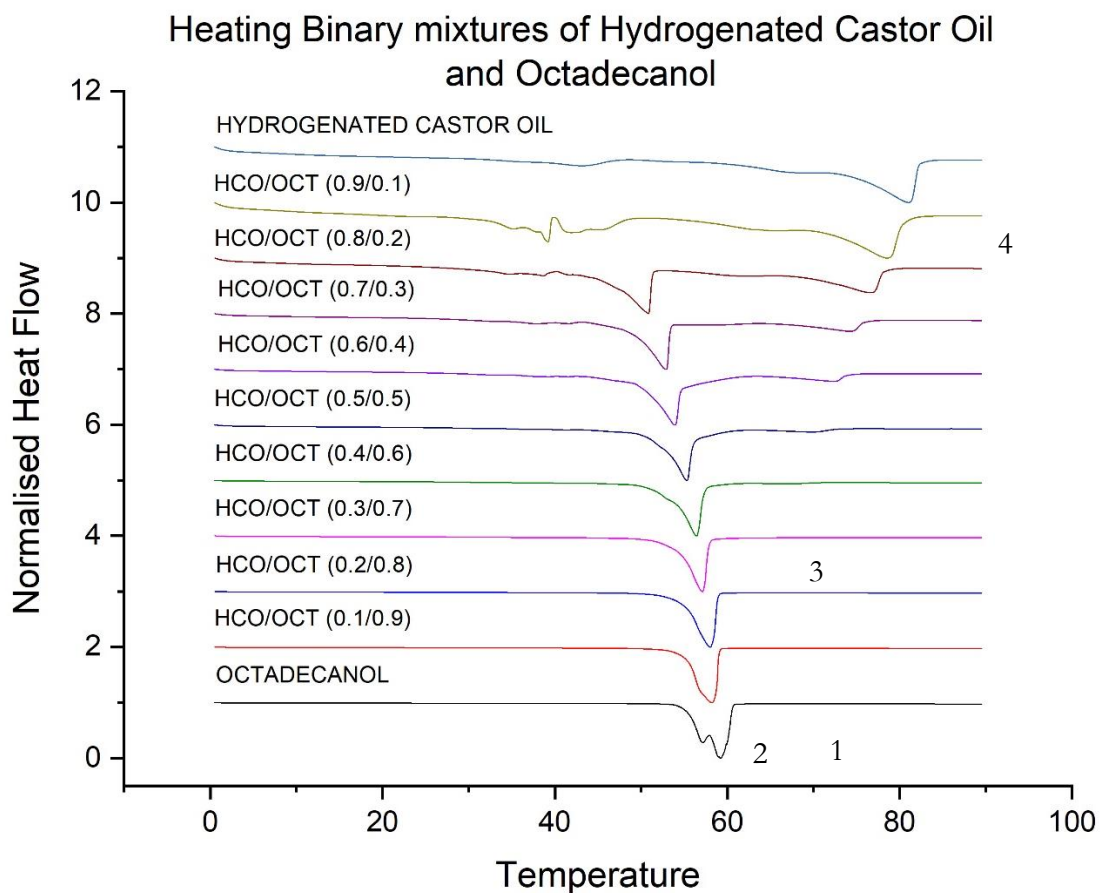


Figure 6-3 Stacked normalised Differential Scanning Calorimetry (DSC) measurements of binary mixtures of 1-Octadecanol and Hydrogenated Castor Oil when heated from 0°C at 1°C/min. 1) 1-Octadecanol rotator phase melting, 2) 1-Octadecanol rotator gamma phase transition, 3) 1-Octadecanol rotator/gamma phase melting and 4) Hydrogenated Castor Oil melting.

Table 6-1 Phase transitions of binary mixtures of Hydrogenated Castor Oil and 1-Octadecanol upon cooling at 1°C/min measured by Differential Scanning Calorimetry (DSC)

Hydrogenated Castor Oil/ -1-Octadecanol (Mole Fraction)	1-Octadecanol Rotator Phase Crystallisation (1)			1-Octadecanol Rotator-Gamma Phase Transition (2)			Hydrogenated Castor Oil Crystallisation (3)			1-Octadecanol / Hydrogenated Castor Oil Crystallisation (4)			Hydrogenated Castor Oil Low Temperature Transition (5)		
	Peak centre (°C)	Peak Onset (°C)	Peak Integral (J/g)	Peak centre (°C)	Peak Onset (°C)	Peak Integral (J/g)	Peak centre (°C)	Peak Onset (°C)	Peak Integral (J/g)	Peak centre (°C)	Peak Onset (°C)	Peak Integral (J/g)	Peak centre (°C)	Peak Onset (°C)	Peak Integral (J/g)
(1.0/0.0) HCO							65.02	67.7	43.84				6.53	6.75	0.0645
(0.9/0.1)	38.27	38.71	26.41	35.65	37.1	26.41	62.86	65.12	36.82				14.5	14.52	0.7974
(0.8/0.2)	45.63	45.89	19.53	41.66	42.15	32.37	60.85	62.56	32.53				21.28	21.28	0.9808
(0.7/0.3)	49.36	49.49	24.92	45.05	45.3	44.08	58.54	59.89	25.99						
(0.6/0.4)	51.23	51.5	42.1	46.43	48.02	60.62	56.04	57.22	23.16						
(0.5/0.5)	51.62	52.78	77.66	46.4	47.59	52.47	51.62	52.78	-	51.62	52.78	77.66			
(0.4/0.6)	52.86	53.51	30.47	48.29	48.97	64.49				51.5	53.52	61.27			
(0.3/0.7)	53.8	54.68	62.28	48.9	49.89	74.17				51.37	52.11	37.62			
(0.2/0.8)	54.69	55.68	91.74	49.64	50.49	79.97				51.09	51.77	16.85			
(0.1/0.9)	55.73	56.39	129.7	50.46	50.77	99.61				50.85	51.6	6.607			
(0.0/1.0) OCT	56.44	57.11	143.5	49.7	49.10	81.17									

Table 6-2 Phase transitions of binary mixtures of Hydrogenated Castor Oil and 1-Octadecanol upon heating at 1°C/min measured by Differential Scanning Calorimetry (DSC)

Hydrogenated Castor Oil/1-Octadecanol (Mole Fraction)	1-Octadecanol Rotator Phase Melting (1)			1-Octadecanol Rotator-Gamma Phase Transition (2)			1-Octadecanol Rotator/Gamma Phase Melting (3)			Hydrogenated Castor Oil Melting (4)		
	Peak centre (°C)	Peak Onset (°C)	Peak Integral (J/g)	Peak centre (°C)	Peak Onset (°C)	Peak Integral (J/g)	Peak centre (°C)	Peak Onset (°C)	Peak Integral (J/g)	Peak centre (°C)	Peak Onset (°C)	Peak Integral (J/g)
(1.0/0.0) HCO										81.05	72.59	51.02
(0.9/0.1)							45.14	-	4.091	78.61	69.56	45.43
(0.8/0.2)							50.75	46.12	28.71	76.65	67.58	35.67
(0.7/0.3)							52.71	49	47.03	74.41	67.11	17.02
(0.6/0.4)							53.66	50.05	79.81	72.51	65.66	12.76
(0.5/0.5)							55.01	52.12	108.2	70.16	64.29	7.426
(0.4/0.6)							55.79	53.3	147.6	67.86	63.87	2.789
(0.3/0.7)							56.5	54.26	173.3			
(0.2/0.8)							57.15	54.88	182.3			
(0.1/0.9)							57.31	55.23	223.6			
(0.0/1.0) OCT	58.27	57.02	141.2	56.48	55.41	93.23						

6.2.2 X-ray Diffraction Patterns of Hydrogenated Castor Oil and 1-Octadecanol.

The crystal structures present within the binary mixtures of HCO and 1-Octadecanol have been captured using XRD in Figure 6-4. It must be noted that the binary mixtures in the X-ray study have been measured at room temperature and prepared from the melt by uncontrolled cooling on the lab bench, whilst being stirred with a magnetic flea. In contrast to the binary mixtures studied using AFM and DSC which had been cooled under static conditions at 1°C/min.

At room temperature 1-Octadecanol is in the gamma phase and the peaks at 5.9Å, 6.9Å, 8.2Å, 10.3Å, 13.6Å and 20.2Å correspond to the 004, 006, 008, 0010, 0012 and 0014 reflections in the diffraction pattern of 1-Octadecanol. Upon addition of HCO at HCO/OCT (0.1/0.9), small peaks develop at 16.5Å and 4.5Å. The peak at 4.5Å most likely is due to the HCO reflection at 4.4Å; however, the identity of the reflection at 16.5Å is less clear. The peak at 16.5Å could be either due to the HCO reflection at 15.4Å or the presence of 1-Octadecanol's rotator phase at 16.5Å, as seen in Figure 4-3 or a combination of both. No other rotator phase peaks can be distinguished, possibly due to the 16.5Å peak having a relatively high intensity in Figure 4-3. Two other major HCO and 1-Octadecanol peaks share similar d-spacing at 2.5Å and 4.0-4.1Å.

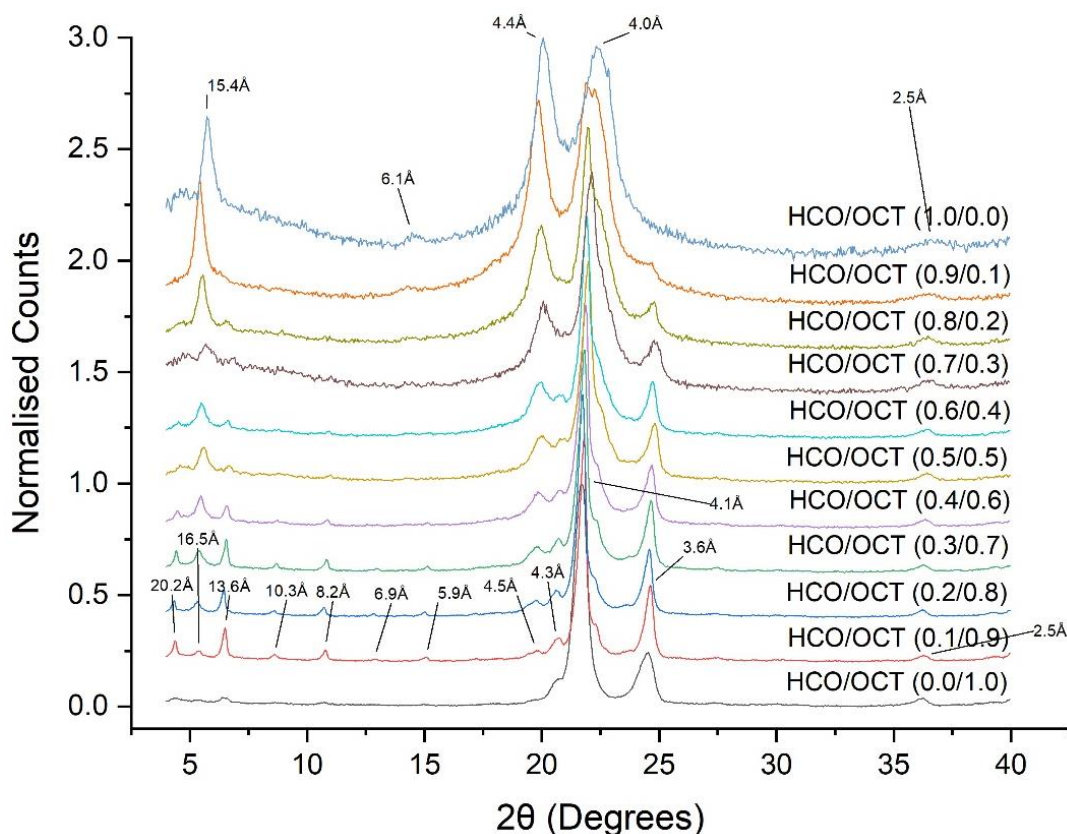


Figure 6-4 Stacked X-ray Diffraction (XRD) patterns of binary mixtures of Hydrogenated Castor Oil and 1-Octadecanol

6.2.3 Binary Phase Diagram of 1-Octadecanol and Hydrogenated Castor Oil

Phase diagram of HCO and 1-Octadecanol created using transition onsets measured using DSC upon cooling at 1°C/min, is displayed in Figure 6-5. The X-ray results suggest the $HCO_{(s)} + Oct_{(\gamma)}$ region of the phase diagram may contain some 1-Octadecanol in the rotator phase.

The phase diagram is annotated with morphology observations from studying each mixture with AFM and optical microscope. The legend at the top of the phase diagram details the composition region where each morphology type exists. There is a large variation in Young's modulus of each morphology measured at different binary mixture compositions. This could be real or due to errors such as calibration and surface roughness.

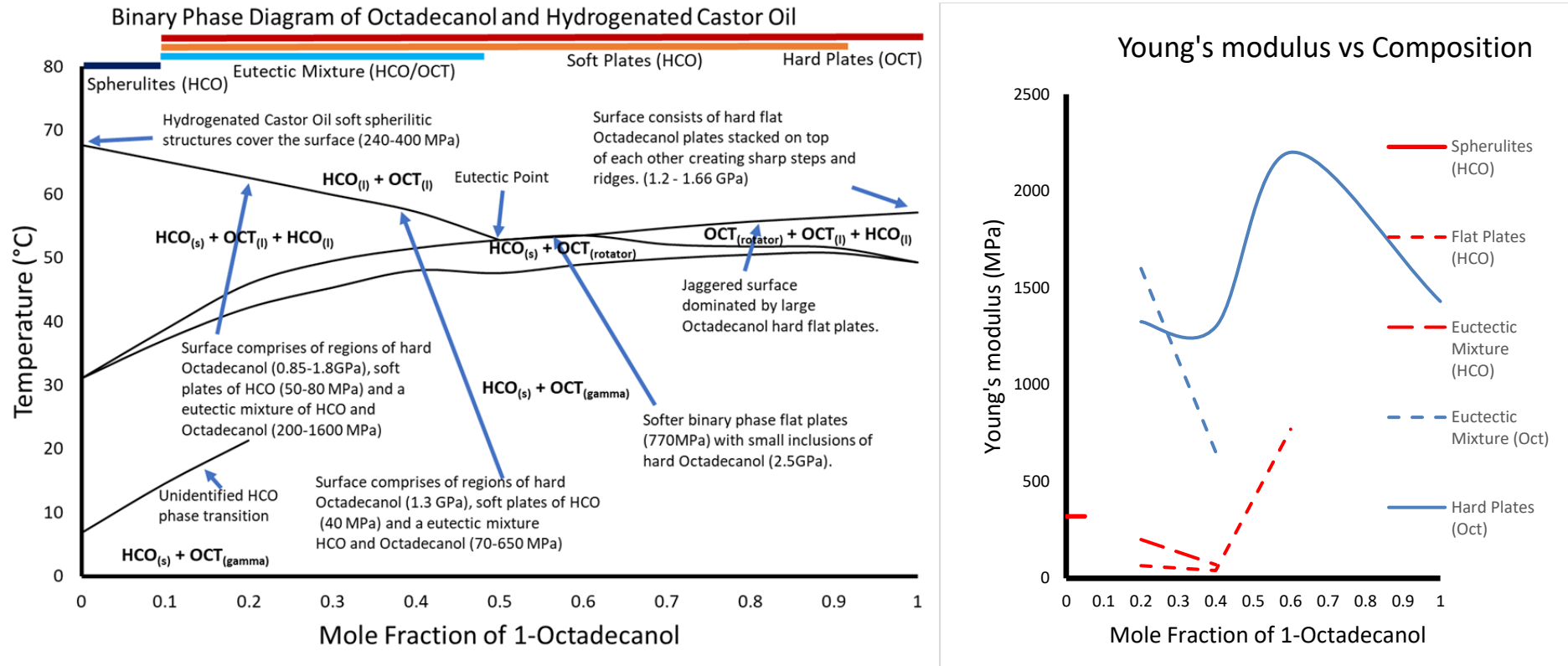


Figure 6-5 Binary phase diagram of Hydrogenated Castor Oil and 1-Octadecanol mixtures produced by plotting the onset of phase transitions measured by Differential Scanning Calorimetry (DSC) upon cooling at 1°C/min (left). Diagram only includes the descriptions of the morphologies observed in each binary mixture with Atomic Force Microscopy (AFM) at room temperature with a legend displayed above the phase diagram. A graph to show measured Young's modulus vs composition (right)

6.2.4 Atomic Force Microscopy of Hydrogenated Castor Oil and 1-Octadecanol Binary Mixture

All AFM samples were measured at room temperature and cooled from the melt under controlled conditions. Binary mixture samples of HCO and 1-Octadecanol were prepared on a glass slide, either under static conditions on a hot-stage microscope at 1°C/min or under shear conditions using a rheometer attached with a cone and plate at 10°C/min.

One tertiary mixture of Petrolatum/HCO/1-Octadecanol was studied using AFM; however, the AFM had not been calibrated, and Young's modulus was not measured across the surface.

When analysing the morphology observed in the optical images and measured using AFM, combined with the mechanical property information for each binary mixture, it is important to consider what was observed for 1-Octadecanol and HCO individually in Chapter 4 and where the binary mixture falls on the phase diagram in Figure 6-5.

6.2.4.1 Cooling Under Static Conditions

The binary phase diagram of HCO and 1-Octadecanol has five distinct morphology regions.

1. 0.0 mole fraction of HCO exhibits only 1-Octadecanol hard plates. (Figure 4-5)
2. 0.0-0.5 mole fraction of HCO exhibits 1-Octadecanol hard plates and HCO soft plates. (Figure 6-6 and Figure 6-7)
3. 0.5 mole fraction of HCO is the eutectic point, and only the eutectic mixture can be observed.
4. 0.5-1.0 mole fraction of HCO 1-Octadecanol hard plates (Figure 6-8, Figure 6-12), HCO soft plates (Figure 6-8, Figure 6-11) and the eutectic mixture are observed (Figure 6-9, Figure 6-10).
5. 1.0 mole fraction of HCO only HCO spherulites are observed. (Figure 4-14)

The AFM results for cooling (HCO/OCT = 0.2/0.8) at 1°C/min under static conditions are displayed in Figure 6-6. The binary mixture contains a high proportion of 1-Octadecanol relative to HCO and as a result, exhibits a surface where hard 1-Octadecanol plates dominate the surface.

Image a) displays a 3D render of a 1-Octadecanol hard flat plate of $\sim 10\mu\text{m}$ in size exiting the surface. The AFM was only able to image a single plate since the surface was too rough to measure a large area with multiple plates. Optical image d) displays the area of the sample where the AFM probe scanned the surface with 1000s of shiny crystalline plates being observable. Image b) displays Young's modulus value measured across the surface; however, the value was found to be too low (51.3 MPa) as a result of the probe becoming blunt, whilst measuring the very rough hard surface. A recalibration was carried out using PS/LDPE before the next sample was measured. Optical image e) displays the edge of the solidified sample droplet on the glass slide.

The surface of the (HCO/OCT = 0.2/0.8) mixture measured was far rougher than pure 1-Octadecanol studied in chapter 4. Perhaps the addition of HCO at this level prevents ordered stacking of the 1-Octadecanol plates in bulk creating a rough surface as 1-Octadecanol plates stack at a range of different angles to the surface

The AFM results for cooling (HCO/OCT = 0.4/0.6) at $1^\circ\text{C}/\text{min}$ under static conditions are displayed in Figure 6-7. Two regions of the surface were studied and, in both regions, HCO and 1-Octadecanol have been identified using the Young's modulus map. Darker regions of the Young's modulus map are softer (HCO) and lighter areas are harder (1-Octadecanol). HCO here has plate morphology, rather than spherulites which were observed when studying pure HCO. This mixture is near to the eutectic point in the phase diagram; however, no eutectic mixture was observed when studying the sample. In the optical image e), the sample area studied appears to slightly less crystalline than (HCO/OCT = 0.2/0.8).

At (HCO/OCT = 0.6/0.4), two areas of the sample were studied. In the 1st region (Figure 6-8), 1-Octadecanol and HCO plates can be seen next to each other using the Young's modulus map. The peak force error helps to observe the topography and the edges of each plate.

The second region (Figure 6-9) displays the eutectic mixture. As HCO crystallises out of solution, the concentration of the melt moves towards the eutectic at (HCO/OCT = 0.5/0.5) and upon further cooling crystallisation occurs at the eutectic point. At the eutectic point, both HCO and 1-Octadecanol crash out of solution creating the eutectic mixture observed in image a). The Young's modulus map in image b) confirms the eutectic mixture contains HCO and 1-Octadecanol; however, some grains do not appear to be made from a single component. Each grain seems to comprise of either solid

clumps of HCO as seen in image f), a clump of material made from multiple grains of HCO held together by 1-Octadecanol as seen in image c) or many small clumps of HCO surrounded by harder 1-Octadecanol as seen in images d) and e). In general, the morphology of HCO appears to be small grains of material between 50-500nm in size with each clump surrounded by 1-Octadecanol. These observations can be explained by the relative solubilities of HCO and 1-Octadecanol. HCO is less soluble in the melt than 1-Octadecanol and crystallises out of solution first as a small grain of material. Upon further cooling 1-Octadecanol crystallises surrounding the small grains of HCO.

Cooling Hydrogenated Castor Oil/1-Octadecanol (0.2/0.8) at 1°C/min

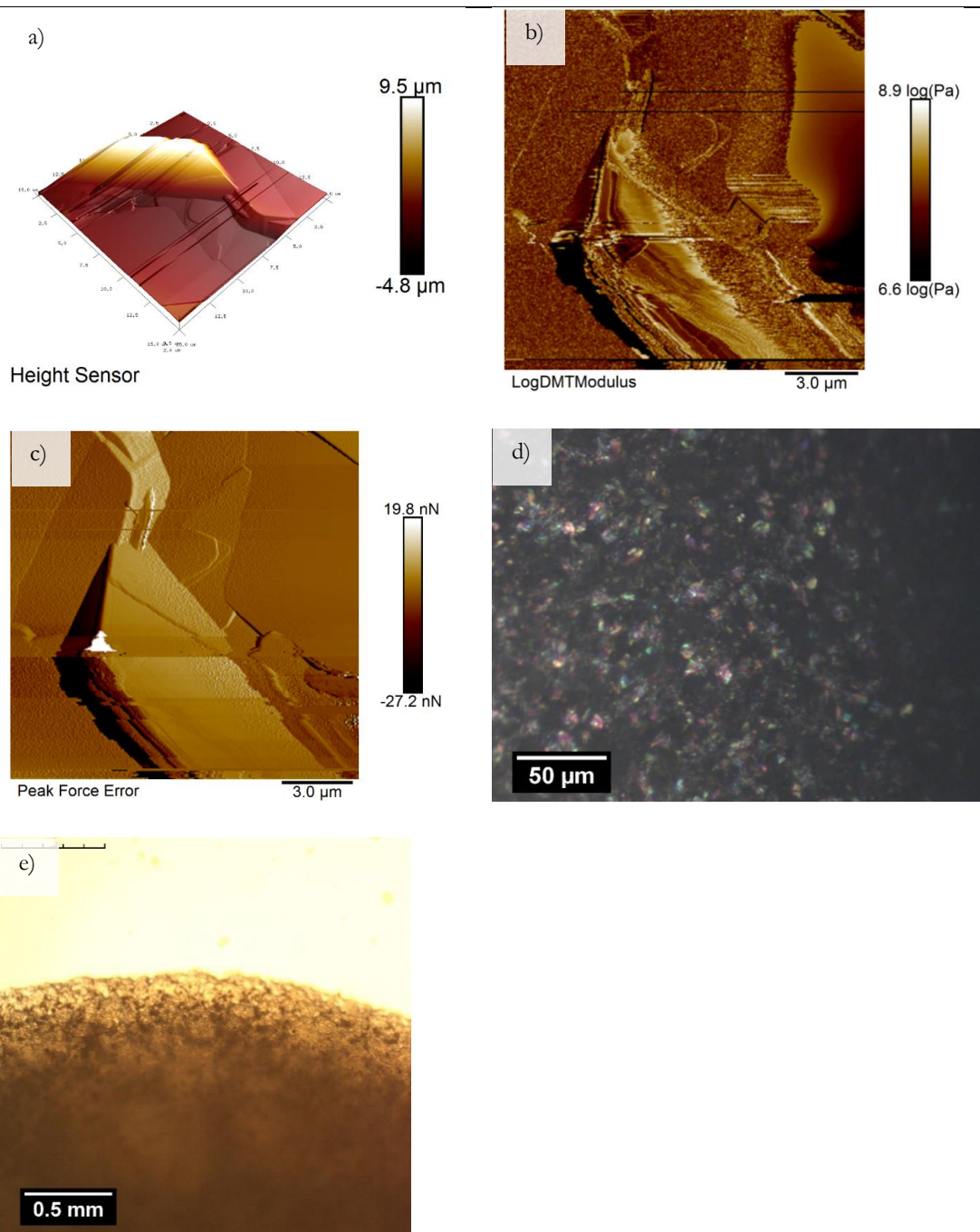
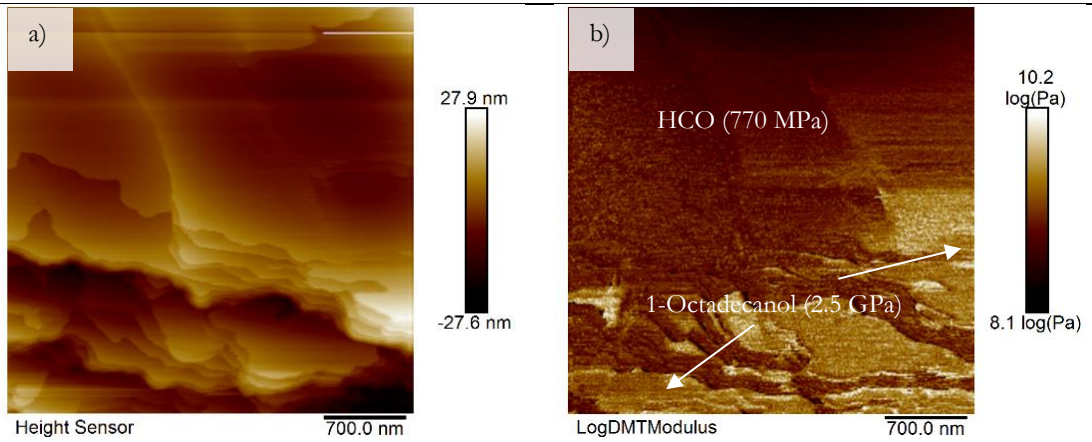


Figure 6-6 Studying Hydrogenated Castor Oil/1-Octadecanol (0.2/0.8) cooled at 1°C/min using Atomic Force (AFM) and Optical (OM) Microscopy. A ridge of hard 1-Octadecanol plate was observed a) is a 3D render of the surface measured (AFM), b) Young's modulus map of the surface (AFM), c) Peak force error displaying topographical information (AFM), d) Optical image of area measured (OM) and e) the edge of the bulk sample (OM).

Cooling Hydrogenated Castor Oil/1-Octadecanol (0.4/0.6) at 1°C/min

1st region – 1-Octadecanol/Hydrogenated Castor Oil Plates



2nd Region – Hydrogenated Castor Oil Plates with small inclusions of 1-Octadecanol

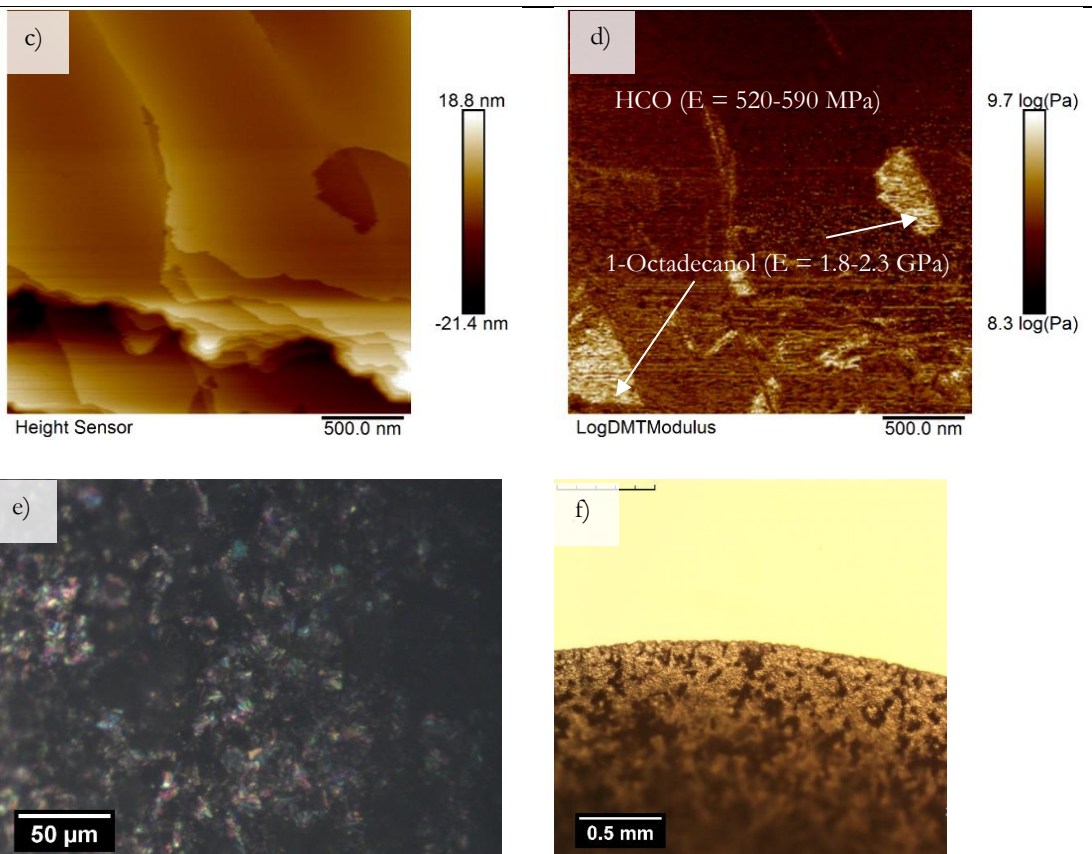


Figure 6-7 Studying Hydrogenated Castor Oil/1-Octadecanol (0.4/0.6) cooled at 1°C/min using Atomic Force (AFM) and Optical (OM) Microscopy. 1st and 2nd region displays adjacent 1-Octadecanol and Hydrogenated Castor Oil plates: a, c) is a height map across the area measured (AFM), b, d) Young's modulus map of the surface (AFM), e) Optical image of area measured (OM) and f) the edge of the bulk sample (OM).

Cooling Hydrogenated Castor Oil/1-Octadecanol (0.6/0.4) at 1°C/min

1st Region 1-Octadecanol/Hydrogenated Castor Oil Plates

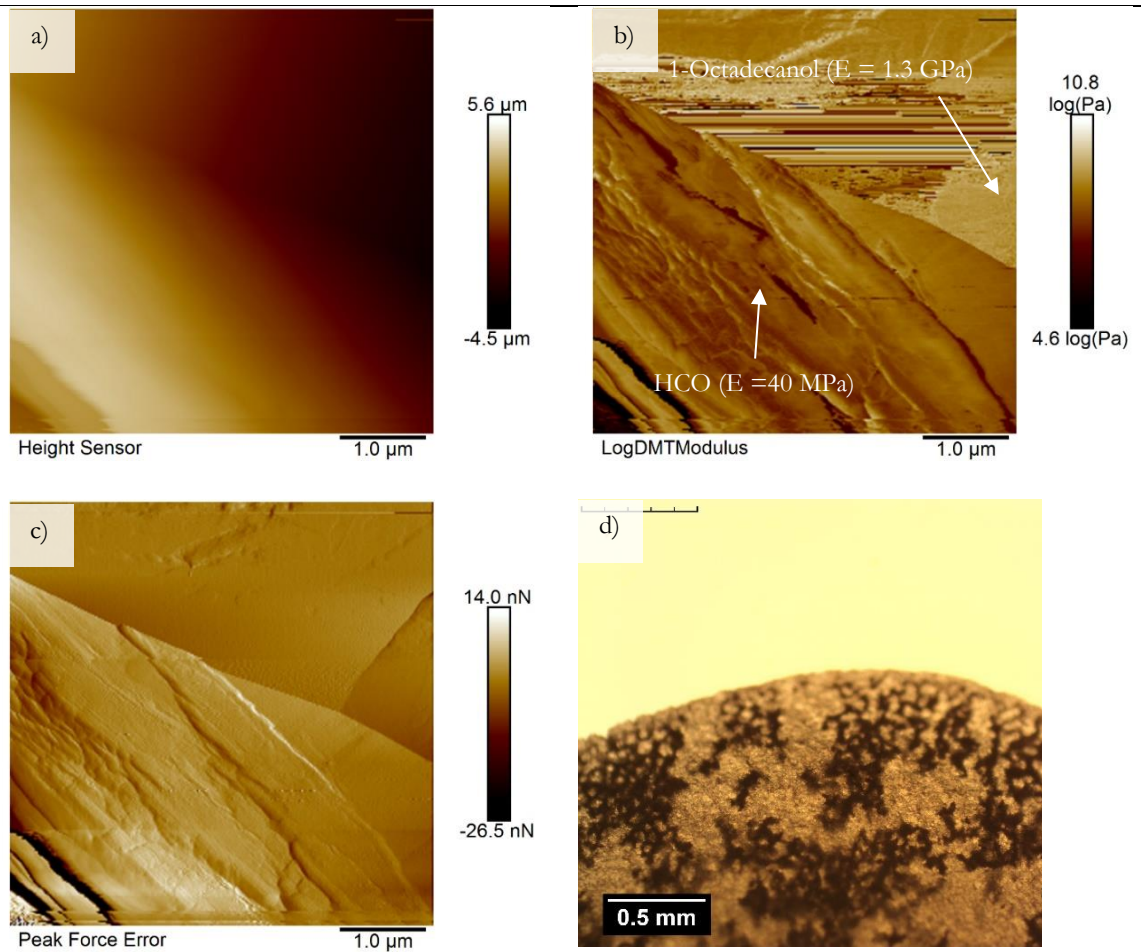


Figure 6-8 Studying Hydrogenated Castor Oil/1-Octadecanol (0.6/0.4) cooled at 1°C/min using Atomic Force (AFM) and Optical (OM) Microscopy. 1st region displays adjacent 1-Octadecanol and Hydrogenated Castor Oil plates; a) is a height map across the area measured (AFM), b) Young's modulus map of the surface (AFM), c) is a map of the peak force error (AFM) and d) the edge of the bulk sample (OM).

2nd Region – Eutectic Mixture

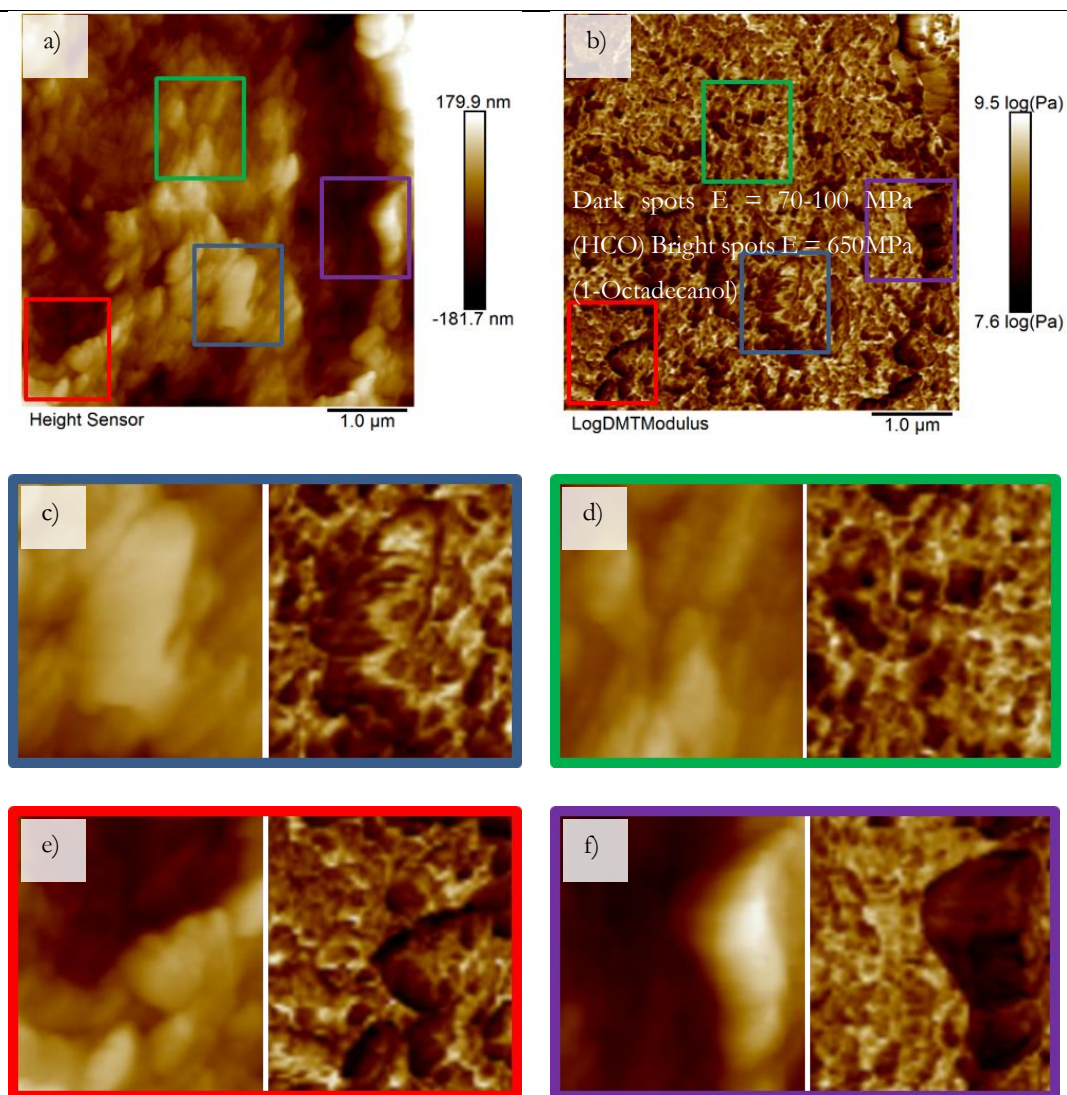


Figure 6-9 Studying Hydrogenated Castor Oil/1-Octadecanol (0.6/0.4) cooled at 1°C/min using Atomic Force (AFM) and Optical (OM) Microscopy. 2nd region displays a eutectic mixture between 1-Octadecanol and Hydrogenated Castor Oil; a) is a height map across the area measured (AFM) and b) is Young's modulus map of the surface (AFM), c, d, e and f) displays enlarged areas of the height and Young's modulus maps..

The AFM results for cooling (HCO/OCT = 0.8/0.2) at 1°C/min under static conditions reveal three different regions of the surface, eutectic mixture (Figure 6-10), 1-Octadecanol plates (Figure 6-12) and HCO plates (Figure 6-11). The 1st region studied is the eutectic mixture, displaying small grains of HCO surrounded by 1-Octadecanol that had crashed out of solution when the eutectic point was reached. This area imaged appears to have been scratched with straight grooves travelling across the sample and is visible in both the optical and AFM images. The areas with the eutectic mixture appear to amorphous and non-crystalline when looking at optical image d). The eutectic mixture in (HCO/OCT = 0.8/0.2) appears to contain darker areas relative to lighter areas than

(HCO/OCT = 0.6/0.2), suggesting the eutectic mixture contains a higher concentration of HCO.

The second region studied contains HCO flat plates and has a clear difference in morphology to the 1-Octadecanol plates studied in the third region. HCO plates appear very flat with defined edges, and 1-Octadecanol plates appear rounded with a rough surface. The optical images show the area studied with 1-Octadecanol appears more crystalline than the area of the surface containing HCO. Image e) in Figure 6-12, shows a low magnification image of the bulk where it is clear there are opaque and clear regions of the bulk. The clear region most likely contains the eutectic mixture and HCO plates, whilst the opaque area contains more 1-Octadecanol and HCO crystals.

Cooling Hydrogenated Castor Oil/1-Octadecanol (0.8/0.2) at 1°C/min

1st Region – Eutectic Mixture

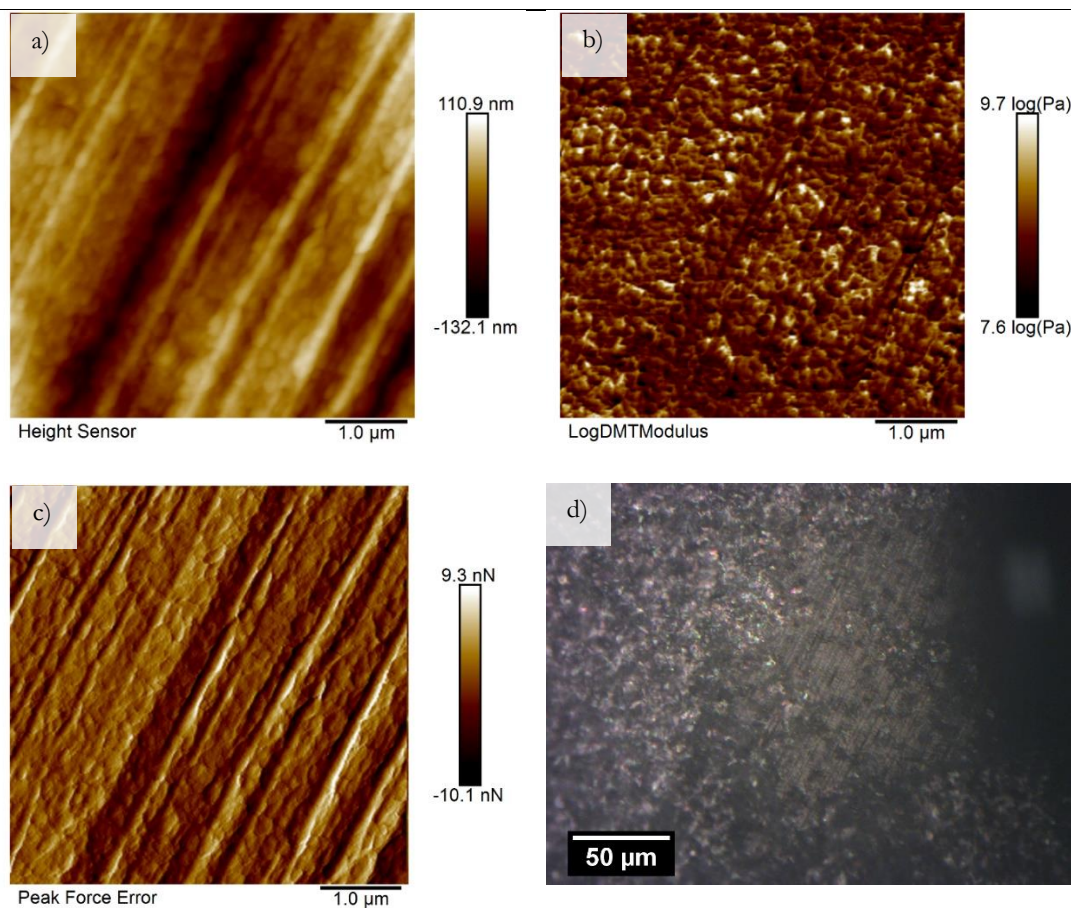


Figure 6-10 Studying Hydrogenated Castor Oil/1-Octadecanol (0.8/0.2) cooled at 1°C/min using Atomic Force (AFM) and Optical (OM) Microscopy. The region observed is a eutectic mixture between Hydrogenated Castor Oil and 1-Octadecanol; a) is a height map across the area measured (AFM), b) Young's modulus map of the surface (AFM), c) Peak force error displaying topographical information (AFM) and d) Optical image of the area of the sample measured (OM).

2nd Region – HCO Flat Plates

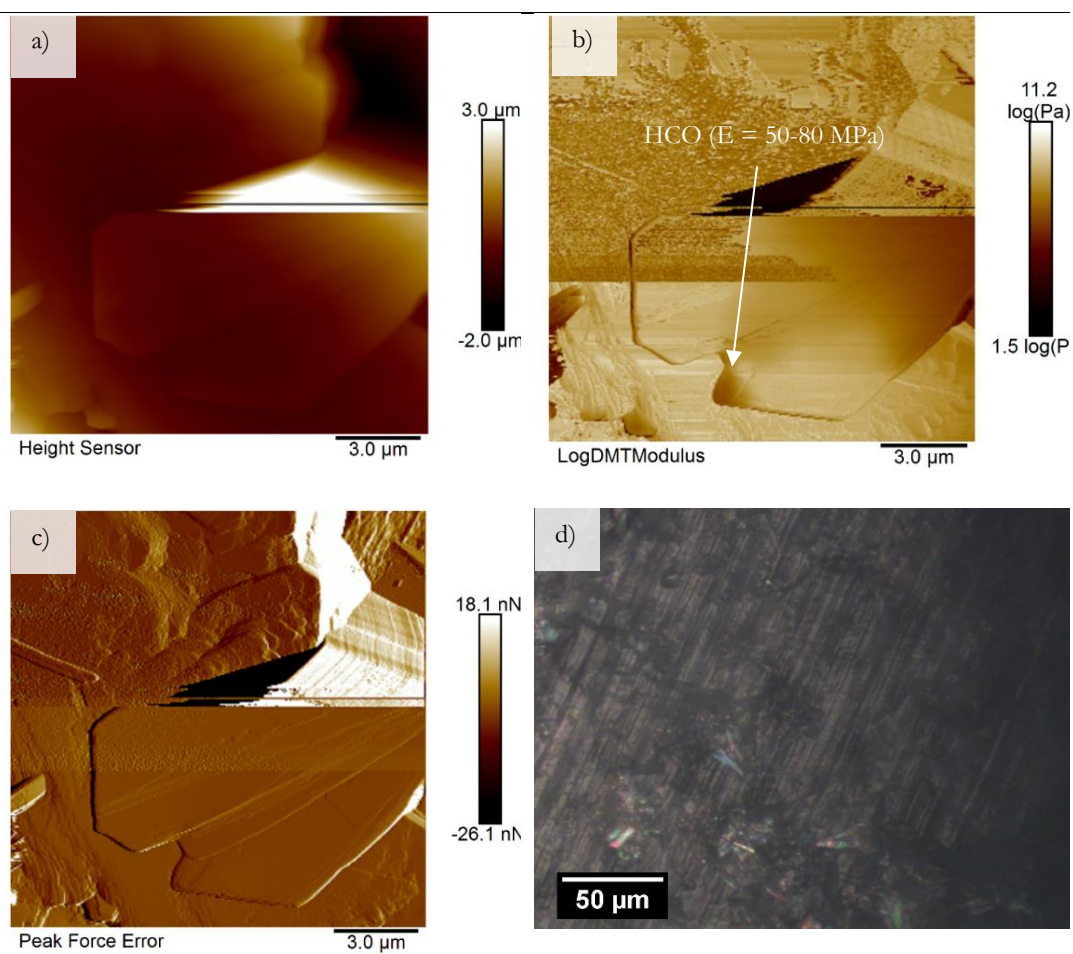


Figure 6-11 Studying Hydrogenated Castor Oil/1-Octadecanol (0.8/0.2) at 1°C/min using Atomic Force (AFM) and Optical (OM) Microscopy. The region displays soft HCO flat plates; a) is a height map across the area measured (AFM), b) Young's modulus map of the surface (AFM), c) Peak force error displaying topographical information (AFM) and d) Optical image of the area of the sample measured (OM).

3rd Region – 1-Octadecanol Plates

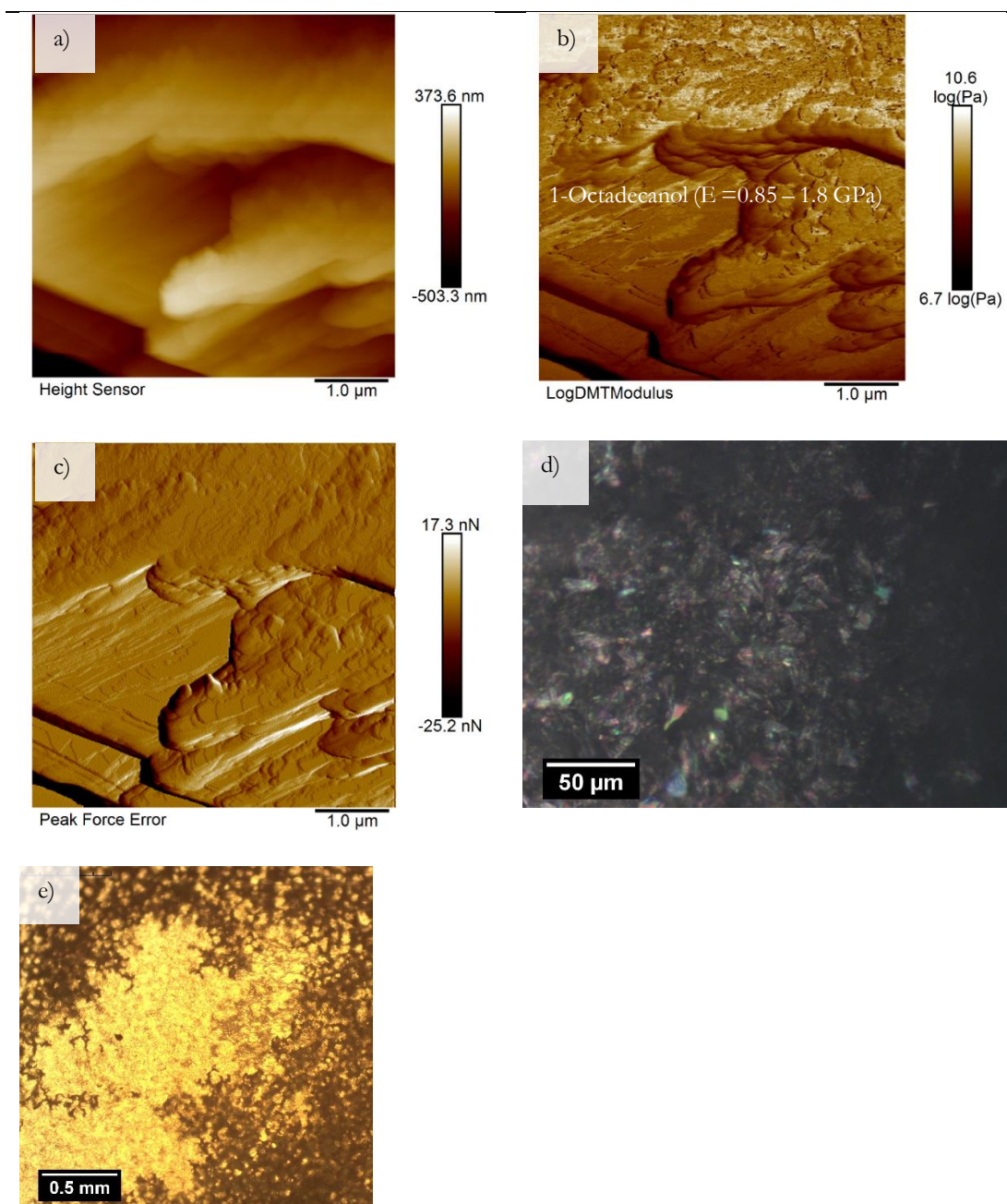


Figure 6-12 Studying Hydrogenated Castor Oil/1-Octadecanol (0.8/0.2) at cooled 1°C/min using Atomic Force (AFM) and Optical (OM) Microscopy. The region displays hard 1-Octadecanol plates; a) is a height map across the area measured (AFM), b) Young's modulus map of the surface (AFM), c) Peak force error displaying topographical information (AFM), d) Optical image of the area of the sample measured (OM) and e) the bulk sample (OM).

A tertiary mixture of HCO and 1-Octadecanol combined with a small proportion of Petrolatum shown in Figure 6-13. The AFM wasn't calibrated prior to the measurement, so no meaningful Young's modulus data could be extracted. Images a) and b) display height maps of two different regions of the surface at two different scales. The images show a network of plate crystals on the surface; however, the composition of the plates cannot be identified. Optical image d) displays the bulk sample with the structures

created at a far smaller scale and appearing more homogeneous compared to image e) in Figure 6-12. The smaller crystals created will be due to the fast cooling rate and the Petrolatum might help to make the mixture more homogenous through acting as a solvent. Turbidity studies have shown that 1-Octadecanol is more soluble in alkanes than HCO, resulting in the eutectic point shifting to higher concentrations of 1-Octadecanol.

Cooling Hydrogenated Castor Oil/1-Octadecanol/Petrolatum (0.8/0.2/0.01) at 20°C/min

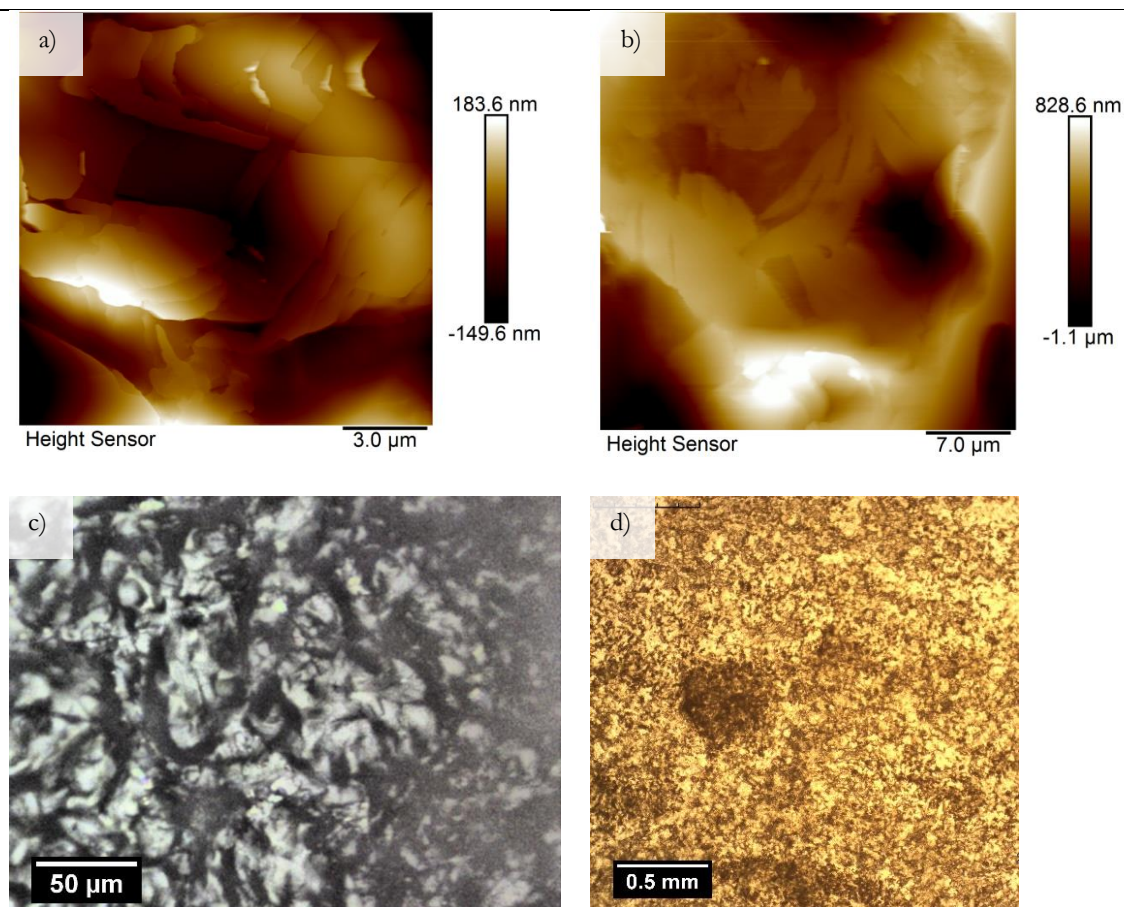


Figure 6-13 Studying Hydrogenated Castor Oil/1-Octadecanol/Petrolatum (0.8/0.2/0.01) cooled at 20°C/min using Atomic Force (AFM) and Optical (OM) Microscopy; a) is a height map across the area measured (AFM), b) c) Optical image of the area of the sample measured (OM) and d) the bulk sample (OM).

6.2.4.2 Cooling Under Shear Conditions

To investigate the impact of shear a sample at 200s⁻¹ containing (HCO/OCT = 0.8/0.2) is displayed in Figure 6-14. The sheared sample was cooled at 10°C/min rather than 1°C/min for the static sample. This makes it harder to compare the static system with the sheared system, as two variables have been changed. However, the impact cooling rate has been studied on HCO and 1-Octadecanol individually, so the impact of an increase in cooling rate is known. Essentially higher cooling rates cause smaller crystals

to be formed as can be seen when comparing image e) in Figure 6-12 to image e) in Figure 6-14. Shearing of the system appears have mixed all the 1-Octadecanol and HCO crystals together so different composition crystals can be seen side by side in one image. This contrasts with the static sample where each crystal type was separated and in a different region of the surface. The optical images d) confirms this by displaying what appears to be a homogenous mixture.

Cooling Hydrogenated Castor Oil/1-Octadecanol (0.8/0.2) at 10°C/min under shear at 200s⁻¹

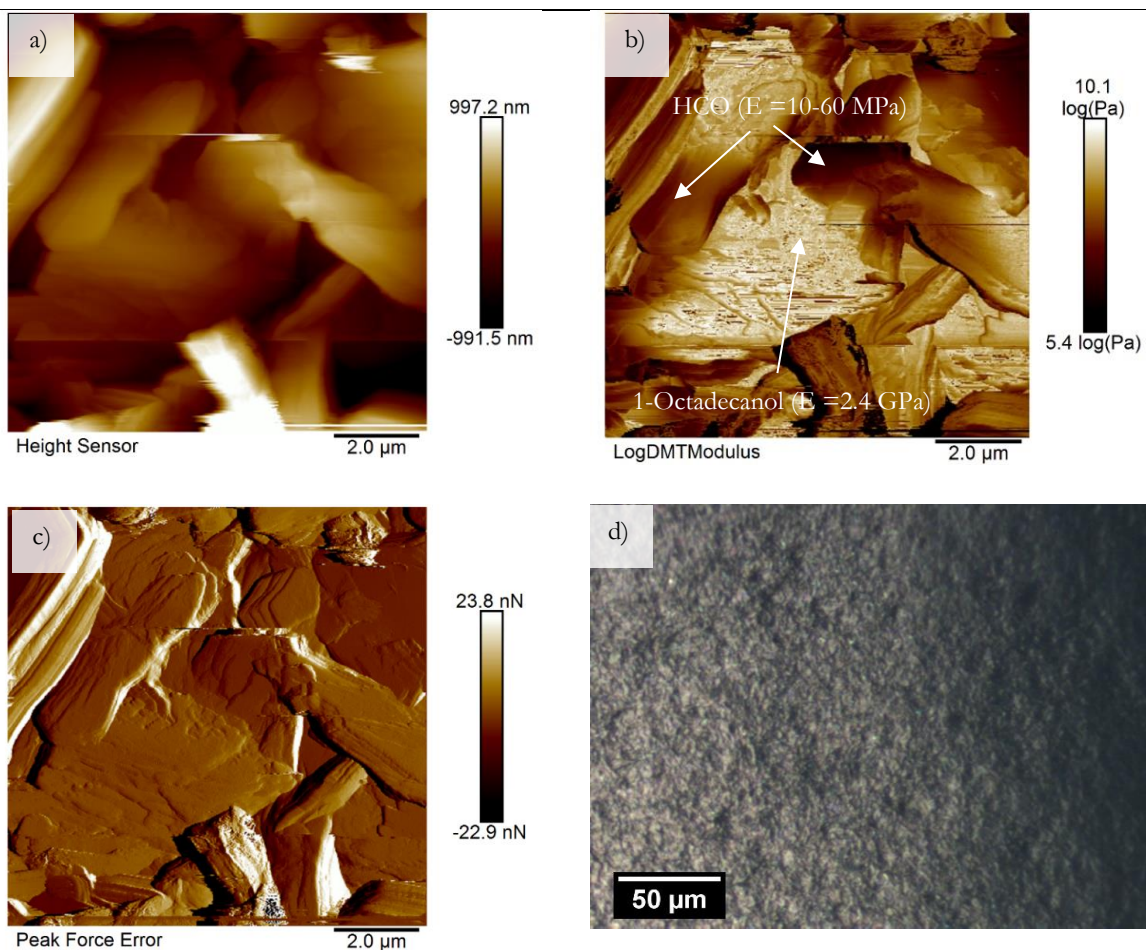


Figure 6-14 Studying Hydrogenated Castor Oil/1-Octadecanol (0.8/0.2) cooled at 10°C/min under shear at 200s⁻¹ using Atomic Force (AFM) and Optical (OM) Microscopy; a) is a height map across the area measured (AFM), b) Young's modulus map of the surface (AFM) c) Optical image of the area of the sample measured (OM) and d) the bulk sample (OM).

6.3 1-Octadecanol and Alkanes

6.3.1 Thermal Analysis of 1-Octadecanol and Dodecane Binary Mixtures

Petrolatum is a complex mixture of straight chain alkanes with chain lengths between 18-47 and Dodecane has a chain length of 12. For simplification, the 1-Octadecanol/n-

alkane synchrotron shear experiments in Chapter 7 were completed using Dodecane as a model for Petrolatum. Turbidity experiments in Chapter 5 demonstrate there was no difference in crystallisation and dissolution behaviour between odd and even parity chain lengths of n-alkanes. For analysis and understanding, thermal transitions between binary mixtures of 1-Octadecanol and Dodecane have been recorded using DSC. Studying 1-Octadecanol in both Petrolatum and Dodecane gives insight to the impact to varying chain length and mixtures on the phase diagram.

The thermal transitions upon cooling binary mixtures of 1-Octadecanol and Dodecane were measured using DSC and shown in Figure 6-15. Peak 1 displays the crystallisation of 1-Octadecanol's rotator phase and Peak 2 displays the thermal transition from 1-Octadecanol's rotator to the stable gamma phase. When increasing the level of Dodecane to DOD/OCT (0.1/0.9) crystallisation of the rotator phase occurs at a lower temperature, and the rotator to gamma phase transition occurs at a higher temperature. At DOD/OCT (0.1/0.9) there is an additional small initial crystallisation peak occurring at the same temperature as the crystallisation of the rotator phase of pure 1-Octadecanol and must be due to phase separation between 1-Octadecanol and Dodecane. Upon further increasing the concentration of Dodecane the rotator crystallisation and rotator-gamma phase transition move to lower temperatures and by DOD/OCT (0.3/0.7) the peaks converge. Increasing concentration beyond DOD/OCT (0.4/0.6) the single peak moves to lower temperatures.

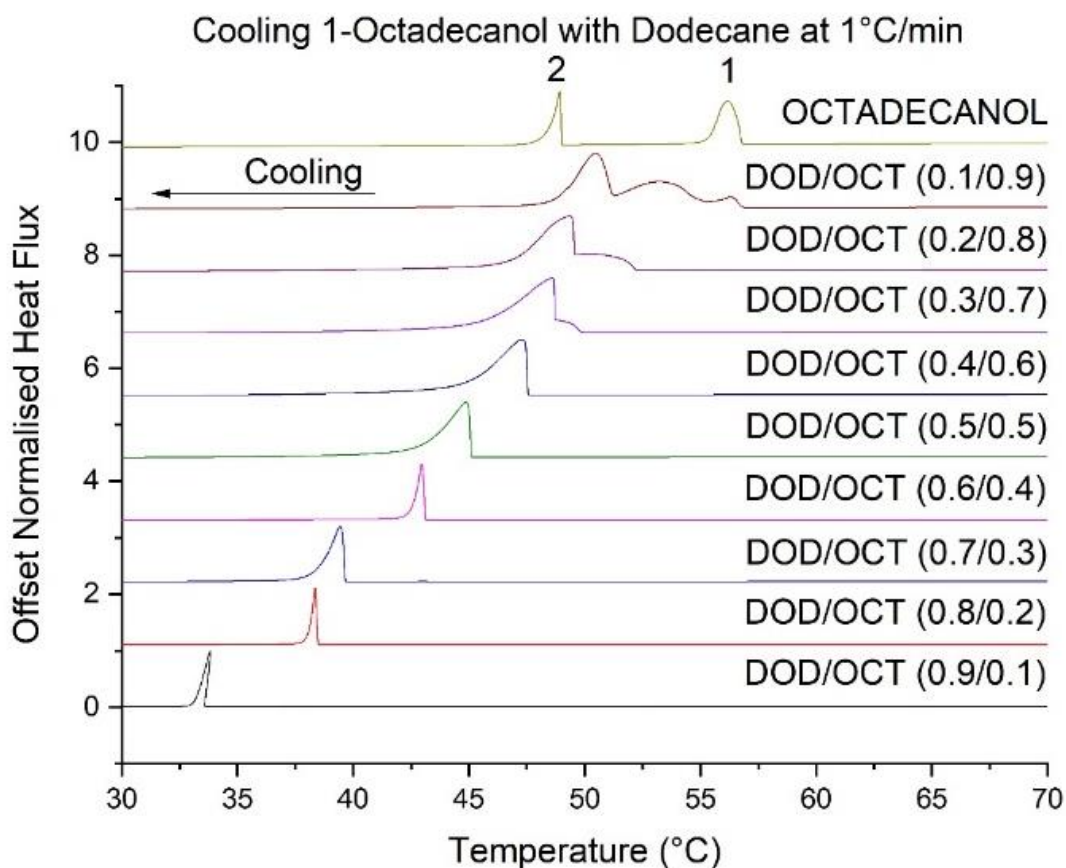


Figure 6-15 Stacked normalised Differential Scanning Calorimetry (DSC) measurements of binary mixtures of 1-Octadecanol and Dodecane when cooled from the melt at 1°C/min.

The phase diagram of 1-Octadecanol and Dodecane is shown in Figure 6-16. 1-Octadecanol's rotator phase is only present at low concentrations of Dodecane below DOD/OCT (0.4/0.6) at a temperature between the crystallisation of the rotator phase and rotator-gamma transition temperature. Below the rotator-gamma transition temperature, only the gamma phase of 1-Octadecanol is present. Dodecane is in the liquid phase throughout the temperature range studied using DSC, since it is known to have a melting point of -9.6°C and a boiling point of 216.3°C.

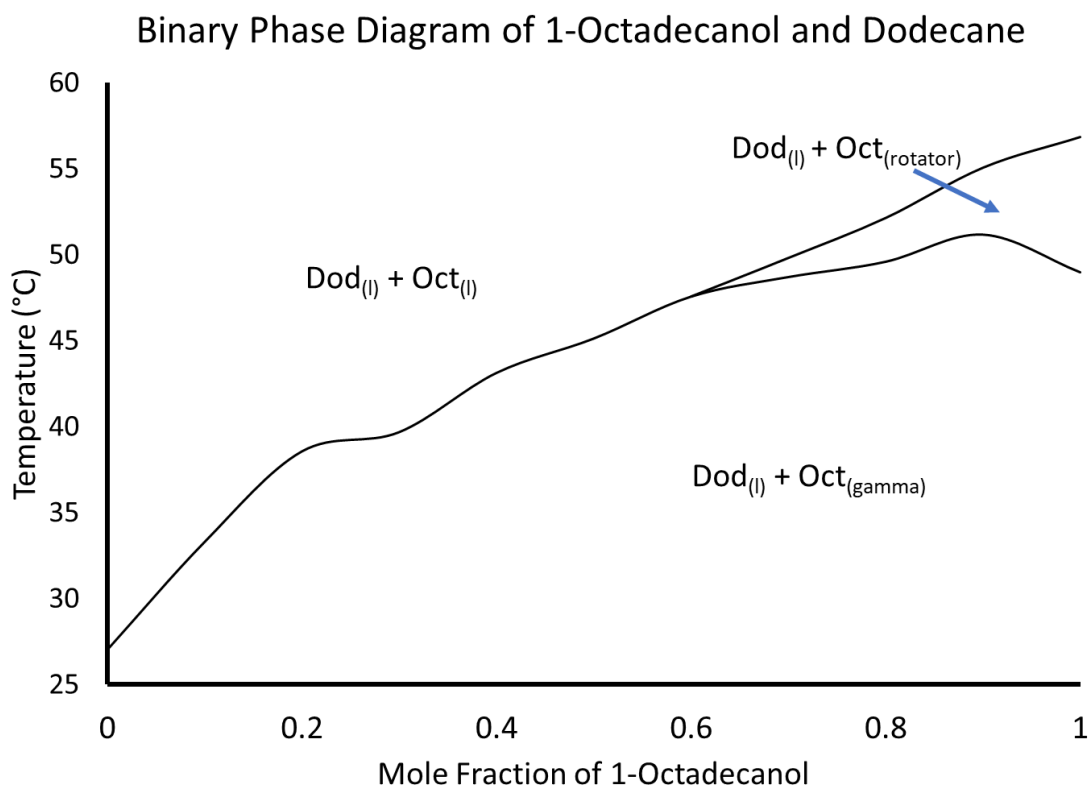


Figure 6-16 Binary phase diagram of Dodecane and 1-Octadecanol mixtures produced by plotting the onset of phase transitions measured by Differential Scanning Calorimetry (DSC) upon cooling at 1°C/min.

6.3.2 Thermal Analysis of 1-Octadecanol and Petrolatum Binary Mixtures

Thermal transitions of Petrolatum and 1-Octadecanol binary mixtures have been measured using DSC, upon heating and cooling at 1°C/min between 0°C and 90°C. Cooling of the binary mixtures is displayed in Figure 6-17, the heating is displayed in Figure 6-18, and the tabulated phase transitions are recorded in Table 6-3. It must be noted that Figure 6-17 contains peaks with abnormal shapes, caused by exothermic events raising the temperature of the DSC oven, during the cooling cycle. The peak shape may affect the accuracy of the measured peak integral data presented in Table 6-3.

Upon cooling, 1-Octadecanol crystallises in the metastable rotator phase (peak 1) before converting into the stable gamma phase (peak 2). Upon a small addition of Petrolatum PET/OCT (0.1/0.9), the temperature of the rotator-gamma phase transition increases in temperature and crystallisation of the rotator phase decreases in temperature. With the further addition of Petrolatum, the rotator phase crystallisation and rotator to gamma phase transitions move to lower temperatures whilst converging to form a single peak by PET/OCT (0.9/0.1).

Petrolatum displays a single broad crystallisation peak upon cooling since its wide range of chain lengths have very different crystallisation temperatures. Upon small additions of 1-Octadecanol, a low energy melting peak can be observed (peak 3).

Upon heating 1-Octadecanol, the rotator-gamma phase transition appears as a defined shoulder on the 1-Octadecanol melting peak. As Petrolatum is increasing added the rotator-gamma phase becomes less defined, and by PET/OCT (0.2/0.8) the shoulder cannot be seen.

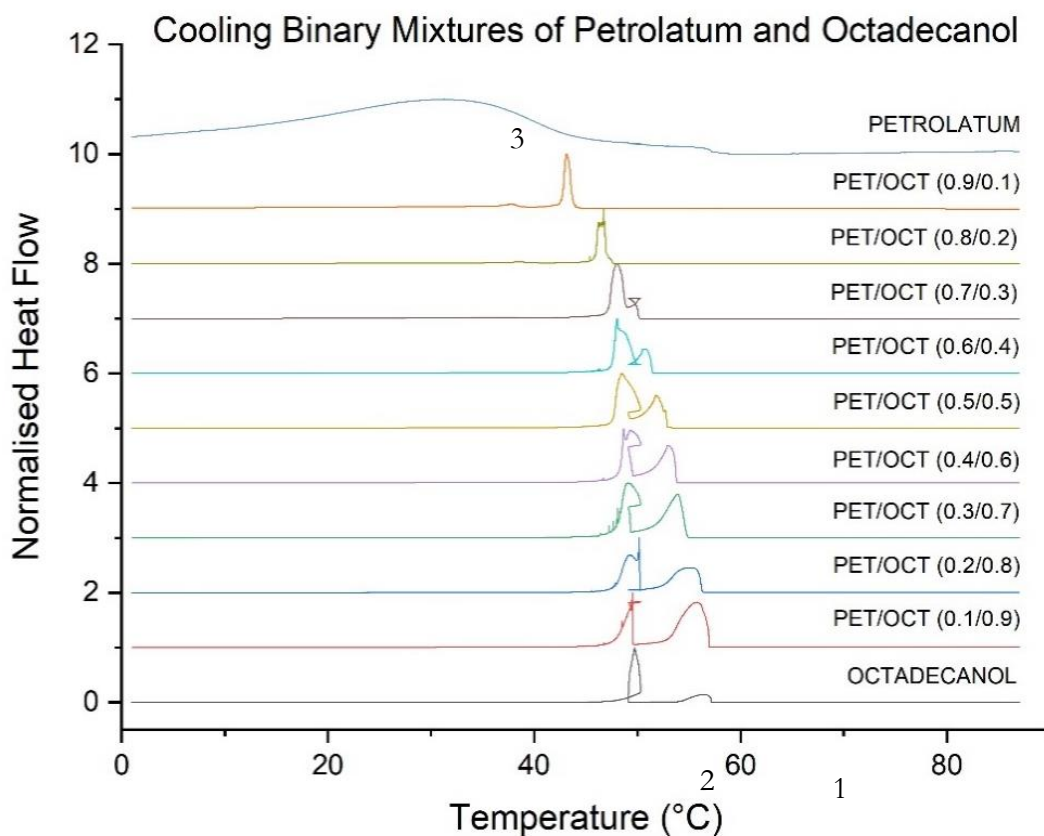


Figure 6-17 Stacked normalised Differential Scanning Calorimetry (DSC) measurements of binary mixtures of 1-Octadecanol and Petrolatum when cooled from the melt at 1°C/min. 1) 1-Octadecanol rotator phase crystallisation, 2) 1-Octadecanol rotator-gamma phase transition and 3) Petrolatum crystallisation.

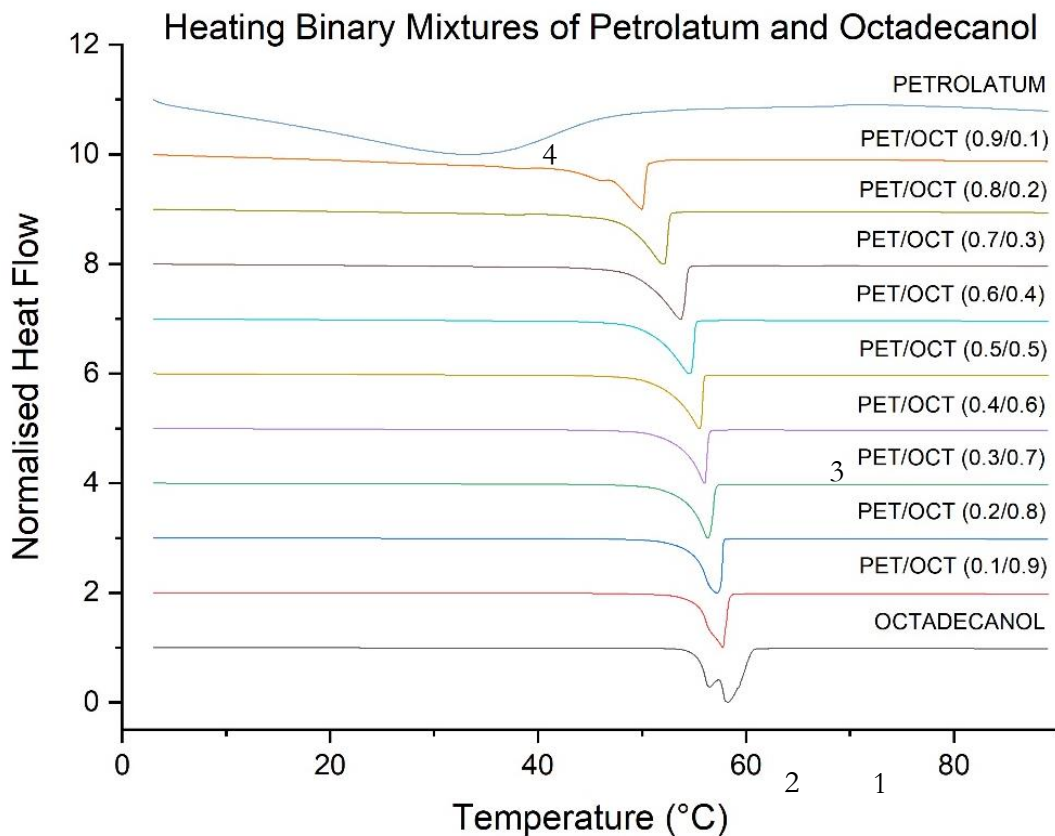


Figure 6-18 Stacked normalised Differential Scanning Calorimetry (DSC) measurements of binary mixtures of 1-Octadecanol and Petrolatum when cooled from the melt at 1°C/min. 1) 1-Octadecanol rotator phase melting, 2) 1-Octadecanol rotator-gamma phase transition, 3) 1-Octadecanol Rotator/Gamma Phase Melting and 4) Petrolatum melting.

Table 6-3 Phase transitions of binary mixtures of Petrolatum and 1-Octadecanol upon cooling at 1°C/min measured by Differential Scanning Calorimetry (DSC)

Petrolatum/1-Octadecanol (Mole Fraction)	1-Octadecanol Rotator Phase Crystallisation (1)			1-Octadecanol Rotator-Gamma Phase Transition (2)			Petrolatum Crystallisation (3)		
	Peak centre (°C)	Peak Onset (°C)	Peak Integral (J/g)	Peak centre (°C)	Peak Onset (°C)	Peak Integral (J/g)	Peak centre (°C)	Peak Onset (°C)	Peak Integral (J/g)
(1.0/0.0) PET							32.73	46.58	24.36
(0.9/0.1)				43.52	43.64	28.3	37.77	38.67	2.908
(0.8/0.2)				47.19	47.43	54.47	38.59	40.18	3.174
(0.7/0.3)	50.1	49.36	27.32	48.45	48.53	62.07	36.52	39.37	1.893
(0.6/0.4)	51.08	51.39	47.43	48.87	48.44	70.56	35.88	39.13	1.154
(0.5/0.5)	52.16	52.85	77.53	48.75	49.44	69.21	36.26	39.18	0.5027
(0.4/0.6)	53.39	53.71	83.34	48.8	49.74	88.94	38.97	38.97	0.5863
(0.3/0.7)	54.27	54.3	78.29	49.06	49.44	99.91			
(0.2/0.8)	55.03	55.35	140	49.24	49.06	92.22			
(0.1/0.9)	55.57	56.25	128.8	49.66	49.59	82.96			
(0.0/1.0) OCT	56.44	57.11	143.5	49.7	49.10	81.17			

Table 6-4 Phase transitions of binary mixtures of Petrolatum and 1-Octadecanol upon heating at 1°C/min measured by Differential Scanning Calorimetry (DSC)

Hydrogenated Castor Oil/1- Octadecanol (Mole Fraction)	1-Octadecanol Rotator Phase Melting (1)			1-Octadecanol Rotator-Gamma Phase Transition (2)			1-Octadecanol Rotator/Gamma Phase Melting (3)			Petrolatum Melting (4)		
	Peak centre (°C)	Peak Onset (°C)	Peak Integral (J/g)	Peak centre (°C)	Peak Onset (°C)	Peak Integral (J/g)	Peak centre (°C)	Peak Onset (°C)	Peak Integral (J/g)	Peak centre (°C)	Peak Onset (°C)	Peak Integral (J/g)
(1.0/0.0) HCO										33.95	10.4	22.65
(0.9/0.1)				49.92	45.86	24.56				38.43	34.74	2.22
(0.8/0.2)				51.95	48.4	48.57						
(0.7/0.3)				53.45	49.76	81.03						
(0.6/0.4)				54.26	50.73	110.9						
(0.5/0.5)				55.22	52.18	141.6						
(0.4/0.6)				55.83	53.29	166.9						
(0.3/0.7)				56.37	53.59	171						
(0.2/0.8)				56.94	54.5	226.6						
(0.1/0.9)				57.61	55.22	206.4						
(0.0/1.0) OCT	58.27	57.02	141.2				56.48	55.41	93.23			

6.3.3 XRD patterns of 1-Octadecanol and Petrolatum binary mixtures

The stacked normalised X-ray diffraction patterns of 1-Octadecanol and Petrolatum binary mixtures are displayed in Figure 6-19. The binary mixtures were prepared by uncontrolled cooling from the melt whilst stirring. At room temperature 1-Octadecanol is in the gamma phase as seen by the characterised by the d-spacings at 20.6, 13.7, 10.3, 8.3, 6.9 and 5.9Å corresponding to lattice planes 004, 006, 008, 0010, 0012 and 0014. As the level of Petrolatum increases the intensity of the main 1-Octadecanol peak at 4.1Å decreases relative to the low angle peaks. The peak at 16.5Å increases in relative intensity as increasing Petrolatum is added, suggesting a possible rotator phase present at PET/OCT (0.9/0.1). This peak was also observed in the X-ray diffraction pattern of HCO/OCT, making it more likely to 1-Octadecanol phase. At PET/OCT (0.9/0.1) a double peak was observed at 4.1Å, most likely due to the 1-Octadecanol and Petrolatum peak at 4.1Å combining.

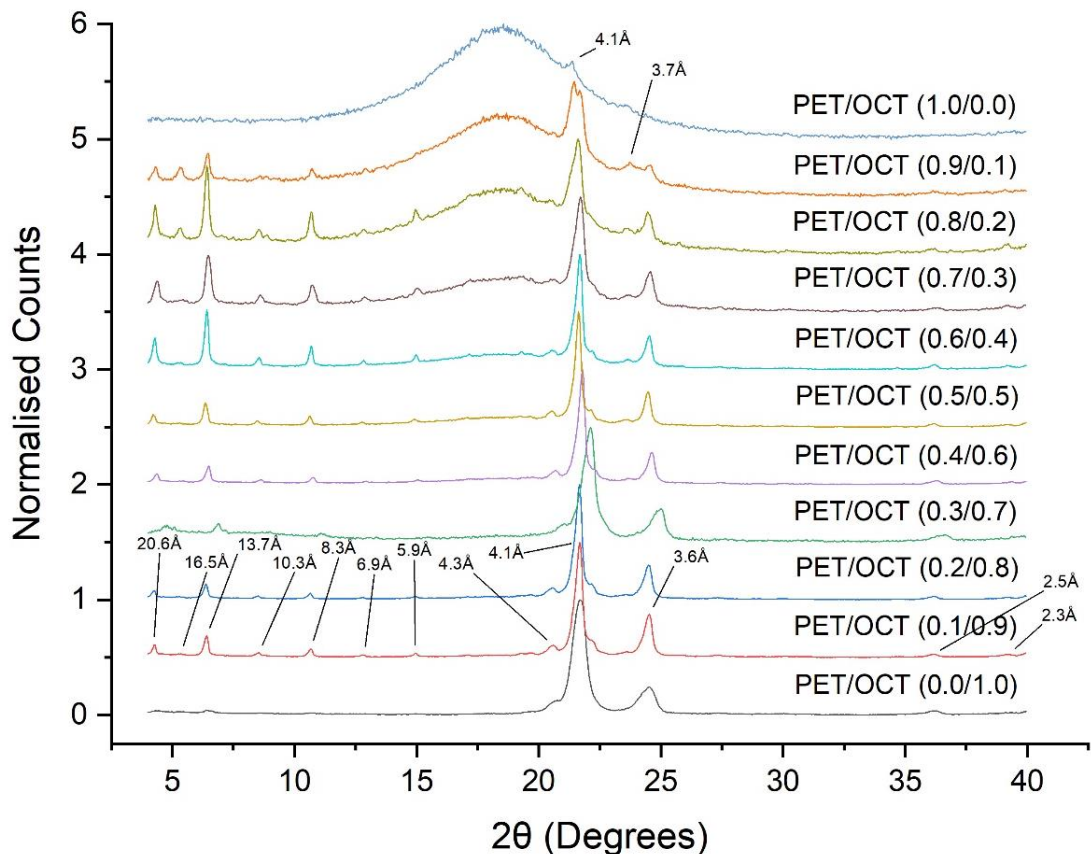


Figure 6-19 Stacked X-ray Diffraction (XRD) patterns of 1-Octadecanol and Petrolatum binary mixtures

6.3.4 Binary Phase Diagram of 1-Octadecanol and Petrolatum

The phase diagram of 1-Octadecanol and Petrolatum is shown in Figure 6-20. 1-Octadecanol's rotator phase is present at concentrations of Petrolatum below PET/OCT (0.2/0.8) at a temperature between the crystallisation of the rotator phase and rotator-gamma transition temperature. Below the rotator-gamma transition temperature, only the gamma phase of 1-Octadecanol is present. In the phase diagram, the onset of crystallisation of Petrolatum is included and indicates the point at which the longest chain length alkanes in the mixture crystallise out of the mixture. As a result, below the onset of crystallisation is a mixture of alkanes in liquid and solid states. The enthalpy of Petrolatum crystallisation became lower upon increasing addition of 1-Octadecanol until the peak disappeared beyond PET/OCT (0.5/0.5). A eutectic point is indicated where both the crystallisation temperature of 1-Octadecanol and Petrolatum is equal at around PET/OCT (0.05/0.95).

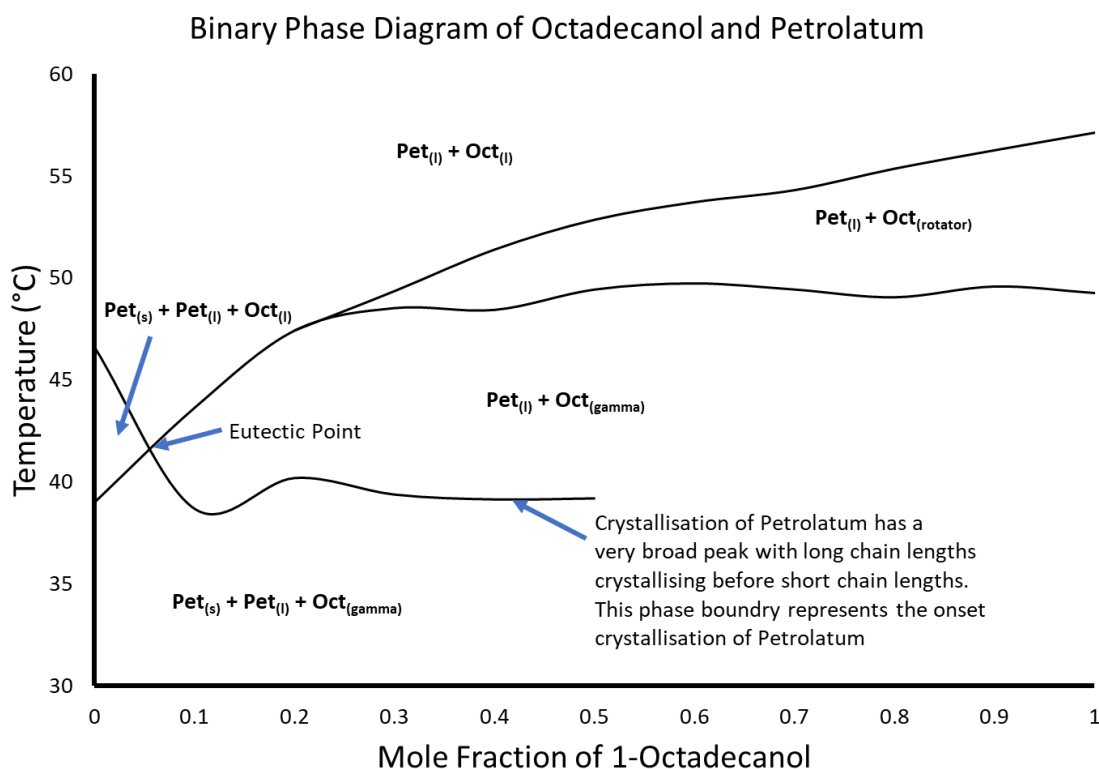


Figure 6-20 Binary phase diagram of Petrolatum and 1-Octadecanol mixtures produced by plotting the onset of phase transitions measured by Differential Scanning Calorimetry (DSC) upon cooling at 1°C/min.

6.4 1-Octadecanol in D5 solvent

Decamethylcyclopentasiloxane (D5) is used as the main solvent in APDO sticks as well as in many other cosmetics. As a result, this industrial solvent was chosen as one of the

solvents studied during the simultaneous temperature-shear synchrotron study alongside Dodecane.

The normalised DSC results upon cooling a binary mixture of 1-Octadecanol and D5 are shown in Figure 6-21. Peak 1 displays the crystallisation of 1-Octadecanol's rotator phase and Peak 2 displays the thermal transition from 1-Octadecanol's rotator to the stable gamma phase. Upon increasing the concentration of D5 in the binary mixture, the rotator phase crystallisation temperature (peak 1) incrementally decreases. The rotator-gamma phase transition (peak 2) initially increases in temperature between D5/OCT (0.0/1.0)-(0.1/0.9), keeps a constant temperature between D5/OCT (0.1/0.9)-(0.3/0.7), decreases in temperature between D5/OCT (0.3/0.7)-(0.5/0.5), before finally increasing in temperature once near to the rotator form crystallisation temperature at D5/OCT (0.7/0.3).

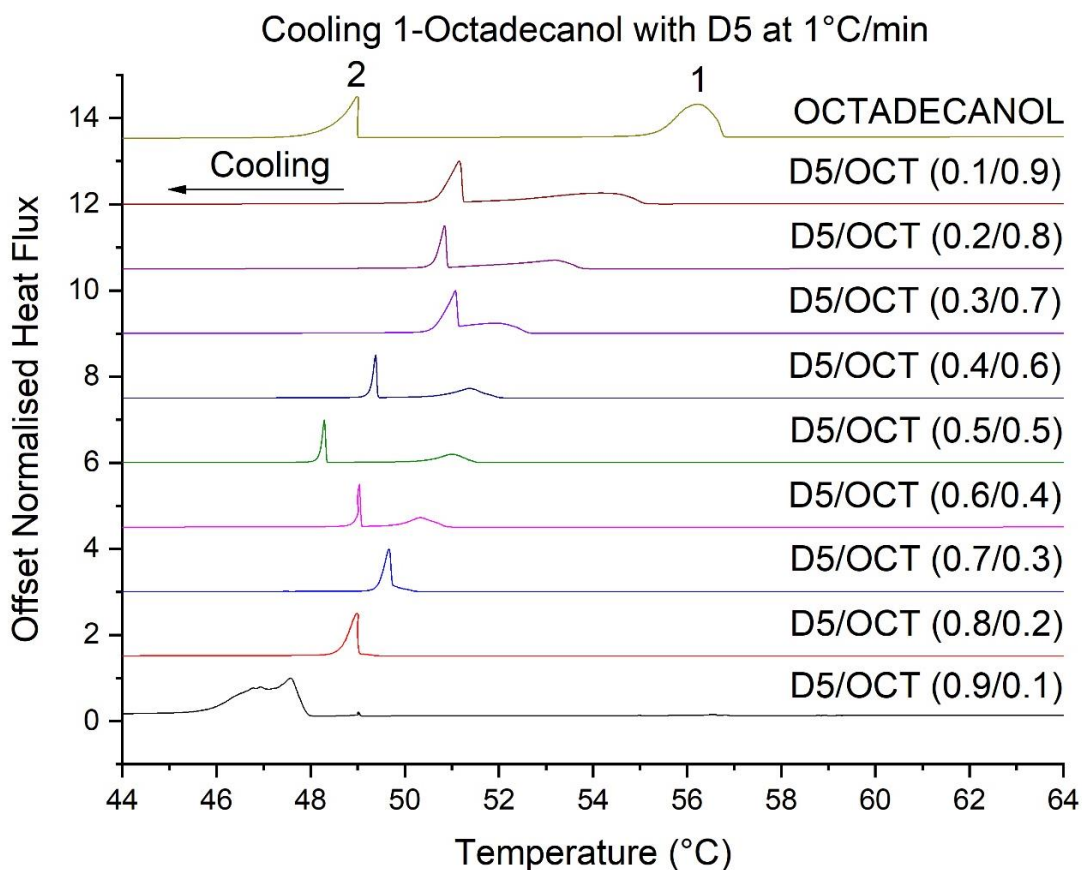


Figure 6-21 Stacked normalised Differential Scanning Calorimetry (DSC) measurements of binary mixtures of 1-Octadecanol and D5 when cooled from the melt at 1°C/min. 1) 1-Octadecanol rotator phase crystallisation, 2) 1-Octadecanol rotator-gamma phase transition.

The binary phase diagram of 1-Octadecanol and D5 is displayed in Figure 6-22. The rotator phase of 1-Octadecanol is present between D5/OCT (0.1/0.9)-(1.0/0.0) between the rotator phase crystallisation and rotator-gamma transition temperatures. Below the

rotator-gamma transition temperature, 1-Octadecanol is present in the gamma phase. D5 is in the liquid phase throughout the temperature range measured using DSC and has a melting point of -47°C .

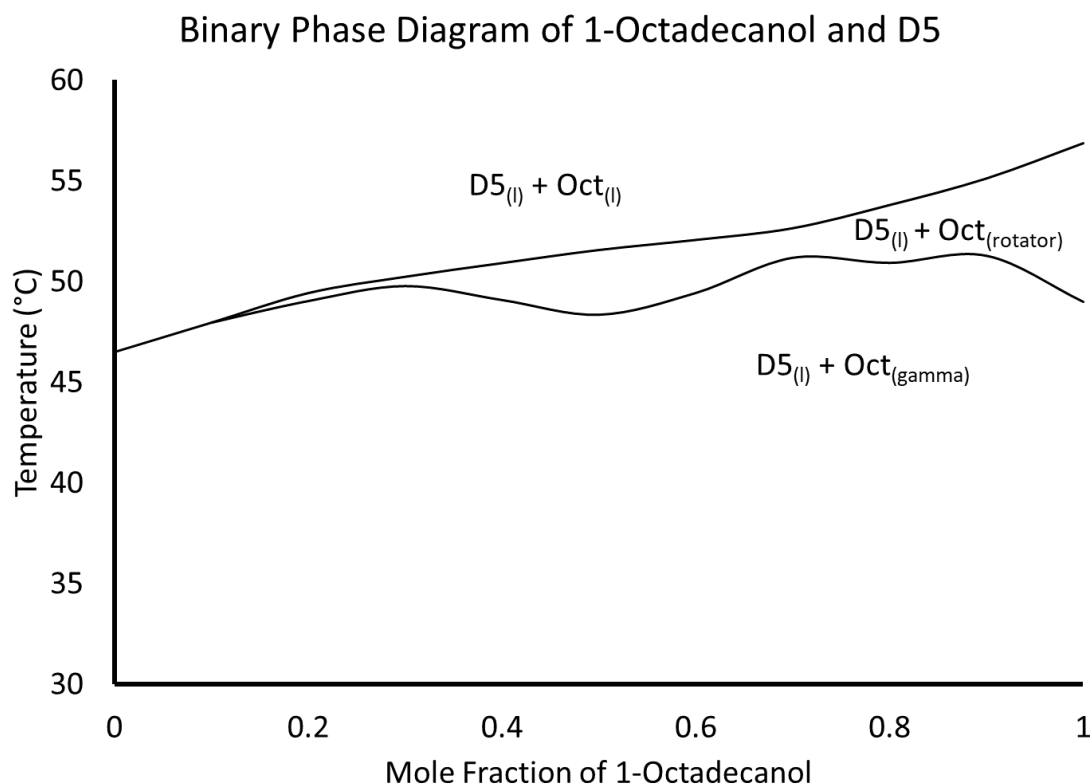


Figure 6-22 Binary phase diagram of D5 and 1-Octadecanol mixtures produced by plotting the onset of phase transitions measured by Differential Scanning Calorimetry (DSC) upon cooling at $1^{\circ}\text{C}/\text{min}$.

6.5 Discussion

The phase diagrams created between 1-Octadecanol and liquid phase solvents resemble the DSC crystallisation curves recorded in the literature between 1-Eicosanol and Peanut Oil shown in Figure 2-20.[57] This confirms the DSC result and phase diagram are similar for other n-alkanol chain lengths and solvents. The identity of the thermal transitions in the binary phase diagrams of 1-Octadecanol/Dodecane and 1-Octadecanol/D5 has been confirmed at the LNLS synchrotron with the displayed

The rotator phase is present between D5/OCT (0.1/0.9)-(1.0/0.0) for D5, PET/OCT (0.2/0.9)-(1.0/0.0) for Petrolatum and DOD/OCT (0.6/0.4)-(1.0/0.0) for Dodecane. There is a correlation between the solubility of 1-Octadecanol in the liquid solvent and mole fraction range the rotator phase is stable. Higher solubility solvents more readily dissolve the rotator phase of 1-Octadecanol, creating a smaller area of the phase that the rotator phase is present. Also, higher solubility solvents lower the temperature at which

1-Octadecanol crystallises at high concentrations of solvent in the binary mixture. For example, D5 is a far poor solvent than Dodecane as seen from Figure 5-4, and the drop in crystallisation temperature is 8.91°C for D5 and 23.59°C for Dodecane across the binary phase diagram. The binary mixture X-ray diffraction patterns of 1-Octadecanol/HCO and 1-Octadecanol/Petrolatum both show an unidentified peak at 16.5Å, upon a high level of HCO and Petrolatum. This peak is in the same position as 1-Octadecanol rotator peak deflection, as seen in Figure 4-3; however, no other characteristic rotator phase peaks are present.

The AFM was used to probe the mechanical properties across the binary phase diagram between HCO and 1-Octadecanol. The results rely on the Quantitative Material Property Mapping technique recently developed by Bruker. This technique allows areas of different material composition to be identified and superimposed over the topographical data. This gives us the ability to observe different morphology and microstructure features on the surface, relate it to material composition and position on the binary phase diagram created using DSC. AFM has been shown in the literature to be an effective technique for deciphering complex tertiary phase diagrams[100] and peakforce tapping with QNM in the has been found to produce complementary results with other material contrast surface mapping techniques such as EDX, backscattering SEM and HarmoniX.[97, 98]

AFM allowed four distinct morphology types to be identified including HCO spherulites, HCO/OCT eutectic mixture, HCO soft plates and 1-Octadecanol hard plates. The soft and hard can plates can be distinguished by mechanical properties and appearance. At high concentration of HCO, hard 1-Octadecanol plates are rough with rounded edges, and soft HCO plates are flat with sharp edges, but at high concentration of 1-Octadecanol plates of HCO and 1-Octadecanol both are flat with sharp edges. The morphology formed at each binary mixture composition can be understood with reference to the phase diagram. Pure HCO crystallises as spherulites; however, HCO crystallises as plates in the presence of 1-Octadecanol. 1-Octadecanol acts as a morphology modifier of HCO through a possible templated nucleation step and the plates formed in general are softer with a lower elastic modulus.

1-Octadecanol and HCO plates can be observed throughout the phase diagram; however, the eutectic mixture can be only observed between HCO/OCT (0.8/0.2) – (0.6/0.4). This can be explained through comparing the temperature drop between HCO/OCT (1.0/0.0) – (0.5/0.5) and HCO/OCT (0.5/0.5) – (0.0/1.0), which is 14.92°C and 4.33°C

respectively. The HCO side displays a far higher temperature gradient than the 1-Octadecanol side, allowing time for HCO to crystallise out, moving the concentration of the melt towards the eutectic point at HCO/OCT (0.5/0.5), forming the eutectic mixture. The eutectic mixture was found to contain grains of HCO surrounded by 1-Octadecanol, formed due to the poor solubility of HCO in the melt compared to 1-Octadecanol. The HCO grains formed in the eutectic mixture had a similar morphology to pure HCO when crash cooled at 20°C per minute. Perhaps the cosmetic performance of the eutectic mixture might be similar to a crash cooled melt.

When the Young's modulus of each morphology type was measured across the range of compositions, there was a large variation in the value measured, especially at HCO/OCT (0.4/0.6). This could be the real result or due to an error in the measurement caused by surface roughness[97] or poor calibration.

A tertiary mixture was studied of HCO/1-Octadecanol/Petrolatum (0.8/0.2/0.01) using AFM and Optical microscopy. Plate morphology was observed, but the AFM hadn't been calibrated, and no meaningful Young's modulus data were recorded. The addition of Petrolatum made the sample appear more homogenous, possibly due to the solubility of 1-Octadecanol in n-alkanes.

A sheared sample was also studied of HCO/1-Octadecanol (0.8/0.2), and shear upon cooling also mixed the different morphology type crystals together so HCO and 1-Octadecanol plates could clearly be seen side by side in one image.

6.6 Conclusion

Binary mixtures of 1-Octadecanol and other liquid/solid materials have been understood with the aid of phase diagrams created using DSC and XRD. The solubility of the liquid solvent that 1-Octadecanol is mixed with strongly influences the region of the phase diagram that the rotator phase is present. AFM with peakforce tapping was proven to be effective at mapping out the morphologies present when mixing HCO and 1-Octadecanol utilising both topographical and mechanical property measurement for phase identification. The morphologies found, have been superimposed onto the phase diagram. The AFM was excellent at measuring relative mechanical properties at a single composition but less effective at measuring over a range of compositions, due to errors caused by surface roughness and calibration.

Chapter 7 Influence of Shear on the Structure of 1-Octadecanol in Solution

In this chapter, we gain insight into the impact of processing 1-Octadecanol in the melt and solution on its crystal structure. Through simultaneous measurement of rheology and X-ray crystal structure, relationships between crystal structure and physical properties can be further understood.

7 Influence of Shear on the Structure of 1-Octadecanol in Solution

7.1 Introduction

Complex multi-component formulations, as used in cosmetic products often contain a large range of function specific ingredients that when added together, create a product with tailored properties designed to fulfil a product application.

Often complex formulations include ingredients that may be immiscible or have a different density relative to the other components. In this case, the processing (mechanical shear) combined with structuring ingredients is key for producing a homogenous formulation that will not separate over the time period intended for the usage of the product. Processing of wax deodorant sticks relies on the formulated mixture being a structured liquid with a viscosity sufficient to avoid formation separation, but a viscosity low enough for the formulation to flow through nozzles into deodorant canisters without trapping air bubbles. For ease of processing the formulation should be designed to have a less temperature sensitive viscosity around the ideal viscosity.

This chapter will focus on the relationships between temperature and shear for formulations with 1-Octadecanol as the main structuring ingredient. 1-Octadecanol has been studied in binary mixtures with Decamethylcyclpentasiloxane (D5) and Dodecane solvents. D5 is the main solvent used in industry when manufacturing wax deodorant stick formulations and selected due to its emollient properties. Dodecane was studied in addition, since it has a larger X-ray attenuation length compared to D5. N-alkanes are commonly used in wax stick deodorants to soften the final product and to utilise its emollient properties. Dodecane was used as a model for Petrolatum for simplification, since it contains a single chain length, rather than a mixture of chain lengths. Phase diagrams of 1-Octadecanol with D5 and Dodecane have been produced using DSC in chapter 6. To study the impact of shear on a 1-Octadecanol structured formulation, an online study was conducted using a custom-made cup and bob shear cell, a viscometer and a synchrotron radiation source.

For many years X-ray diffraction has been used as a tool for measuring residual stress within crystallisation materials. Residual stress within a crystalline material can be caused by either mechanical, thermal or chemical action.[88] Experimentally residual stress can

be measured through a comparison between the X-ray patterns of the stressed lattice with the unstressed lattice. Residual stress causes a shift in the lattice d-spacings, lower d-space is because of compression and higher d space is as a result of lattice tension.

Experimentally peak splitting has been observed because of shear and or the presence of D5 solvent. In this chapter, we will investigate the impact of shear, solvent and temperature on the crystal structure of 1-Octadecanol.

7.2 Preparation Work for Temperature and Shear Synchrotron Study at the Brazilian Synchrotron Light Laboratory

After submitting beamtime experimental proposals to ESRF, Diamond and LNLS, I was granted two days of synchrotron time at LNLS, Brazil in May 2018. Extensive preparatory work was carried out in Leeds to maximise the chance of obtaining useful data at the synchrotron. The experimental proposal was outlined how we wanted to investigate the impact of shear on the crystallisation of long chain hydrocarbons, using a shear cell positioned in the path of the X-ray beam. This section will detail the shear cell design process, reason for material section and preliminary experiments.

7.2.1 Influence of Shear on the Crystallisation and Melting Temperature of Long-chain Hydrocarbons

Varying the amount shear in the system is known to impact the crystallisation and melting behaviour. For instance, crystalline materials can be made to be amorphous through milling and the amorphous variant will have very different melting properties. Varying shear also can impact the crystallisation through accelerating the creation nuclei, due to increased molecule interactions in the melt which increases the probability of creating critical sized clusters of molecules. Also shear can cause particle breakage, breaking large crystals into smaller crystals which increases the number of binding sites that molecules in solution can adsorb onto, further accelerating crystal growth.

The rheology profile of 1-Octadecanol, HCO and Petrolatum were studied upon heating and cooling at different shear rates, using an Anton Parr, cone and plate rheometer fitted with a Peltier plate. Each wax material was sheared at a range of shear rates from 5 – 1000s⁻¹, whilst being cooled at 10°C/min. The aim of the study was to see if shear will impact the crystallisation/melting temperature of the wax materials and whether

polymorphic transitions can be detected using rheology. The 1st derivative of the torque vs temperature was used to observe the point at which crystallisation occurs. The 1st derivative of torque upon heating and cooling of 1-Octadecanol, HCO and Petrolatum are displayed in Figure 7-1, along with the tabulated melting and crystallisation temperatures listed in Table 7-1.

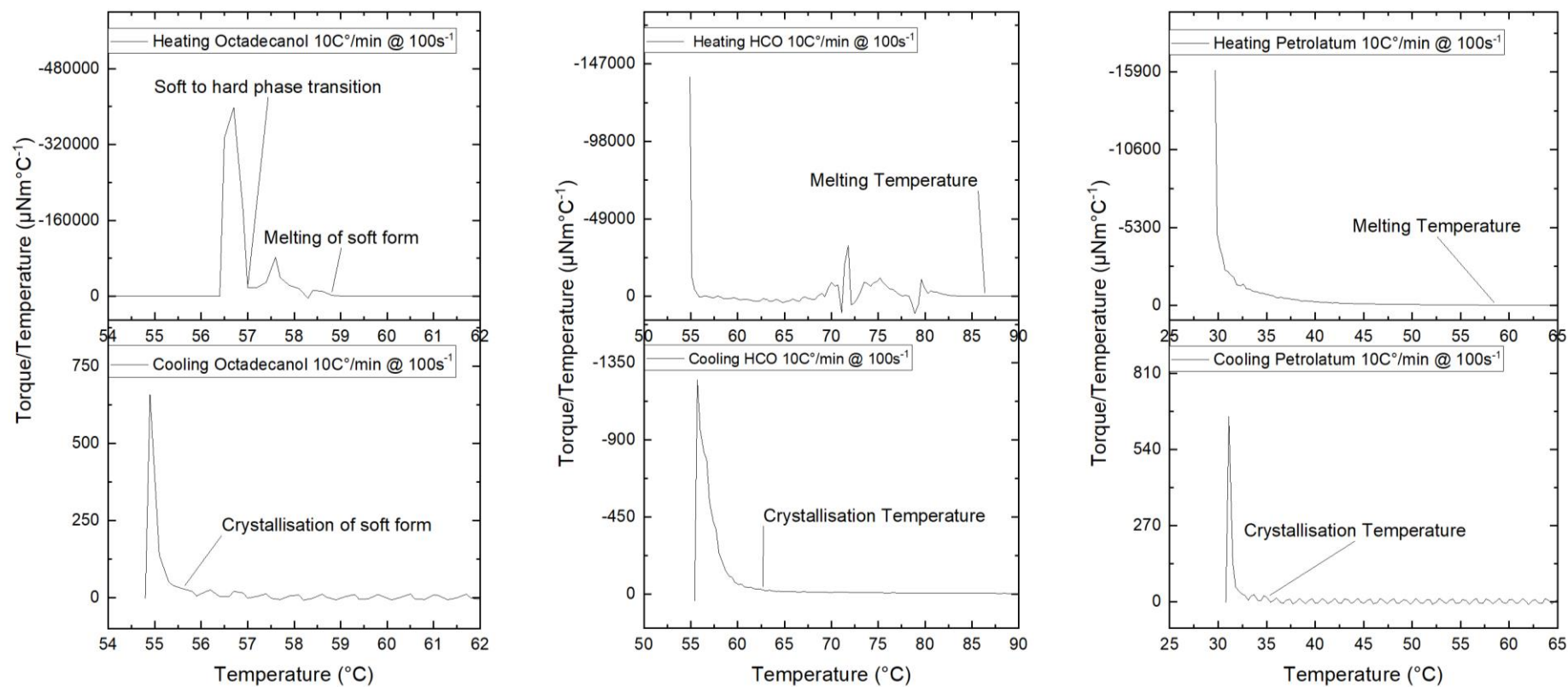


Figure 7-1 Graphs displaying the 1st derivative of torque measured against temperature for 1-Octadecanol (left), Hydrogenated Castor Oil (middle) and Petrolatum (right) whilst being cooled (bottom) and heated (top) at $10^\circ\text{C}/\text{min}$ and sheared at 100s^{-1}

Table 7-1 Crystallisation and melting temperatures of 1-Octadecanol, Hydrogenated Castor Oil and Petrolatum measured using the Anton Parr rheometer at a cooling and heating rate of 10°C/min and a shear rate of 100s⁻¹

1-Octadecanol		
Shear Rate (s⁻¹)	Crystallising Temperature (°C)	Melting Temperature (°C)
5		64.4
25	57.4	63.4
100	57.4	63.0
200	57.4	
500	57.4	
1000	57.3	
Hydrogenated Castor Oil		
Shear Rate (s⁻¹)	Crystallising Temperature (°C)	Melting Temperature (°C)
5	61.0	
25	63.0	86.8
100	63.4	86.8
200	63.0	86.8
500	63.3	86.7
Petrolatum		
Shear Rate (s⁻¹)	Crystallising Temperature (°C)	Melting Temperature (°C)
5	36.3	60.1
25	35.0	57.7
100	35.4	59.0
200	36.1	57.7
500	35.7	59.3
1000	35.8	

The onset of crystallisation of 1-Octadecanol was observed through measuring the torque upon cooling and heating. In the literature, 1-Octadecanol is known to exhibit a soft rotator phase and a hard gamma phase.[53] This phase transition can be seen on the heating of 1-Octadecanol in Figure 7-1 through the formation of a peak at 57.5°C. This peak can be explained through the thermodynamic disappearance of the gamma phase, reducing torque measured, then a structural phase transition occurs, the new 1-

Octadecanol structure forms, binding to the cone and plate, increasing the torque, before melting reducing torque measured. In the literature, even chain length n-alkanols are seen to initially form a rotator phase before forming a gamma phase.[53] This result confirms that it's possible to study the phase behaviour of wax materials through measuring the rheology. The melting and crystallisation temperatures at each shear rate is displayed in Figure 7-1. Varying shear rate is seen to have no effect on the crystallisation temperature of both the soft and hard phases, however as the shear is increased the temperature at which 1-Octadecanol melts is seen to reduce 64.4°C @ 5s^{-1} to 63°C @ 100s^{-1} . This reduction in melting temperature can be explained by the 1-Octadecanol sample being heated due to the increased frictional forces when the solid sample was sheared at a higher shear rate. The temperature is measured by a temperature sensor within the Peltier and will not measure the internal temperature of the sample. Shear rates above 100s^{-1} whilst heating were not conducted, to avoid damage to the rheometer.

Crystallisation temperature was seen to increase with shear rate between 61°C @ 5s^{-1} and 63°C @ 25s^{-1} for HCO when cooled @ $10^{\circ}\text{C}/\text{min}$. Shear rates above 25s^{-1} had no further impact on the crystallisation temperature. Shear rate was seen to have no impact on the melting of HCO. Sharp increases and decreases in torque are observed upon heating, between $70\text{-}80^{\circ}\text{C}$ before HCO completely melts. One possible mechanism is that HCO breaks apart under shear, creating loose chunks that get trapped under the cone and plate, increasing torque and then released from the cone and plate reducing torque.

For Petrolatum the crystallisation temperature was seen to slightly decrease with increasing shear rate, which is in contrast to what I was expecting to observe. Also, upon heating Petrolatum, the melting temperature was seen to fluctuate between 60.1 and 57.7°C with no clear trend upon increasing shear rate. Of the three wax materials, the point which crystallisation of Petrolatum occurs is very difficult to judge, due to the large range of chain lengths in Petrolatum crystallising/melting over a large temperature range and the fact the transition is from a liquid to a soft jelly. The great difficulty in judging the point of crystallisation increases the measurement error of the temperature which could explain the trends observed.

In summary, shear does not seem to conclusively impact the crystallisation temperature of 1-Octadecanol and Petrolatum, suggesting the crystallisation temperature is mainly driven by thermodynamics when cooling at 10°C per minute. HCO there was a

noticeable difference in the crystallisation temperature between a shear rate of 5s^{-1} and 25s^{-1} , possibly due to a kinetically driven crystallisation mechanism.

Upon heating at different shear rates, no conclusive difference in melting temperature was observed for Hydrogenated Castor Oil and Petrolatum. The melting temperature of 1-Octadecanol was seen to decrease with increasing shear rate, however, this was probably due to the increased frictional forces internally heating the sample. Hydrogenated Castor Oil and Petrolatum are both softer materials than 1-Octadecanol and far less heat was generated when shearing these samples.

Perhaps if the experiments were conducted at a very slow cooling rate, the impact of shear on the crystallisation and melting temperature would be more clear, since the crystallisation and melting processes would be less driven by thermodynamics.

Upon heating 1-Octadecanol, the rotator and gamma phases can be clearly distinguished using rheological measurements, in contrast to HCO and Petrolatum as seen in Figure 7-1, making 1-Octadecanol the subject of study. Another reason for the selection of 1-Octadecanol is after conducting turbidity experiments of HCO and 1-Octadecanol in a solvent; it's visibly clear that 1-Octadecanol provides the structure in the formulation. Very high torque is required to shear pure crystalline 1-Octadecanol which can put excessive strain on equipment, so as a result synchrotron shear experiments used 1-Octadecanol in solvent.

7.2.2 Shear Cell Design

Initials plans for shear experiments involved the use of an existing shear cell, designed by Scott MacMillan.[134] Scott designed two shear cells for online crystallisation with shear and temperature control. His two designs were based upon a cone and plate rheometer with temperature control provided by Peltier plates and water cooling. Shear was provided by a rotating polycarbonate flat disk, between two cones. His designs involved injecting the sample into the cell using a syringe which would make changing sample between synchrotron runs time consuming and difficult. After considering these factors, it was decided that we would design a new shear cell.

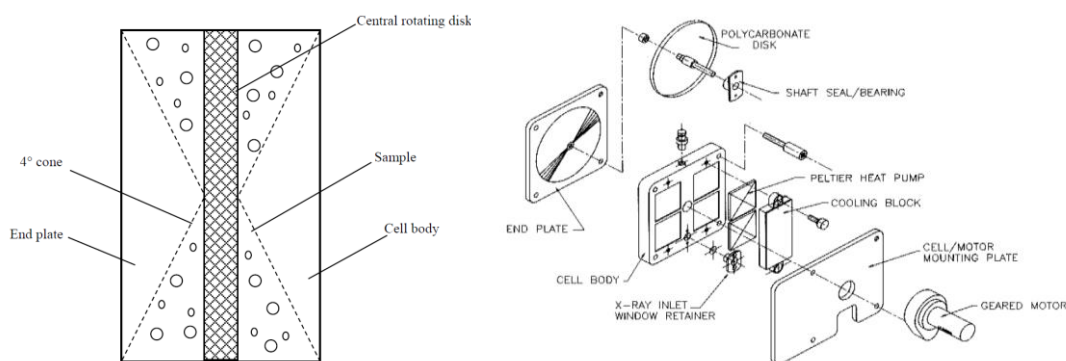


Figure 7-2 Image of Scott Macmillan's shear cell taken from Scott Macmillan's thesis.[134]

7.2.2.1 Design Criteria for New Shear Cell

After it became apparent using an existing shear cell wasn't an option, we turned our attention to creating a new design. We wanted the design to meet the following criteria.

- A simple design (previous designs were too complex).
- Easy to clean.
- Compact and easy to transport to Brazil.
- Incorporate existing Brookfield viscometer.
- Easy and fast for the workshop to manufacture.
- Path length through shear cell needs to be less than or equal to the sample attenuation length

The solution I came up with was based upon a cup and bob rheometer design that incorporated a Brookfield viscometer available in the Leeds engineering department and water bath supplied by the synchrotron. A compact modular design was needed since the experimental setup was to be shipped to and from Brazil. The bob chosen was the Brookfield DIN-87 spindle which has the smallest diameter Brookfield supply designed to work with the HBDV-II+P viscometer. A small diameter spindle allows a high torque to be measured and applied to the sample, whilst keeping the path length through the sample to a minimum. The cup was designed using AutoCAD[135] and machined out of a block of stainless steel with a flat bottom and inlets/outlets laser welded to the cup by the Leeds University engineering workshop. The dimensions of the cup decided upon, based on the ratio between cup and bob radius used by Anton Parr for their cup and bob rheometer (1.0847:1). The dimensions of the cup are as follows, 2mm thick stainless-steel walls, internal diameter is 13mm, and the internal height is 38mm. The diameter of the DIN-87 spindle was 11.82mm, giving a gap between the cup and spindle

of 0.59mm; however, the internal wall of the cup was coated with polyimide film (100HN) supplied by DuPont and fixed using chemically/temperature resistant Araldite 2014-1 supplied by Huntsman, creating a new gap of approximately 0.5mm. Temperature control is provided by the rheological cup being surrounded a machined stainless-steel water jacket, connected by rubber piping to a water bath. The water bath pumps the water throughout the reservoir whilst provides heating or cooling. The temperature of water flowing through the shear cell was measured by a temperature probe positioned inside the water inlet of the water jacket. Rheology and Temperature data was outputted to a laptop by serial port with the data displayed on Brookfield's Rheocalc32 software. The data was recorded by parallels desktop screen record function and collated in an Excel spreadsheet. A 2D cross section with dimensions, a 3D model. An image of the shear cell *in situ* on the beamline, along with a 2D cross section and a 3D model of the design is displayed in Figure 7-3.

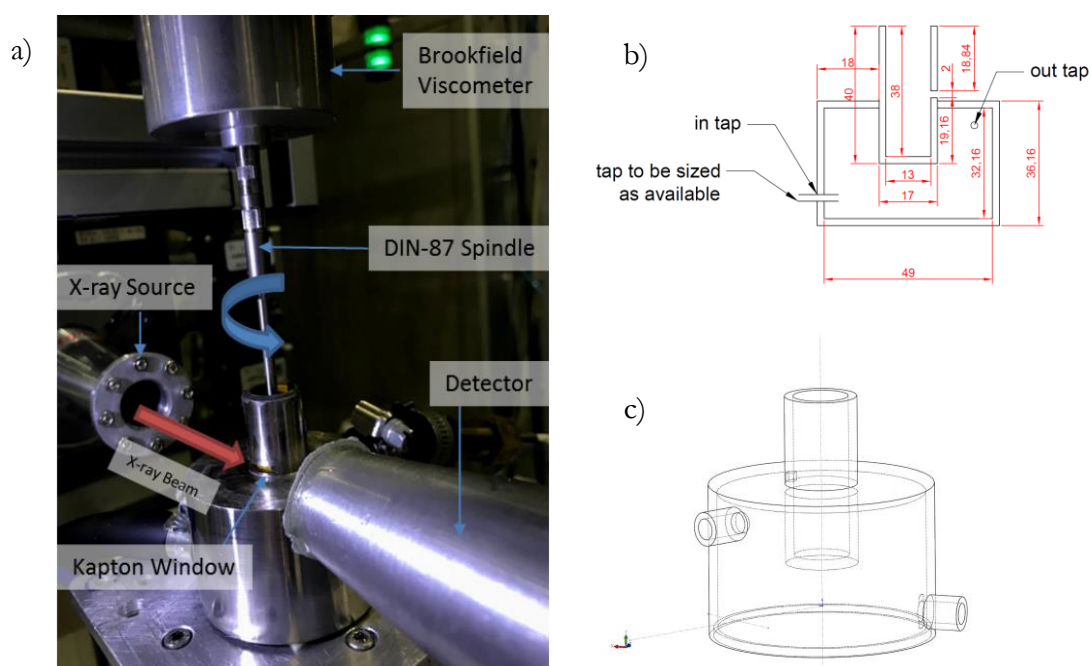


Figure 7-3 Image a) of shear cell *in-situ* at LNLS beamline, b) 2D cross section design of shear cell with dimensions[135] and c) a 3D image of the shear cell design where water inlet and outlet, along with the cup can be clearly seen.[136]

7.2.2.2 Attenuation Length Calculations

The following attenuation length predictions have been calculated using an online tool[137], which a prediction of attenuation length is based upon, chemical formula, density, beam energy and angle of incidence. The calculation relies on a series of tables that have been produced using experimental measurements on theoretical calculations.[138, 139]

Table 7-2 Table displaying attenuation length calculations of materials the X-ray beam will pass through at the LNLS synchrotron

Material	Material Density (g/cm ³)	Photon Energy (eV)	Attenuation Length (mm)
Polyimide (Kapton)	1.43	8000	1.18
1-Octadecanol	0.810	8000	2.92
Dodecane	0.750	8000	3.54
D5	0.958	8000	0.38

The attenuation length of D5 is very short at 0.38mm and for synchrotron experiments using D5 solvent to be successful, either the photon energy has to be increased, or a really short path length through the shear cell is needed. The beam energy at the SAXS1 beamline was fixed at 8.3 keV, and the final shear cell design displayed in Figure 7-3 has a maximum path length through the sample of 4.96 mm. The beam grazes the edge of cylindrical bob, so in reality, there is a range of path lengths from 0-4.96mm that the beam can pass through the sample, Dodecane with an attenuation length of 3.54mm was chosen to be studied alongside D5.

7.2.3 Calibration of the Anton Parr Rheometer and the Brookfield Viscometer

Calibration of both the Anton Rheometer and the Brookfield Viscometer was conducted using Viscosity Oil Standard S600. The viscosity oil standard is a Newtonian Fluid and exhibits constant viscosity at different shear rates at a constant temperature. This was experimentally confirmed by conducting a series of shear sweep experiments at a range of temperatures on the Anton Parr rheometer. Table 7-3 displays an excellent agreement between the Dynamic Viscosity of the S600 oil measured by the Anton Parr rheometer and the viscosity standard values stated on the bottle. This result confirms the Anton Parr rheometer measured viscosity values are accurate.

Table 7-3 Comparison between dynamic viscosity stated on the bottle of the S600 calibration standard, and measured viscosity of the calibration standard using the Anton Parr rheometer fitted 50mm-1° cone and plate shearing at 100s⁻¹ while heating at 1°C/min.

Temperature (°C)	S600 Dynamic Viscosity (cP)	Measured Viscosity Anton Parr (cP)
20	2190	2155
25	1421	1410
40	461.5	460
50	244.3	250

The Brookfield viscometer readings using the DIN-87 spindle were inaccurate when measuring the standard fluid and a calibration experiment was performed to correct the viscosity. Two temperature sweep experiments between 0°C and 65°C measured the viscosity of the standard fluid using the Anton Parr rheometer and the Brookfield viscometer fitted with the DIN-87 spindle, and the results are shown in Figure 7-4. The viscosity measured by the Brookfield was plotted as a function of the viscosity measured by the Anton Parr and a linear region of the graph can be seen for viscosity values measured between 8-17°C. This linear region has a gradient of 4.651 and can be explained by nature the experiment was conducted. Accurate temperature control of the standard oil, during the Anton Parr rheometer measurements, was provided by a Peltier attachment. The temperature control of the Brookfield viscometer experiments was provided by an ice bath, the ambient temperature of the room and a hot plate. The experiment started when a beaker containing the standard oil was removed from the ice bath and left to increase in temperature on the lab bench, whilst the Brookfield viscometer was measuring the change in viscosity and a temperature probe measured the change in temperature. To measure temperatures above 17°C a water bath and a hot plate was used to heat the standard oil. The linear region was the period with the slowest, most controlled heating rate from 8-17°C. At temperatures below 8°C, there was a higher heating rate, a higher viscosity making the stirring less effective, resulting in less accurate temperature measurement.

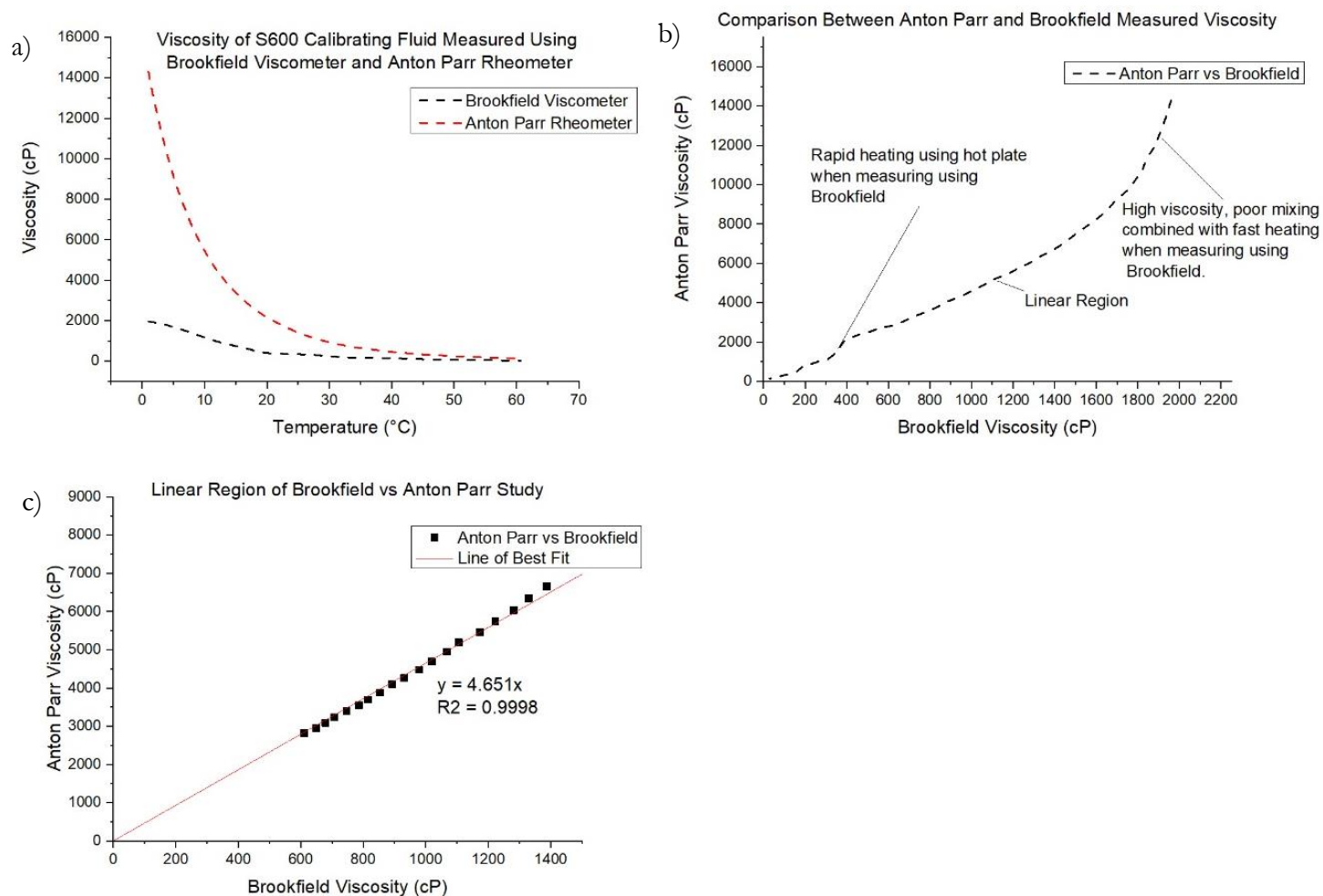


Figure 7-4 Viscosity of S600 standard fluid measured in a) using Brookfield viscometer and Anton Parr rheometer during a temperature sweep, b) Anton Parr viscosity plotted as a function of Brookfield viscosity during the temperature sweep and c) Linear region of the graph where Anton Parr viscosity has been plotted as a function of Brookfield viscosity.

7.3 Online Simultaneous Shear/Temperature Studies on 1-Octadecanol With and Without Solvent

Experiments were carried out using SAXS1 beamline at the Brazilian Synchrotron Light Laboratory. SAXS1 has the capability for small and wide angle X-ray diffraction in two different set-ups at a fixed beam energy of 8.3 keV with a $\Delta E/E$ of 0.1 keV. The camera length is variable, allowing structures to be resolved between 1-1000Å in two setups. The flight path of the X-ray beam was fully vacuumed at 10^{-2} mbar up until the shear cell and the detector. The detector used to capture the scattered X-ray beam was a Dectris, Pilatus 300K with 487 x 689 pixels of 172 μm in size with a frame rate 200Hz. The X-rays pass through a 2mm wide slit cut in the edge of a bespoke shear cell sample holder detailed above.

Detail of the methodology and a table listing all the experiments performed is in Chapter 3 – Materials and Methods.

At the synchrotron, a water bath with temperature control was not provided, so the heating and cooling rates were dictated by the ambient temperature of the hutch and the water bath provided. Crash cool experiments were performed by swapping the supply of water circulating through the shear cell between two water baths, one containing water of 25°C and one containing water of 80°C. Graphs detailing typical heating and cooling profiles of the experiments performed are shown in Figure 7-5.

Typical Crashcool, Cooling and Heating Experimental Temperature Profiles

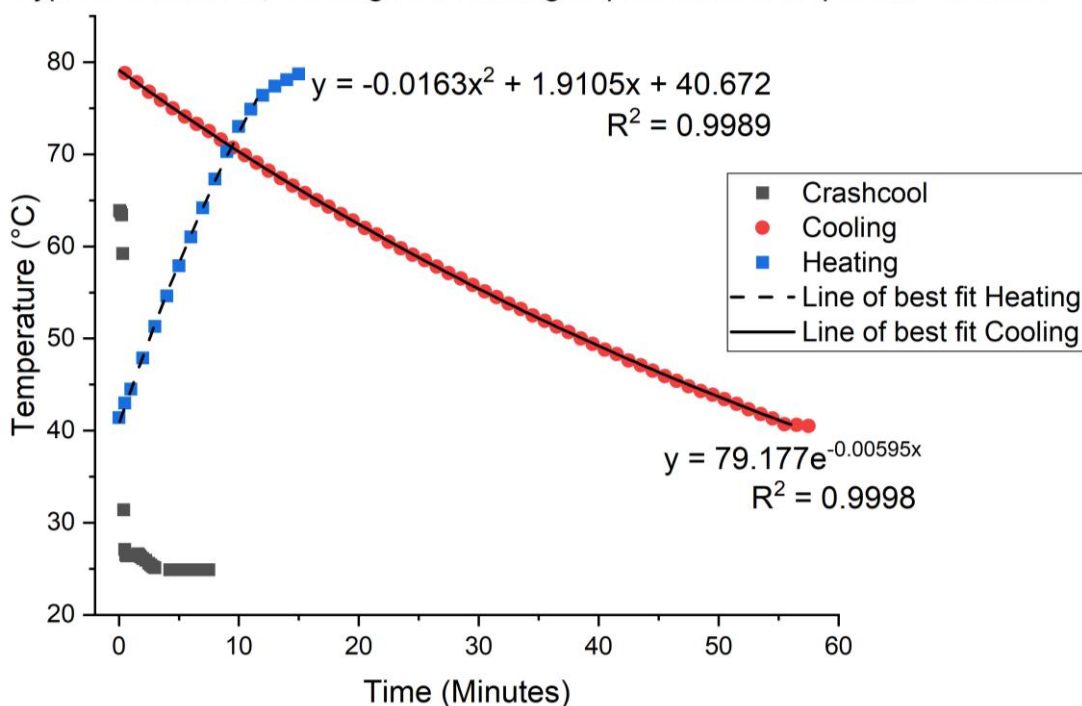


Figure 7-5 Experimental temperature profiles for heating, cooling and crash cooling OCT/PET (0.2/0.8) mole fraction binary mixture of 1-Octadecanol in Dodecane, along with the line of best fits and the equation.

The temperature shown in the above profiles was measured by a temperature probe placed situated in the inlet. As a result, there was a temperature differential between the probe and the sample. The size of this temperature differential increases upon faster heating and cooling rates. The heating and cooling rates were approximately -0.692°C per minute and 3.023°C per minute, respectively when the profiles were fitted with a straight-line equation. The measured cooling temperature data can be fitted with a high degree of accuracy to an exponential curve and heating to a polynomial curve. Both lines of best fit have the equation and R^2 value given on the graph. The crash cool took 15 seconds for the temperature probe to drop from 53°C to 26.5°C at an approximate cooling rate of $\sim 106^{\circ}\text{C}$ per minute. This is only a very rough indication of the heating/cooling rates seen by the sample since the temperature probe is positioned in the flow of cold water entering the cell at the inlet. After 2 minutes 40 seconds, the water flowing into the cell reaches equilibrium and maintains 24.9°C for a further 4.5 minutes until the run had finished. The cooling rate is $\sim 9.94^{\circ}\text{C}$ per minute until equilibrium temperature has been reached. Both cooling rate measurements are approximations since the cooling profile will be an exponential curve.

The 3D waterfall plots show the 1st, 2nd and 3rd order data plotted on the same axis, where x represents counts, y represents q -space, and the z -axis represents temperature as seen

in Figure 7-6. There is a large magnitude of difference between the intensity of the 1st order and 2nd and 3rd order peaks; as a result, the stacked line graphs shown in Figure 7-7 have the 1st order data plotted on a different set of axis to the 2nd and 3rd order. The 1st order and 2nd and 3rd order axis have a q range of between 0.5-2.5 nm^{-1} and 2.5-5.2 nm^{-1} respectively. The stacked graphs have photon counts on the x-axis and q space on the y-axis with each data set offset, so the individual peaks can be observed. If the original offset still doesn't show all the detail, another graph will be below, allowing the trends to be seen on a smaller scale. The stacked line graphs for experiments involving shear, also feature a green/red bar to the right of the axis showing whether the viscometer motor was on or off during the experiment. To avoid the damage to the viscometer during the experiment, it was turned off when the resistance of the sample became too great, and the spindle became stuck in the same position.

It is important to consider that the stacked graphs omit parts of the data, but the 3D waterfall graphs include all the data sets. Each X-ray spectra measured over 30 seconds for heating and slow cooling and over 5 seconds in the case of crash cooling.

In this chapter, first, we shall examine the crystallisation of 1-Octadecanol when cooled from the melt under static conditions, before looking at the impact of shear and addition of solvent to the crystal structure.

7.3.1 1-Octadecanol

The section explores the crystallisation of 1-Octadecanol without the presence of any solvent. At the synchrotron experiments using no solvent were completed first to avoid contamination. 1-Octadecanol is a white crystalline solid at room temperature and was loaded into the shear cell in the solid phase, before being melted by the hot 80°C water passing through the shear cell. 1-Octadecanol was added to the shear cell, ensuring the bob and the Kapton window were completely covered.

The monoclinic crystal structure of the stable gamma phase of 1-Octadecanol is well known and studied with the space group 15 and point group 2/a.[119] The crystal structure of 1-Octadecanol's rotator phase is less well defined, and in recent studies, it is reported to be pseudo-monoclinic; however, the lattice parameters haven't been published.[53, 57, 58]

The full powder XRD pattern of 1-Octadecanol at room temperature under static conditions is displayed in Figure 4-3.

7.3.1.1 1-Octadecanol Under Static Conditions

For simplicity, we will consider the least complex experiment first, 1-Octadecanol under static conditions and no thermal cycling.

When 1-Octadecanol is initially cooled from the melt, the rotator phase is first seen to crystallise at 58.3°C with the 1st order peak forming at 1.312nm⁻¹, before shifting to lower q with further cooling as the crystal structure grows between 58.3-56.2°C. By 57.6°C, the 2nd and 3rd order peaks are first seen at 2.599 and 3.893 nm⁻¹, as shown in Figure 7-6 and Figure 7-7 b). Upon further cooling the gamma phase is first seen at 52.3°C with 3 peaks at 1.520, 3.038 and 4.524 nm⁻¹ being formed, corresponding to 002, 004 and 006 lattice planes. A solid-solid transition occurs, converting the rotator phase to the gamma phase. Both the rotator and gamma phases exhibit 3 peaks with equal separation, suggesting lamellar type repeating unit ordered structure. Upon the formation of the gamma phase, the existing rotator phase 1st, 2nd and 3rd order peaks gradually shift towards lower values of q space upon cooling. This suggests the rotator phase structure is inter-linked with the gamma phase with the growth of the new gamma phase placing tensional stress on existing rotator phase structure. The change in the d spacing is plotted against temperature for the 1st order rotator and gamma phase peaks can be seen in Figure 7-10 a) and b). The d-spacing of the 1st order rotator phase peak increases by over 2 angstroms as 1-Octadecanol is cooled from 58°C to 40°C, whilst the d spacing of the 1st order gamma 002 peak changes by approximately 0.1 angstroms over the same temperature range. This variation d spacing is due to both crystal structures competing for the same space, and the result demonstrates the gamma phase has a very rigid crystal structure compared to the rotator phase. When looking at the 3D waterfall plot in Figure 7-6, its clear to see the relative peak intensity rotator phases is higher than the gamma phase. Also, peak intensity decreases through increasing order.

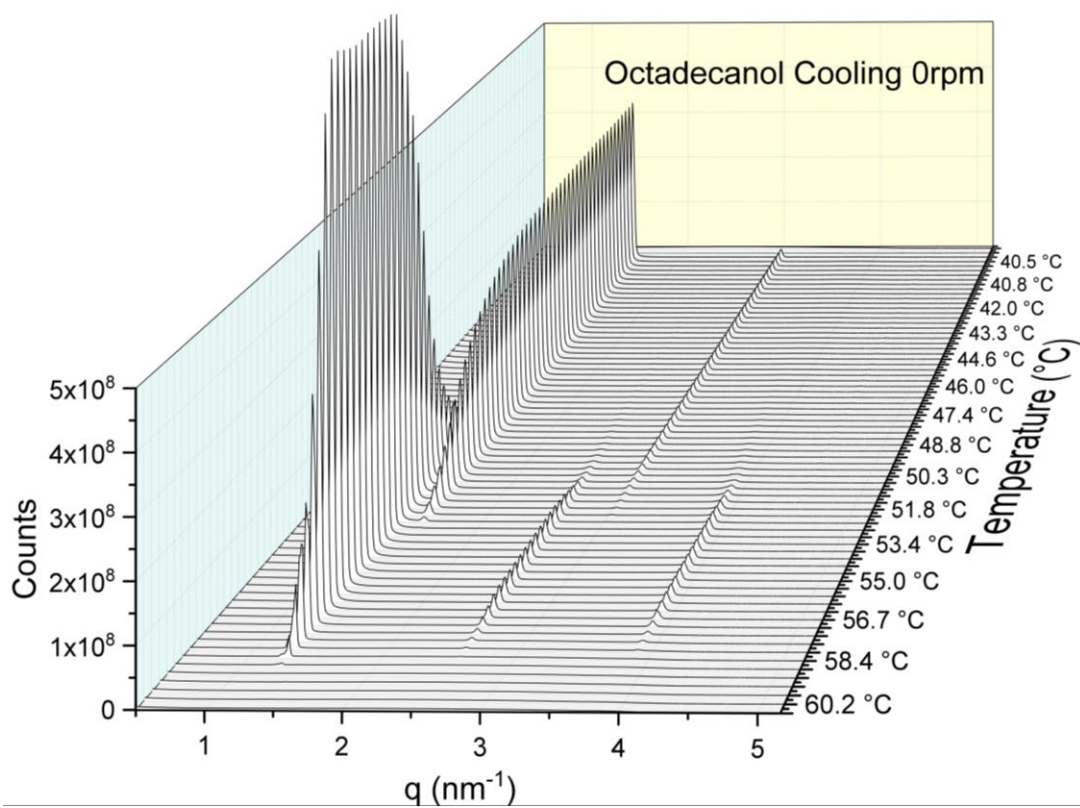


Figure 7-6 3D Waterfall Plot displaying crystallisation of 1-Octadecanol's rotator phase and the transition of rotator to gamma phase upon slow cooling from the melt under static conditions.

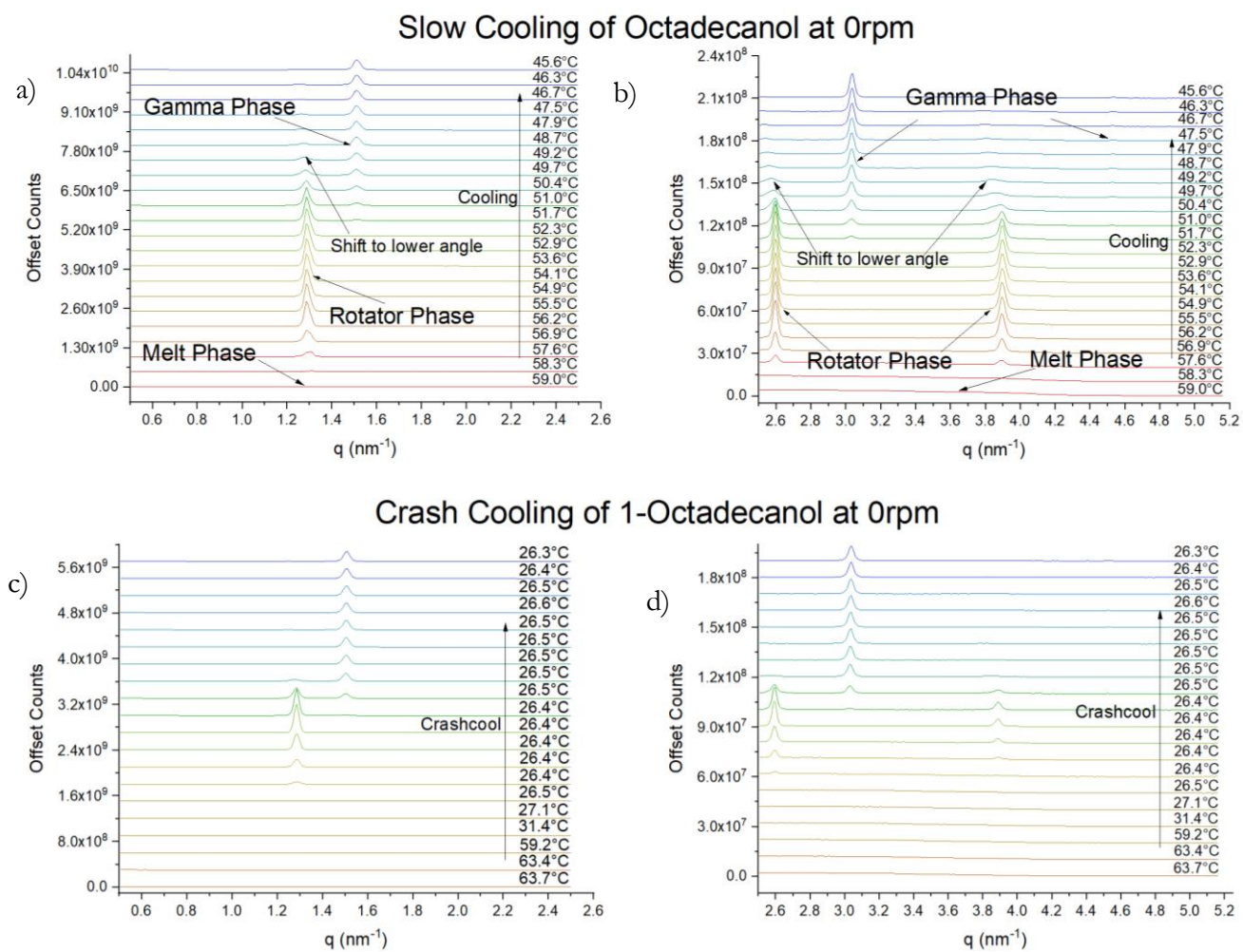


Figure 7-7 Stacked plots display 1-Octadecanol cooled under static conditions from the melt probing a range of q from 0.5 – 2.5 nm^{-1} (a) and 2.5 – 5.2 nm^{-1} (b). 1-Octadecanol crash cooled under static conditions from the melt observing a range of q from 0.5 – 2.5 nm^{-1} (c) and 2.5 – 5.2 nm^{-1} (d)

Figure 7-10 also displays the variation in full width half maximum (FWHM) of the 1st order rotator and gamma phase peaks with temperature. The peak width for both phases is at a minimum when the phase in question is dominant and has an established crystal structure. Upon crystallisation of the rotator phase and the solid-solid transition to the gamma phase, the 1st order rotator phase peaks broaden. Also, a small degree of peak broadening was observed upon the formation of the 1st order gamma phase peak.

Upon rapidly crash cooling 1-Octadecanol from 80°C to 25°C no new crystal structures were formed, however by 26°C by rotator phase has completely transformed to the gamma phase and displayed in Figure 7-7 c) and d). In the slow cooling experiments, due to experimental time constraints, the sample was only cooled to 45°C and conversion from the rotator to gamma had not completed.

7.3.1.2 1-Octadecanol Under Shear Conditions

The shear experiments on 1-Octadecanol were conducted sequentially using the same 1-Octadecanol sample loaded into the shear cell. The 100rpm cooling and heating run was conducted first, followed by the 0rpm and then the 20rpm last. The 1st order rotator and gamma phase peaks formed upon cooling in different shear regimes are displayed in Figure 7-8. Without shear, 1-Octadecanol's 1st order rotator phase is represented by a single peak and split peaks upon shear. This split peak becomes increasingly defined as shear is increased, with an increased d spacing between the split peaks. The rotator phase is represented at 55°C by a single peak with a d spacing of 48.66Å at 0rpm, a peak with a shoulder at 48.76Å when sheared at 20rpm and two peaks at 48.29Å and 49.48Å when sheared at 100rpm. The split peaks centre around the same position as when no shear is occurring as seen in Figure 7-10 a), but the peaks increase in separation when shear is increased from 20rpm to 100rpm, with the lower d spacing peak having a lower intensity, relative to the higher d spacing split peak. During the formation of the gamma phase, 1-Octadecanol solidifies, and the viscometer becomes stuck and is turned off. Despite no shear being applied during the solid-solid transition from rotator phase to gamma phase, the gamma phase formed displays the same two peak splitting as observed in the rotator phase for both 20 and 100 rpm experiments in Figure 7-8. This evidence suggests that the metastable rotator phase acts as a template for the stable gamma phase. The gamma phase at 45°C and 0rpm displays a single peak with a d spacing of 41.54Å, 20rpm displays two peaks of 41.31Å and 42.15Å and 100rpm displays two peaks at 41.24Å and 42.22Å. When the 100rpm sheared gamma phase is heated under static conditions, no annealing

effect occurs and the gamma phase maintains the split peak nature, until the gamma to rotator phase, solid-solid transition occurs and the 1st order split gamma phase peak transforms into a single rotator peak with shoulder as can be seen in Figure 7-9 a). This suggests that the gamma phase also acts as a template for the rotator phase when heating, however, because of relatively high temperature and soft nature of the rotator phase, some reordering occurs during the solid-solid transition.

Increasing shear has been found to increase the peak width of 1st order rotator and gamma phase peaks. Figure 7-10 displays the change in FWHM of the sheared split peaks. The FWHM of the 1st order rotator phase increased from 0.03nm⁻¹ under static conditions to 0.05nm⁻¹ with shear at 20rpm. At 100rpm the rotator phase splits into two distinct peaks, so the FWHM result is not directly comparable with the single peaks exhibited under static and 20rpm shear. The FWHM of the two split 1st order gamma phase peaks at 20rpm and 100rpm are very similar in magnitude. The combined width of both peaks will be significantly larger than the FWHM of the single gamma phase peak formed under static conditions.

The initial crystallisation peaks of 1-Octadecanol's rotator phase is observed at 0 rpm (1.312nm⁻¹ @ 58.7°C), 20 rpm (1.3037nm⁻¹ @ 57.8°C) and 100 rpm (1.2954nm⁻¹ @ 57.3°C). The temperature which the first crystallisation peak can be observed in the X-ray data decreases with increasing shear. From a nucleation theory perspective, you would expect the opposite, so it is likely shear is impacting the crystallinity of the sample, reducing the intensity of peaks observed in the data.

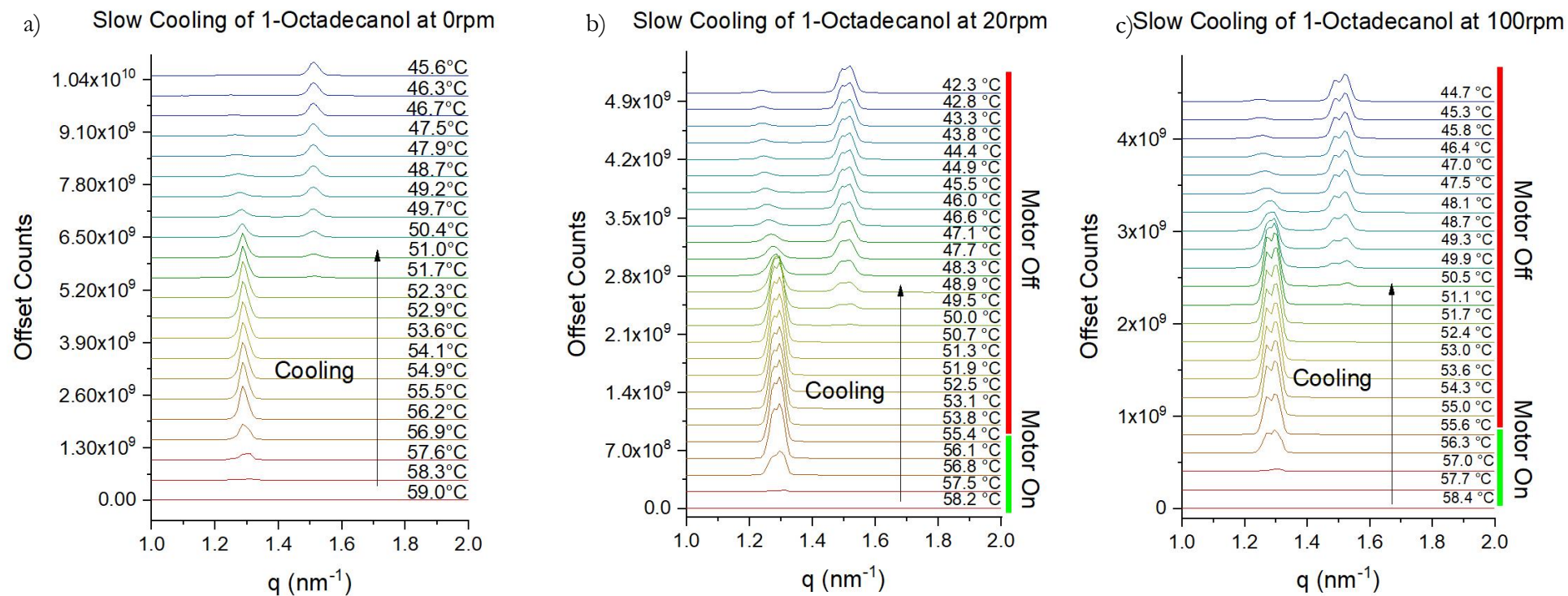


Figure 7-8 1st Order Crystallisation Peaks of 1-Octadecanol with a) no shear, b) shear @ 20rpm and c) shear @ 100rpm.

Heating of 1-Octadecanol at 100rpm

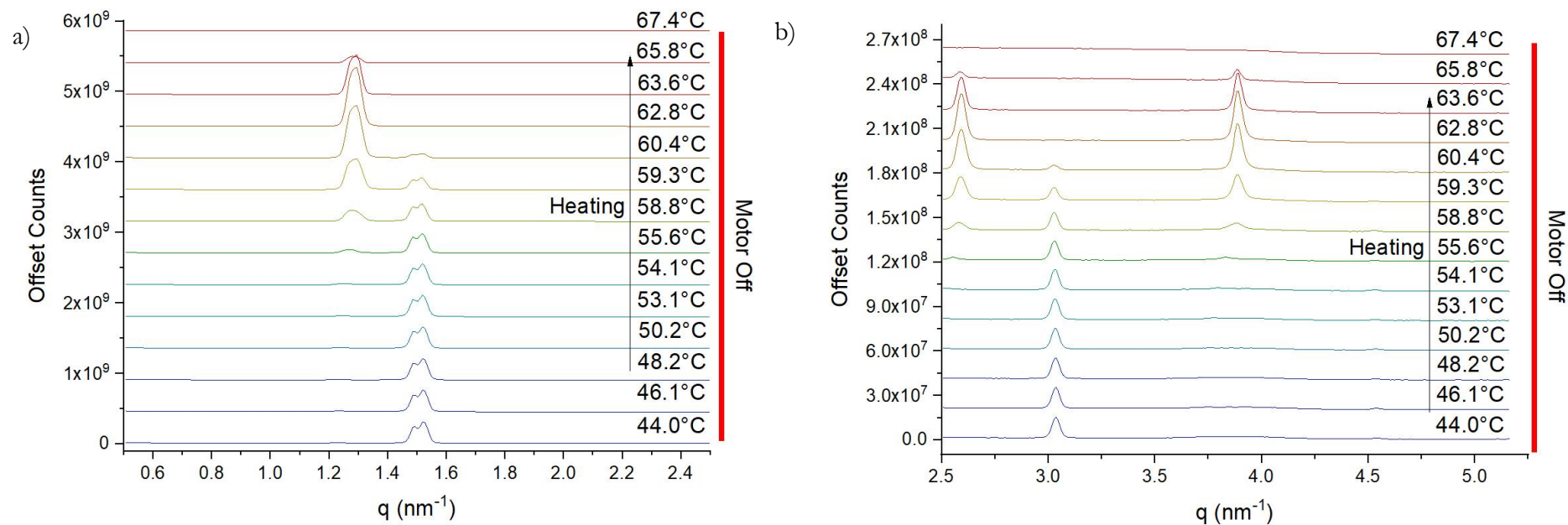


Figure 7-9 Heating 1-Octadecanol which had been at 100rpm under static conditions, a) 0.5-2.5 nm^{-1} and b) 2.5-5.75 nm^{-1} .

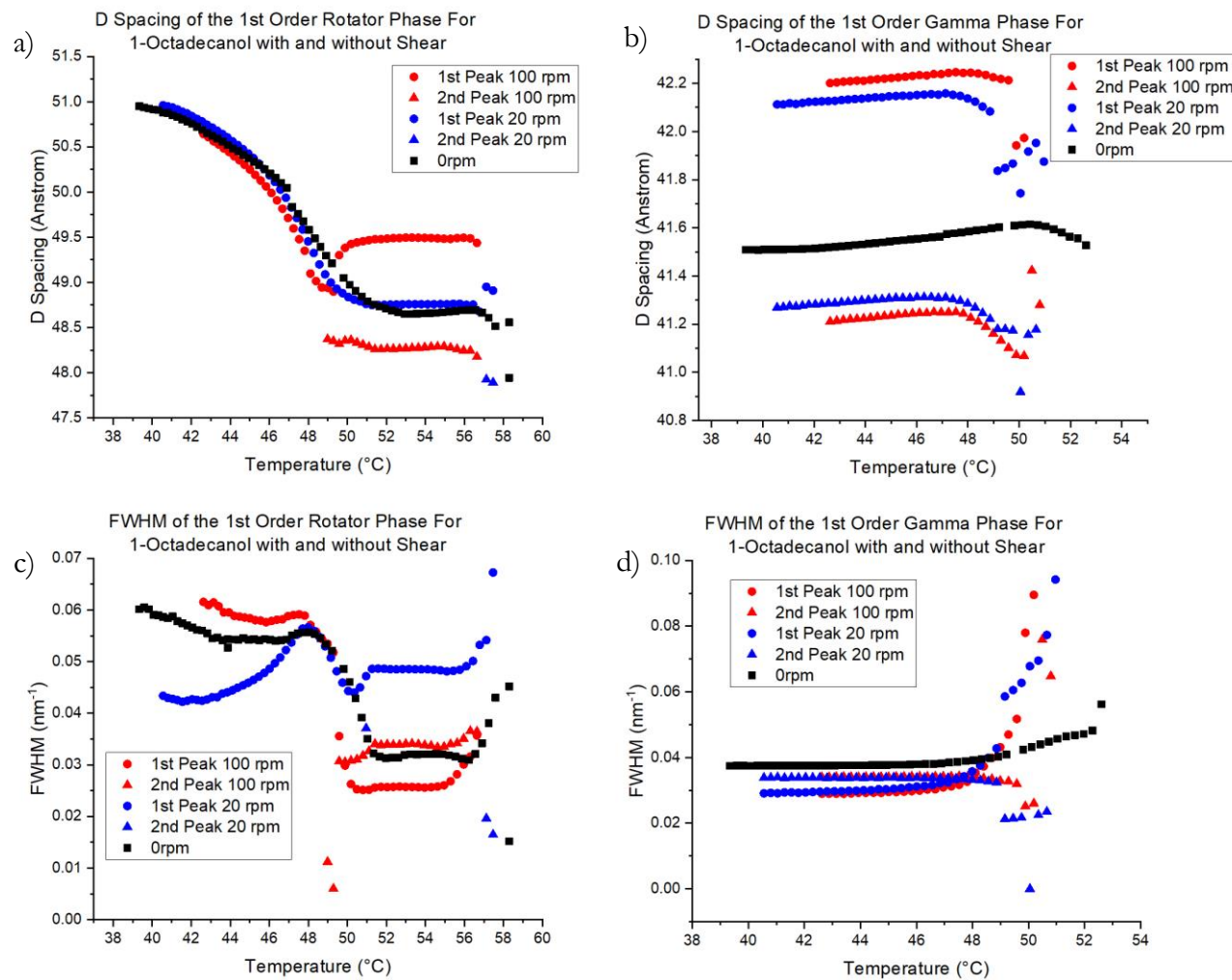


Figure 7-10 Variation in d spacing of a) rotator and b) gamma and Full-Width Half Maximum c) rotator and d) gamma phases of 1-Octadecanol upon cooling at different shear regimes

The apparent viscosity of the sheared 1-Octadecanol was measured by the Brookfield Viscometer whilst 1-Octadecanol was cooled from the melt and sheared at 100rpm. The viscosity profile with the changing 1st order peak area of the gamma and rotator phases is displayed in Figure 7-14 a). When 1-Octadecanol crystallises from the melt, the rotator forms first at 57.3°C and a viscosity of 1986 cP is detected. After 2 minutes of further cooling, the temperature reached 56.4°C, and the viscosity was at the limit of what the viscometer can measure at 43149 cP. This rapid growth in viscosity is entirely due to the growth in the rotator phase, and on further cooling, the spindle stops turning, due to solidification of the sample. At 50.5°C the gamma phase forms and by 48.7°C the rotator form disappears. The viscometer couldn't measure the physical properties of the 1-Octadecanol gamma phase; however, the physical properties of both the gamma and rotator phases can be measured for 1-Octadecanol in a solvent.

There was no evidence of peak spitting in gamma and rotator phases whilst crash cooling and shearing 1-Octadecanol at 100rpm. The rapid crystallisation kinetics meant 1-Octadecanol was only being sheared for 40 seconds before 1-Octadecanol solidified and the spindle stopped. In contrast on slow cooling, 1-Octadecanol was sheared for 3.5 minutes after it's first crystallised. This result could be explained if the smaller crystals formed during crash cooling are more resistant to shear or the short time period of shear was not long enough to alter the structure of the rotator phase.

The splitting of the rotator phase 1st order peaks most probably due to a phase separation caused by shearing 1-Octadecanol.

7.3.2 1-Octadecanol with Decamethylcyclpentasiloxane (D5) Solvent

1-Octadecanol in Decamethylcyclpentasiloxane (D5) solvent was studied at D5/OCT (0.2/0.8) and (0.8/0.2) mole fractions with shear applied at 0rpm, 20rpm, and 100rpm. D5 is used in industry as the main solvent, but 1-Octadecanol is poorly soluble in D5 as discovered in the turbidity studies shown in Figure 5-4. 1-Octadecanol in D5 has been studied using the DSC and results are displayed in Chapter 6.

7.3.2.1 1-Octadecanol with Decamethylcyclpentasiloxane (D5) Solvent under Static Conditions

When looking at the DSC in Figure 6-21, the rotator phase is first seen to crystallise at 53.7°C as a broad peak, and at 49.5°C as a peak with a shoulder, for D5/OCT (0.2/0.8)

and (0.8/0.2) and the Gamma phase is seen to form at 50.9°C and 49.0°C for D5/OCT (0.2/0.8) and (0.8/0.2) mole fractions respectively. Due to the X-ray absorbing nature of D5, no structural signal could be observed for the D5/OCT (0.8/0.2) mole fraction sample, so we can only analyse the X-ray pattern from the D5/OCT (0.2/0.8) mole fraction sample.

X-ray data for cooling 1-Octadecanol in D5, under static conditions is displayed in Figure 7-11 a). D5/OCT (0.2/0.8) mole fraction has a similar relative intensity for the rotator and gamma phase as 1-Octadecanol without solvent, with the rotator phase being the most intense 1st order peak. This is possibly due to 1-Octadecanol being poorly soluble in D5.

Interestingly the presence of D5 solvent has caused peak splitting of 1-Octadecanol's rotator and gamma phase under static conditions. The peak splitting is similar to that created by the mechanical shear of 1-Octadecanol. The rotator phase is first seen to crystallise at 54.9°C (1.3027 nm^{-1}) and a lower q shoulder appears at 53.8°C (1.2705 nm^{-1}) then decreases the intensity with cooling. The rotator phase slowly shifts to lower q after the gamma phase forms. The gamma phase first crystallises as two 1st order peaks at 1.4863 nm^{-1} and 1.5195 nm^{-1} and upon further cooling the higher q peak gains a higher intensity relative to the lower q peak.

Upon heating under static conditions, the lower q peak of the split gamma phase drastically decreases in intensity close to the melting point at 61.1°C in Figure 7-12 a). This could be a sign that the gamma phase undergoes an annealing atomic rearrangement before melting. Before melting, a low-intensity rotator phase forms at 54.2°C, however complete conversion from the gamma to the rotator phase before melting was not observed, as seen when melting pure 1-Octadecanol in Figure 7-12.

7.3.2.2 1-Octadecanol with Decamethylcyclpentasiloxane (D5) Solvent Under Shear Conditions

The 1st order crystallisation X-ray peaks formed upon shear are displayed in Figure 7-11 b) 20rpm and c) 100rpm. The 1-Octadecanol and D5 mixture is softer than pure 1-Octadecanol allowing for the viscometer to be on during the whole cooling experiment. Previously we have discussed how a shoulder is seen to form in the rotator phase, and two peaks form in the gamma phase when cooled under static conditions. Increasing shear seems to make the shoulder appearance in the rotator phase more prominent. The rotator phase, however, does not split into two distinct peaks when sheared in contrast

to pure 1-Octadecanol. This could be due to the 1-Octadecanol soft rotator phase combined with the solvent having a lower viscosity, reducing the energy put into the system by the viscometer. Another factor could be that the solvent molecules surround the 1-Octadecanol rotator phase structure, acting as a lubricant and dissipate the energy inputted into the system. The gamma phase exhibits much more rigid, harder mechanical properties and appears to be altered by shear. The gamma phase of 1-Octadecanol in D5 without shear exhibits two 1st order peaks at 1.4863 and 1.5195 nm⁻¹. At 48°C the lower q gamma phase peak grows in intensity with increasing shear, relative to the higher q peak, until at 100rpm the lower q peak has a larger intensity than the higher q peak. Upon cooling and shearing at 100rpm, the gamma phase initially forms at 53.3°C with the high q split peak having the greatest intensity. On further shearing and cooling the relative intensity of the split peaks invert, demonstrating the peak splitting is linked shearing.

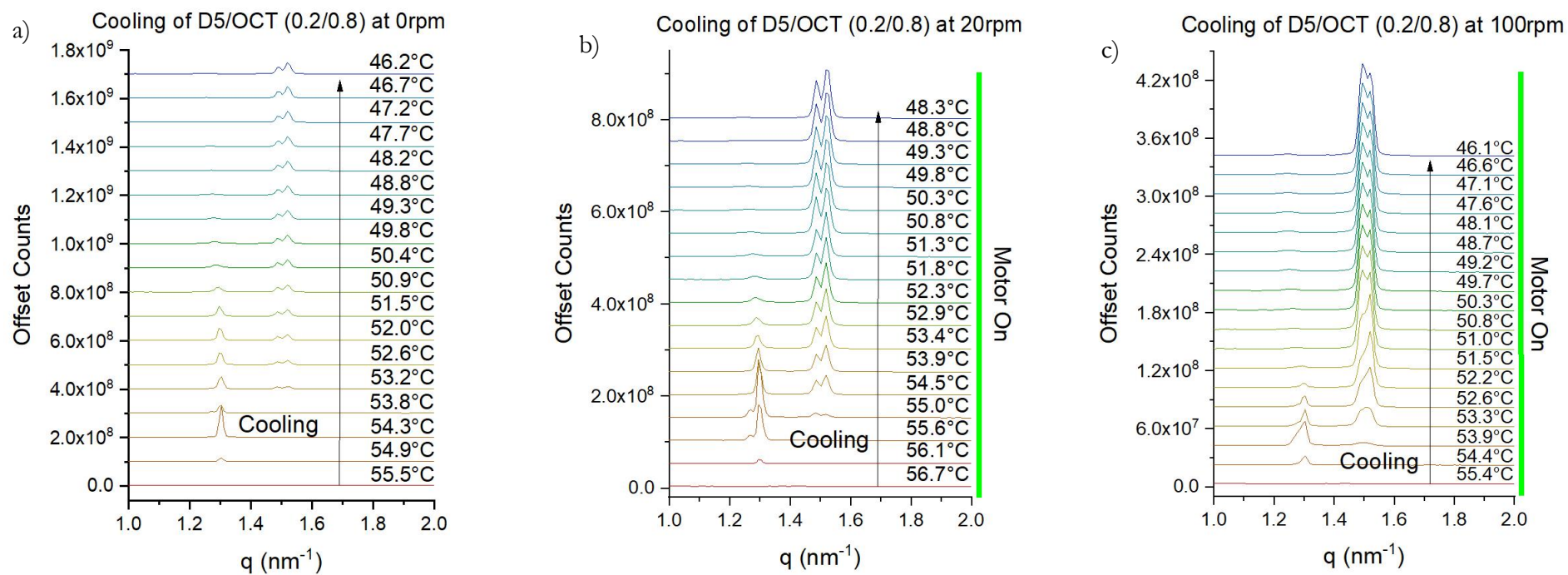


Figure 7-11 1st Order Crystallisation Peaks of D5/OCT (0.2/0.8) with a) no shear, b) shear @ 20rpm and c) shear @ 100rpm

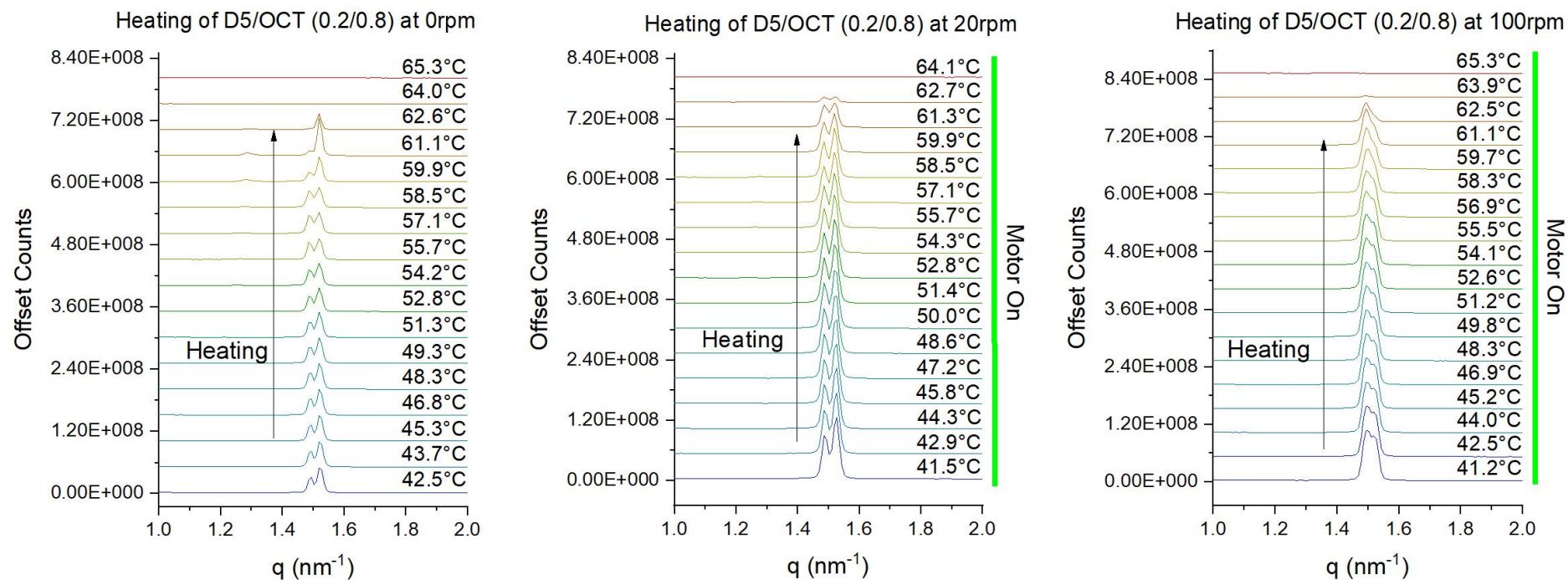


Figure 7-12 1st Order Melting Peaks of D5/OCT (0.2/0.8) with a) no shear, b) shear @ 20rpm and c) shear @ 100rpm

As seen in Figure 7-13, increasing shear rate shifts the rotator phase to increasingly larger d spacing and FWHM at 54°C and decreasing temperature increases the d spacing of the rotator phase at 0rpm and 20rpm. At 100rpm the rotator phase intensity was the weakest, allowing only 4 data points to be fitted to the Gaussian curve and displays a decrease in d spacing upon increasing temperature. The trend is less clear when looking at the d spacing of the split gamma phase peaks. The d spacing split between the two peaks increases when the sample is sheared 20rpm, relative to the sample cooled under static conditions. This trend fails to continue when the sample was sheared at 100rpm; in fact, the distance between the two peaks becomes smaller. This trend possibly fails to continue, due to the inversion in peak intensity at shear rates beyond 20rpm. The FWHM increases upon increasing shear rate for the gamma phase. Gamma phase d spacing slightly decreases with decreasing temperature and the FWHM stays fixed with respect to temperature, apart from a step increase in FWHM and decrease in d spacing at 45°C for 100rpm. This step-change may be because of a shear-induced phase transition.

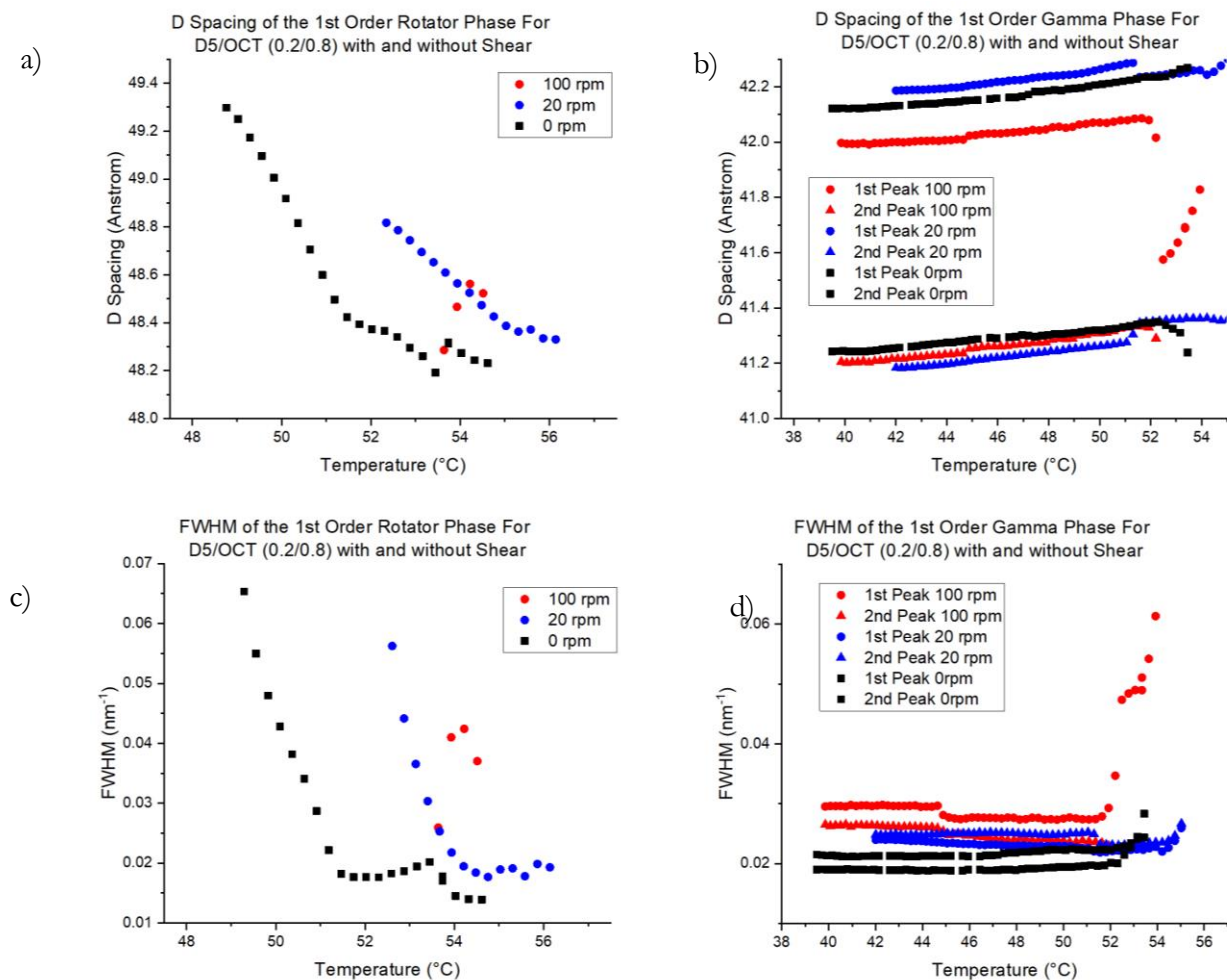


Figure 7-13 Variation in d spacing of a) rotator and b) gamma and Full-Width Half Maximum c) rotator, d) gamma phases of D5/OCT (0.2/0.8) mole fraction upon cooling at shear regimes of 0rpm, 20rpm, and 100rpm.

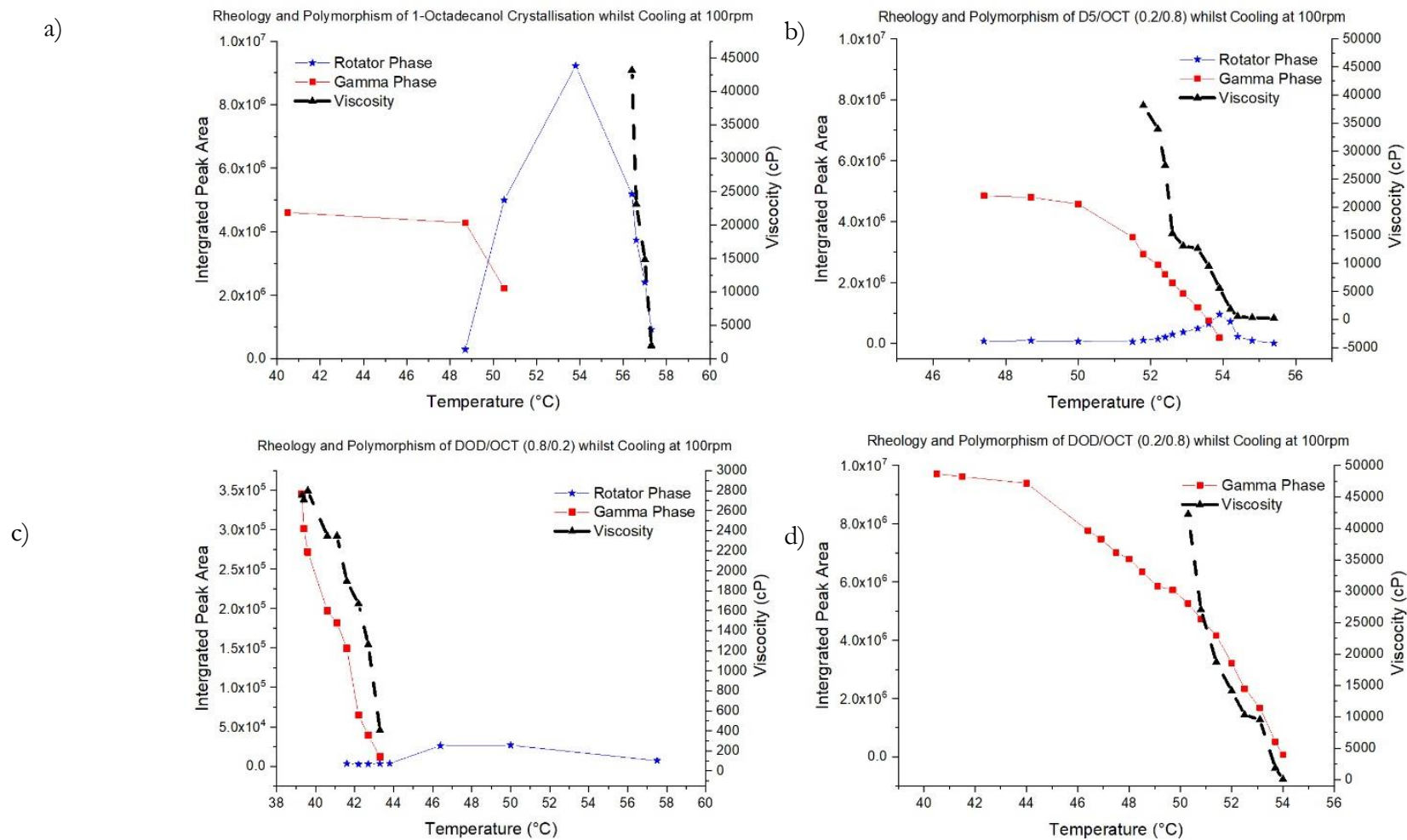


Figure 7-14 Displaying relationship between viscosity measured using Brookfield viscometer and changing peak area of the 1st order 1-Octadecanol gamma and rotator phases with and without solvent being formed during slow cooling. a) Pure 1-Octadecanol, b) D5/OCT (0.2/0.8), c) DOD/OCT (0.8/0.2) and d) DOD/OCT (0.2/0.8) mole fraction.

D5/OCT (0.2/0.8) is first seen to crystallise in the rotator phase at 55.4°C with a viscosity of 226 cP in Figure 7-14. Between 55.4°C and 54.2°C the viscosity only increases to 1851 cP over a 2 minute period allowing the binary mixture to behave as a structured liquid. At 53.9°C, the viscosity starts increasing rapidly due to the formation of the gamma phase, as the structure becomes a rigid solid. The Brookfield viscometer's measuring limit is reached at 51.8°C at a viscosity of 38140 cP, after cooling for 6 minutes.

7.3.3 1-Octadecanol with Dodecane Solvent

1-Octadecanol was studied in mixtures with Dodecane at DOD/OCT (0.2/0.8) and (0.8/0.2) mole fraction, under static conditions and shear at 100rpm. Solubility studies of 1-Octadecanol in Dodecane have been carried out using polythermal turbidity studies (Chapter 5), and the binary phase diagram has been produced using DSC in Chapter 6, Figure 6-16. Unlike D5, 1-Octadecanol is soluble in Dodecane and can be fully dissolved at 0.2 mole fraction at temperatures over 45.7°C.

7.3.3.1 1-Octadecanol with Dodecane Solvent Under Static Conditions

At low concentrations of Dodecane, DOD/OCT (0.2/0.8) mole fraction, the DSC displays two peaks upon cooling at 1 degree per minute, corresponding to the crystallisation of the rotator phase at 52.3°C and solid-solid transition between rotator to gamma phase at 49.6°C.[53] When looking at the X-ray pattern, the obvious observation is that the 1st order rotator phase has a very low intensity relative to the gamma phase. This is due to the 1-Octadecanol rotator phase having a very high solubility in Dodecane of approximately 11.8kg per litre of solvent at 56°C, with DOD/OCT (0.15/0.85) being a saturated solution. Figure 7-15 shows the result of a turbidity experiment where Dodecane was added to 1-Octadecanol present in the rotator phase at a fixed temperature of around 56°C. When the scale of the graph is reduced, it's clear a 1st order rotator phase is still present; however, the 2nd and 3rd order rotator phase peaks cannot be seen upon cooling DOD/OCT (0.2/0.8). The rotator phase is first seen to form at 57.4°C (1.2788nm⁻¹), the gamma form first appears at 53.8°C (1.4946nm⁻¹), and the rotator form decreases in peak intensity, becomes broader whilst shifting to lower q at 48.2°C. The reason for the greatly reduced intensity must be that a large proportion of 1-Octadecanol rotator will be in solution.

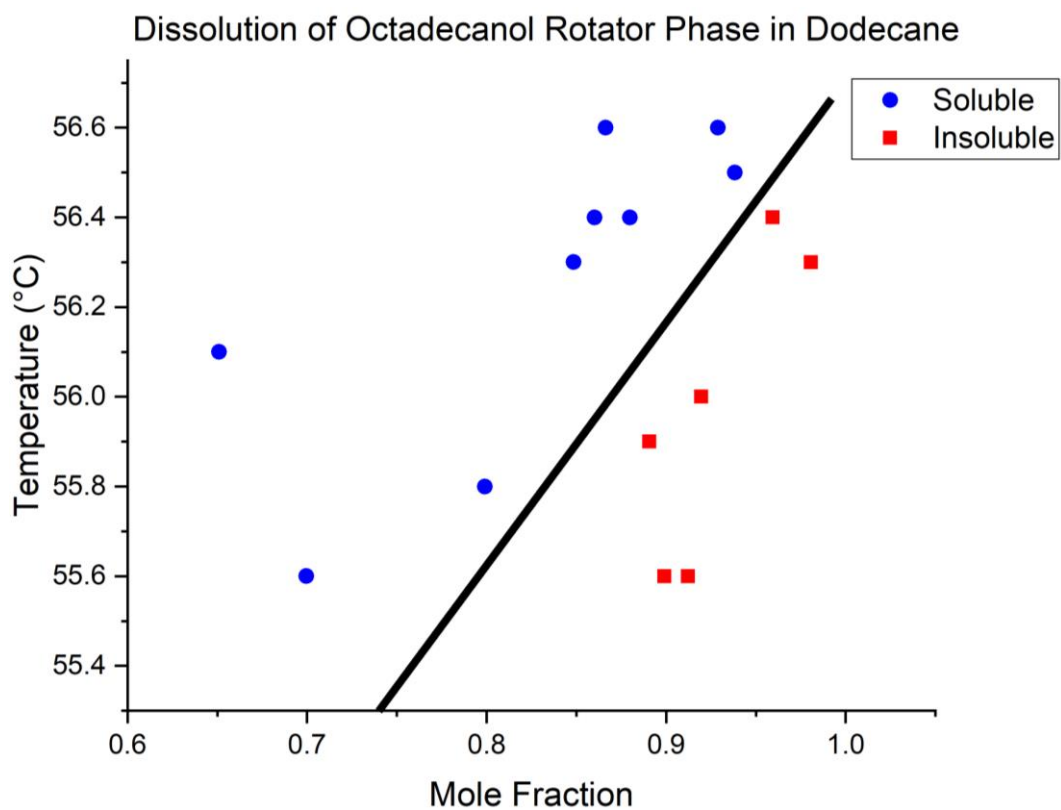


Figure 7-15 Turbidity study to measure the solubility of 1-Octadecanol's rotator phase in Dodecane

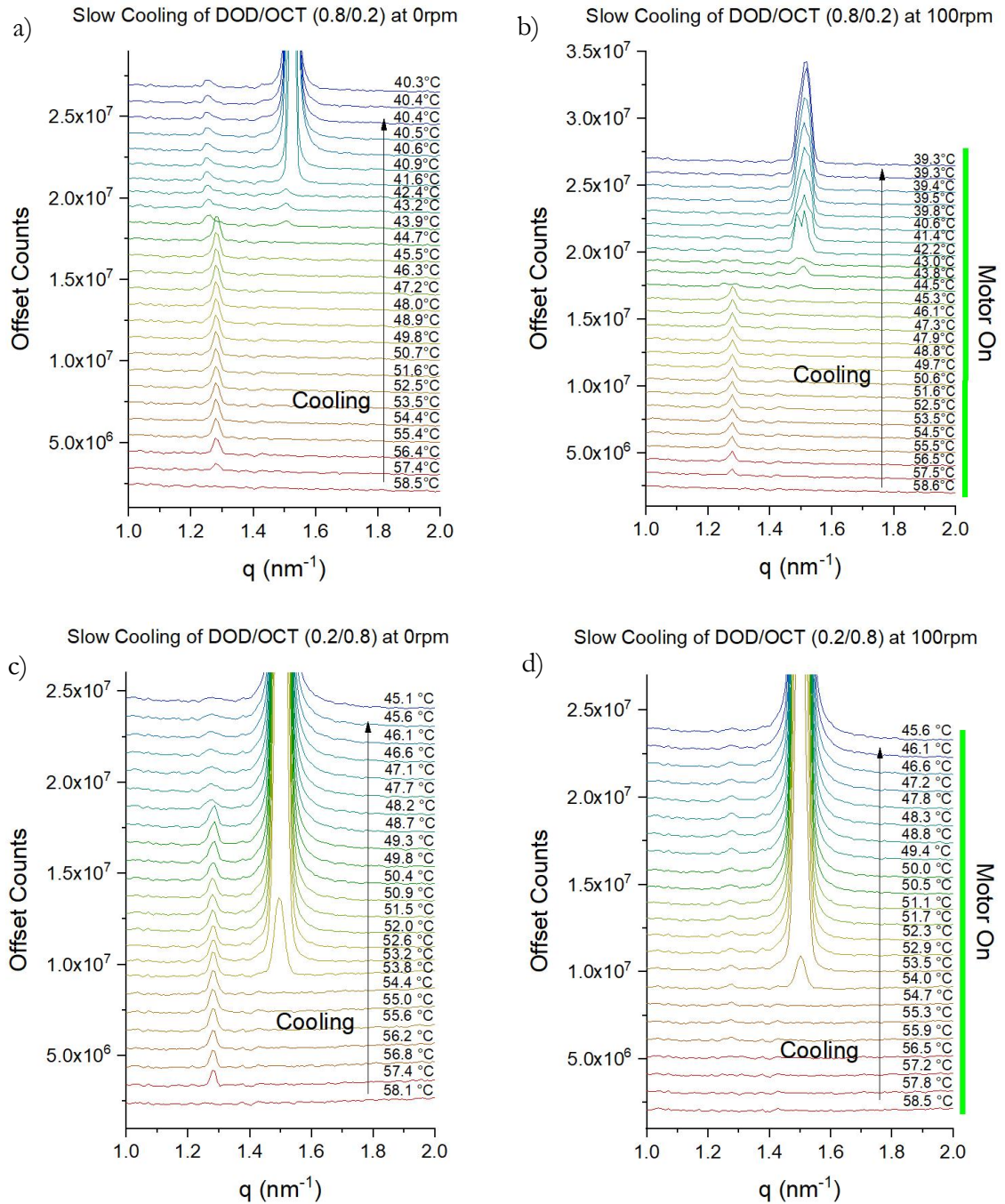


Figure 7-16 1st order rotator and gamma phases of 1-Octadecanol upon slow cooling when sheared. Dodecane/1-Octadecanol (0.8/0.2) at a) 0rpm and b) 100rpm shear. Dodecane/1-Octadecanol (0.2/0.8) at c) 0rpm and d) 100rpm shear.

Only a single peak is observed at 38.5°C in the DSC of DOD/OCT (0.8/0.2) upon cooling from the melt at 1°C per minute in Figure 6-15. This suggests that only one phase transformation is occurring. Examining the X-ray data in detail shows the crystallisation of the rotator form at 56.7°C (1.2788 nm^{-1}) and the formation of the gamma phase at 44.2°C (1.5112 nm^{-1}) in Figure 7-16. Upon the formation of the gamma phase to rotator phase shifts to lower values of q . Between 44.2°C and 41.9°C, there is a region where both the gamma and rotator phases are present, but both have low intensity. At

41.9°C the intensity of the gamma phase peak greatly increases and the peak shifts to higher q (1.5278 nm^{-1}). Turbidity studies found the crystallisation temperature of DOD/OCT (0.8/0.2) to be 42.68°C and the rotator/gamma phase detected between 56.7-41.9°C must be in a liquid crystalline phase. At 41.9°C the solid crystalline gamma phase structure forms and the intensity of the gamma phase reflection sharply increases.

7.3.3.2 1-Octadecanol with Dodecane Solvent Under Shear Conditions

DOD/OCT (0.8/0.2) and (0.2/0.8) mole fractions were studied under no shear conditions and at shearing at 100rpm. Shear causes a drastic decrease in peak intensity of the crystalline gamma phase formed at DOD/OCT (0.8/0.2). No peak splitting was observed in the rotator phase or the gamma phase, apart from briefly at 42.2°C in the 1st order gamma phase with the DOD/OCT (0.8/0.2) mole fraction sample under shear. No clear rotator phase peaks were observed for the DOD/OCT (0.2/0.8) mole fraction sample when sheared; however, the rotator phase could be distinguished at (0.8/0.2) mole fraction upon shear.

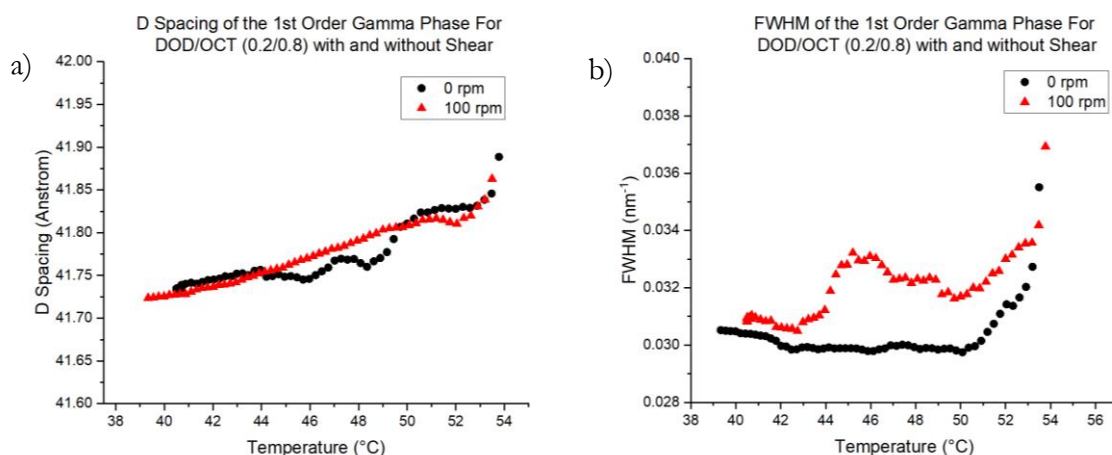


Figure 7-17 Variation in a) d spacing and b) FWHM with temperature and shear of 1st order gamma phase of Dodecane/1-Octadecanol (0.2/0.8).

The d spacing position of the gamma phase peak does not seem to be impacted by shear, as seen in Figure 7-17. Shear at 100rpm, however, does increase the FWHM of the gamma phase peak upon cooling.

Previously in this chapter, we covered how the rotator phase of 1-Octadecanol is inhibited by Dodecane. In Figure 7-14, the viscometer only senses a viscosity for DOD/OCT (0.8/0.2) and (0.2/0.8) when the gamma phase forms. The gamma phase exhibits rigid crystal lattice, resulting in solid hard mechanical properties. There is no structured liquid region, as exhibited by D5/OCT (0.2/0.8) and the viscosity rapidly rises

after the viscosity is first measured by the viscometer. If we compare the temperature a viscosity reading is measured first by the viscometer for D5/OCT (0.2/0.8) (55.4°C) and DOD/OCT (0.2/0.8) (54.0°C), it's clear that Dodecane's dissolution of the rotator phase has a large impact on the temperature the melt begins to structure. The gamma phase forms at a similar temperature for D5/OCT (0.2/0.8) (53.9°C) and DOD/OCT (0.2/0.8) (54.0°C), demonstrating that it is not affected by the change of solvent at this mole fraction. At high concentrations of Dodecane such as DOD/OCT (0.8/0.2), the viscometer can only measure a viscosity when gamma phase forms at 43.3°C, despite the rotator phase first being detected at far higher temperatures of 57.5°C, suggesting liquid crystal behaviour. As seen in Figure 7-15, the rotator phase has a high solubility in Dodecane, preventing precipitation from solution.

Upon crash cooling, no changes to the crystal structure were observed, compared to when slowing the sample. Upon heating, the rotator phase can be observed upon the melting of DOD/OCT (0.8/0.2) and (0.2/0.8) under static and shear conditions.

7.4 Discussion

The crystallisation behaviour of n-alkanols is known and very similar to the crystallisation of n-alkanes. In general, it follows the following path upon cooling of liquid phase → rotator form → solid. The solid crystal structure of n-alkanols is known to be a gamma phase for even chain lengths and beta phase for odd chain lengths.[53] In the literature, there are a couple of previous studies of n-alkanol binary mixtures including Steric acid[140] and Peanut Oil[57, 87]; however no previous studies have involved shear. The DSC showing the cooling of 1-Octadecanol and Dodecane binary mixture is very similar to a previously published DSC of Eicosane and Peanut Oil. Both DSC studies show two exothermic peaks form upon cooling at low solvent concentration and higher temperature and at high solvent concentration the two peaks have converged to form a single exothermic peak at a low temperature. In the X-ray synchrotron experiments, we found that the presence of Dodecane drastically reduced the intensity of the rotator phase of 1-Octadecanol when cooling under static conditions. This result was supported by the online viscosity measurement, were DOD/OCT (0.2/0.8) and D5/OCT (0.2/0.8) mole fraction became structured at 54.0°C (gamma phase formation) and 55.4°C (rotator phase formation) respectively. The viscosity profile for 1-Octadecanol in Dodecane shows a sharp increase viscosity, due to the rigid nature of the solid gamma phase. D5 is an ideal solvent for 1-Octadecanol to structure since the rotator phase is not inhibited

and a structured flowing liquid is formed between 55.4 - 54.2°C. This is desirable when processing cosmetics since the viscosity achieved is high enough to prevent formulation separation and low enough for the formulation to flow with no trapping of air bubbles upon filling of canisters.

Shear was found to have no effect on the crystallisation temperature of 1-Octadecanol when sheared $5\text{s}^{-1} - 1000\text{s}^{-1}$, whilst cooling at 10°C per minute. This suggests that the crystallisation was thermodynamically rather than kinetically driven. 1-Octadecanol was sheared whilst cooling during the formation of the rotator phase. The shear resulted in the splitting of the 1st order rotator form and gamma form upon further cooling under static conditions. However, the split gamma forms a single peak rotator form upon heating under static conditions. This could be explained by the gamma phase converting directly from the rotator phase when cooling, but on heating, the extra energy available in the system may allow the most stable rotator phase arrangement to be reached. Also, the shear rate was found to influence the relative intensity of the split peaks, peak definition, and splitting size. In my literature search, I haven't found any similar splitting induced by shear, but it's clear this splitting phenomenon is not only caused by shear. D5 solvent also causes splitting of the 1-Octadecanol's gamma phase under static conditions. One theory that could explain this would be that upon cooling of 1-Octadecanol, D5 cyclic molecules become trapped between the layers of the newly formed 1-Octadecanol gamma phase crystalline structure, creating strain within the structure. One example of solvent changing the solid phase of an n-alkanol is with Eicosane in Peanut Oil, where Eicosane's solid form changed from gamma to beta upon the increasing level of Peanut Oil.

7.5 Conclusion

In this chapter, solvent selection and shear conditions have been shown to be crucial to the processability of cosmetic products. Through understanding the influence solvent and shear on the polymorphic forms of the structuring ingredients present, the rheology profile of the formulation upon cooling can be designed and fine-tuned. D5/OCT (0.2/0.8) mole fraction upon cooling has been found to behave as a structured liquid between 55.4-54.2°C after the rotator phase has crystallised, before solidifying at 54.0°C once the gamma phase forms. This structured liquid rheology behaviour is critical for the production of many cosmetic products. The combination of shear and Dodecane has been found to reduce the presence of the rotator phase of 1-Octadecanol at 0.8 mole

fraction and to cause the rheology profile to change through destroying the structured liquid behaviour. The peak splitting is likely an indication of a phase separation occurring within the existing gamma and rotator phases of 1-Octadecanol and appears to be influenced by both solvent and shear conditions. In the future, we would like to understand further the causes of peak splitting and why the rotator phase inhibited by certain solvents. This understanding will help improve cosmetic product performance whilst aiding processing.

Chapter 8 Conclusions

This section brings together all the findings from all the results chapters to form a conclusion based on all the work completed in this project. The findings are compared against the original, aims and objectives before future work ideas are presented.

8 Conclusions

8.1 Introduction

The work detailed in earlier chapters aims to extend fundamental knowledge of how process parameters impact the crystallisation, polymorphism and physical properties of long chain hydrocarbon structuring ingredients. Formulation science is developed through an iterative process using trial and error. As a result, little fundamental research has been carried out regarding mixtures of long chain hydrocarbon formulation ingredients. This research was carried out using a methodical approach, first gaining an understanding of the individual materials, before studying the ingredients in their mixtures.

The four result chapters in this thesis aim to investigate long chain hydrocarbon structuring ingredients using an array of approaches and techniques from different viewpoints and fields. The foundation work for this study was completed in Chapter 4, with the chosen long chain structuring industrial samples, 1-Octadecanol, Hydrogenated Castor Oil (HCO) and Petrolatum being characterised using a whole host of different techniques. Chapter 5 investigates the crystallisation behaviour of 1-Octadecanol and HCO in a range of polar and non-polar solvents using the polythermal method, optical microscopy and electron microscopy. Different analysis approaches were employed to probe the thermodynamics, nucleation kinetics and morphology of the crystals. The knowledge gained from characterising the individual structuring materials combined in chapter 4 with the solution crystallisation studies in chapter 5 provides a basis for the following binary mixture and shear studies to build from. Chapter 6 provides an insight into the thermal behaviour and physical properties of the structuring ingredients in their binary mixtures using a combination of phase diagrams and AFM. Chapter 7 investigates the impact of shear and solvent present in the crystal structure of 1-Octadecanol using a custom designed and manufactured on-line shear cell.

These experimental studies are concluded by focusing on the links between process conditions, crystallisation, polymorphism, and physical properties. This chapter ends with a review of the original aims and objectives before finally suggesting future work based on the outcomes of this study.

8.2 Conclusions Focused on Relationships between Process Parameters, Crystallisation, Polymorphism and Physical Properties of Wax Stick Structuring Ingredients

8.2.1 Characterisation of the Structuring Long Chain Hydrocarbon Ingredients

8.2.1.1 Polymorphism

The polymorphism of the structuring ingredients 1-Octadecanol, Petrolatum and HCO were characterised using a combination of thermal analysis, X-ray diffraction, microscopy and chromatography with reference to the literature. In the literature, polymorphism of alkanes and alkanols are reported to be very similar, with both systems converting from liquid → rotator phase (metastable) → solid phase (stable) upon cooling from the melt. When cooling 1-Octadecanol, these transitions are very distinct with sharp peaks detected using DSC, Clear XRD pattern and clear visual change observed with the hot-stage microscope. Petrolatum, however, contains a complex mixture of different straight chain length alkanes as defined by GC analysis and only the net result of all the phases transitions can be detected, giving an extremely broad exothermic DSC crystallisation peak and an amorphous XRD pattern, with no clear peaks detected.

The polymorphism of HCO, specifically, has not been previously reported in the literature; however, the polymorphic behaviour of triglycerides, in general, has been reported.[36] Tristearin has a very similar structure to HCO minus three hydroxyl groups. The β' tristearin XRD pattern in the literature is remarkably like the room temperature pattern of HCO, and the morphology is observed to be spherulites, suggesting HCO is in a β' polymorph. The XRD pattern of HCO does not change between 53°C and 33°C implying it remains in the same polymorph over this temperature range. This is supported by HCO only having one sharp crystallisation peak in the DSC upon cooling.

8.2.1.2 Physical Properties

HCO, Petrolatum and 1-Octadecanol all exhibit very different physical properties despite crystallising at a similar temperature between 57.1°C and 68.2°C. The crystallising temperature of these materials would have been one of the main reasons these materials were chosen to be used in wax deodorant stick formulations. Melting and Crystallisation

temperature is influenced by the molecular interactions present. HCO and Petrolatum achieve this melting point, due to containing relatively large molecules with stronger van der Waal's interactions. 1-Octadecanol is a smaller molecule with weaker van der Waal's forces; however, it makes up for this by also exhibiting hydrogen bonding, due to the presence of a hydroxy group at the end of the molecule.

The rheological properties and mechanical hardness of the materials have been measured using a rheometer and AFM. At room temperature, Petrolatum has the properties of a thick gel, and HCO and 1-Octadecanol are both solids. 1-Octadecanol was found to be measurably harder than HCO with Young's modulus at room temperature being 1.43 and 0.32 GPa respectively. This was likely to be due to the stronger intermolecular forces and higher material purity of 1-Octadecanol. The hardness of each material at room temperature was found to be independent of the cooling rate, and all the materials were found to have shear thickening behaviour when studied at a range of shear rates at a range of different temperatures.

8.2.1.3 Solubility

Solubility studies were only completed on HCO and 1-Octadecanol as they are both solids at room temperature. HCO and 1-Octadecanol were found to be more soluble in polar solvents, than non-polar solvents and of the polar solvents tested, both materials proved to be more soluble in protic than aprotic polar solvents. HCO was found to be far less soluble in all solvents tested than 1-Octadecanol and proved to be completely insoluble in non-polar solvents. This was rationalised by 1-Octadecanol being a simple straight long chain molecule with both non-polar and polar features at opposite ends, allowing it to interact positively with both polar and non-polar solvents. HCO, on the other hand, has a complex molecular structure with three legs and polar and non-polar features. The combination of having a complex structure and the non-polar and polar features makes it interact poorly with both polar and non-polar solvents.

8.2.1.4 Crystallisation Thermodynamics and Kinetics

van 't Hoff analysis was employed to reveal the dissolution thermodynamics of the system and the KBHR method was used to calculate the nucleation kinetics.

van 't Hoff analysis revealed high solubility systems such as 1-Octadecanol in Ethanol, were the closest to ideality and low solubility systems such as HCO in Acetone was the

least ideal. High solubility systems had lower dissolution values of enthalpy and entropy, compared to low solubility systems.

KBHR analysis showed that the nucleation mechanism of HCO and 1-Octadecanol in all solvents was progressive, with HCO having the most progressive mechanism. Nucleation parameters have been successfully calculated for all the progressive systems.

8.2.1.5 Crystal Morphology from the Melt and Solution

Crystal morphology of the wax hydrocarbons was investigated using hot-stage microscopy, crystal growth cell, SEM and AFM. Upon cooling from the melt, both 1-Octadecanol and Petrolatum display needle-shaped crystals upon initial crystallisation. Randomly oriented 1-Octadecanol needle crystals display rapid growth through the melt, developing a crystal network within the melt before complete solidification occurs. Upon further cooling, the rotator phase to solid gamma phase transition was observed, where transparent regions of the bulk suddenly appeared opaque under the microscope. Petrolatum displays slow crystal growth with increasing density of needle crystals floating throughout the melt upon cooling, as increasingly smaller chain length fractions crystallise out of the melt. HCO forms spherulites upon initial crystallisation, and these crystals appear as Maltese crosses under cross polarised light.

The surface topography of 1-Octadecanol and HCO upon cooling from the melt was studied using AFM. The surface of 1-Octadecanol consists of a series of flat plates with sharp steps between plates. The spherulites on the surface of HCO have been mapped out, displaying doughnut-like topography and have been observed to decrease in size with increasing cooling rates.

Crystals formed from solution have been imaged using SEM and a crystal growth cell. The single crystal of 1-Octadecanol formed in Dodecane solution has been observed to be a rectangular plate with two opposite fast-growing faces and two opposite slow growing faces. HCO spherulites are spherical and appear in clusters. Irregular spherulites have been imaged alongside regular spherulites.

8.2.2 Combining of Formulation Ingredients in Mixtures

The thermal behaviour of binary mixtures of HCO + 1-Octadecanol and Petrolatum + 1-Octadecanol have been captured using DSC. Phase diagrams have been derived from the thermal behaviour information with each phase being identified with reference to literature and variable temperature XRD. Thermal behaviour respect to the composition

for Petrolatum + 1-Octadecanol was similar to previously reported thermal behaviour of 1-Eicosanol + Peanut Oil in literature. The phase diagram is shaped by the highly soluble nature of the n-alkanol rotator phase and the fact it remains in solution at high solvent concentrations.

HCO and Petrolatum are immiscible; hence, no binary phase diagram was created. If a tertiary phase diagram were to be made, I would expect there to be a region where all three components mix, since HCO is soluble in 1-Octadecanol and 1-Octadecanol is soluble in Petrolatum.

AFM was used to probe the mechanical properties and morphology across a range of HCO + 1-Octadecanol compositions. The morphological and mechanical property information was superimposed on the phase diagram. Four distinct types of morphology were identified: HCO spherulites, HCO/1-Octadecanol eutectic mixture, HCO soft plates, and 1-Octadecanol hard plates. HCO was found to crystallise as plates as opposed to spherulites in the presence of 1-Octadecanol. The eutectic mixture consisted of HCO spherical grains surrounded by 1-Octadecanol. This was likely due to the fact HCO was dissolved in 1-Octadecanol, rapidly crashing out of solution at the eutectic point. A similar morphology was observed for HCO present in the eutectic mixture and upon being crash cooled from the melt at 20°C/min. 1-Octadecanol is known to have a higher Young's modulus allowing the regional composition of surface to be identified. AFM was proven to be excellent at determining the relative hardness of the surface, but less reliable at benchmarking mechanical properties across a range of compositions due to surface roughness and calibration induced errors.

8.2.3 Influence of Shear and Solvent on Crystal Structure of Formulation Ingredients

Temperature controlled rheological measurements showed that the shear rate had no impact on the crystallisation temperature of 1-Octadecanol measured upon cooling at 10°C/min. This result suggests at this cooling rate; crystallisation was thermodynamically driven rather than kinetically driven.

A custom shear cell was designed and built specifically for this study to provide simultaneous on-line structural, rheological and temperature measurements under a range of different process conditions. The shear cell was proven to work effectively with

a simpler and more compact design than previous shear cells used by the Roberts group, essential for carrying out experiments on a different continent.

Shearing of pure 1-Octadecanol upon cooling whilst performing online structural measurements resulted in the splitting of the 1st order rotator phase X-ray diffraction peak. Due to solidification of the sample, the motor was turned off to avoid it burning out before the gamma had formed. Under static conditions the split the rotator phase converted into a split gamma phase on further cooling. This demonstrates that the rotator phase must have acted as a template for the newly formed gamma phase. Increasing shear rate was found to increase split peak separation, definition and intensity.

No peak splitting of the pure 1-Octadecanol's rotator and gamma phase was observed upon cooling under static conditions, however, upon the addition of D5 solvent, a similar peak splitting behaviour was observed. Upon addition of Dodecane to 1-Octadecanol in contrast, caused no peak splitting under both static and shear conditions when cooling from the liquid phase.

Upon addition of Dodecane, 1-Octadecanol's rotator phase intensity decreases, further supporting the theory behind the 1-Octadecanol + Petrolatum, where the alkane solvent was thought to dissolve the rotator phase of 1-Octadecanol. On-line rheology measurements displayed a large disparity between the temperature which a crystal structure was first measured upon cooling 1-Octadecanol + D5 relative to 1-Octadecanol + Dodecane. As a result, the dissolution of the rotator phase was found to impact the viscosity profile measured upon cooling dramatically. When filling the wax deodorant canisters in the factory, viscosity is critical. If viscosity is too high, the mixture may become blocked in pipes and air can become trapped in the canister as it is filled. If the viscosity is too low, the formulation can separate, and the dissolution of the rotator phase makes viscosity more temperature dependent, increasing the difficulty of processing in the factory.

The splitting is likely to be an indication of a phase separation occurring within the rotator and gamma phases of 1-Octadecanol, which is induced by both shear and temperature. In previous studies on alkanes in Kevin Robert's crystallisation group have observed similar peak splitting behaviour under static conditions; however, I have found no explanation of what this phenomenon is previously in the literature.

Sheared mixtures were prepared on the rheometer before being studied using AFM. Shear mixed up the different morphologies contained within the sample and allowed 1-Octadecanol plates to be imaged next to HCO plates in the same image.

8.3 Revisiting the Original Aims and Objectives

Considering the original aims and objectives, the cooling rate has been found to influence polymorphism and morphology. The cooling rate has been observed to have an impact on crystal size with possible impact on surface roughness; however, this hasn't been measured. In the literature, crash cooling has been found to form a meta-stable n-alkanol polymorph at room temperature.

Shear has been found to modify the crystal structure and morphology of the formulation. Shear causes the redistribution of different crystal types, changing the morphology of the surface and induces a phase separation of the 1-Octadecanol rotator and gamma crystal structures.

The changing of formulation composition has found to impact solubility, crystallisation kinetics, crystal structure, morphology, rheology, mechanical properties, and thermodynamics. 1-Octadecanol, HCO and Petrolatum have been found to have very different solubility behaviour, crystallisation kinetics, crystal structure, mechanical properties, rheology, and thermodynamics. As a result, changing the proportion of each material has a massive impact on the final formulation. This has been experimentally demonstrated by creating phase diagrams and assessing variation in mechanical properties and morphology with respect to composition. For example, the morphology of HCO has been found to be modified by the presence of 1-Octadecanol.

Some objectives have not been met in this study, for instance, the impact of composition and process conditions on the performance of the final product. From this study, I can speculate how process conditions and composition can impact the final product performance; however, I haven't conducted experiments to support this. Also, no tertiary phase diagram was completed, which incorporates all three components.

8.4 Ideas for Future Work

The original aim of the project is to discover links between composition and process parameters with the resulting crystallisation, physical properties and product performance of the final was stick deodorant. The aims of this project were tailored to

specifically wax deodorant sticks; however, the findings of the research can be applied to food, pharmaceuticals and other industries that used combinations of alkanes, alcohols and triglycerides in their product formulations.

The findings of this project had an emphasis on the resultant the crystallisation and physical properties of the formulation. The next step would be to design a set of experiments to assess how the learnings of the study would affect the product performance. The product performance, however, can be a difficult task, because the perception of the product and how the product might be used will be different for each end user.

In industry, penetration testing is used to assess the mechanical properties of the bulk material and glide testing of semisolids, measuring deposition and friction gives insight into sensory feel performance. Through performing these industry-standard tests across the same compositions used to produce the phase diagrams in this study, allows links to be made between composition, surface morphology, phases present, mechanical properties of the bulk and sensory feel.

It also would be of interest to conduct mechanical and physical properties characterisation experiments on sheared and statically cooled 1-Octadecanol to assess what impact the observed phase separation of the gamma and rotator phases have on the physical behaviour of the material.

In this project, only binary phase diagrams were produced. The data from the binary phase diagrams could be combined and expanded to create a tertiary phase diagram between 1-Octadecanol, Petrolatum, and HCO. Further morphological, mechanical property and sensory data could be mapped out on the tertiary phase diagram to gain a complete overview of the system.

Chapter 9 Bibliography

9 Bibliography

1. Laden, K., *Antiperspirants and Deodorants, Second Edition*. 1999: Taylor & Francis.
2. Molina, M.J. and F.S. Rowland, *Stratospheric sink for chlorofluoromethanes: chlorine atom-catalysed destruction of ozone*. *Nature*, 1974. **249**: p. 810.
3. Schaefer, K., *Spray Deodorants Are Rehabilitated, With Help From Europeans*, in *The New York Times*. 2015.
4. Bunting, H., G.B. Wislocki, and E.W. Dempsey, *The chemical histology of human eccrine and apocrine sweat glands*. *The Anatomical Record*, 1948. **100**(1): p. 61-77.
5. Katsutoshi, A., et al., *Foot odor due to microbial metabolism and its control*. *Canadian Journal of Microbiology*, 2006. **52**(4): p. 357-364.
6. Quatralle, R.P., et al., *The mechanism of antiperspirant action by aluminum salts. II. Histological observation of human eccrine sweat glands inhibited by aluminum chlorohydrate*. *J Soc Cosmet Chem*, 1981. **32**: p. 107-36.
7. Quatralle, R.P., et al., *The mechanism of antiperspirant action by aluminum salts. I*. *J. Soc. Cosmet. Chem*, 1980(32): p. 67-73.
8. Farris, R.D., J.P. Luebbe, and G.J. Quinlivan, *Antiperspirant stick composition and process for preparing the same*. 1989, Google Patents.
9. Elsnau, W.H., *Antiperspirant stick*. 1977, Google Patents.
10. Wildgust, P., *Project proposal: Shear rate and cooling modeling for APDO stick wax crystallization*. 2014: Procter and Gamble.
11. Lewis, P., *Conversation with Procter and Gamble*. 2017.
12. Tanner, P.R., R.G. Nunn, and J.P. Luebbe, *Low residue antiperspirant sticks*. 1991, Google Patents.
13. Gamble, P.a. *P&G Body Care for Men*. 2019 [cited 2019 20th January 2019]; Available from: <https://www.pgshop.com/pgshop-his-body-deodorant/>.
14. Benson, H.A.E., et al., *Cosmetic Formulation: Principles and Practice*. 2019: CRC Press.
15. Sawin, P.A., J.P. Luebbe, and G.J. Quinlivan, *Deodorant cosmetic stick composition*. 1997, Google Patents.
16. Geary, D.C. and H. Kreveld, *Wax-like antiperspirant stick compositions*. 1979, Google Patents.
17. Geria, N., *Antiperspirant stick composition*. 1980, Google Patents.
18. Laba, D., J.J. Margres, and K. Burkhardt, *Antiperspirant/deodorant stick compositions*. 1985, Google Patents.
19. Shevade, M., R.J. Bianchini, and W. Lee, *Low residue antiperspirant solid stick composition*. 1996, Google Patents.
20. Tanner, P.R., R.G. Nunn, and J.P. Luebbe, *Low residue antiperspirant sticks*. 1992, Google Patents.
21. Mullin, J.W., *Crystallization*. 4th ed. 2001: Butterworth-Heinemann.
22. Smart, L.E. and E.A. Moore, *Solid State Chemistry: An Introduction, 2nd Edition*. 1995, Boca Raton: Taylor & Francis.
23. Beckmann, W., *Crystallization: Basic Concepts and Industrial Applications*. 2013, Hoboken: John Wiley & Sons.
24. Szwacki, N.G. and T. Szwacka, *Basic Elements of Crystallography*. 2nd Edition ed. 2016, Boca Raton: CRC Press.
25. L.H., L., *Fundermentals of Adhesion*. 1991, New York: Springer.
26. D.L., P., et al., *Introduction to Organic Laboratory Techniques: A Small Scale Approach*. 2005, Belmont: Thomson Learning.
27. Boothroyd, S., et al., *Solubility prediction from first principles: a density of states approach*. *Physical Chemistry Chemical Physics*, 2018. **20**(32): p. 20981-20987.

28. Çengel, Y.A. and M.A. Boles, *Thermodynamics: An Engineering Approach*. 1998: McGraw Hill.
29. G.W.F., D. *Thermodynamics*. [cited 2019 9th August 2019]; Available from: <https://www.britannica.com/science/thermodynamics>.
30. Ostwald, W., *Studien über die Bildung und Umwandlung fester Körper*. Zeitschrift für Physikalische Chemie, 1897. **22U(1)**: p. 289.
31. Miers, H.A. and F. Isaac, *The spontaneous crystallisation of binary mixtures.— Experiments on Salol and Betol*. Proceedings of the Royal Society of London. Series A, Containing Papers of a Mathematical and Physical Character, 1907. **79(531)**: p. 322-351.
32. Miers, H.A. and F. Isaac, *XLVII.—The refractive indices of crystallising solutions, with especial reference to the passage from the metastable to the labile condition*. Journal of the Chemical Society, Transactions, 1906. **89(0)**: p. 413-454.
33. Rodríguez - hornedo, N. and D. Murphy, *Significance of controlling crystallization mechanisms and kinetics in pharmaceutical systems*. Journal of Pharmaceutical Sciences, 1999. **88(7)**: p. 651-660.
34. Cejka, J., A. Corma, and S. Zones, *Zeolites and Catalysis, Synthesis, Reactions and Applications*. 2010, Weinheim: WILEY.
35. Yang Yang, B.C., *Functions of triacylglycerols during plant development and stress*. Current Opinion in Biotechnology, 2018. **49**: p. 191-198.
36. Himawan, C., V.M. Starov, and A.G.F. Stapley, *Thermodynamic and kinetic aspects of fat crystallization*. Advances in Colloid and Interface Science, 2006. **122(1)**: p. 3-33.
37. Sreenivasan, B., N.R. Kamath, and J.G. Kane, *Studies on castor oil. II. Hydrogenation of castor oil*. Journal of the American Oil Chemists Society, 1957. **34(6)**: p. 302-307.
38. Magauran, E.D., et al., *Rheological additive comprising derivatives of castor oil*. 1994, Google Patents.
39. Patel, V.R., et al., *Castor Oil: Properties, Uses, and Optimization of Processing Parameters in Commercial Production*. Lipid insights, 2016. **9**: p. 1-12.
40. ACME-HARDESTY, *Hydrogenated Castor Oil - Safety Data Sheet*. 2013.
41. Sato, K., *Crystallization behaviour of fats and lipids — a review*. Chemical Engineering Science, 2001. **56(7)**: p. 2255-2265.
42. Gioielli, L.A., I.S. Simões, and J.N. Rodrigues, *Crystal morphology and interactions of binary and ternary mixtures of hydrogenated fats*. Journal of Food Engineering, 2003. **57(4)**: p. 347-355.
43. Larsson, K., *Classification of glyceride crystal forms*. Acta Chem. Scand, 1966. **20**: p. 2255-2260.
44. Sato, K., *Solidification and phase transformation behaviour of food fats — a review*. Lipid / Fett, 1999. **101(12)**: p. 467-474.
45. Gaonkar, A.G. and A. McPherson, *Ingredient Interactions: Effects on Food Quality, Second Edition*. 2nd Edition ed. 2016, Boca Raton: CRC Press.
46. Da Silva, E., S. Bresson, and D. Rousseau, *Characterization of the three major polymorphic forms and liquid state of tristearin by Raman spectroscopy*. Chemistry and Physics of Lipids, 2009. **157(2)**: p. 113-119.
47. Matovic, M., et al., *Thermal Properties of Tristearin by Adiabatic and Differential Scanning Calorimetry*. Journal of Chemical & Engineering Data, 2005. **50(5)**: p. 1624-1630.
48. Garti, N. and K. Sato, *Crystallization Processes in Fats and Lipid Systems*. 2001: Taylor & Francis.
49. Kellens, M., W. Meeussen, and H. Reynaers, *Study of the polymorphism and the crystallization kinetics of tripalmitin: A microscopic approach*. Journal of the American Oil Chemists' Society, 1992. **69(9)**: p. 906-911.

50. Himawan, C., et al., *Polymorphic occurrence and crystallization rates of tristearin/tripalmitin mixtures under non-isothermal conditions*. European Journal of Lipid Science and Technology, 2007. **109**(1): p. 49-60.
51. Lush. *Stearic Acid*. 2019; Available from: <https://www.lush.co.uk/stearic-acid>.
52. lowimpact.org. *Why some soap-makers refuse to use palm oil and how you can help them* 2013; Available from: <http://www.lowimpact.org/why-some-soap-makers-refuse-to-use-palm-oil-and-how-you-can-help-them/>.
53. Ventolà, L., et al., *Polymorphism of N-Alkanols: 1-Heptadecanol, 1-Octadecanol, 1-Nonadecanol, and 1-Eicosanol*. Chemistry of Materials, 2002. **14**(2): p. 508-517.
54. Centre, C.C.D. *1-Octadecanol γ form crystal structure CSD Entry - ZZZAKJ01*. 1996 20th May 2018]; Available from: <https://www.ccdc.cam.ac.uk/structures/Search?Compound=octadecanol&DatabaseToSearch=Published>.
55. Ishikawa, S. and I. Ando, *Structural studies of n-octadecanol by variable-temperature solid-state high-resolution ^{13}C NMR spectroscopy*. Journal of Molecular Structure, 1993. **291**(2): p. 183-190.
56. Izumi, K., *Lattice Defects in Normal Alcohol Crystals*. Japanese Journal of Applied Physics, 1977. **16**(12): p. 2103-2108.
57. Valoppi, F., S. Calligaris, and A.G. Marangoni, *Phase Transition and Polymorphic Behavior of Binary Systems Containing Fatty Alcohols and Peanut Oil*. Crystal Growth & Design, 2016. **16**(8): p. 4209-4215.
58. Ventolà, L., et al., *Melting behaviour in the n-alkanol family. Enthalpy–entropy compensation*. Physical Chemistry Chemical Physics, 2004. **6**(8): p. 1786-1791.
59. Ventola, L., et al., *Solid state equilibrium in the n-alkanols family: the stability of binary mixed samples*. Physical Chemistry Chemical Physics, 2003. **5**(5): p. 947-952.
60. Gallagher, H.F., *Process of making white petrolatum*. 1931, Google Patents.
61. Fontana, B.J., *The Relation of Crystal Habit to the Polymorphic Behavior of Long-Chain Paraffin Hydrocarbons*. The Journal of Physical Chemistry, 1953. **57**(2): p. 222-226.
62. Ferris, S.W. and H.C. Cowles, *Crystal Behavior of Paraffin Wax*. Industrial & Engineering Chemistry, 1945. **37**(11): p. 1054-1062.
63. Edwards, R.T., *Crystal habit of paraffin wax*. Industrial & Engineering Chemistry, 1957. **49**(4): p. 750-757.
64. Warth, A.H., *The chemistry and technology of waxes*. Soil Science, 1956. **82**(4): p. 344.
65. Bekker, M., et al., *Petrolatum composition*. 2013, Google Patents.
66. Birdwell, B.F. and F.W. Jessen, *Crystallization of Petroleum Waxes*. Nature, 1966. **209**(5021): p. 366-368.
67. Hoffman, J.D. and B.F. Decker, *Solid State Phase Changes in Long Chain Compounds*. The Journal of Physical Chemistry, 1953. **57**(5): p. 520-529.
68. Buerger, M.J., *The Theory of Crystal Structure Analysis. A. I. Kitaigorodskii. Translated from the Russian by David and Katherine Harker. Consultants Bureau, New York, 1961. xi + 275 pp. Illus. \$12.50*. Science, 1961. **134**(3488): p. 1412-1413.
69. Muller, A., *A Further X-Ray Investigation of Long Chain Compounds (n-Hydrocarbon)*. Proceedings of the Royal Society of London A: Mathematical, Physical and Engineering Sciences, 1928. **120**(785): p. 437-459.
70. Smith, A.E., *The Crystal Structure of the Normal Paraffin Hydrocarbons*. The Journal of Chemical Physics, 1953. **21**(12): p. 2229-2231.
71. Carpenter, J.A., *The Physical and Chemical Properties of Paraffin Wax, Particularly in the Solid State*. Journ. Inst. Petrol. Technol, 1926. **12**: p. 288-315.
72. Clarke, E.W., *Crystal types of pure hydrocarbons in the paraffin wax range*. Industrial & Engineering Chemistry, 1951. **43**(11): p. 2526-2535.

73. Müller, A. *Crystal structure of the normal paraffins at temperatures ranging from that of liquid air to the melting point.* in *Proc. R. Soc. London A.* 1930.
74. Bragg, W.L., *The crystalline state : a general survey.* 1949, London: Bell.
75. Buchler, C.C. and G.D. Graves, *The Petroleum Waxes.* Industrial & Engineering Chemistry, 1927. **19**(6): p. 718-724.
76. Padgett, F.W., D.G. Hefley, and A. Henriksen, *Wax Crystallization A Preliminary Report.* Industrial & Engineering Chemistry, 1926. **18**(8): p. 832-835.
77. Ferris, S.W., H.C. Cowles, and L.M. Henderson, *Composition of paraffin wax.* Industrial & Engineering Chemistry, 1929. **21**(11): p. 1090-1092.
78. Espeau, P., et al., *Review on the energetic and crystallographic behaviour of n-alkanes .1. series form C₈H₁₈ up to C₂₁H₄₄.* Journal de Chimie Physique et de Physico-Chimie Biologique, 1996. **93**(7-8): p. 1217-1238.
79. Ungar, G. and N. Masic, *Order in the rotator phase of n-alkanes.* The Journal of Physical Chemistry, 1985. **89**(6): p. 1036-1042.
80. Severtson, S.J. and M.J. Nowak, *Molecular Restructuring Kinetics and Low-Velocity Wetting of n-Alkane Rotator Phases by Polar Liquids.* Langmuir, 2002. **18**(24): p. 9371-9376.
81. Hammami, A. and A.K. Mehrotra, *Thermal behaviour of polymorphic n-alkanes: effect of cooling rate on the major transition temperatures.* Fuel, 1995. **74**(1): p. 96-101.
82. Genovese, A., et al., *Crystallisation, melting, recrystallisation and polymorphism of n-eicosane for application as a phase change material.* Thermochimica Acta, 2006. **443**(2): p. 235-244.
83. Gerson, A.R., et al., *Novel kinetic and structural studies of wax crystallisation.* Journal of Crystal Growth, 1990. **99**(1-4): p. 145-149.
84. Blach, C., et al., *Revisiting the crystallization behavior of stearyl alcohol : stearic acid (SO : SA) mixtures in edible oil.* RSC Advances, 2016. **6**(84): p. 81151-81163.
85. Gandolfo, F.G., A. Bot, and E. Flöter, *Structuring of edible oils by long-chain FA, fatty alcohols, and their mixtures.* Journal of the American Oil Chemists' Society, 2004. **81**(1): p. 1-6.
86. Schaink, H.M., et al., *Crystal network for edible oil organogels: Possibilities and limitations of the fatty acid and fatty alcohol systems.* Food Research International, 2007. **40**(9): p. 1185-1193.
87. Valoppi, F., S. Calligaris, and A.G. Marangoni, *Structure and physical properties of oleogels containing peanut oil and saturated fatty alcohols.* European Journal of Lipid Science and Technology, 2017. **119**(5): p. 1600252.
88. Fitzpatrick, M.E., et al., *Determination of residual stresses by X-ray diffraction,* in *A National Measurement Good Practice Guide.* 2005.
89. Sonwai, S. and M.R. Mackley, *The effect of shear on the crystallization of cocoa butter.* Journal of the American Oil Chemists' Society, 2006. **83**(7): p. 583-596.
90. MacMillan, S.D., et al., *In Situ Small Angle X-ray Scattering (SAXS) Studies of Polymorphism with the Associated Crystallization of Cocoa Butter Fat Using Shearing Conditions.* Crystal Growth & Design, 2002. **2**(3): p. 221-226.
91. Kennedy, J.F. and M. Thorley, *Crystal Structure Determination, William Clegg, Oxford University Press, Oxford, 1998, 84 pp., ISBN 0-19-855-901-1.* Bioseparation, 1999. **8**(6): p. 339-339.
92. B.D., C., *Elements of X-RAY DIFFRACTION.* Second ed. 1978, Boston: ADDISON-WESLEY PUBLISHING COMPANY INC.
93. Struble, L.J. and X. Ji, *9 - Rheology,* in *Handbook of Analytical Techniques in Concrete Science and Technology,* V.S. Ramachandran and J.J. Beaudoin, Editors. 2001, William Andrew Publishing: Norwich, NY. p. 333-367.

94. J., P.P., M.A. T., and F. R.W., *Introduction to Fluid Mechanics*. 2009, Hoboken: John Wiley & Sons.
95. Britannica, T.E.o.E. *Encyclopaedia Britannica*. Shear stress 2018 June 12, 2018 [cited 2019 12th June 2019]; Available from: <https://www.britannica.com/science/shear-stress>.
96. Günther Höhne, W.H., H.-J. Flammersheim, *Differential Scanning Calorimetry*. 2003: Springer Science & Business Media.
97. Trtik, P., J. Kaufmann, and U. Volz, *On the use of peak-force tapping atomic force microscopy for quantification of the local elastic modulus in hardened cement paste*. Cement and Concrete Research, 2012. **42**(1): p. 215-221.
98. Schön, P., et al., *Quantitative mapping of elastic moduli at the nanoscale in phase separated polyurethanes by AFM*. European Polymer Journal, 2011. **47**(4): p. 692-698.
99. Young, T.J., et al., *The use of the PeakForce™ quantitative nanomechanical mapping AFM-based method for high-resolution Young's modulus measurement of polymers*. Measurement Science and Technology, 2011. **22**(12): p. 125703.
100. Aufderhorst-Roberts, A., U. Chandra, and S.D. Connell, *Three-Phase Coexistence in Lipid Membranes*. Biophysical Journal, 2017. **112**(2): p. 313-324.
101. Derjaguin, B.V., V.M. Muller, and Y.P. Toporov, *Effect of contact deformations on the adhesion of particles*. Journal of Colloid and Interface Science, 1975. **53**(2): p. 314-326.
102. Pittenger, B., N. Erina, and C. Su, *Quantitative Mechanical Property Mapping at the Nanoscale with PeakForce QNM*. 2010.
103. Toledo, M. *Hot stage microscopy systems*. 2015 5th May, 2019]; Available from: http://us.mt.com/us/en/home/products/Laboratory_Analytics_Browse/TA_Family_Browse/hot-stage_systems.html.
104. Sparkman, O.D., Z. Penton, and F. Kitson, *Gas Chromatography and Mass Spectrometry: A Practical Guide*. 2nd Edition ed. 2011, Antioch: Elsevier.
105. Nagoshi, M., T. Aoyama, and K. Sato, *Extraction of topographic and material contrasts on surfaces from SEM images obtained by energy filtering detection with low-energy primary electrons*. Ultramicroscopy, 2013. **124**(0): p. 20-25.
106. Goodhew, P., J. Humphreys, and J. Beanland, *Electron Microscopy and Analysis*. 2000.
107. Lloyd, G.E., *Atomic number and crystallographic contrast images with the SEM: a review of backscattered electron techniques*. Mineralogical Magazine, 1987. **51**: p. 3-19.
108. Brookfield, *BROOKFIELD DV-II+ Pro PROGRAMMABLE VISCOMETER Operating Instructions*.
109. Laboratories, B.E., *Rheocalc32*. 2006, Brookfield Engineering Laboratories.
110. AnyDesk, *Anydesk*. 2018, AnyDesk Software GmbH.
111. Parallels, *Parallels desktop for mac*. 2018, Parallels International GmbH.
112. Nguyen, T.T.H., et al., *Precision measurement of the growth rate and mechanism of ibuprofen {001} and {011} as a function of crystallization environment*. CrystEngComm, 2014. **16**(21): p. 4568-4586.
113. Turner, T.D., et al., *The influence of solution environment on the nucleation kinetics and crystallisability of para-aminobenzoic acid*. Physical Chemistry Chemical Physics, 2016. **18**(39): p. 27507-27520.
114. Nordström, F.L. and Å.C. Rasmuson, *Prediction of solubility curves and melting properties of organic and pharmaceutical compounds*. European Journal of Pharmaceutical Sciences, 2009. **36**(2): p. 330-344.
115. Schneider, G.M., *J. M. Prausnitz: Molecular Thermodynamics of Fluid Phase Equilibria. International Series in the Physical and Chemical Engineering Sciences*.

- Prentice-Hall Inc., Englewood Cliffs, New Jersey, 1969. 523 Seiten Preis: 145 s.
- Berichte der Bunsengesellschaft für physikalische Chemie, 1970. **74**(3): p. 308-308.
116. Kashchiev, D., et al., *Effect of cooling rate on the critical undercooling for crystallization*. Journal of Crystal Growth, 2010. **312**(5): p. 698-704.
117. Camacho Corzo, D.M., et al., *Nucleation mechanism and kinetics from the analysis of polythermal crystallisation data: methyl stearate from kerosene solutions*. CrystEngComm, 2014. **16**(6): p. 974-991.
118. van Langevelde, A., R. Peschar, and H. Schenk, *Structure of [beta]-trimyristin and [beta]-tristearin from high-resolution X-ray powder diffraction data*. Acta Crystallographica Section B, 2001. **57**(3): p. 372-377.
119. Fujimoto, K., T. Yamamoto, and T. Hara, *Crystal structure and molecular motion in octadecanol (C₁₈H₃₇OH)*. Rep. Prog. Polym. Phys. Jpn., 1985. **28**: p. 163-166.
120. Reuter, J. and A. Würflinger, *Differential Thermal Analysis of Long-Chain n-Alcohols under High Pressure*. Berichte der Bunsengesellschaft für physikalische Chemie, 1995. **99**(10): p. 1247-1251.
121. van Miltenburg, J.C., H.A.J. Oonk, and L. Ventola, *Heat Capacities and Derived Thermodynamic Functions of 1-Octadecanol, 1-Nonadecanol, 1-Eicosanol, and 1-Docosanol between 10 K and 370 K*. Journal of Chemical & Engineering Data, 2001. **46**(1): p. 90-97.
122. Mazzanti, G., et al., *Orientation and Phase Transitions of Fat Crystals under Shear*. Crystal Growth & Design, 2003. **3**(5): p. 721-725.
123. Nagappa, S.K. Nataraju, and D. Krishnamurti, *Optical Behavior of Natural Oils and Fats of Plant Origin*. Molecular Crystals and Liquid Crystals, 1986. **133**(1-2): p. 31-54.
124. Parveen, S., et al., *Linking solution chemistry to crystal nucleation: the case of tetrolic acid*. Chemical Communications, 2005(12): p. 1531-1533.
125. Chiarella, R.A., et al., *The nucleation of inosine: the impact of solution chemistry on the appearance of polymorphic and hydrated crystal forms*. Faraday Discussions, 2007. **136**(0): p. 179-193.
126. Granberg, R.A., et al., *Primary nucleation of paracetamol in acetone–water mixtures*. Chemical Engineering Science, 2001. **56**(7): p. 2305-2313.
127. Kashchiev, D., et al., *Dependence of the Critical Undercooling for Crystallization on the Cooling Rate*. The Journal of Physical Chemistry B, 2010. **114**(16): p. 5441-5446.
128. systems, T.c. *Crystal 16*. 2019; Available from: <https://www.crystallizationsystems.com/crystal16>.
129. Kaskiewicz, P.L., et al., *Isothermal by Design: An Accelerated Approach to the Prediction of the Crystallizability of Slowly Nucleating Systems*. Organic Process Research & Development, 2019. **23**(9): p. 1948-1959.
130. Davies, M. and B. Kybett, *Sublimation and vaporization heats of long-chain alcohols*. Transactions of the Faraday Society, 1965. **61**(0): p. 1608-1617.
131. Mohsen-Nia, M., H. Amiri, and B. Jazi, *Dielectric Constants of Water, Methanol, Ethanol, Butanol and Acetone: Measurement and Computational Study*. Journal of Solution Chemistry, 2010. **39**(5): p. 701-708.
132. Dornte, R.W. and C.P. Smyth, *The dielectric polarization of liquids. X. The polarization and refraction of the normal paraffins*. Journal of the American Chemical Society, 1930. **52**(9): p. 3546-3552.
133. Gelest. *Properties of Decamethylcyclopentasiloxane*. [cited 2019 20th July 2019]; Available from: <https://www.gelest.com/product/decamethylcyclopentasiloxane/>.
134. MacMillan, S.D., *Studies of the Crystallisation of Mixed Confectionery Fats under Sheared Conditions using On-line Synchrotron Radiation SAXS Techniques in Department of Mechanical and Chemical Engineering 2000 Heriot-Watt University*
135. AUTODESK, *AUTOCAD*. 2018.
136. SolidWorks, *SolidWorks*. 2018, Dassault Systèmes.

137. Gullikson, E. *X-ray Attenuation Length*. 2010; Available from: http://henke.lbl.gov/optical_constants/atten2.html.
138. Henke, B.L., E.M. Gullikson, and J.C. Davis, *X-Ray Interactions: Photoabsorption, Scattering, Transmission, and Reflection at E = 50-30,000 eV, Z = 1-92*. Atomic Data and Nuclear Data Tables, 1993. **54**(2): p. 181-342.
139. Hubbell, J.H., et al., *Atomic form factors, incoherent scattering functions, and photon scattering cross sections*. Journal of physical and chemical reference data, 1975. **4**(3): p. 471-538.
140. Gandolfo, F.G., A. Bot, and E. Flöter, *Phase diagram of mixtures of stearic acid and stearyl alcohol*. Thermochemica Acta, 2003. **404**(1–2): p. 9-17.